DGK Deutsche Geodätische Kommission
der Bayerischen Akademie der Wissenschaften

Reihe B Angewandte Geodäsie Heft Nr. 318

e^2.motion

Earth System Mass Transport Mission (Square)

– Concept for a Next Generation Gravity Field Mission –

Final Report of Project
"Satellite Gravimetry of the Next Generation (NGGM-D)"

Prepared by the

NGGM-D Team

München 2014

Verlag der Bayerischen Akademie der Wissenschaften
in Kommission beim Verlag C. H. Beck

ISSN 0065-5317 ISBN 978-3-7696-8597-8

DGK Deutsche Geodätische Kommission
der Bayerischen Akademie der Wissenschaften

Reihe B Angewandte Geodäsie Heft Nr. 318

e^2.motion

Earth System Mass Transport Mission (Square)

– Concept for a Next Generation Gravity Field Mission –

Final Report of Project
"Satellite Gravimetry of the Next Generation (NGGM-D)"

Prepared by the

NGGM-D Team

München 2014

Verlag der Bayerischen Akademie der Wissenschaften
in Kommission beim Verlag C. H. Beck

ISSN 0065-5317 ISBN 978-3-7696-8597-8

Adresse der Deutschen Geodätischen Kommission:

Deutsche Geodätische Kommission
Alfons-Goppel-Straße 11 ● D – 80 539 München
Telefon +49 – 89 – 23 031 1113 ● Telefax +49 – 89 – 23 031 - 1283 / - 1100
e-mail hornik@dgfi.badw.de ● http://www.dgk.badw.de

ISSN 0065-5317 ISBN 978-3-7696-8597-8

Note

The project "Next Generation Gravity Field Mission" is supported by the

German Federal Ministry of Economics and Technology (BMWi) on the basis of a decision of the German Bundestag

and the

Project Management Agency of the German Aerospace Center (DLR)

Coordinating Institution
Technische Universität München (TUM)
Institut für Astronomische und Physikalische Geodäsie (IAPG)
Arcisstrasse 21, 80333 München, Germany

Project Management & Report Compilation
Thomas Gruber & Michael Murböck
Technische Universität München (TUM)
Institut für Astronomische und Physikalische Geodäsie (IAPG)
e-mail: thomas.gruber@tum.de & murboeck@bv.tum.de

Contributing Partners
– Institut für Geodäsie und Geoinformation (IGG), Universität Bonn
– Geodätisches Institut (GIS), Universität Stuttgart
– SpaceTech GmbH (STI), Immenstaad
– Max-Planck-Institut für Gravitationsphysik (AEI), Teilinstitut Hannover
– Institut für Erdmessung (IfE), Leibniz Universität Hannover
– Helmholtz-Zentrum Potsdam Deutsches GeoForschungsZentrum (GFZ)
– Airbus Defence & Space (ASG), Immenstaad
– Gesellschaft für Technologietransfer mbH (TransMIT), Gießen

NGGM-D Team Composition

Name	*Institution*	*Name*	*Institution*	*Name*	*Institution*
Baldesarra Mark	ASG	Heinzel Gerhard	AEI	Naeimi Majid	IfE
Brieden Phillip	IfE	Iran Pour Siavash	GIS	Pail Roland	IAPG
Danzmann Karsten	AEI	Kusche Jürgen	IGG	Raimondo Jean	GFZ
Daras Ilias	IAPG	Langemann Manfred	ASG	Reiche Jens Claude	AEI
Doll Bernhard	STI	Löcher Anno	IGG	Reubelt Tilo	GIS
Feili Davar	TransMIT	Müller Jürgen	IfE	Sheard Benjamin	AEI
Flechtner Frank	GFZ	Müller Vitali	AEI	Sneeuw Nico	GIS
Flury Jakob	IfE	Murböck Michael	IAPG	Wang Xinxing	STI
Gruber Thomas	IAPG				

Executive Summary

The main goal of this study was the development of a mission concept for the long term high precision and homogeneous determination of the time variable gravity field with significant improved sensitivity and spatial resolution as compared to nowadays techniques, which are used on GRACE and GRACE-FO. This goal is supported by the international science community and is content of resolutions issued by several institutions and science communities like for example resolution No. 2 of the International Union of Geodesy and Geophysics (IUGG; Melbourne, 2011, refer to: http://iugg.org/resolutions). Long duration, higher sensitivity and improved spatial/temporal resolution of mass variation observations are required by more or less all geoscience disciplines in order to make their models more realistic and in order to assimilate them into these models. Long term analyses and calibration of geophysical models contribute to a better understanding of the coupling of the different phenomena and consequently improve models and provide more realistic prediction capabilities. For this reason, in future a continuous monitoring of mass distribution in the Earth system is required.

The proposed mission concept is a first step to fulfil these requirements in future. The concept we have developed is called e^2.motion, because it was further developed from the e.motion mission proposal now making use of a dual pair satellite to satellite tracking concept. It relies on one hand on improved measurement accuracies of inter-satellite distance measurements and of the non-gravitational forces with accelerometers and on the other hand on innovative orbit configurations with multiple satellite pairs. Improved measurement accuracy can be obtained by using a laser interferometer (LRI) instead of a microwave system for inter-satellite observations and by improved sensitivity of the accelerometers as compared to the one used for GRACE in all three axes. These improvements are needed in order to take full advantage of the envisaged satellite and orbit configuration, which is required to reach improved sensitivity, spatial and temporal resolution. To increase sensitivity a lower orbit height is needed (around 400 km), which requires a concept for drag compensation or drag reduction in order to compensate for the non-gravitational forces and in order to measure with higher accuracies. Only multi-directional inter-satellite observations provide a quasi isotropic error distribution and consequently are needed for a global homogeneous monitoring of mass variations. This can be realized either by a so-called pendulum orbit (for a single pair mission) for which the ascending nodes of the two orbital planes are slightly shifted against each other or by a multi pair mission concept where each satellite pair has a different inclination (one polar pair and one inclined pair). The pendulum configuration requires more complex methods for attitude determination, attitude control and thruster techniques, in order to guarantee a permanent precise pointing of the two satellites against each other**,** which is required to maintain the laser link for permanent range measurements. For this reason in this study a dual pair mission concept was investigated in more detail as it offers similar or even more advantages as a pendulum orbit, but in general is less complex from a technological point of view.

Some of the above mentioned scientific and technological challenges have been analysed in pre-studies, but without regarding the total complexity of such a mission in detail. Here in particular it is referred to the following studies and projects: e.motion mission proposal for Earth Explorer 8 call (opportunity mission), ESA Next Generation Gravity Field Mission Studies (NGGM); BMBF Geotechnology project „Future concepts of gravity field satellite missions“. The results of these studies are regarded as an important starting point for this study. The following paragraphs describe the major steps performed in this study and summarize the main conclusions we derived from the various analyses and simulation steps.

Science and Mission Requirements and Orbit Configuration:

Science and mission requirements have been analysed by various pre-studies (e.motion, NGGM studies). The identified requirements for geophysical applications strongly diverge (by a factor of 10) and are influenced by the studies boundary conditions (financial volume of an Earth Explorer Opportunity Mission or technological boundary conditions at the time of the study). Therefore, a consolidated view of these requirements has been derived, which form the baseline of the e^2.motion mission concept. With the help of realistic simulators an optimal balance between science and mission requirements, measurement accuracies of the various instruments and orbit configuration has been determined. As a result, not only science requirements, but also requirements on measurement systems and on the orbit configuration have been specified. In particular for e^2.motion the following requirements were identified:

(1) 1 mm monthly geoid height error at 200 km (minimum) or 150 km (optimum) spatial resolution.
(2) Weekly or shorter temporal resolution of the global gravity field with reduced spatial resolution.
(3) Mission duration at least one decade.
(4) Dual-pair mission with a polar pair and an inclined pair with 70 degree inclination.
(5) Orbit altitude 420 km with 31 days repeat cycle and sub-cycles.
(6) Inter-satellite distance 100 km.
(7) Instrument accuracies at a level of 40 to 200 $\text{nm/Hz}^{1/2}$ ($f > 10$ mHz) for the ranging and $4 \cdot 10^{-11}$ to $2 \cdot 10^{-10}$ $\text{m/s}^2/\text{Hz}^{1/2}$ ($1 < f < 10$ mHz) for the accelerometers.

Attitude and Orbit Control System and Instrument Concept:

The fundamental measurement quantity to be observed in a satellite to satellite tracking mission is the distance variation between the two satellites. With the microwave instrument on GRACE and GRACE-FO this is observed with a noise level of about 2 $\mu\text{m}/\sqrt{\text{Hz}}$. A heterodyne laser interferometer, as it is developed since several years for the LISA mission and as it is implemented as a demonstrator on GRACE-FO, in principle is able to reduce this noise level by some orders of magnitude (e.g. to 80 $\text{nm}/\sqrt{\text{Hz}}$ for GRACE-FO and to 25 $\text{nm}/\sqrt{\text{Hz}}$ for e^2.motion). Then other error noise sources become dominant. The practical realization of the laser interferometer has been studied theoretically and experimentally based on experiences gained with LISA and GRACE-FO. Some limiting factors for the laser interferometer performance like frequency noise, pointing jitter noise, readout noise and others were analysed in detail and were identified as not critical to reach the envisaged performance. Both optical axes of the satellites need to be aligned to each other and kept at a level of better than 100µrad accuracy. This aspect cannot be regarded on instrument level only, but needs to be studied by multi system investigations on mission level, e.g. because the laser interferometer can provide additional information about the satellite alignment to the attitude control system by making use of a differential wavefront sensor. For this reason also GNSS receivers as well as high precision star cameras also play an important role for the instrument concept foreseen for this mission.

As a second fundamental measurement quantity, the non-gravitational forces have to be observed. These observations are needed either to subtract them in the data analysis or to compensate them at satellite level with fast reacting and scalable thrusters (drag compensation or drag-free operation). In times of high solar activity and regarding the chosen orbit height, the non-gravitational accelerations could be outside the measurement range of the accelerometers. In order to avoid saturation of the accelerometers and to measure the accelerations with the desired sensitivity (10^{-11} m/s^2 and one order of magnitude better than for GRACE and GRACE-FO) it has been identified that drag compensation is required. Concerning the thrust technology for drag compensation and orbit maintenance a number of options were assesses including cold gas and µ-Newton radio-frequency thrusters taking into account a lower satellite height and high solar activity. Due to reduced system complexity as actuators pulse width modulated cold gas thrusters and magnetic torquers were chosen, which are adequate for drag compensation, formation control and pointing requirements at the chosen orbit altitude.

Simulation of Observations and Numerical Analyses:

Because in satellite gravimetry always the satellite or the satellite pair represents the sensor it is required to setup a total error budget for the mission, which takes into account instrumental errors, orbit accuracy, attitude determination and control as well as their coupling. This was done with satellite and instrument simulators, which delivered error spectra of the parameters needed for data analysis. In a second step these error spectra, simulated observations as well as external support parameters and their errors were used in a numerical simulation process for gravity field determination. In an inverse computation the achievable accuracy for the chosen satellite configuration was quantified under the assumption of realistic parameters. Such highly complex simulators require themselves an inspection of the applied algorithms and their numerical accuracy in order to make sure that representative results for achievable accuracy and resolution of gravity field variations can be achieved. From pre-studies a number of simulators were available, for which the results were compared in order to ensure that the derived conclusions are meaningful. By combining satellite and gravity field simulators the total system performance was investigated with closed-loop tests, which further on were applied for optimization of the mission layout. The main results which were obtained from the simulation steps were:

1. Error free closed loop simulations showed that all applied numerical simulators are compatible and by far meet the science and mission requirements.
2. Instrument performances as they have been identified for this study are good enough to reach science and mission requirements.
3. Most critical are model errors needed in the gravity field retrieval process in order to avoid temporal aliasing. Here on one hand the atmosphere and ocean models as well as the tide model plays a critical role. Assuming specific model errors at a level of 10 to 15% of the signal and assuming a monthly gravity field retrieval one can meet the minimum science and mission requirements, but not the optimum requirements as they have been specified in this study (1 mm geoid height error at a spatial resolution of 182 km is reachable under these conditions).
4. Model uncertainties can be further reduced by observing higher frequent mass variations than a month. For the chosen mission layout (double pair and orbit sub-cycles) this becomes feasible. Further simulations about this aspect need to be done and currently are topic of another study. Preliminary results are promising and one can expect that the optimum science requirements are reachable.
5. Compared to a single pair mission a double pair mission as specified in this study delivers a quasi homogeneous error structure without dominant errors in North-South direction as it is the case of a polar single pair mission. Only some latitude error patterns could be identified from the numerical simulation results, which need to be further investigated.

Conclusions

In summary, the study results show that a double pair mission as proposed in the e^2.motion concept with a polar and an inclined orbit, has significant advantages compared to a single pair mission. First of all, in order to achieve a specific performance, which by far is better than what one can get with a GRACE type mission (polar non pendulum orbit), the technological complexity can be significantly reduced. A single pair pendulum mission in principle is capable to deliver a similar performance (may be with a less homogeneous error pattern) than a double pair mission, but requires much more technological effort on attitude and orbit control as well as on instrument design. Therefore, by placing two pairs into two different inclinations and by choosing the right orbit height, repeat cycles and sub-cycles one can reach without the pendulum option at least the same, but probably even better performance. Special emphasis needs to be given to the temporal aliasing of model errors, which have impact on the monthly gravity field performance. It is essential to enable observability of higher frequent mass signals by choosing the right orbit configuration and its repeatability. By this, a large part of the models can be replaced by observations, which helps to reduce the model errors significantly. This requires adapted gravity field processing strategies, which are currently under investigation.

Table of Contents

1 NGGM-D Study Approach

In spring 2012 the German Federal Ministry of Economics and Technology announced a competitive invitation to tender to study innovative space-based Earth observation concepts. Under the coordination of the Technische Universität MünchenTechnical a larger team of German universities, research facilities and industry agreed to submit a preliminary proposal to study a next generation gravity field mission concept in this framework. The preliminary proposal was positively evaluated in autumn 2012 and the team was asked to submit a full proposal for a study over one year. The full proposal was submitted in early 2013 and accepted in May 2013. After some preparatory administrative issues were solved, finally the project started in June 2013 and lasted until May 2014. The project was managed by the Project Management Agency of the German Aerospace Center (DLR).

The project was structured by three major steps following each other (see Figure 1-1). As initial step a consolidation of science requirements from previous studies was performed in order to derive a baseline set of science and mission requirements. In addition investigations about optimal orbit configurations needed to reach the science goals were done. Here also a trade-off analysis between pendulum and double-pair (Bender type) missions was performed, which led to the conclusion that a double pair mission with a monthly repeat cycle (and short period sub-cycles) should be the baseline for all follow-on steps. Step number two was the definition and design of an adequate attitude and orbit control system (AOCS) and an instrument concept, which is capable to meet the requirements identified in step 1. The AOCS was defined in a way that on one hand the requirements driven by the instrument concept are met and that on the other hand the science goals can be reached. The definition of the AOCS and instrument concepts needed a close interaction and an iterative approach in order to determine the optimum design for the mission concept. The third step, finally intended to make a complete numerical simulation applying the defined mission concept in order to identify if the science requirements can be met. From simulated observations applying specific noise scenarios for the instruments and model errors monthly gravity fields were recomputed by different approaches, which gave us more confidence about the numerical simulation results. These recomputed fields were compared with the original gravity field model and performance parameters for the designed mission concept were determined.

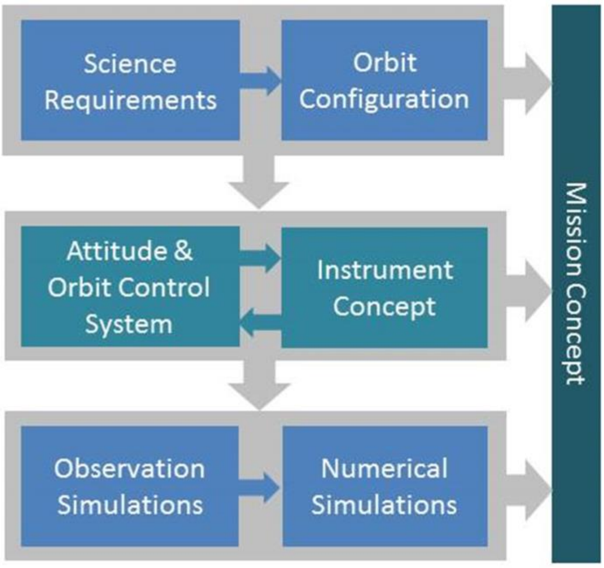

Figure 1-1: NGGM-D study approach

Each of the steps as shown in Figure 1-1 was under responsibility of one team involved in the study, but with contributing partners from several other teams (refer to Table 1-1; for the individuals involved refer to the team composition page above). By this a close interaction between the various groups was ensured, which was important in order to take into account specific boundary conditions or technical constraints, which might have impact to the overall mission design. In addition we could make use of all available expertise in the different teams, which was required to investigate some specific issues.

Table 1-1: Study responsibilities

Project Step	Responsibility	Contributions by
Project Management	IAPG	
Science and Mission Requirements	IGG	IfE, IAPG, GIS
Orbit Configuration	GIS	GFZ, IAPG, STI
Attitude and Orbit Control System	STI	AEI, TransMIT, ASG
Instrument Concept	AEI	STI, IfE, IAPG, STI, GIS, ASG
Simulation of Observations	IfE	IAPG, GFZ
Numerical Simulations	GFZ	IGG, IAPG
Mission Concept	IAPG	All

The following chapters provide detailed reports about the study results obtained from the various steps. Sometimes specific technological issues are repeated in different chapters, but special emphasis was given to consistency within the study. Each of the main chapters (2 to 7) was written by the responsible team always incorporating contributions from the study partners involved. The final chapter about the mission concept (section 8) provides summary and conclusions about the results obtained from the individual steps and tries to figure out the baseline concept for a next generation gravity field mission.

The mission concept which is presented in this report was named e^2.motion (Earth system mass transport mission – square). The reason behind this is, that it was on one hand based on the e.motion proposal [9], which was submitted in 2010 to ESA answering the Earth Explorer 8 call, and on the other hand, that it consists of 2 pairs of satellites, which means that we square the number of satellites as compared to the original e.motion mission concept.

2 Science and Mission Requirements

This section summarizes the basic figures for the e^2.motion mission design as they have been derived from a user/science requirements analysis. Sections 2.1 and 2.2 review the science requirements as proposed by previous studies and derive recommendations for the envisaged accuracy and science requirements to be applied in the present study. In section 2.3 these figures are transferred into instrument requirements, while section 2.4 discusses the transfer into orbit configuration requirements.

2.1 Science Requirements from Previous Studies

As an initial step science and user requirements are analysed specifically for the following five science application areas, which are: ocean signals, hydrology signals, solid Earth, cryosphere, geodesy. To this end, a number of previous studies have been assessed.

The list of previous studies is found in section 9.1. All studies point more or less to similar science and user requirements for future satellite missions. However there are some different views in specific applications that are merged into representative ones in the numbers given further below and from which science requirements to be applied in this study are derived. The tables can be thus considered as the union of the results of the previous studies.

It is not always clear whether science and user requirements are derived purely from the applications point of view ("what is desirable") or from the simulations point of view ("what is possible"). One should recognize that specific "requirements" derived from gravity mission simulation studies are not strictly independent from each other; in the sense that favoring one area of application inevitably causes loss of quality in other areas (e.g. spatial vs. temporal resolution).

2.1.1 Ocean Signal

Mass-driven ocean signals appear to be present at all temporal and spatial scales. It is common in ocean research to exploit mass change through space gravimetry in combination with other quantities sensors, such as sea surface height from altimetry or steric height from modeling and/or temperature/salinity measurements. Future requirements for space gravimetry thus have to be seen in conjunction with the evolution of resolution and accuracy of these techniques. Increasing spatial resolution is generally desired in all applications since, in the common situation, the much stronger land signals tend to leak into ocean mass in the processing of space gravimetry.

Table 2-1: Science and user requirements in ocean sciences

Science area	Temporal requirements	Spatial requirement	target	Geoid error
basin scale mass change	month to decades	1000 - 5000 km	1000 km	0.1 – 2 mm
sea-level change	Inter-annual to decades	200 - 4000 km	200 km	0.17 – 0.3 mm/a
bottom barotropic currents	10d to decades	10 - 200 km	100 km	0.1 – 10 mm

Requirements on spatial domain and temporal coverage can be summarized for all science areas as follows:

- Spatial domain: Global oceans (-90 to +90 latitude)
- Temporal coverage: Continuous (minimum 10 years)

2.1.2 Hydrology Signal

Space gravimetry is the only technique that allows determining total, integrated water mass change, and thus provides an important constraint for all hydrological and hydro-meteorological modeling activities at the relevant scales. Catchments in hydrology and 'tiles' in land surface modeling can be defined at any resolution; meaning that there is no inherent spatial target resolution for these applications. Most studies in fact appear to consider monthly resolution as satisfying for hydrological applications. They tend to note that in specific situations (e.g. onset of the monsoon) hydrological signals may have a high temporal dynamics. Models generally run at time steps of one day or below.

Table 2-2: Science and user requirements for hydrosphere

Science area	Temporal requirements	Spatial requirement	target	Geoid error
Ground water	1-10 days (optimal) – 90 days	10 – 1000 km	200 km (?)	0.5-10 mm 1mm@200km
Soil moisture/ snow	1 day (optimal) – 90 days	10 – 1000 km	150 km	0.5-10 mm 1mm@150km

Requirements on spatial domain and temporal coverage can be summarized for all science areas as follows:

- Spatial domain: Continents (-60 to +60 latitude)
- Temporal coverage: Continuous (minimum 10 years)

2.1.3 Solid Earth

Applications of space gravimetry in solid Earth research are rather diverse, ranging from Earthquake modeling to assessing rheological properties.

Table 2-3: Science and user requirements for solid Earth

Science area		Time scale main period	Expected signal	Precision @resolution	priority
			Geoid/ gravity/EWH		
Lithosphere, upper mantle density		Static		1-2 mgal @ 100km	
Continental lithosphere	Sedimentary basins	Static		1-2 mgal @ 50-100km	
	Rifts			1-2 mgal @ 20-100km	
	Tectonic motion			1-2 mgal @ 100-500km	
Seismic hazards		Static		1 mgal @ 100km	
Ocean Lithosphere Asthenosphere		Static		0.5 mgal @ 100-200km	
Earthquakes Mw 7-8	Co-seismic	Instantaneous	Sub-mm geoid	0.5 mm @ 10-100km	Medium
	Post-seismic	Decadal			Medium
	Slow-earthquakes	Decadal			---
Volcanoes		Secular/ instantaneous	< 1 mm geoid/year		Medium
Plate tectonics			0.05 mm geoid/year	0.01 mm >500 km	Medium
Core motions				0.01 mm > 5000 km	Low
Mantle convection					---
Glacial Isostatic Adjustment		10000-100000 years	1-2 mm geoid/year	1-10 µm @400-500km	High

2.1.4 Cryosphere

Space gravimetry has provided spectacular insight into mass balance of the ice sheets and large glacier systems; and this will likely continue to provide a major driver in the development of requirements. Glacier systems occur at all spatial scales and no specific target resolution may be considered. Unlike with hydrology, temporal requirements are usually less stringent.

Table 2-4: Science and user requirements for cryosphere

Science area		Time scale main period	Expected signal	Precision @resolution	Priority
			Geoid/ gravity/EWH		
Ice sheets	Rock basement	Static		1-5 mgal @ 5-100 km	
	Ice vertical movement			2 cm geoid @ 100-1000 km	
Ice mass balance		Monthly – Seasonal to decades	dm to mm EWH dm EWH/year	1 cm EWH @400km 10cm EWH @200km 1mm EWH/y @400km	High
Polar ice and glaciers		Secular		5 µgal @ 100-1000 km	
Bottom topography Ice compactation		Quasi static		0.01-0.1 mgal @ 20-50 km	
Geoid for sea ice thickness		Static		100 mm @ 10-100 km	
Large ice-stream dynamics Accumulation variability		Monthly to seasonal		0.05 – 0.2 mm	High

2.1.5 Geodesy

Applications of space gravimetry in geodesy are diverse and often related to other disciplines as well: For example, improved satellite orbits find applications in satellite altimetry and help to determine sea level at better precision.

Table 2-5: Science and user requirements for geodetic applications

Science area	Time scale	Expected signal	Precision @resolution	Priority
Leveling by GPS	Static		5-20 mm geoid @20-50 km	
Unified height system	Hours to decadal	Few cm geoid Few mgal	1 mm geoid @200 km 1 µgal gravity @200km	
Inertial navigation system	Static		0.1 mgal @ 5-10 km	
Satellite orbits	Hours to decadal		1 mm geoid @200 km 1 µgal gravity @200km	

2.2 Science Requirements – Consolidated View

Science and user requirements to be applied for the derivation of the e^2.motion mission requirements are to be found by a consolidation of figures from the previous studies (see Table 2-1 to Table 2-5). For deriving a preliminary consolidated suggestion of science requirements we focus on the following study reports (refer to section 9.1):

- e.motion proposal [9] and the related paper (Panet, et al., 2013),

- the ESA study „ Assessment of a Next Generation Mission for Monitoring the Variations of Earth's Gravity by the Alenia consortium [10], here referred to as „NGGM",
- the parallel study by the Astrium consortium [11], here referred to as „NG2".

Each of these studies starts with defining accuracies and science requirements considered as necessary to observe individual geophysical signals. In a second step, these figures are generalized to overall mission accuracies by making trade-offs, which are not always well explained.

A comparison of some of the requirements of the first type is given in the following. The tables and plots arrange science requirements for selected topics from the three studies mentioned above. If necessary, the original values have been converted to geoid errors per monthly solution. The conversion of equivalent water heights (EWH) was performed using the values given in [9], p. 17:

1cm EWH corresponds to	0,04 mm Geoid @ 100km
	0,08 mm Geoid @ 200km
	0,15 mm Geoid @ 400km
	0,30 mm Geoid @ 800km
	0,50 mm Geoid @ 2000km

In converting the trend accuracies from e.motion and NG2 the approach described [11], p. 7-141, was used. Assuming a mission lifetime of 10 years, this led to the relationship:

$$\sigma(\text{month}) = \sigma(\text{trend}) \text{ times } 63.64$$

Trend accuracies from NGGM were not subject to conversion since the table includes monthly errors as well. The conversion within the table is based on a mission lifetime of 11 years leading to a conversion factor 36. This disagreement with the value determined by NG2 remains unresolved.

Hydrology

Table 2-6: Science Requirements for hydrosphere identified by mission studies

	requirement in study	conversion	geoid error monthly solution
e.motion	1cm EWH @ 400km 10cm EWH @ 200km	applied	0,15mm @ 400km 0,8mm @ 200 km
NGGM	0,5mm Geoid @ 500km 1cm Geoid @ 10km	=	0,5mm @ 500km 1cm @ 10km
NG2	0,1mm Geoid @ 200km	=	0,1mm @ 200km

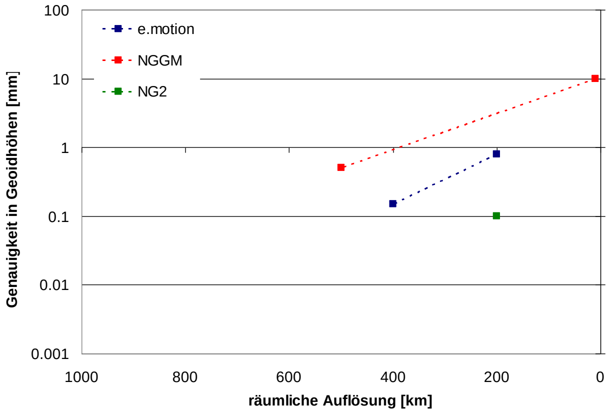

Figure 2-1: Science Requirements for hydrosphere identified by mission studies

Ocean (Basin Scale Mass Change)

Table 2-7: Science Requirements for ocean basin scale mass change identified by mission studies

	requirement in study	conversion	geoid error monthly solution
e.motion	5mm EWH @ 500km	applied	0,1mm @ 500km
NGGM	0,1mm Geoid @ 5000km 3,6mm Geoid @ 1000km	=	0,1mm @ 5000km 3,6mm @ 1000km
NG2	0,2mm Geoid @ 1000km	=	0,2mm @ 1000km

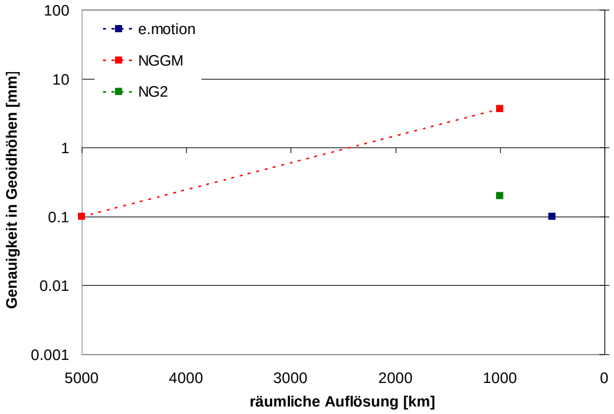

Figure 2-2: Science Requirements for ocean basin scale mass change identified by mission studies

Seal Level

Table 2-8: Science Requirements for sea level identified by mission studies

	requirement in study	conversion	geoid error monthly solution
e.motion	5mm EWH @ 500km	applied	0,1mm @ 500km
NGGM	0,17mm Geoid @ 5000km 3,6mm Geoid @ 2000km	=	0,17mm @ 5000km 3,6mm @ 2000km
NG2	0,03mm Geoid/yr @ 200km	applied	2mm @ 200km

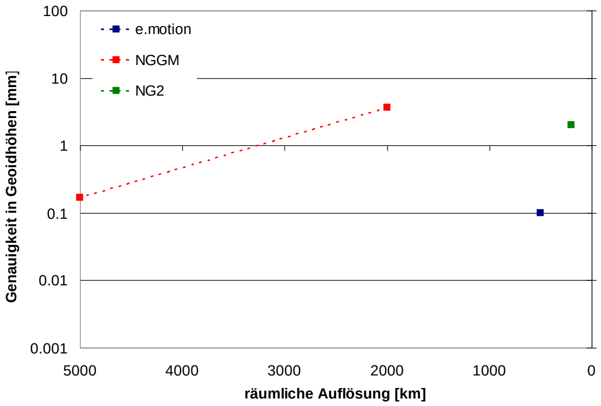

Figure 2-3: Science Requirements for sea level identified by mission studies

Ice Mass Balance

Table 2-9: Science Requirements for ice mass balance identified by mission studies

	requirement in study	conversion	geoid error monthly solution
e.motion	1cm EWH @ 400km 10cm EWH @ 200km	applied	0,15mm @ 400km 0,8mm @ 200 km
NGGM	0,017mm Geoid @ 5000km 36mm Geoid @ 100km	=	0,017mm @ 5000km 36mm @ 100km
NG2	0,04mm Geoid/yr @ 200km	applied	2,5mm @ 200km

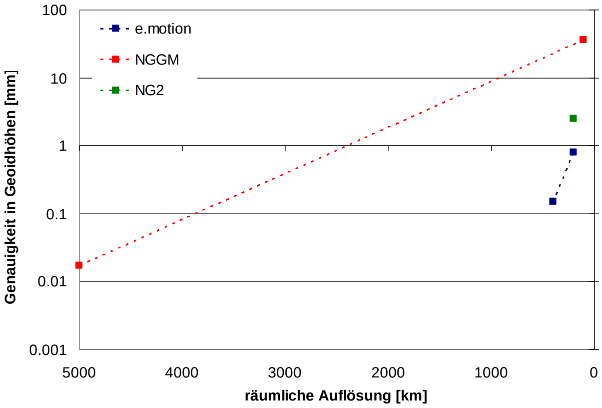

Figure 2-4: Science Requirements for ice mass balance identified by mission studies

Glacial Isostatic Adjustment (GIA)

Table 2-10: Science Requirements for GIA identified by mission studies

	requirement in study	conversion	geoid error monthly solution
e.motion	0,01mm Geoid/yr @ 400km	applied	0,6mm @ 400km
NGGM	0,036mm Geoid @ 1000km 36mm Geoid @ 200km	=	0,036mm @ 1000km 36mm @ 200km
NG2	0,02mm Geoid/yr @ 300km	applied	1,3mm @ 300km

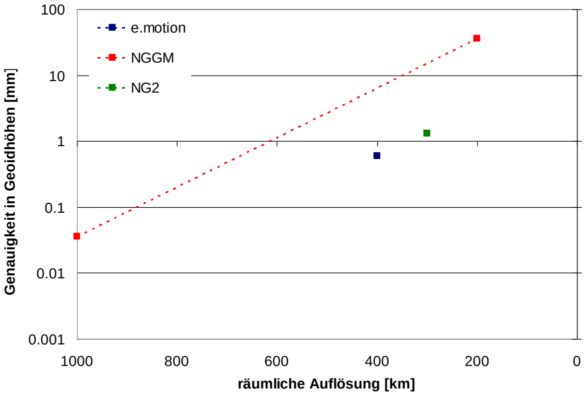

Figure 2-5: Science Requirements for GIA identified by mission studies

It is seen that in these details the studies are not in good agreement. In NGGM all requirements seem to be more conservative, while in most cases, also the two other studies do not agree as well.

In contrast to the individual figures the studies are closer to each other in the generalized requirements. What is finally demanded are a global coverage, a mission lifetime of at least 10 years (NGGM: 11 years) and the following accuracies in terms of monthly geoid errors:

- e.motion: 1mm @ 200km,
- NGGM: 10mm @ 80km,1mm @ 100 km, 0.1 mm @ 133km,

- NG2: 1mm @ 150 km.

The requirements thus reduce to a monthly geoid with millimeter accuracy at a spatial resolution between 100 and 200 kilometers. The value of 200 kilometers seems to be considered as the minimum requirement to outperform the GRACE mission. For example, the e.motion study points out that such an increase of spatial resolution would increase the number of resolvable hydrological basins from 18 to 75 percent. Similar numbers are predicted for ice sheets and glaciers. Without doubt, further improvements in resolution would lead to even better rates, but a value of 100 kilometers seems to be too ambitious. As far as we see, the millimeter accuracy is missed at this spatial scale even in the NGGM study. In order to avoid a similar discrepancy, such a low resolution should not be envisaged for this mission concept.

In summary, it is recommended to define the science requirements in line with e.motion and NG2 and to design the mission with two options as summarized in Table 2-11.

Table 2-11: Science requirements to be adopted as mission requirements for mission design

Requirement Type	Monthly Geoid Error Requirement
Minimal	1mm @ 200km
Optimal	1mm @ 150km

2.3 From Science to Observation Requirements

In this section observation requirements are derived for the proposed satellite mission in order to meet the science requirements in section 2.2. This is done with semi-analytical estimations of the gravity field performance of basic mission scenarios (section 2.3.1) with different altitudes. The basic noise model for the low-low SST observations contains typical spectral noise characteristics of the two main instruments. These are the laser interferometer and the accelerometer. The results of the semi-analytical simulations are shown in section 2.3.2 in terms of formal cumulative geoid errors depending on the spherical harmonic degree. In section 2.3.3 the required instrument noise levels are derived from the relation between the cumulative geoid error and the science requirements at two spatial scales (cf. section 2.2, minimal and optimal). These noise levels must be applied to the total noise on the distance and acceleration observations.

The semi-analytical simulations in this study do not take any temporal aliasing errors into account. And one of the main restrictions of monthly global temporal gravity recovery with the current mission GRACE (Gravity Recovery and Climate Experiment) is temporal aliasing from background model errors. But it can be expected that the quality of the de-aliasing products (typically atmospheric and oceanic mass variation models) will further increase with more sensitive observations. Furthermore the proposed satellite mission provides gravity field observations, which are less sensitive to temporal aliasing than GRACE (double pair with different inclinations or Pendulum). And there is a very promising processing method to reduce temporal aliasing by estimating short period low resolution gravity fields in addition to one high resolution field over a longer period (Wiese, Visser, & Nerem, 2011). With this method significant parts of high frequent signals (mainly atmosphere and ocean) can be observed and partly separated from the low frequent signals (mainly hydrology and ice).

2.3.1 Basic Scenario

At first a basic mission scenario is defined for which the instrument requirements are estimated in the following sections. The parameters for the basic mission scenario are defined in

Table 2-12. The constellation is a double low-low SST in-line pair with different inclinations (one polar and one inclined pair).

Table 2-12: Basic mission parameters

Constellation	Double low-low SST pair (one polar and one inclined)
Inclination [deg.]	Polar pair on 90 and inclined pair on 75 and 97 respectively
Inter-satellite distance [km]	100 and 200

Period [days]	30
Altitude range [km]	From 300 to 500 in steps of 50

The two main instrument noise contributions to the low-low SST observations are the accelerometer (ACC) noise and the laser interferometer (SST) noise. Therefore the basic noise model contains typical noise models for these two types of sensors. The analytical description of this model in terms of amplitude spectral densities is given in Eq. (2-1).

$$
\begin{aligned}
d_{SST}(f) &= 10^{-8}\sqrt{\left(\frac{0.01}{f}\right)^2+1}\left[\frac{m}{\sqrt{Hz}}\right] \\
d_{ACC}(f) &= 10^{-11}\sqrt{\left(\frac{0.001}{f}\right)^4+1+\left(\frac{f}{0.01}\right)^4}\left[\frac{m}{s^2\sqrt{Hz}}\right] \\
d_{total}(f) &= \sqrt{\left(d_{SST}(f)\cdot(2\pi f)^2\right)^2+\left(d_{ACC}(f)\right)^2}\left[\frac{m}{s^2\sqrt{Hz}}\right]
\end{aligned}
\qquad (2\text{-}1)
$$

As in the semi-analytical simulations range accelerations are used as observation model the total noise model is given in terms of accelerations. Figure 2-6 shows the amplitude spectra of the basic noise models in terms of distance (left) and accelerations (right).

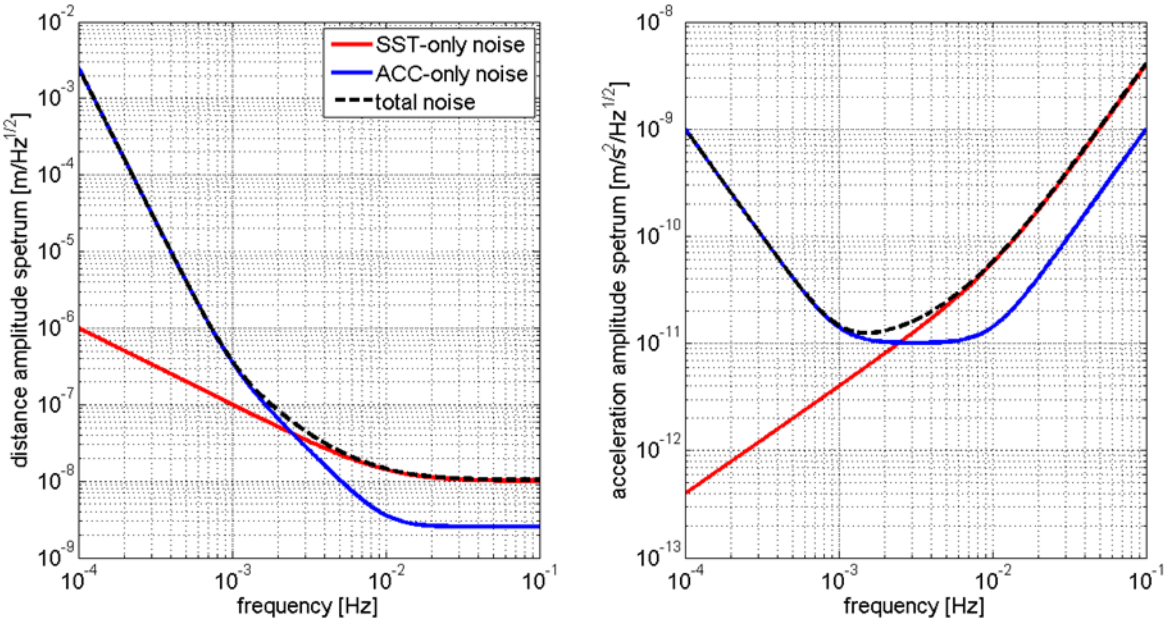

Figure 2-6: Basic noise models for the SST-link (SST, red), the accelerometer (ACC, blue) and the total noise (black) in terms of distances (left in [m/Hz$^{1/2}$]) and accelerations (right in [m/s^2/Hz$^{1/2}$]).

2.3.2 Semi-analytical Gravity Field Performance

In semi-analytical simulations (Sneeuw, 2000) the basic noise models (cf. (2-1) and Figure 2-6) are applied to the basic mission parameters (cf.

Table 2-12) in order to derive formal errors of the resulting SH coefficients of the monthly gravity fields. These simulations do not take any errors of temporal aliasing into account. Therefore the resulting errors reflect the sensitivity of the measurement system without temporal aliasing. Figure 2-7 shows the cumulative geoid error per SH degree in mm for basic mission scenarios on different altitudes (inclined pair on 75 degrees inclination, inter-satellite distance of 200 km, basic total noise).

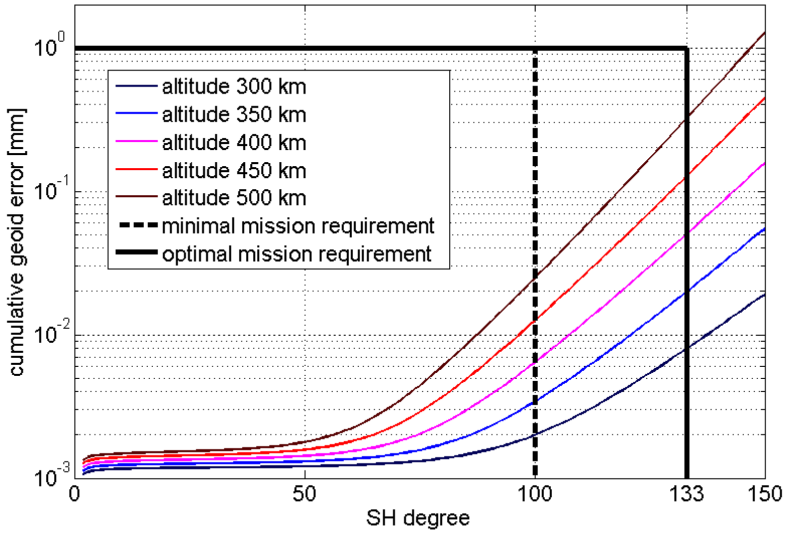

Figure 2-7: Cumulative geoid errors per SH degree in [mm] for the reference mission scenario (double low-low SST pair, monthly period, inclinations 90 and 75 degrees, inter-satellite distance 200 km, altitudes from 300 to 500 km, basic total noise) compared with the science requirements (1 mm geoid accuracy @ SH degrees 100 and 133 respectively).

With the basic noise models (cf. Figure 2-6, SST-noise on 10 nm/Hz$^{1/2}$, ACC-noise on 10^{-11} m/s^2/Hz$^{1/2}$) applied on the basic mission scenario the global average monthly geoid errors at 150 km spatial resolution (SH degree 133) are 0.01, 0.02, 0.05, 0.13 and 0.32 for altitudes of 300, 350, 400, 450 and 500 km. Compared to the science requirement of 1 mm these values are factors of 126, 50, 20, 8 and 3 smaller.

2.3.3 Observation Requirements

Based on the basic noise models in this section the requirements for the SST-link and the accelerometer are derived. As there is a linear relationship between the noise level and the geoid errors the requirements are derived by estimating from the relation between the science requirements (1 mm geoid accuracy) and the cumulative geoid errors of the basic scenarios. This is done for all basic scenarios (different inclinations for the inclined pair, different inter-satellite distances and different altitudes) applying the total noise, only the SST-noise and only the ACC-noise respectively.

Figure 2-8 shows the required observation noise levels to reach the science requirements (minimal and optimal) in terms of noise level within the measurement bandwidth (SST: $f > 10$ mHz, ACC: $1 < f < 10$ mHz). As expected the noise levels mainly depend on the orbital altitude. Table 2-13 shows the required noise levels (minimal and optimal) for the two main sensors depending on the altitude. The values are derived from the minimum total noise values of the four cases with different inclined pair inclinations and different inter-satellite distances.

Assuming altitudes of the two low-low SST pairs between 350 and 450 km the range of the required noise levels for SST and ACC are in-line with the estimated performances of the instruments proposed in the e.motion, the NGGM and the NG2 studies. The distance observation noise ($f > 10$ mHz) must be between 40 and 200 nm/Hz$^{1/2}$ (minimum: 300 and 1000 nm/Hz$^{1/2}$). The ACC observation noise amplitude ($1 < f < 10$ mHz) must be between 4E-11 and 2E-10 m/s²/Hz$^{1/2}$ (minimum: 3E-10 and 1E-9 m/s²/Hz$^{1/2}$). These noise level requirements belong to the total noise on the observations from which the gravity field parameters are retrieved. Therefore the total error budget of the distance and acceleration observations must meet these requirements.

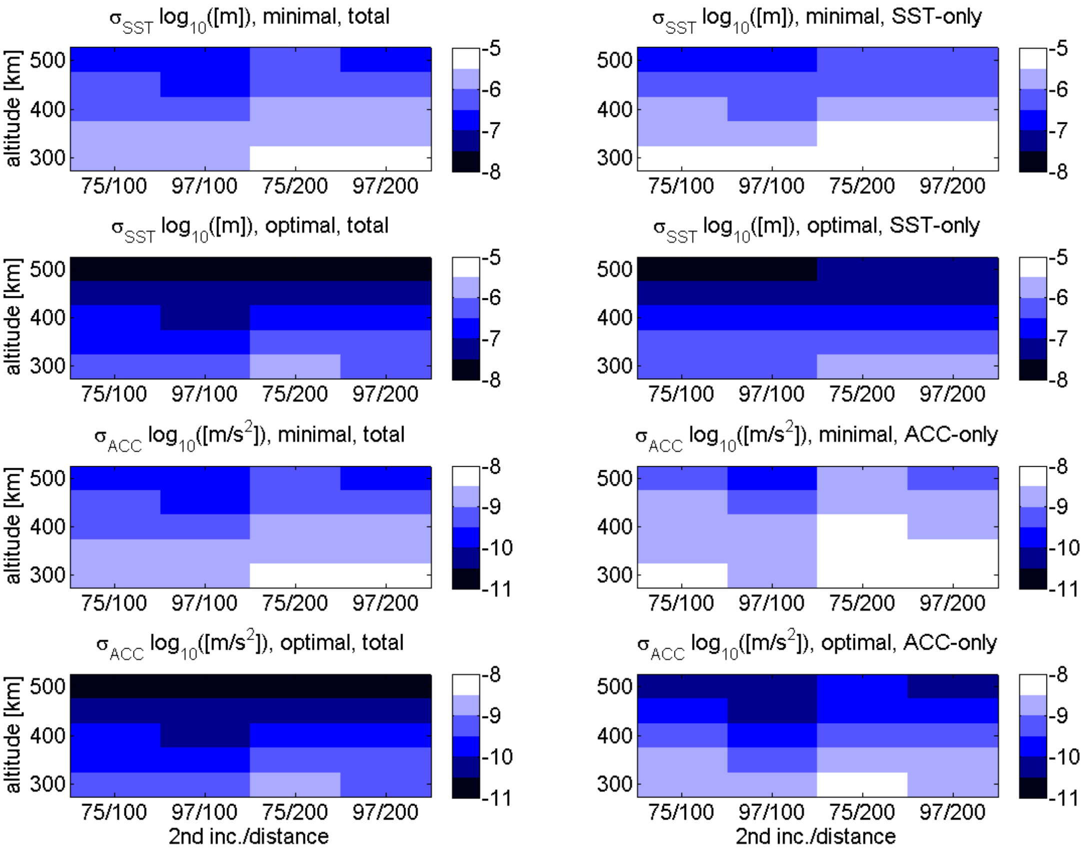

Figure 2-8: Required observation noise levels for the basic double pair scenarios for altitudes from 300 to 500 km (two different inclinations of the inclined pair of 75 and 97 degrees; two different inter-satellite distances of 100 and 200 km). Top four plots: SST in $\log_{10}$([m]). Bottom four plots: ACC in $\log_{10}$([m/s²]). Left column: assessment of the total noise as the sum of SST and ACC noise. Right column: assessment of the sensor-only noise, SST and ACC respectively.

Table 2-13: Required observation noise levels (minimal and optimal) for SST and ACC for altitudes from 300 to 500 km (derived from the total noise cases in Figure 2-7).

		SST [m]		ACC [m/s²]	
		Minimal	Optimal	Minimal	Optimal
Altitude [km]	500	1E-7	1E-8	1E-10	1E-11
	450	3E-7	4E-8	3E-10	4E-11
	400	6E-7	9E-8	6E-10	9E-11
	350	1E-6	2E-7	1E-9	2E-10
	300	2E-6	6E-7	2E-9	6E-10

2.4 From Science to Orbit Requirements

Two sampling theorems mainly govern the space-time sampling of a satellite-mission: (i) A Heisenberg-type uncertainty theorem which states the product of spatial resolution and time resolution is constant, and (ii) the Colombo-Nyquist rule (CNR) which requires the number of satellite revolutions in the full repeat cycle of satellite mission at least twice the maximum spherical harmonic degree to be detected ($\beta > 2L_{max}$ *or* $2M_{max}$). However, several studies have shown that with the modified Colombo-Nyquist rule at $\beta \approx L_{max}$ *or* M_{max}, a significant error improvement in gravity solutions happens. This new law allows us to go to higher temporal resolution within a specific spatial resolution, or on the other hand, to obtain higher spatial resolution within a fixed temporal resolution. Within the main sampling theorems, it is also expected that the quality of the gravity solution for any given time-span is a function of the homogeneity of the ground-track spacing and the ground-track gap size within that time frame. Therefore, it would be of great interest to investigate the effect of orbital parameters (esp. gap evolution of the different repeat orbits) on the gravity retrievals.

In order to investigate potential satellite mission design options, a series of methodologies and tools have been employed from the previous studies. The employment of the tools also includes the concerns of analysis challenges within the methodologies. In this work pocket, the quick-look tools for sensitivity analysis and aliasing analysis are employed for selecting, designing and evaluating future mission scenarios. These tools are described in the following sections.

2.4.1 Quick-look Tools

In order to identify suitable satellite missions for gravity recovery, a huge number of satellite orbits and gravity recovery simulations are required. A variety of satellite orbit parameters such as inclination, repeat orbit and altitude, the inter-satellite distance, the formation type and orientation and the measurement noise level contribute to the search space of optimal future gravity missions. To avoid time-consuming full-scale gravity recovery simulations, two quick-look tools (QLT) have been employed as fast simulation software for sensitivity analysis and time-variable gravity recovery for aliasing analysis from ll-SST (low-low satellite-to-satellite tracking) missions. The QLT for sensitivity analysis employs a semi-analytic error propagation to investigate the influence of the orbital parameters and measurement error PSD (Power Spectral Density) on the gravity field estimates, whereas the aliasing analysis tool uses the formulation of the observation equation for gravity recovery of certain time intervals.

Quick-look tool for sensitivity analysis

Within a circular orbit with constant inclination ($r=r_0$, $I=I_0$), it is possible to perform an order-wise efficient block-diagonal error propagation with even and odd degree separation from the observational and stochastic model to gravity field errors. The gravitational signal *f(t)* along the satellite orbit can be represented by the lumped coefficients:

$$\begin{aligned} f\left(r,u,I,\Lambda\right) &= \sum_{m}\sum_{k} A_{mk}^{f}(r,I)e^{i\psi_{mk}} \\ A_{mk}^{f}(r,I) &= \sum_{l} \underbrace{\frac{GM}{R}\left(\frac{R}{r}\right)^{l+1} \bar{F}_{lmk}(I)}_{H_{lmk}^{f}(r,I)} K_{lm} \end{aligned} \tag{2-2}$$

where K_{lm} are the complex spherical harmonic (SH) coefficients, $\bar{F}_{lmk}(I)$ is inclination function, and the composite angular variable is $\psi_{mk} = ku + m\Lambda$. Since, the transformation coefficients $H_{lmk}^{f}(r,I)$ and the lumped coefficients $A_{mk}^{f}(r,I)$ are constant for nominal orbit, the normal equation becomes order-wise block-diagonal structure. For a ll-SST-mission with inline (GRACE-like) formation, the transfer coefficient $H_{lmk}^{f}(r,I)$ reads as:

$$H_{lmk}^{\rho} \approx 2\sin(\eta\beta_{mk})H_{lmk}^{\Delta x}, \text{ with } \sin\eta = 0.5\frac{\rho_0}{r} \text{ and } \beta_{mk} = \frac{\dot{\psi}_{mk}}{n} \tag{2-3}$$

Utilizing block-wise variance-covariance propagation, the SH accuracy can be estimated:

$$\mathbf{Q}_{\hat{x}} = \left(\mathbf{A}^{T}\mathbf{Q}_{y}^{-1}\mathbf{A}\right)^{-1} \tag{2-4}$$

where Q_y is the variance-covariance matrix of the observations.

The semi-analytical quick-look tool can be employed for the investigation of the effect of orbital parameters and measurement noise on the gravity products, where they can be illustrated as the formal errors in terms of degree RMS and triangle plots, spatial covariance functions, formal geoid error per latitude, etc. The derivation of constant transfer coefficients for other formations rather than the inline formation has not been achieved yet. For these advanced formations, a pseudo-QLT is usually employed. As an example, Figure 4 shows the impact of different SST distance and orbit altitude on the accuracy of the gravity field recovery.

The semi-analytical quick-look tool can be employed for the investigation of the effect of orbital parameters and measurement noise on the gravity products, where they can be illustrated as the formal errors in terms of degree rms and triangle plots, spatial covariance functions, formal geoid error per latitude, etc. The derivation of constant transfer coefficients for other formations rather than the inline formation has not been achieved yet. For these advanced formations, a pseudo-QLT is usually employed. As an example, Figure 4 shows the impact of different SST distance and orbit altitude on the accuracy of the gravity field recovery.

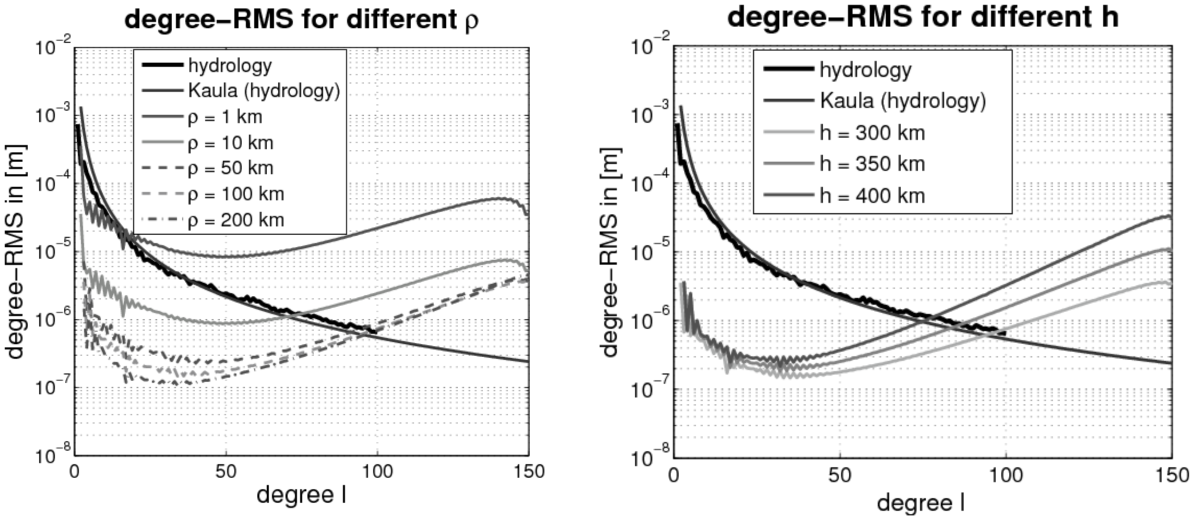

Figure 2-9: Impact of different SST distance (left) and orbit height (right) on the accuracy of the gravity field recovery.

Quick-look tool for aliasing analysis

The quick-look tool for aliasing analysis (reduced scale simulation tool) is based on the formulation of the equation for range accelerations:

$$\ddot{\rho} - \frac{1}{\rho}\left((\Delta\dot{X}_{12})^2 - \dot{\rho}^2\right) = e_{12}\left(\nabla V\left(X_2\right) - \nabla V\left(X_1\right)\right) \tag{2-5}$$

The right side of the observation equation above contributes to the design matrix, where the positions of the satellites at time epoch *t* are calculated by assuming the center of both satellites to move along the circular nominal repeat orbit and calculation of the relative movement of the two satellites by the homogeneous solution of the Hill's equations. The time-variable potential gradients of the Earth at the positions of the two satellites *1* and *2* are calculated by the provided time-variable gravity field models at those epochs. Then, the calculated values of the right side of the equation are set to the left side as the observables in the dimension of range acceleration. At the end, the gravitational potential on the Earth in terms of spherical harmonics coefficients is estimated through the system of equations.

Validation of the results by QLT

It is very important to validate the results of the quick-look tool with the result of a more realistic orbit simulation approach. Here, an evaluation of the quick-look tool with its nominal orbit assumption is made with the ll-SST acceleration approach applied to orbits from real orbit integration. In the orbit integration approach, the observations are generated directly from the orbit by evaluating the left side of equation (2-5) then by multiplication of the design matrix with the coefficients of the time-variable gravity field of the individual epochs, as it has to be done for nominal orbits. Figure 2-10 shows that despite the differences between both methods, a very strong correlation between the results of the two approaches for both, 7 and 32 days gravity solutions of a near-polar GRACE-like mission at the altitude of 333.8 km can be observed.

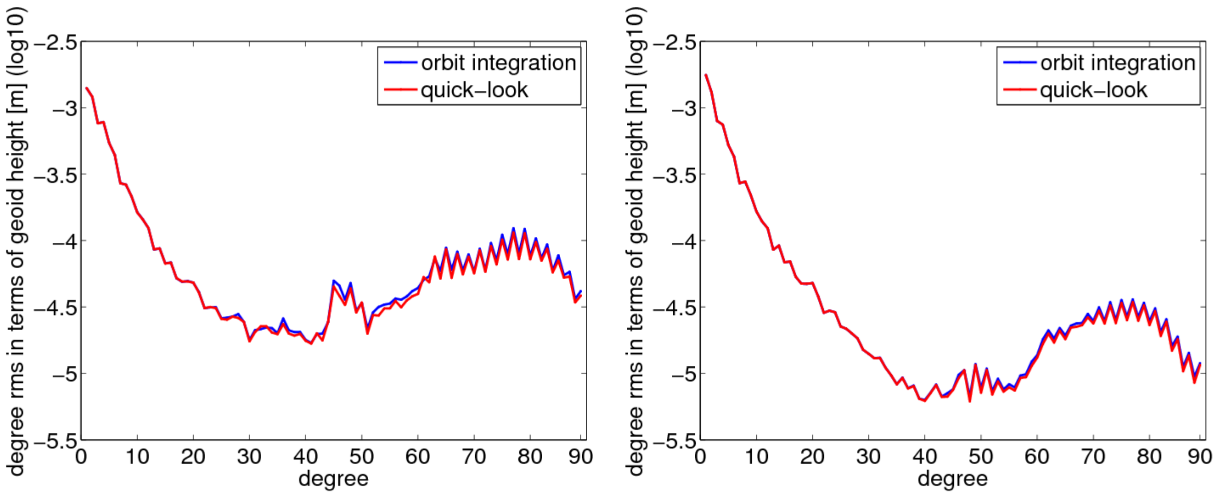

Figure 2-10: Error degree RMS plots of recovered gravity fields by the orbit integration approach and the quick-look tool for 7-day (left) and 32-day (right) recoveries of near-polar inline mission at the altitude of 333.8 km. The simulation input models are smoothed by 220 km Gaussian filter to avoid the ringing effects by SH truncation error.

2.4.2 Ground-track Gap Evolution Analysis Tool

Former studies have shown that the quality of the gravity solution of any given time span is a function of the homogeneity of the ground-track spacing within that time frame. For example, it is known that the drifting orbits with very slow gap evolution or gap fill-in result in low quality solutions, while the skipping orbits with fast ground-track gap evolution show higher quality performance. The homogeneity of ground-track distribution pattern of a satellite mission scenario as well as the small gap size between the ground-tracks, play an important role in gravity recovery quality. Figure 2-11 illustrates three different gap evolution scenarios: A drifting orbit, a slow skipping orbit, and a fast skipping orbit.

For the dual satellite missions with two pairs of satellites, it is also very important to study the influence of different combinations of repeat orbits (e.g. fast and slow repeat orbits, drifting and fast skipping orbits, etc.).

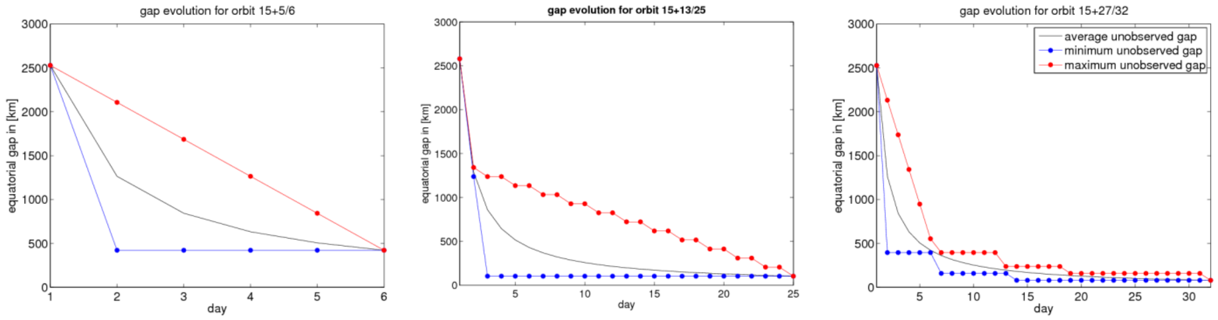

Figure 2-11: Gap evolution graphs of a drifting orbit β/α = 95/6 (left), a slow skipping orbit β/α = 388/25 (middle), and a fast skipping orbit β/α = 507/32 (right).

2.4.3 Selection Procedure towards the optimal orbital Parameters

The quick-look tools and the gap evolution analysis are employed to find optimal orbit configurations and formations from the very large search space of mission scenarios (see section 3). The search procedure for optimal scenarios also deals with the technical issues. In general, two factors play the most important roles in choosing the optimal satellite mission scenarios: (i) the performance of the mission in retrieving the geophysical signals (for user requirements), and (ii) technical and stability issues connected with the mission. From the technical aspect of view, the altitude of the satellite mission, the inter-satellite distance and the extra measurement components of alternative (advanced) formations rather than only the along-track component in GRACE-like formation are the most important challenges. Obviously, the search procedure for optimal mission scenarios should concern the technical and cost issues when they look for reaching the geodetic requirements. These subjects are discussed in the subsequent chapters.

2.5 Baseline Mission Requirements

From the analyses performed in the previous sub-chapters 2.1 to 2.4 a number of baseline science, observation and orbit requirements to be applied for the design of a future gravity field mission have been specified. These requirements, specifically related to the orbit and observations have to be seen as a first iteration, which need to be refined further on. All together the results obtained from the initial analyses can be transferred into a set of baseline mission requirements. The follow-on sections 3, 0 and 0 in more detail investigate these baseline mission requirements related to orbit configuration, attitude determination and control and observation performances and identify a set of consolidated mission requirements.

Table 2-14: Overview of baseline mission requirements

Requirement Type	Requirement Value	Reference Section
Monthly Geoid error	1mm @ 200km (minimum) 1mm @ 150km (optimum)	2.2
Temporal Resolution Gravity Field	weekly or shorter	2.1
Mission Duration	One decade	2.1
Orbital Height	350 to 450 km	2.3
Ground Track Coverage	Number of satellite revolutions in the full repeat cycle of satellite mission at least equal to the maximum spherical harmonic degree to be detected	2.4
Observation Noise	Distance: 40-200 nm/Hz$^{1/2}$ ($f > 10$ mHz) Accelerometer: 4E-11 and 2E-10 m/s²/Hz$^{1/2}$ ($1 < f < 10$ mHz)	2.3

3 Orbit Configuration

This chapter summarizes the identification of an orbit configuration, which is required to meet the science and mission requirements determined in section 2.2. Section 3.1 discusses search strategy towards the identification of optimal missions. Section 3.2 is about the trade-off between pendulum formation and double inline missions. In section 3.4. optimal orbits regarding temporal aliasing, in particular the effect of spherical harmonic resonance orders, is discussed. Finally, section 3.5 discusses some of the most important technological conditions for orbit configurations, while section 3.6 summarizes the suggested orbit parameters.

3.1 Search Strategy to optimal Mission Scenarios Identification

Two selection factors play the most important roles in choosing the optimal satellite mission scenarios: (i) the performance of the mission in retrieving the geophysical signals, and (ii) technical and stability issues connected with the mission.

Several studies in the last years have compared the performance of various formation types e.g. (Sharifi, Sneeuw, & Keller, 2007), (Wiese, Folkner, & Nerem, 2009), (Elsaka, 2010) and (Iran-Pour, Reubelt, & Sneeuw, 2013). The studies investigated the performance of alternative/advanced (e.g. Pendulum and Cartwheel) formations and 2 pairs of inline satellite missions. In addition, two ESA funded studies investigated the capability of single inline formations and multi inline-formation missions with identical and different inclinations [6], (Visser, Sneeuw, Reubelt, Losch, & van Dam, 2010), (Reubelt, Sneeuw, & Sharifi, Future mission design options for spatio-temporal geopotential recovery, 2010) Moreover, the performance and technical realization of different formations and double pair missions has been studied in [10]. The arrangement of a second, inclined satellite pair in double pair design suggested by (Bender, Wiese, & Nerem, 2008) was also studied by (Wiese, Nerem, & Lemoine, 2011). In that paper, a Monte-Carlo method was employed to deal with the enormous search space for orbit optimization, while (Ellmer, 2011) studied genetic algorithms for the purpose. All these studies have shown that a significant increase in accuracy and sensitivity is reached by alternative formations and double pair missions. The studies also discuss the feasibility of different mission configurations in terms of the new technical developments, while the science requirements are still reached. In particular, the mission altitude, inter-satellite distance and the formation type are in the focus of the studies.

Concerning the geodetic requirements, the sampling distribution and gap evolution behaviour of a mission plays an important role. For example, (Iran-Pour, 2013) and (Iran-Pour, Reubelt, & Sneeuw, 2013) discuss the importance of sampling theories' role in retrieval of gravity field. The modified Colombo-Nyquist rule (Weigelt, Sneeuw, Schrama, & Visser, 2012) states that the spatial resolution of gravity recovery of a satellite mission is noticeably improved with the number of satellite revolutions to be equal the maximum spherical harmonic. The rule enables higher temporal resolution of gravity solutions, while the high noise level, caused by spatial aliasing of the sub-Nyquist solutions, can be dealt by post-processing methods. That means for a single pair satellite mission, an almost good quality of gravity recovery of 6-day for maximum degree 90 is achievable (provided that the ground-track coverage is homogeneous enough). By employing two satellite pairs, one in near-polar orbit and the other in an inclined orbit, this is even achievable by 3-day solutions according to an interpretation of the modified Colombo Nyquist rule for mission consisting of two satellite pairs (dual formation missions). Strictly speaking, the latter solution is actually of higher quality. The reason is that an inclined formation rather increases isotropy by adding East-West measurement components instead of only doubling the amount of samples. Moreover, the 3-day solution benefits from higher temporal resolution and consequently less temporal aliasing. An important benefit of having such short time-interval solutions would be then that they can be applied as de-aliasing products (Wiese, Visser, & Nerem, 2011) independent from state of the art geophysical models when aiming at time-variable gravity recoveries of longer time spans (e.g. monthly solutions). However, to avoid spatial aliasing in the gravity solutions, the original Colombo-Nyquist rule is still valid.

In order to select optimal repeat orbits, the gap evolution graph [10], (Iran-Pour, Reubelt, & Sneeuw, 2013) and the reduced-scale simulation tool (quick-look tool QLT for aliasing analysis) are employed. For example, Figure 3-1 shows gap evolution graphs of two repeat orbits 503/32 and 511/32. The skipping repeat orbit of 503/32 shows a homogeneous gap evolution, while the drifting orbit (511/32) orbit illustrates large unobserved gaps over the time. For this purpose, (Iran-Pour, Reubelt, & Sneeuw, 2013) studied a variety of repeat patterns with the reduced-scale simulation tool for gravity recovery. It was found that a homogeneous gap evolution is not only important for a full repeat cycle recovery, but also for the estimation of short time interval sub-Nyquist solutions.

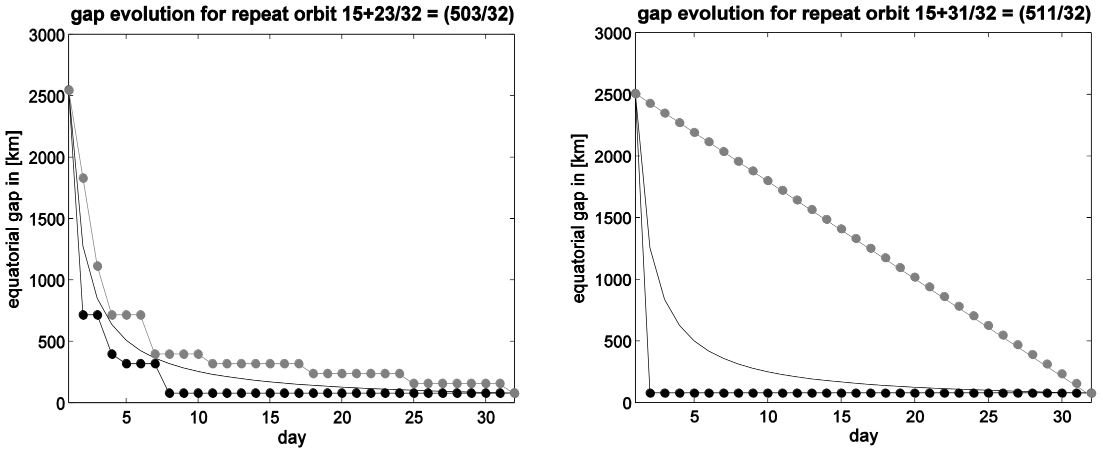

Figure 3-1: Gap evolution (maximum gap: grey circles; minimum: black circles; average: black line) for fast skipping (left) and drifting (right) orbits (Reubelt, et al., 2014)

The intersatellite distance ρ of inline polar SST missions and the orbit height h of the missions are investigated by the semi-analytic quick look tool (Sneeuw, 2000), where a noise scenario of a future laser and accelerometer/drag-free system is assumed [19], (Sheard, et al., 2012). Figure 3-2 shows that the best geodetic sensitivity is reached for a large SST distance and a low orbit altitude. However, a low orbit height is challenging due to air drag increase which in turn limits the mission lifetime. In addition, a large satellite distance would be problematic when the laser technology is employed (pointing issues, signal strength, noise). Therefore, several studies suggest an orbit height of at least 300 km and a satellite distance of ρ = 100 km to compromise between geodetic sensitivity and technological feasibility. Indeed, Figure 3-2 states that the increase of accuracy is quite low for SST-distances larger than 100 km, while the influence of the distance dependent laser noise becomes more severe.

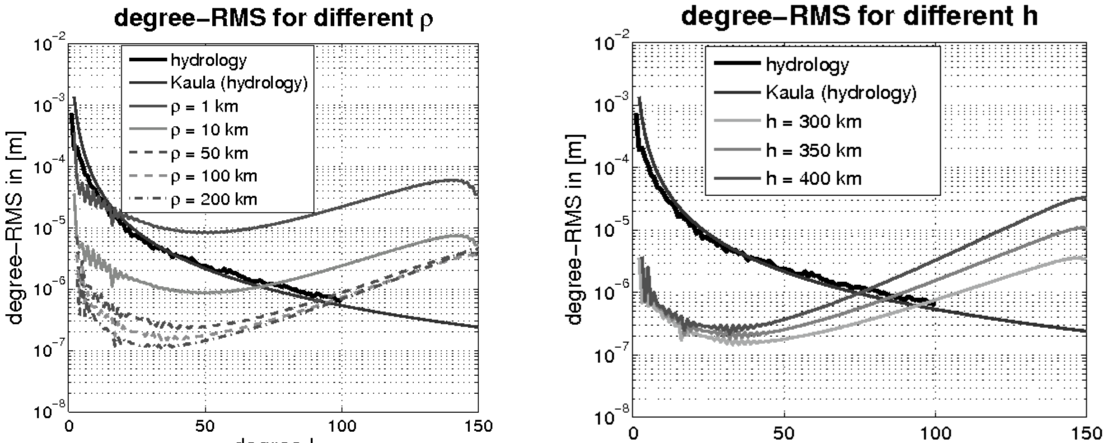

Figure 3-2: Impact of different SST distances and orbit heights on the accuracy of the gravity field recovery (Reubelt, et al., 2014)

Concerning the double inline pair missions, one important orbital parameter of orbit optimization is the inclination of the second pair. For a single pair mission, the inclination of a near polar orbit (I = 89.5°) is usually selected to avoid larger polar gaps and consequently achieve a better global coverage, esp. for the benefit of ice studies. For the inclination selection of the second pair in a double pair mission, the reduced-scale simulation tool for aliasing analysis of gravity recovery can be employed. Figure 3-3 shows the corresponding geoid errors for 5° steps in the interval [45°,90°]. As a result, a choice between $I \approx 70°$ and $I \approx 75°$ is suggested.

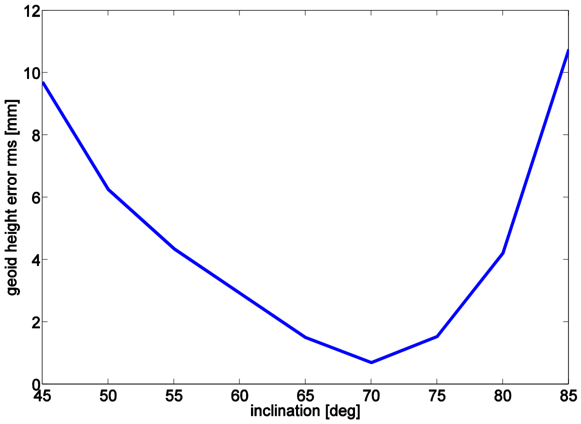

Figure 3-3: Geoid errors for different inclinations of the second pair in double pair mission, estimated with the reduced-scale simulation tool for aliasing analysis of gravity recovery

In order to investigate the impact of extra measurement components of advanced formations and constellations (rather than only the along-track component of an inline formation), the orbit and formation parameters of six selected basic missions are investigated by sensitivity and aliasing analysis tools in (Reubelt, et al., 2014). The results showed that a significant increase in the absolute error level for the laser-based missions can be observed from the results of the aliasing analysis tool compared to those of the sensitivity analysis tool (especially for degrees below 50). This implies that the aliasing error, if it is not observed by the satellite system itself, is above the laser noise. In contrast, the error curves for GRACE as reference (using K-band ranging and Super-STAR sensors) are similar for both tools which proves that the K-band measurement noise is the dominant error source in this case. As one result, one can conclude that an improvement of the error level of about two orders of magnitude by laser/drag-free systems, as suggested by sensitivity analysis, seems not feasible with the current knowledge of background models and is restricted to approximately one order of magnitude (Reubelt, et al., 2014). As a second results it can be concluded that, if the high frequency temporal aliasing can be observed and doesn't need to be modelled from geophysical background data, a further improvement a the error level can be achieved. This needs to be investigated in the context of analyzing satellite constellations instead of single satellite pairs.

3.2 Trade-off between Pendulum and Bender Configuration

With the processing of the GRACE mission data, it became obvious that the inline configuration of one pair of satellites was providing an anisotropic gravity field recovery error (striping effects) due to the inline satellite-to-satellite tracking (SST) measurement (along-track direction only). Scientists started then to design and investigate other mission scenarios with the aim to reduce the anisotropy inherent to the GRACE mission.

Due to their relative technological simplicity, the Pendulum and the Bender configuration are the more promising configurations compared to more exotic formations such as Helix or Cartwheel (Wiese, Folkner, & Nerem, 2009) which could be able to provide also satisfactory results for gravity field recovery but are much more difficult to implement. What is meant here with Pendulum configuration are two satellites at the same altitude and flying on near polar orbits (I ~ 90°) and having orbital planes separated by ΔΩ (difference in longitude of ascending node) adding therefore an additional cross-track component to the along-track direction for the SST measurement. The Bender configuration, proposed by (Bender, Wiese, & Nerem, 2008), consists of two pairs of satellites where one pair is flying on a nearly polar orbit (to avoid a polar gap), while the second pair flies on a lower inclined orbit (typically 63°-75°). The Pendulum formation has been investigated in different studies such as [10] Anselmi et al. (2011), the BMBF Geotechnology project (Reubelt, et al., 2014) as well in various articles, e.g. (Sharifi, Sneeuw, & Keller, 2007), (Elsaka, et al., 2014). The Bender configuration has been also studied by different authors, e.g. (Visser, Sneeuw, Reubelt, Losch, & van Dam, 2010), (Wiese, Nerem, & Lemoine, 2011), in ESA studies such as [10] and in the BMBF Geotechnology project (Reubelt, et al., 2014), as well as in (Elsaka, et al., 2014).

However in most of the conducted studies the mission scenarios were not investigated for the same altitude therefore it was decided in this work to run full-scale simulations for the same altitude (here 315 km) for the Bender configuration as well as for different Pendulum missions with various yaw angles. The simulations were performed for a 32-day time period up to degree and order 90 taking into account colored noise for the SST and accelerometer measurements and background model errors for the static and time variable gravity fields as well as for the ocean tides. In Table 3-1 below the four investigated formations are listed. Three Pendulum missions with increasing yaw angles of 7°, 24° and 45° corresponding to equatorial cross-track separations of 25, 43 and 83 km respectively and the Bender configuration have been tested. From the technology point of view it can be seen that the Pendulum with yaw angle of 7 and 24 degree yield a maximum SST range-rate around 10 m/s or below which can be still acceptable, while the pronounced Pendulum (45 degree yaw angle) with a maximum range-rate of about 40 m/s can be considered to be a very challenging formation. The results in terms of weighted root mean squared (wRMS) geoid height differences [mm] show the superiority of the Bender formation compared to the Pendulum formations.

Table 3-1: Missions investigated at an altitude of 315 km

Formation	Max. Yaw Angle [°]	Intersatellite Distance [km]	Max. SST range-rate [m/s]	Geoid Height Differences wRMS [mm]
Pendulum 25 km	7	215	2.7	0.926
Pendulum 43 km	24	96/106	10.8	0.354
Pendulum 83 km	45	83/120	39.6	0.460
Inline Bender	0.5	105	0.3	0.200

In the following Figure 3-4 the results of the gravity field recovery are presented in the spatial domain and it can be noted that the greater the yaw angle of the Pendulum is the greater the reduction of the striping effects is achieved. The Bender configuration is yielding the best results in terms of stripes reduction.

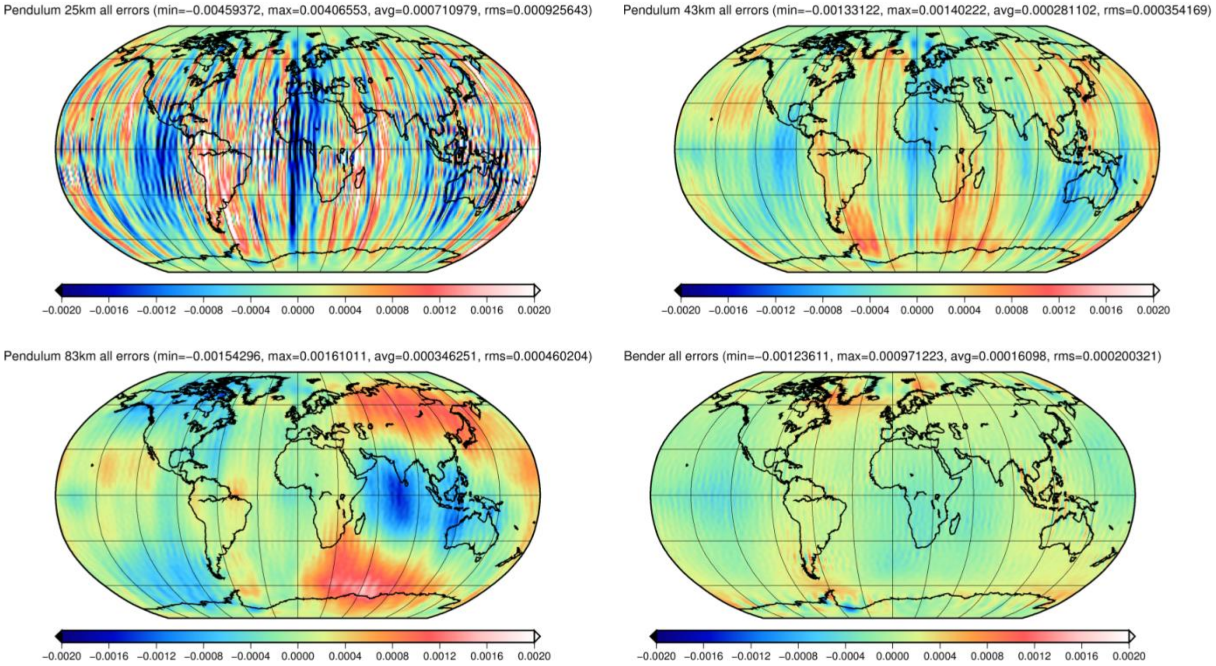

Figure 3-4: Spatial domain representation of gravity field recovery for different satellite mission scenarios (units are in meter). Top left: 7 degree yaw Pendulum, top right: 24 degree yaw Pendulum, bottom left: 45 degree yaw Pendulum, bottom right: Bender constellation.

Figure 3-5 below shows the full-scale simulations results in the spectral domain in terms of degree variances. It can be see that the Bender configuration outperforms all the Pendulum missions for degree inferior to approximately 50 and that only the Pendulum formation with large yaw angle (45°) surpasses the Bender configuration for degree larger than 50.

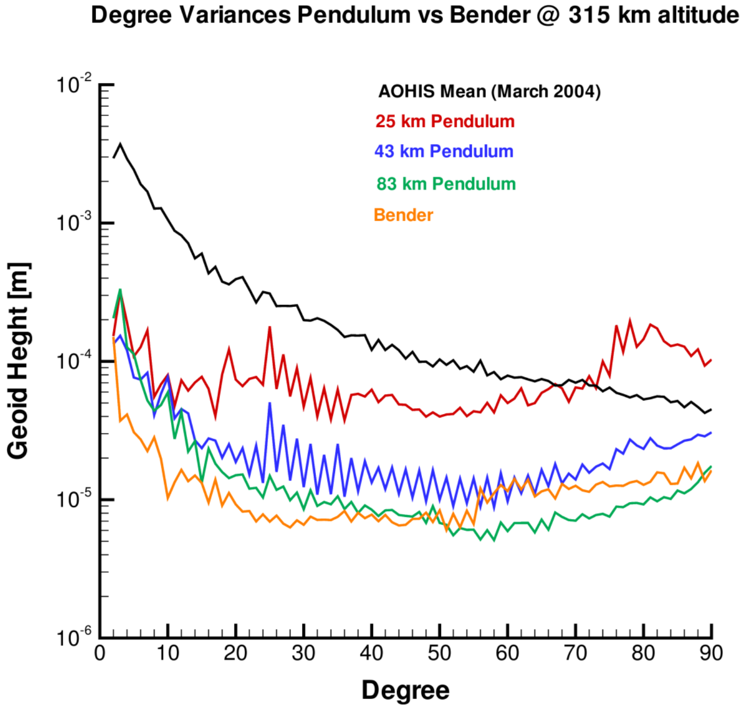

Figure 3-5: Full-scale simulations results in the spectral domain in terms of degree variances for different satellite missions

Figures Figure 3-6a-d below illustrate the individual error in the spherical harmonic coefficients for the four investigated missions. The blue colour represents larger errors, while the red colour shows smaller errors.

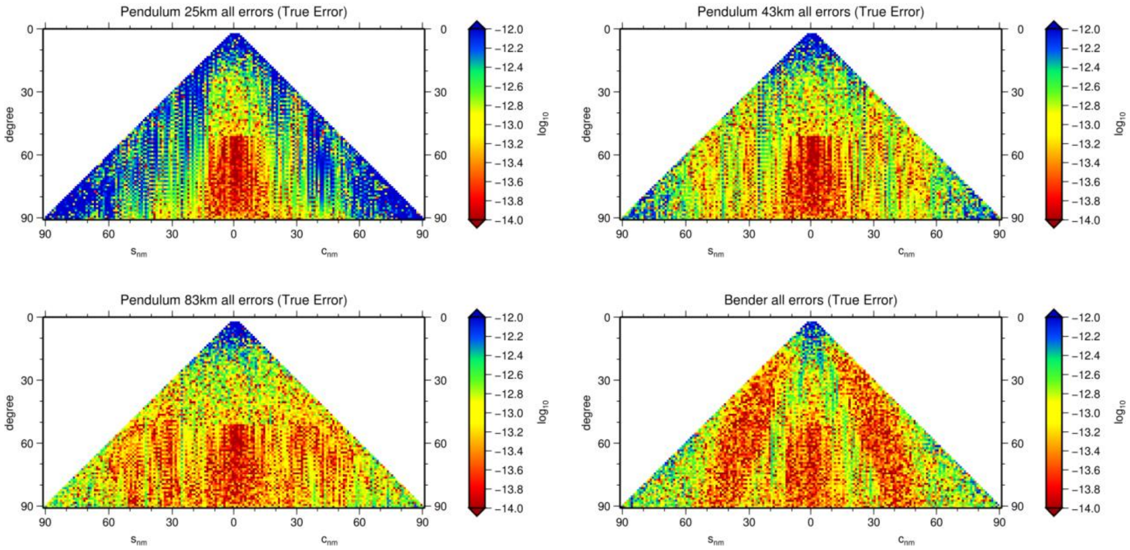

Figure 3-6: Spherical harmonic coefficients errors for the four investigated missions. Top left: 7 degree yaw Pendulum, top right: 24 degree yaw Pendulum, bottom left: 45 degree yaw Pendulum, bottom right: Bender constellation.

Pro and contra of Pendulum and Bender

Advantages of Pendulum:

- Only two satellites and therefore only one launch are needed. This fact can make the mission less expensive if the cost for technology development remains inferior to an additional launch and two extra satellites.

Disadvantages of Pendulum:

- Accurate pointing of the laser is more difficult to achieve

- From full-scale simulations it has been shown that the Pendulum becomes competitive with Bender only for large yaw angle leading to large SST range-rate and therefore a more challenging technology.
- There is a need to fly higher than Bender due to increased atmospheric drag

Advantages of Bender:

- Reduced demand on the technology (SST range-rate < 1m/s)
- Can fly at a lower altitude due to the comparatively reduced atmospheric drag
- Better performance for the lower spherical harmonics less than degree 50, more isotropy in the errors leading to better science return

Disadvantages of Bender:

- Four satellites and hence two launches are needed (due to the very different inclinations of the orbital planes), meaning an increase in cost.

3.3 Optimal Inter-Satellite Distance and Inclinations

3.3.1 Selection of optimal Inter-Satellite Distance

The noise PSDs for SST and accelerometer, eq. (3-1), were defined by the project team as a result from earlier and ongoing studies. Figure 3-7 shows the PSDs for different intersatellite distances and Figure 3-8 shows results obtained for different intersatellite distances ρ for a single polar pair obtained with the semi-analytic QLT (Sneeuw, 2000). The following simulation parameters have been assumed: inclination I = 89.5°, orbit height h = 420 km, maximum spherical harmonic resolution L = 130, observation interval T = 30 d).

$$\begin{aligned}
d_{SST}(f) &= 10^{-9}\sqrt{\left(8\cdot\frac{\rho}{100\,\mathrm{km}}\cdot\sqrt{1+\left(\frac{0.01}{f}\right)^2}\right)^2+3\cdot 100}\left[\frac{m}{\mathrm{Hz}}\right]\\
d_{ACC}(f) &= 10^{-11}\sqrt{\left(\frac{0.001}{f}\right)^4+1+\left(\frac{f}{0.01}\right)^4}\left[\frac{m}{s^2\sqrt{\mathrm{Hz}}}\right]\\
d_{total}(f) &= \sqrt{\left(d_{SST}(f)\cdot(2\pi f)^2\right)^2\left(d_{ACC}(f)\right)^2}\left[\frac{m}{s^2\sqrt{\mathrm{Hz}}}\right]
\end{aligned} \tag{3-1}$$

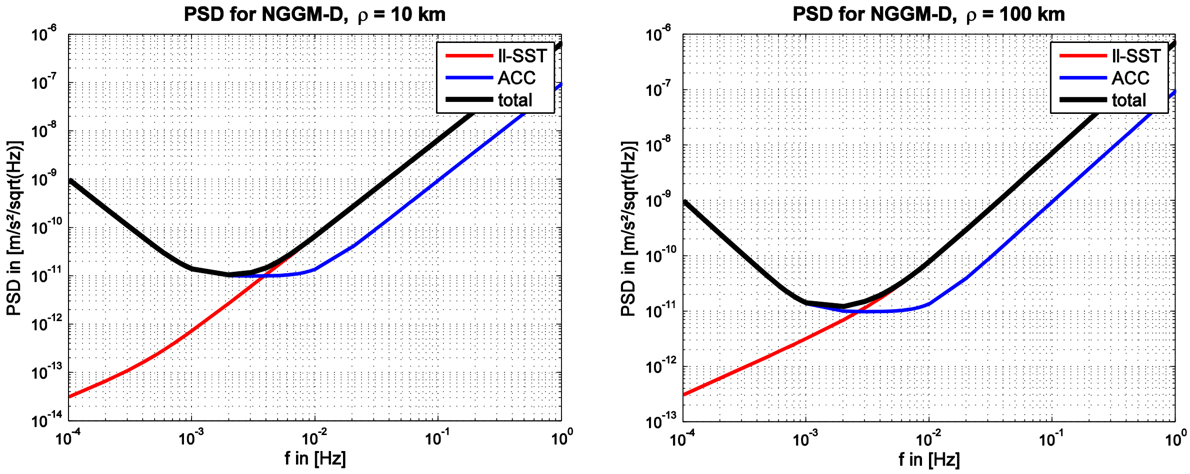

Figure 3-7: PSDs of ll-SST system, ACC and total noise (SST-ACC) for two inter-satellite distance scenarios (ρ = 10 km/100 km)

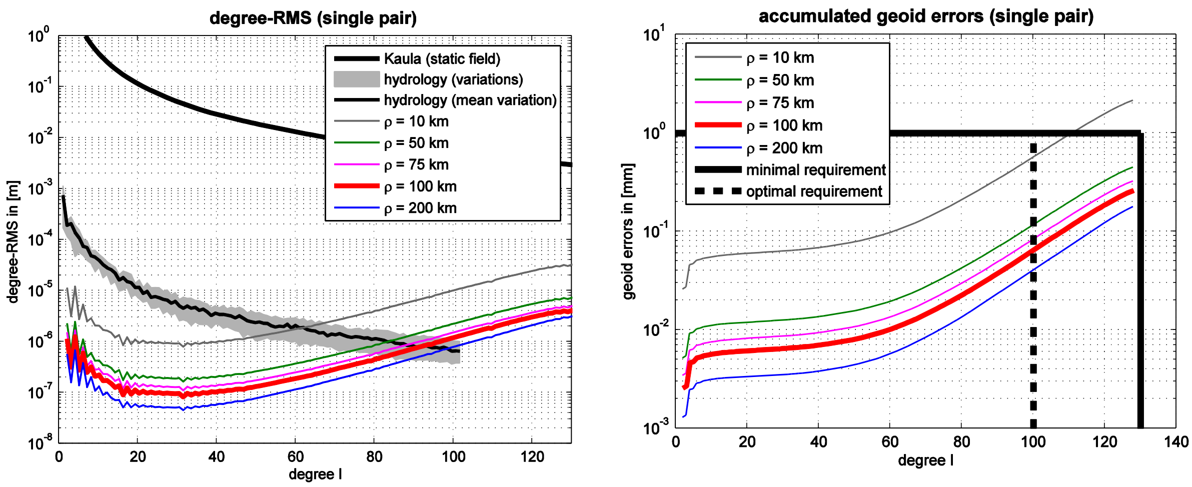

Figure 3-8: Performance of single polar pairs (I = 89.5°, h = 420 km, L = 130, T = 30 d) with different intersatellite distances; degree-RMS (left) and accumulated geoid errors (right).

From these results the following conclusions can be drawn:

- All satellite distances ≥ 50 km fulfill the mission requirements
- The larger the satellite distance the lower the formal gravity field errors. The relation is almost linear with satellite distance ρ. This is clear from sensitivity point of view, but since the SST error increases with ρ it was expected that this effect is less prominent.
- No significant improvements were found for satellite distances ρ > 70 km. Here, this is different, as mentioned before. However, a satellite distance of ρ = 100 km is a good compromise between sensitivity and technological instrument issues (higher error bounds are possible for shorter distance) and is suggested for e^2.motion. Furthermore full-scale simulations in (Reubelt, et al., 2014) haven't shown much benefit by using larger distances of 150 km/200 km.

From the analysis and the conclusions a satellite distance of ρ = 100 km is suggested as some kind of optimal choice.

3.3.2 Selection of optimal Inclination

The performance of Bender constellations consisting of a polar pair and an inclined pair with different inclinations I ∈ [55°,80°] have been investigated (outside this limits the Bender constellations begin to perform worse). The following simulation parameters have been assumed: inclination of first satellite I_1 = 89.5°, satellite distance ρ = 100 km, orbit height h = 420 km, maximum spherical harmonic resolution L = 130, observation interval T = 30 d and PSDs (d_{total}) from eq. (3-1) for observation noise. Figure 3-9 shows the performance of various Bender constellations (compared to the single polar pair) in terms of different performance measures (degree-RMS, accumulated geoid errors, geoid error per latitude, spatial correlations (at equator) w.r.t North azimuth) and Figure 3-10 displays formal error triangle plots and spatial covariance functions. In Table 3-2 values for different performance criteria are specified. These criteria contain on the one hand geoid errors (long-wavelength (L = 50) and short wavelength (L = 130)), quasi local criteria as geoid error over ice/equatorial regions (60° ≤ ϕ ≤ 85° and 0° ≤ ϕ ≤ 30°, respectively) and homogeneity measures as normalized geoid error variation along the meridian (variation of geoid errors per latitude) and average correlation w.r.t. North azimuth (at equator). The best performances w.r.t. this criteria and tolerances within ±22.5° have been identified and finally a best Bender constellation was found which stays within this tolerances. The gain compared to a single polar pair is also declared in this table.

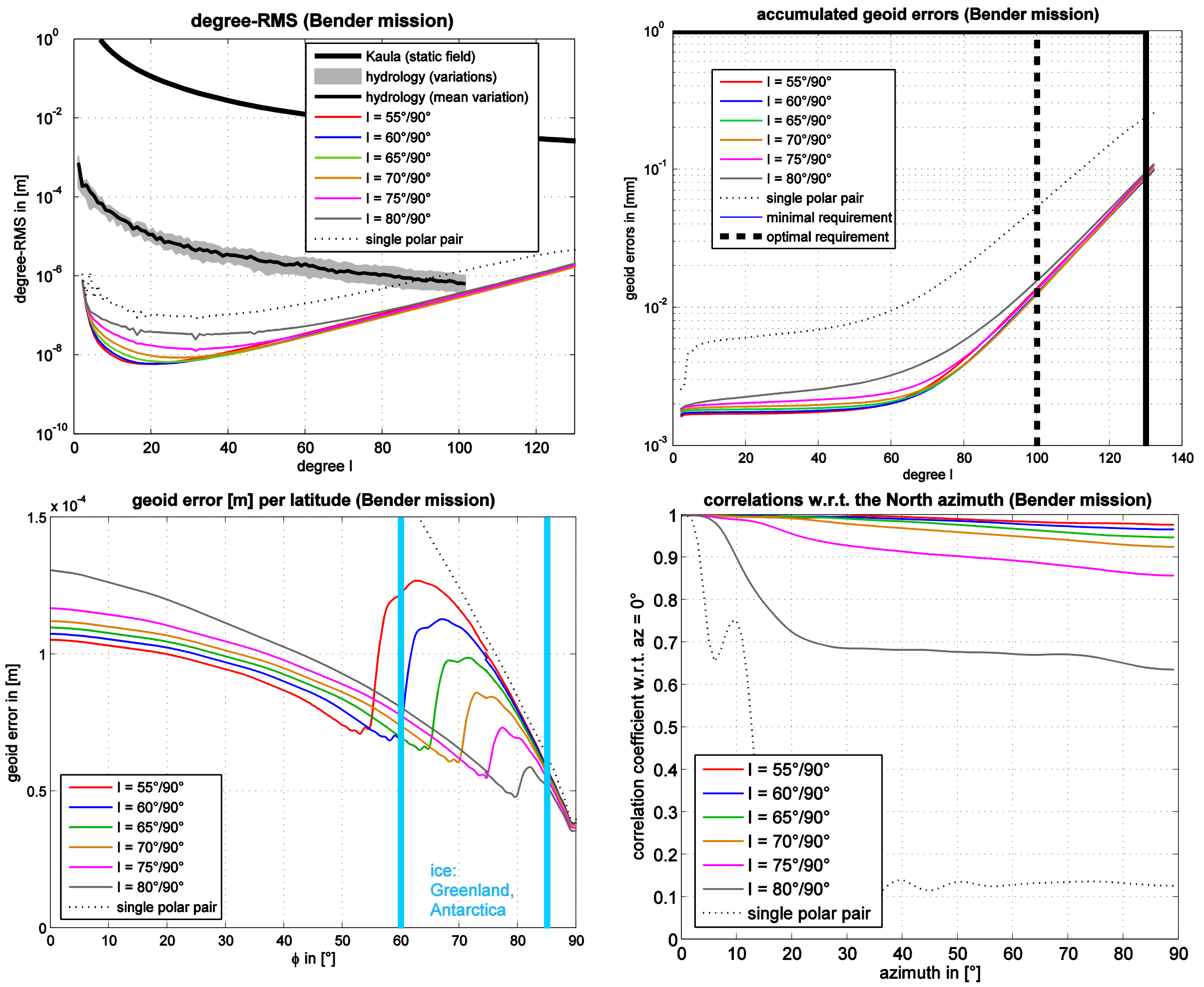

Figure 3-9: Performance of Bender constellations (I_1 = 89.5°, ρ = 100 km, h = 420 km, L = 130, T = 30 d) with different inclinations of the 2nd pair; degree-RMS (top left), accumulated geoid errors (top right), geoid errors per latitude (bottom left) and spatial correlations (at equator) w.r.t North azimuth (bottom right).

Table 3-2: Evaluation of Bender pairs with different inclinations of the 2nd pair w.r.t. different performance criteria; best mission's values are in red and tolerances within 22.5% are in blue. The best constellation (I = 70°/89.5°) fulfilling all tolerances is marked in the red box.

inclination of 2nd pair I [°]	geoid error [mm] (L = 130) (*)	geoid error [mm] (L = 50) (*)	ice region geoid error [mm] (**)	equator region geoid error [mm] (**)	geoid variation (normalized)	average correlation (***)
55	0.0987	0.00079	0.1131	0.1022	0.1324	0.9908
60	0.0974	0.00076	0.1000	0.1043	0.1199	0.9882
65	0.0975	0.00080	0.0828	0.1066	0.1294	0.9805
70	0.0988	0.00092	0.0722	0.1093	0.1469	0.9641
75	0.1016	0.00121	0.0677	0.1134	0.1655	0.9160
80	0.1102	0.00218	0.0675	0.1256	0.1979	0.7244
single pair (I = 89.5°)	0.2591	0.00759	0.1296	0.3072	0.2661	0.2311
gain (****)	2.6	8.3	1.8	2.8	1.8	4.2

(*) from degree l = 3 on

(**) to maximum degree L = 130

(***) average correlation w.r.t. North azimuth (at equator)

(****) gain (factor) of optimal Bender pair (I = 89.5°/70°) w.r.t. single pair (I = 89.5°)

single polar pair (I = 89.5 °)

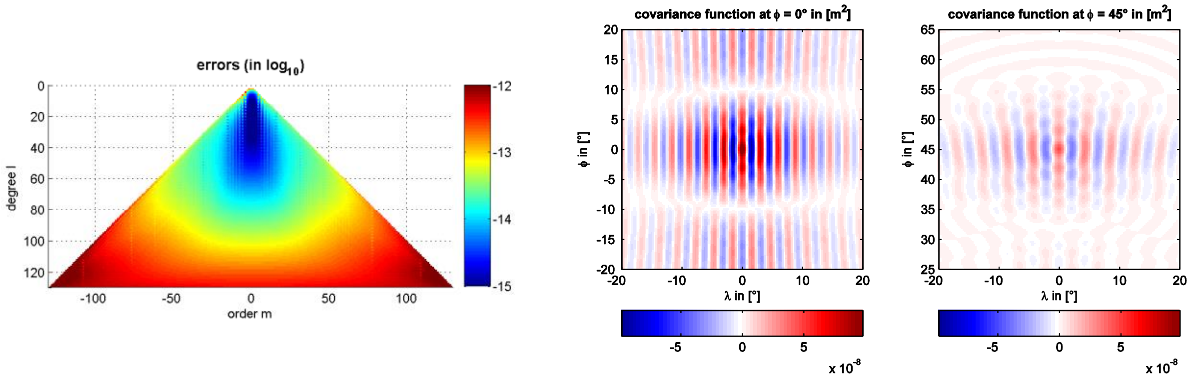

Bender constellation (I = 70°/89.5°)

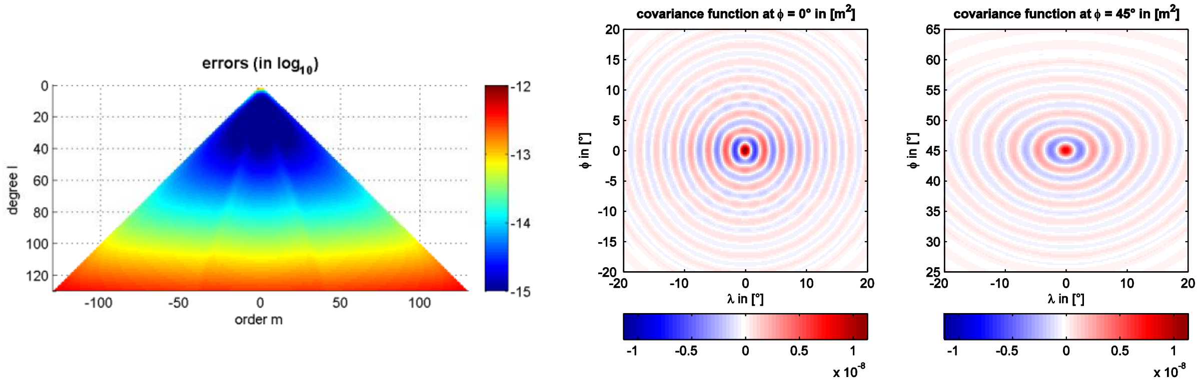

Bender constellation (I = 80°/89.5°)

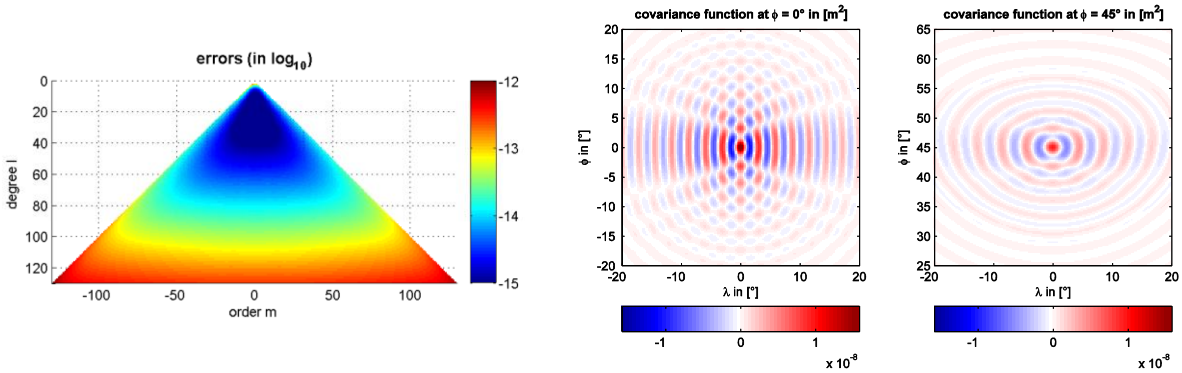

Figure 3-10: Formal error triangle plots and spatial covariance functions for Bender pairs with different inclinations vs. a single polar pair.

From these results the following conclusions can be drawn:

- All investigated Bender mission lead to improvements compared to a single polar pair; the improvement is dependent on the spherical resolution and the inclination and lies mainly between a factor of 3 and 10
- All Bender constellations fulfill the science requirements
- For higher SH resolutions $l > 70$ all Bender constellations lead to similar geoid accuracy (and degree-RMS). However, for longer wavelengths, especially between degrees $5 \leq l \leq 50$ Bender missions with lower inclinations perform better (a factor of 5-6 between the pairs I = (60°/90°) and I = (80°/90°) and a factor of 2-3 between pairs I = (60°/90°) and I = (75°/90°))
- Lower inclinations of the 2nd pair lead to a higher (equatorial) isotropy; for inclinations $I_2 \leq 70°$ it is more than 95%, for $I_2 = 80°$ it drops significantly to 72% (for $I_2 = 75°$ it is still 91%); compare with the single pair, which isotropy measure is only 23% (→ trackiness!)
- Geoid errors per latitude show which latitude regions will benefit most from the Bender design; these are the low and mid latitude regions with $|\phi| \leq I$; the smallest errors in these regions are produced by the lower inclinations, but the difference between the different Bender missions varies not much (less than 25%)
- The largest geoid homogeneity (i.e. the smallest variation of geoid errors along the latitude) is produced by an inclination $I_2 = 60°$; the geoid variation for $I_2 = 80°$ is 65% larger
- For latitudes $|\phi| \geq I$ the geoid errors rises quite rapidly. For lower inclinations this effect is more pronounced (see Figure 3-9). However, the higher latitude regions $60° \leq |\phi| \leq 85°$ are regions for

the important ice-mass loss observations. Thus low geoid errors for these latitudes are welcome. The lowest errors in these regions are produced by higher inclinations, especially for I_2 = 80°. For inclinations of I_2 = 60° and 70° this error is increased by approx. 50% and 7%, respectively.

The analysis shows that it is important to evaluate degree-RMS or accumulated geoid errors, but also homogeneity measures as isotropy and regional measures as geoid errors for certain latitude bands are important. Such criteria are evaluated numerically in Table 3-2. As can be seen, lower inclinations (I_2 ≈ 60°) show a better performance for most of the criteria except for ice latitudes, where a higher latitude (I_2 ≈ 70°- 80°) is beneficial. Since the latter is an important topic for future missions, an inclination of I_2 = 70° is regarded as optimal. Such an inclination balances the criteria and lies within the tolerance of ±22.5% w.r.t. the optimal performance for each criteria. The average gain compared to GRACE is approx. a factor of 3.5.

All in all one can conclude that inclinations of I = 70°/89.5° are suggested for a Bender type mission.

3.3.3 Stand-alone Performance of inclined Satellite Pair

An important aspect is that each of the two pairs of the Bender constellation is a valuable mission on its own. The reason for this is that very likely one agency will be able to launch one pair due to the enormous costs, and this single pair must already be a valuable mission. For a polar pair this is clear, since it covers the whole Earth and will outperform GRACE due to sophisticated instruments, background models and analysis methods (apart from the fact of a continuation of time-variable gravity time series). However it has to be investigated what the benefit is of a stand-alone inclined satellite pair. Due to the large polar gap problems will arise as e.g. missing observability of polar areas and its phenomena (mainly ice) and missing observability a large part of the spherical harmonic spectrum (low orders). In contrast, some benefits can be found, as mentioned below. Figure 3-11 displays formal error triangle plots and spatial covariance functions for the polar and inclined pair and in Figure 3-12 geoid errors per latitude and correlations w.r.t. the North azimuth (at the equator) are compared. To account for the polar gap the inclined solution was regularized by the covariance matrix generated by a polar pair with 1000 times larger measurement noise.

single polar pair (I = 89.5°)

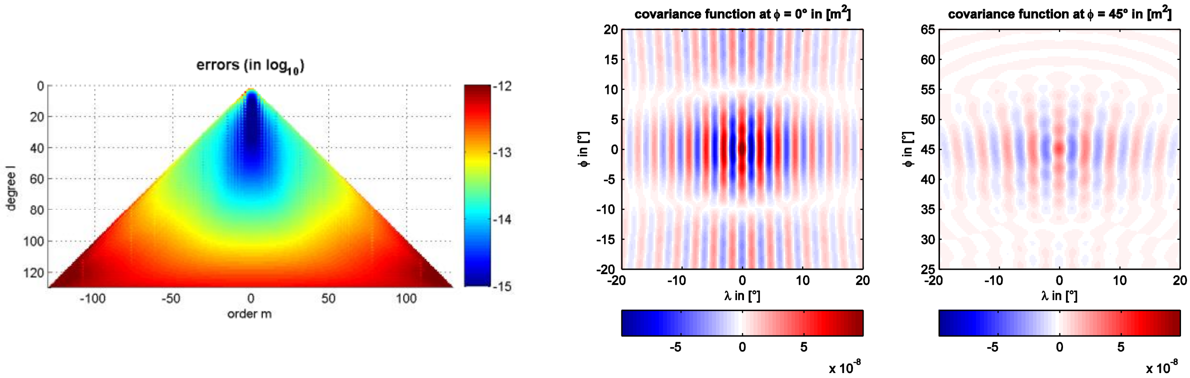

Single inline pair (I = 70°)

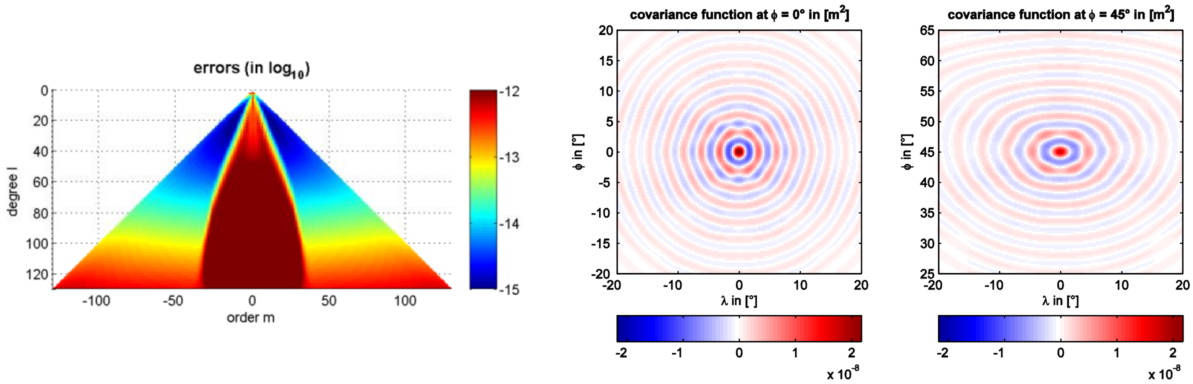

Figure 3-11: Single polar vs. single inclined pair; formal error triangle plots (left) and spatial covariance functions (right); inclined pair regularized by covariance matrix of single polar pair with 1000 times larger noise (i.e. PSD multiplied by 1000)

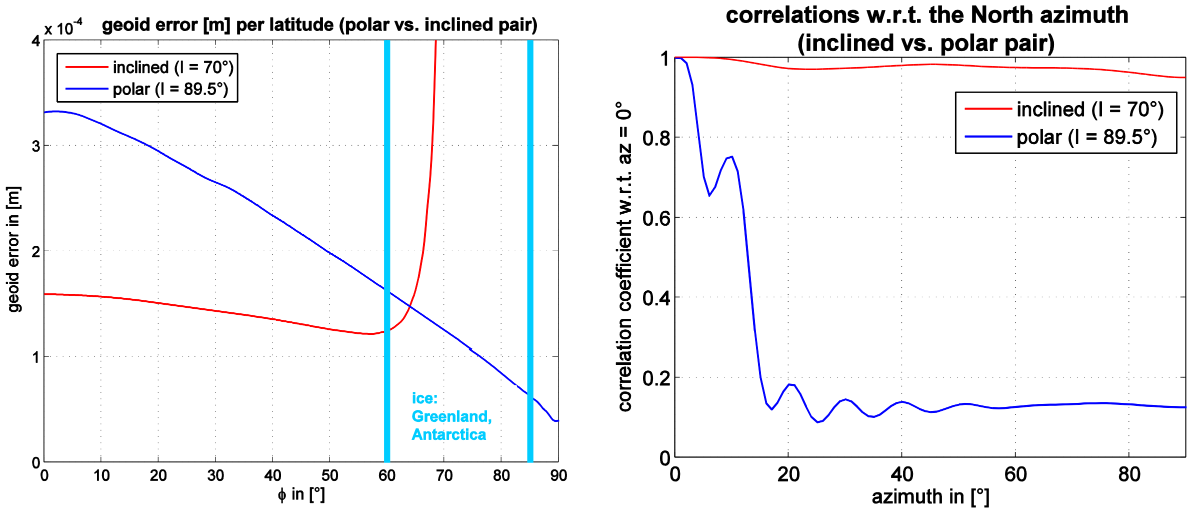

Figure 3-12: Single polar vs. single inclined pair; geoid errors per latitude (left) and spatial correlations (at equator) w.r.t North azimuth (right)

Pros and cons of single inclined pairs (compared to single polar pairs):

Cons:

- Low order SH coefficients cannot be determined due to polar data gap, thus a complete SH spectrum is not available
- Due to the polar data gap time variable gravity phenomena in this regions cannot be investigated; this means in principle no ice mass studies are possible
- For SH analysis regularization is necessary; this might be avoided by alternative parameterizations (local methods as wavelets, Slepian functions, …)
- Leakage effects of the polar gap to lower latitudes (mainly 5° - 10° outside the gap)

Pros:

- Much larger isotropy for all latitudes inside the inclination; thus GRACE type North-South striping is reduced
- Much higher accuracy for low and mid latitude regions
- Probably better recovery of low and mid-latitude geophysical effects, e.g. hydrology in Amazon and Africa

In conclusion one can state that an inclined pair might be a valuable mission on its own; low and mid-latitudes geophysical signals (mainly hydrology) will benefit from the much higher isotropy.

3.4 Optimal Orbits regarding temporal Aliasing

In this section optimal orbits regarding temporal aliasing are derived. Most of this work is published in (Murböck, Pail, Daras, & Gruber, 2014). Temporal aliasing due to undersampling of unmodelled high-frequent mass variations will be one of the largest errors in temporal gravity recovery from future satellite missions. There are several approaches to reduce temporal aliasing within the processing or in a post-processing step (Swenson & Wahr, 2002), (Kusche, Schmidt, Petrovic, & Rietbroek, 2009), (Wiese, Visser, & Nerem, 2011), (Zenner, 2013). (Murböck, Pail, Daras, & Gruber, 2014) analyses the reduction of temporal aliasing from a different point of view. It is shown that by choosing an optimal orbit, the effect of temporal aliasing from both tidal and non-tidal sources on spherical harmonic (SH) coefficients of low orders and degrees can be avoided. With this approach four altitude bands for low Earth orbiters are detected where the effects of temporal aliasing are minimized. The following sections shortly summarize the main findings of (Murböck, Pail, Daras, & Gruber, 2014) and show some further simulation results regarding future sensor accuracies and double pair applications.

3.4.1 Spherical harmonic Resonance Orders

The two main observing frequencies of a satellite orbit correspond to the rates of the argument of the latitude $\dot{u}$ and the Earth-fixed longitude of the ascending node $\dot{\Lambda}$. Depending on these two frequencies the largest effects of temporal aliasing occur at specific SH order bands. These order bands are found around integer multiples of the number of revolutions per day (typically between 15 and 16 for geodetic satellites). These SH orders are called resonance orders. The magnitude with which each of these bands is affected depends on $\dot{u}$ and $\dot{\Lambda}$. The frequencies ω of a signal on the satellite orbit which are mapped on the SH order m are (Sneeuw, 2000):

$$\omega(m) = k\dot{u} + m\dot{\Lambda} \tag{3-2}$$

with $-l_{max} \leq k \leq l_{max}$ and $0 \leq m \leq l_{max}$ (maximum SH degree l_{max}). The largest effects occur when ω contains the smallest frequencies. Then ω contains frequencies which are very close to the integer multiples of $\dot{u}$ as well. Figure 3-13 shows these minimum frequencies for eleven GRACE-like 31-day repeat orbits with altitudes from nearly 500 km (471 revolutions) down to 400 km (481 revolutions).

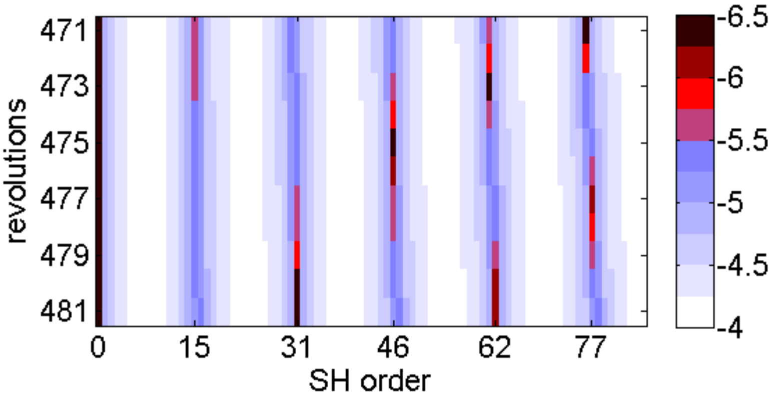

Figure 3-13: Absolute minimum frequencies for the eleven GRACE-like 31 day repeat orbits in $\log_{10}(|f\ [Hz]|)$ (Murböck, Pail, Daras, & Gruber, 2014)

3.4.2 Closed-loop Simulations

In this section the results of closed-loop simulations are discussed regarding single and double pairs with tidal temporal aliasing. The orbits are computed as circular exact repeat orbits. On the orbit positions the low-low SST observations ($\Delta t = 10s$) are computed in terms of gravitational acceleration differences projected onto the Line-of-Sight of two satellites separated by 220 km. The input gravity signal is computed from the difference of the ocean tide models EOT08a (Savcenko & Bosch, 2008) and FES2004 (Lyard, Lefevre, Lettelier, & Francis, 2006) up to the SH degree and order 80. Two types of observation noise are applied. One is a white noise with standard deviation of $5 \cdot 10^{-9}\ \frac{m}{s^2}$. The resulting formal errors lead to SH coefficient errors which are comparable to the accuracy of monthly GRACE solutions. The second is a colored noise with a white part above 1 mHz on $5 \cdot 10^{-10}\ \frac{m}{s^2\sqrt{Hz}}$ and a f^{-2}-part below. Figure 3-14 shows the square root of the Power Spectral Densities of the two noise types together with the mean hydrology plus ice signal (black, Hydrology and Ice (HI)) and the residual ocean tide signal (red). The level of the GRACE-like white noise is $\sqrt{2\Delta t} \cdot 5 \cdot 10^{-9}\ \frac{m}{s^2\sqrt{Hz}} = 2.2 \cdot 10^{-8}\ \frac{m}{s^2\sqrt{Hz}}$.

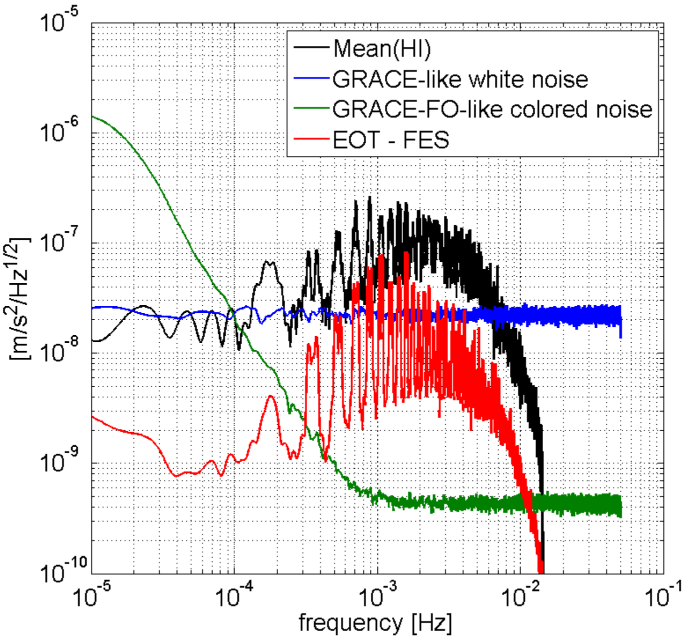

Figure 3-14: Square root of Power Spectral Densities of a GRACE-like white (blue) and a GRACE FO-like colored noise together with the mean hydrology plus ice signal (black) and the difference of the ocean tide models EOT08a and FES2004 (red).

As an example the GRACE-like orbit from Figure 3-13 performing 477 revolutions in 31 days is chosen. It has its strongest resonances at SH order 77 and two less prominent ones at 31 and 46. Figure 3-15 shows the SH order (left) and degree (right) variances of the ocean tide differences including the two noise types (red) together with formal errors (blue). The resonances can be seen prominently in the SH order variances for the GRACE-FO-like noise (less prominently in the SH degree variances). The GRACE-like white noise covers the low resolution resonances and only the largest 77 resonance is visible. From this Figure it can be concluded that for increased sensor accuracy it is much more important to reduce temporal aliasing. Furthermore the knowledge of the resonances might be used to adjust the stochastic modeling of the observations accordingly.

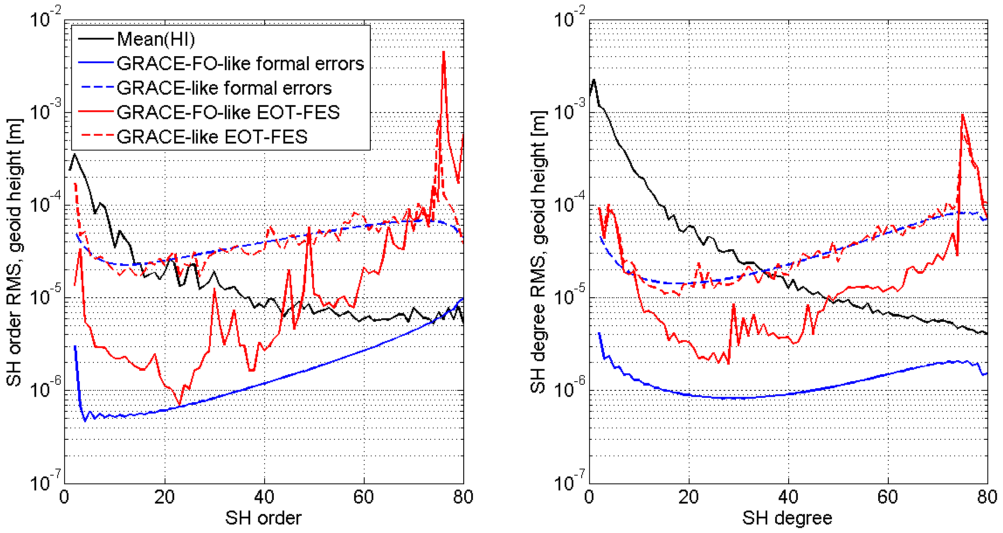

Figure 3-15: Unit-free SH order (left) and degree (right) variances of the ocean tide model differences including the two types of noise (red) together with the corresponding formal errors (blue) and the mean hydrology plus ice signal (black).

In the case of equally weighted double pairs on different altitudes the resonances of both orbits occur in the combined solution. The left part of Figure 3-16 shows the SH order variances of four noise free simulations out of the GRACE-like orbits in Figure 3-13. Each of these four orbits shows an extreme resonance at different SH orders. In this case when targeting HI, one would choose the 477 revolution orbit as optimal because the largest temporal aliasing resonance effect occurs at the highest order and affect the HI less than the other three. But when the 477 orbit is combined with one of the others, one cannot benefit from the double pair because the low order resonance effects deteriorate the 477 solution. The right part of Figure 3-16 shows these noise free double pair solutions. Each of these four double pair solutions has a worse performance in estimating HI than the single 477 solution. Because temporal aliasing is not stochastic, it is not averaged. It has to be said that the two solutions are equally weighted. When adjusting the weighting according to the resonance information, one could improve these combinations.

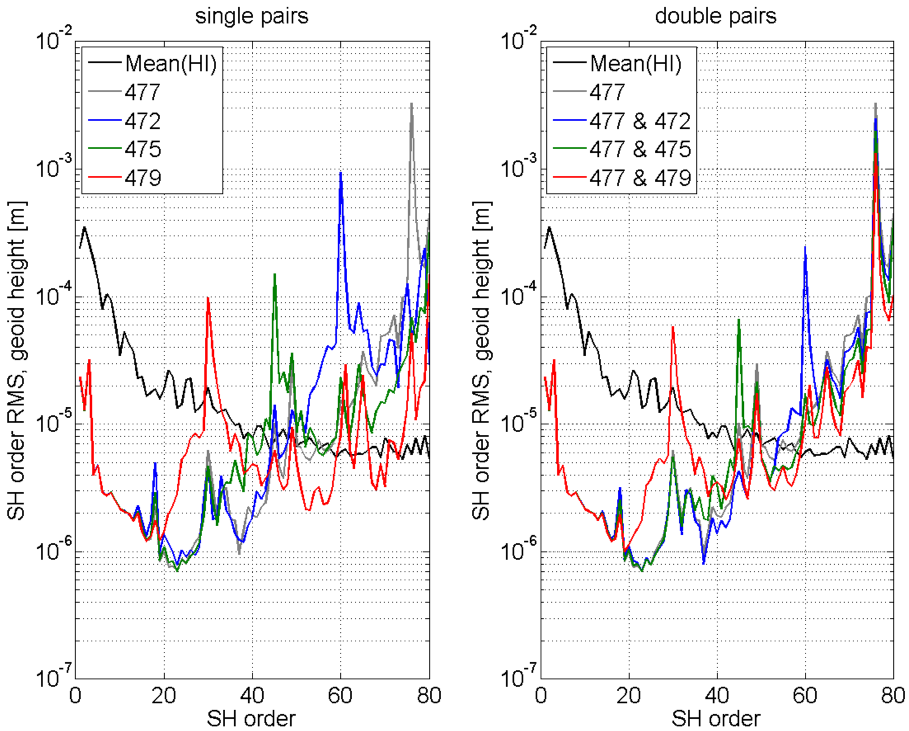

Figure 3-16: Left: Unit-free SH order variances of four noise free single pairs (GRACE-like 31 day orbits with different revolutions, cf. Figure 3-13). The observations are the differences between the ocean tide models EOT08a and FES2004. Right: Equally weighted double pairs of the 477 solution with the other three.

3.4.3 Suggestion for Mission Altitude

(Murböck, Pail, Daras, & Gruber, 2014) also show that the resonance order prediction works for real GRACE solutions as well. From GRACE orbit parameters it is computed that in the first year of the GRACE mission the largest resonances occur at SH order 76. After that for a longer period until 2007 or 2008 the order 61 resonance is dominant and in the last years the order 107 resonance became prominent. In the monthly GRACE solutions ITG-Grace2010 (Mayer-Gürr, Eicker, Kurtenbach, & Ilk, 2010) and GFZ Release 4 (Flechtner, Dahle, Neumayer, König, & Förste, 2010) these resonances clearly can be found according to the predictions from the orbit parameters.

For future gravity satellite missions it is important to select the orbit in that way, that no large resonances occur at low SH orders. For polar orbits between altitudes of 200 and 600 km the resonance orders are shown in Figure 3-17. A nearly symmetric distribution can be seen. A critical frequency is set to $1.8 \cdot 10^{-6}\ Hz$ saying that all SH orders showing frequencies smaller than this are highly affected by temporal aliasing. When looking for orbits without such large effects up to the highest possible order one would end up at four altitude bands. These bands are between 294 and 309 km, 360 and 370 km, 416 and 426 km and between 479 and 495 km (Murböck, Pail, Daras, & Gruber, 2014). Taking the resonances of higher orders than 75 into account, it can be searched for optimal orbits within these bands.

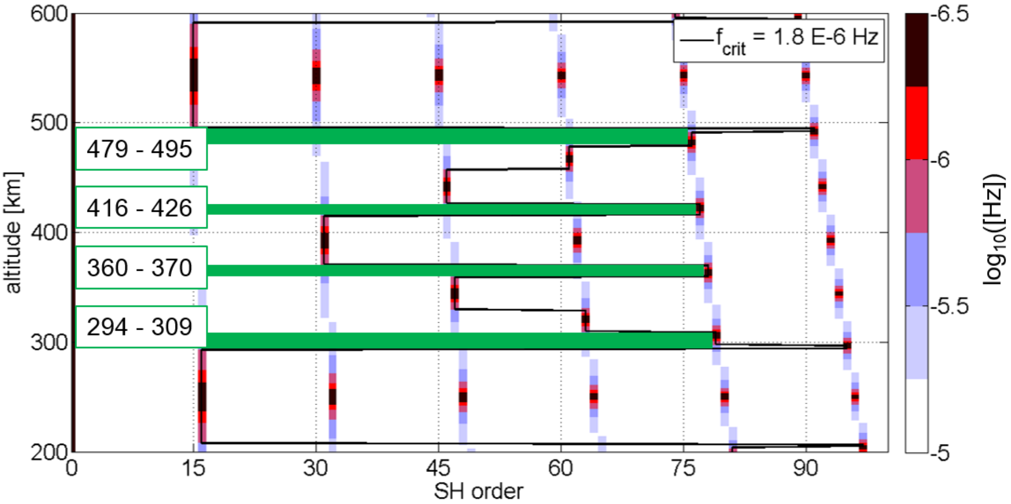

Figure 3-17: Absolute minimum frequencies for polar orbits between 200 and 600 km altitude in $\log_{10}(|f\ [Hz]|)$ together with four optimal bands (green) according to a critical frequency of $\mathbf{1.8 \cdot 10^{-6}}$ **Hz**.

3.5 Technical Conditions for Orbit Configuration

In order to improve the sensitivity for the gravity field, a low orbit height is sighted. However in periods of increased solar activity non-gravitational accelerations may exceed the measurement bandwidth of the accelerometers. To keep the non-gravitational forces (mainly in flight direction, e.g. GOCE) within this bandwidth and to guarantee measurements with desired sensitivity (10^{-11} m/s^2, i.e. one magnitude better as for GRACE and GRACE-FO) a “drag compensation” is needed. The demands for propellant and power for drag-compensation are regarded as an important mission constraint for orbit configuration and mission length. Based on selected orbit configurations and orbit parameters, an analysis for drag-compensation was performed. The goal of these investigations is to evaluate the feasibility of the suggested scenarios concerning the drag-compensation and the involved propellant/power demand. Further constraints concerning the orbit configuration as e.g. the relative velocity and the inter-satellite distance have already been investigated very detailed in pre-studies, e.g. within the BMBF Geotechnologien Programme: (Reubelt, et al., 2014) and are not the scope of this chapter.

3.5.1 Required Inputs for the Analysis

Based on the simulations and analysis of the orbit requirements shown in chapter 2.4, 3.2 and 3.4 the following scenarios for the analysis of the drag compensations have been selected:

Bender configuration, Scenario 1:

h ~ 460 km, β/α = 107/7, I = 89.5°, ρ_x = 100, Ω = 0°

h ~ 450 km, β/α = 471/31, I = 63°, ρ_x = 100, Ω = 180°

Bender configuration, Scenario 2:

h ~ 360 km, β/α = 125/8, I = 89.5°, ρ_x = 100, Ω = 0°

h ~ 372 km, β/α = 484/31, I = 72°, ρ_x = 100, Ω = 180°

Both scenarios differ mainly in the orbit height (~360 km vs. ~460 km) and in the inclination of the second satellite pair (72° vs. 63°). The results of the analysis are presented in section 3.5.3.

3.5.2 Simulation Assumptions

3.5.2.1 Simplified Satellite Model

A simplified satellite model is designed for the simulations (Figure 3-18). The model was generated such that both satellites fit under a Dnepr-Faring in order to avoid a second launcher and reduce costs. The current satellite design pursues a relatively small cross-sectional area (+X / flight direction) of 0.96 m² to minimize the impact of the air drag.

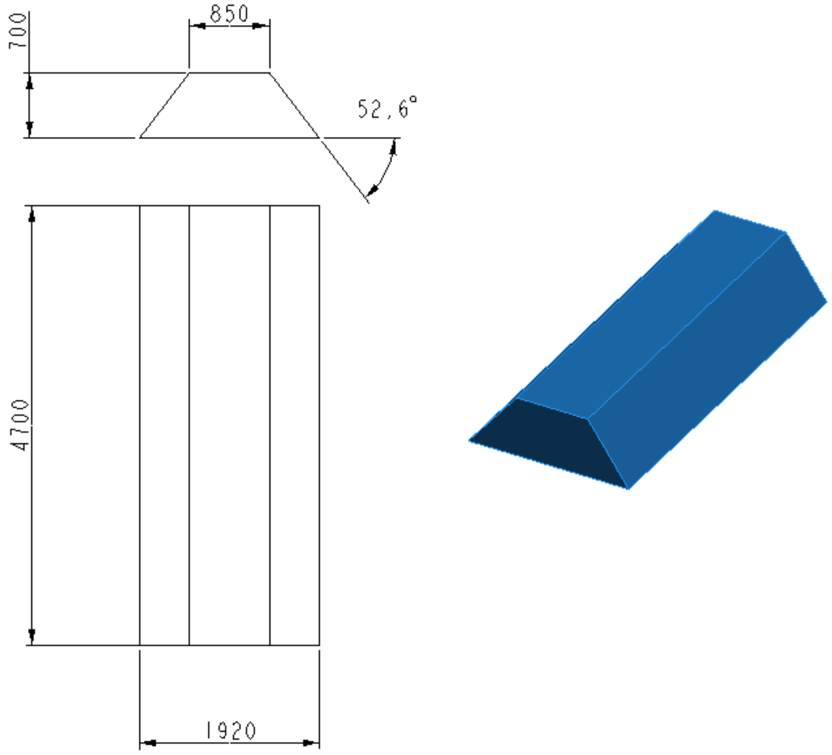

Figure 3-18: Dimensions of the simplified SC (spacecraft) model (in mm)

The internal representation of the satellite in the simulator as surface weighted normal vectors with offset from the center of satellite (CoS) is illustrated in Figure 3-19 w.r.t. the flight coordinate system (LVLH CoS, with x = flight direction (red), y = cross-track (green), z = nadir (blue)).

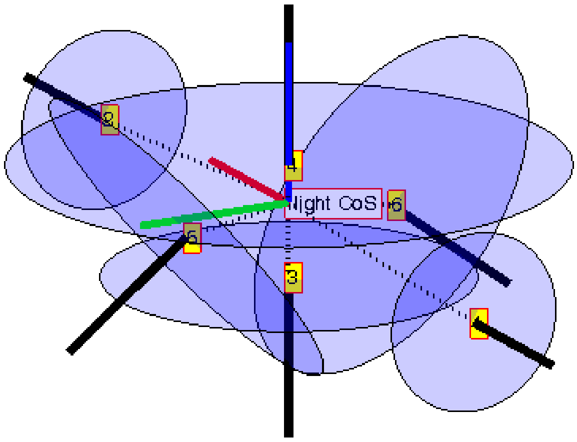

Figure 3-19: Representation of the outer surfaces within the simulator as surface weighted normal vectors with offset from the satellite's center of mass; satellite turned upside down:

The mass is assumed as m = 800 kg and the moments of inertia amount to $MoI(xx,yy,zz)$ = [178, 1504, 1620] kg m^2 and $MoI(xy,xz,yz)$ = 0. The surface properties are selected such that the effective drag coefficient of the satellite is C_D = 2.2 (general assumption), the CoM-offset = 0 and the residual magnetic dipole moment = 0 Am^2 (this corresponds to a balanced and EMC optimized satellite design in order to avoid further disturbances).

3.5.2.2 Assumptions for the Computation of the Air Drag

The launch date (2026) was selected considering the solar cycle and the continuation of gravity field missions and taking into account the pre-studies; e.g. (Reubelt, et al., 2014). Within the simulation the years 2026 to 2039 are investigated and the average annual propellant consumption for a steady-state compensation of the air-drag is identified. Thereby it can be assessed if the current satellite design will meet the planned mission duration of 11 years.

The simulation setup takes the following influences into account:

- Drag forces and resulting moments using the atmosphere model of Jacchia-Bowmann 2006 (JB2006). This is the standard model suggest by ECSS which defines the Earth atmosphere by means of the parameters F10.7 (solar flux with wavelength 10.7 cm) and Ap (magnetic index).
- Earth‘s gravitation model,
- Gravitational forces of sun and moon,
- Solar radiation pressure and resulting moment,
- Gravity gradient moment,
- Magnetic disturbing moment generated by Earth’s magnetic field.

The evaluation of the air density, which depends on the solar activity, plays a central role for the computation of the air drag. The variations of the air density for various orbit heights and solar activities are shown in Figure 3-20.

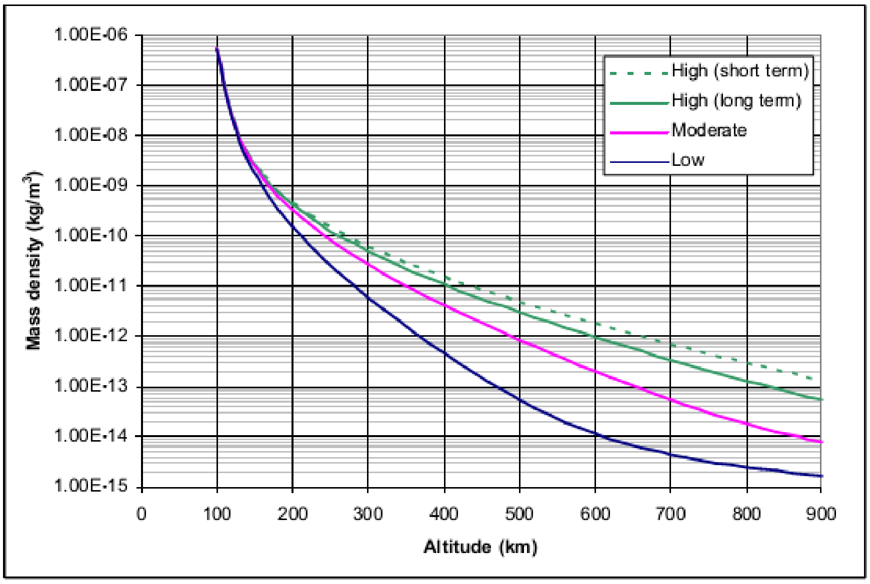

Low, moderate, high long term and high short term solar and geomagenetic activities have the following meanings:
low ($F10.7 = F10.7_{avg} = 65$, $S10.7 = S10.7_{avg} = 60$, $M10.7 = M10.7_{avg} = 60$, $A_p = 0$)
moderate ($F10.7 = F10.7_{avg} = 140$, $S10.7 = S10.7_{avg} = 125$, $M10.7 = M10.7_{avg} = 125$, $A_p = 15$)
high long term ($F10.7 = F10.7_{avg} = 250$, $S10.7 = S10.7_{avg} = 220$, $M10.7 = M10.7_{avg} = 220$, $A_p = 45$)
high short term ($F10.7 = 300$, $F10.7_{avg} = 250$, $S10.7 = 235$, $S10.7_{avg} = 220$, $M10.7 = 240$, $M10.7_{avg} = 220$, $A_p = 240$)

Figure 3-20: Variations of the mean air density (Jacchia-Bowmann model 2006) dependent on orbit height and different solar and geomagnetic activities (from ECSS-E-ST-10-04C)

Some future parameters of the Earth’s atmosphere are estimated based on models, especially for the prediction of the 11-year solar cycle. The estimations of the air density vary considerably dependent on the models and solar activities. This has a significant impact on the estimation of the amount of propellant and is demonstrated by the following simplified computation:

Parameters:

Satellite: m = 800 kg, $MoI(xx,yy,zz)$ = [178, 1504, 1620] kg m², $MoI(xy,xz,yz)$ = 0
m_{mag} = 1 A m², offset CoM-surface center = 0,0 m, C_D = 2,2

Orbit: h = 450 km, I = 63°, 107 revolutions in 7 days, variable RAAN

$F_{drag} = ½ * C_D * \rho * A_{ref} * v_{Orbit}^2$	air drag formula
A_{ref} = 0.97 m²	satellite’s cross-sectional area
v_{Orbit} = 7.6404 km/s	orbital velocity

$dm/ds = F / (Isp*g0)$ propellant consumption per [s] for cold gas thrusters

$Isp\ (N_2) = 60$ s specific impulse of cold gas thruster

The results are summarized in Table 3-3 and are based on standard references for satellite design and ECSS standard values for air densities at orbit height. A margin of 20% was added on m_{1year} and the demand of propellant for 10 years ($m_{10years}$) was estimated. A significant variation of the propellant consumption in the range of 4-10 kg (solar min) to 150-400 kg (solar max) for a mission duration of 10 years can be seen in the Table dependent on the data sources and solar activities. Hence a reliable prediction of the air density and solar activity is very important for an appropriate mission design.

Table 3-3: Estimate of the air density, air drags and the propellant demand (450 km). In the table: source, air density [e-12 kg/m3], F_{drag} [mN], Propellant demand

source	density [e-12 kg/m³]		F_{drag} [mN]	demand of propellant		
				m_{1year} [kg]	+20%	$m_{10years}$ [kg]
SMAaD* - Tabelle	ρ_{min}	0.247	0.0154	0.83	1	10
	ρ_{mean}	1.13	0.0703	3.76	5	50
	ρ_{max}	3.61	0.2247	12.04	15	150
SMAaD* - Figure	ρ_{SolarMin}	0.1	0.0062	0.33	0.4	4
	ρ_{SolarMax}	10	0.6225	33.35	40	400
SADaC* - Tabelle	ρ_{min}	0.09	0.0056	0.30	0.4	4
	ρ_{mean}	1.585	0.0987	5.28	7	70
	ρ_{max}	3.8	0.2366	12.67	16	160
ECSS* - Figure	$\rho_{\text{SolarActivityLow}}$	0.15	0.0093	0.50	0.6	6
	$\rho_{\text{SolarActivityModerate}}$	2.0	0.1245	6.67	8	80
	$\rho_{\text{SolarActivityHigh}}$	5.0	0.3113	16.67	20	200

* SMAaD: Space Mission Analysis and Design, third edition, James R. Wertz and Wiley J. Larson
SADaC: Spacecraft Attitude Determination and Control, James R. Wertz
ECSS: European Cooperation for Space Standardization

The solar activities were further investigated to find a good selection of the air density. Figure 3-21 displays the observed values of F10.7 in blue, its mean value in red as well as different predictions. It is suggested to apply the mean value („F10.7 mean (AGI STK)“ in Figure 3-21) for the mission design (this one also fits best to the observations). The curves for +2 Sigma and -2 Sigma are regarded as too conservative and too optimistic, respectively, and thus are not considered in the following.

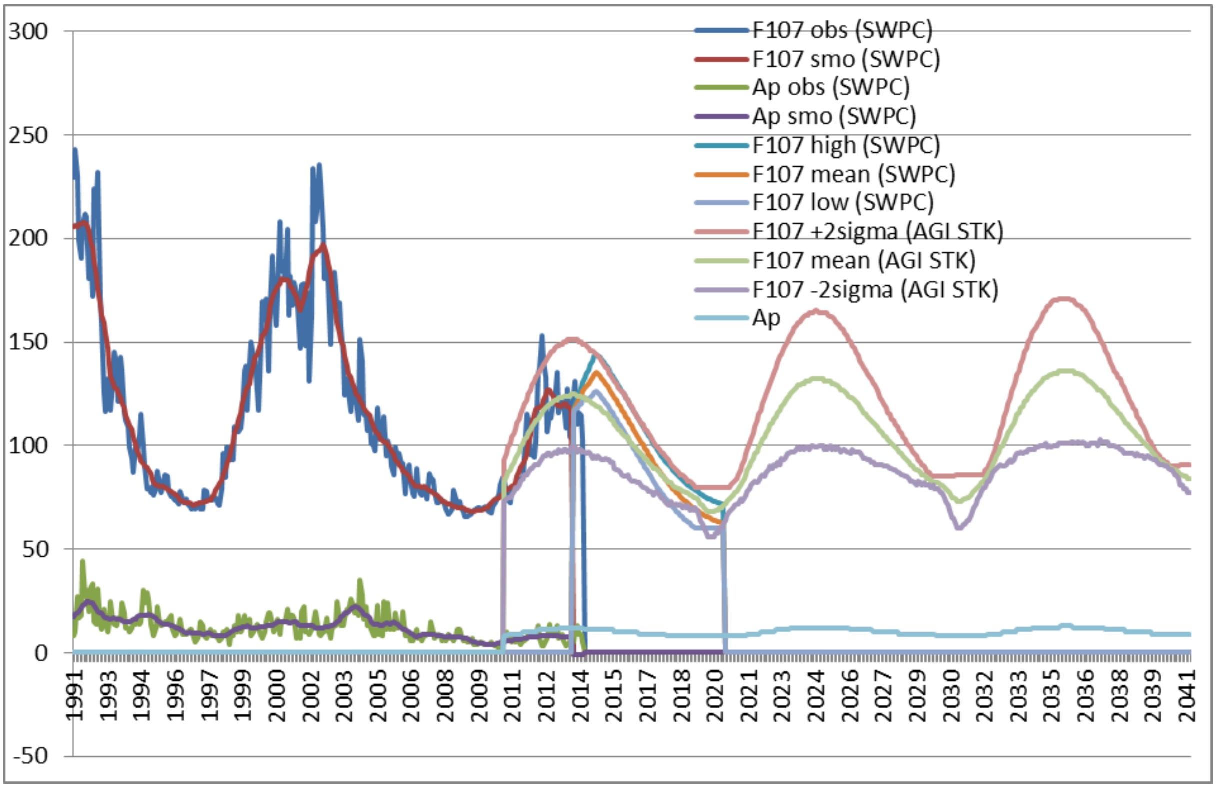

Figure 3-21: Observations and predictions for F10.7 and Ap from different models. Sources: SWPC: Space Weather Prediction Center; AGI STK: Schatten prediction model

3.5.2.3 Orbit Control and Thruster Configuration

Because an AOCS control system design and a thruster configuration do not exist in the actual project phase, the following assumptions are applied:

- The thruster impulse levels correspond to the braking force caused by air drag (other disturbing forces are smaller and periodic +/-; this assumption has been proved in the simulations)
- Only the air drag component in flight direction (x-axis in flight and satellite system coordinate KoS) is compensated, because it is much larger than Y- and Z-component and the Y-component is periodic +/- (also shown in simulation)
- The compensation of the disturbing moments is not added to the propellant estimation because they are also significantly smaller. In addition it is assumed that the attitude control can be guaranteed in parallel to the orbit control by means of slight thruster approach angles and small thrust offsets.

3.5.3 Simulation Results

The following points are valid for both scenarios:

- The mean value for solar activity was applied for the time period 2020-2040
- One orbit was simulated respectively
- Only drag in flight direction is compensated
- Only air drag is considered. Other disturbing forces (e.g. solar pressure, third body influences) can be neglected
- The air drag is dependent on LTAN (Local Time of Ascending Node). The simulations have been carried out in 30° steps for LTAN (= 2h)
- N_2 with a specific impulse *Isp* = 60 s was assumed as propellant for the cold gas system
- The electric propulsion system is supposed to be established by µRITs (micro Radio-frequency Ion Thruster) with Xenon (*Isp* = 2000 s)
- Only the lower satellite pair was considered for each Bender configuration (i.e. 450 km and 360 km)

Results of Scenario 1:

The simulation results are summarized in Table 3-4. The simulator computes air density with min/mean/max values and related min/mean/max values of the air-drag for each orbit. The annual propellant demand has been calculated with the mean F_{drag} which corresponds to the area below the F_{drag}-curve.

Table 3-4: Simulation results for scenario 1 (altitude = 450 km)

LTAN [°]	air density min/mean/max [e-12 kg/m³]	F_{drag} min/mean/max [e-5 N]	annual demand of propellant [kg]
0	0.44 / 0.93 / 1.6	3.4 / 6.2 / 11.2	3.3
30	0.47 / 0.97 / 1.76	3.3 / 6.44 / 12.4	3.45
60	0.46 / 0.93 / 1.63	3.27 / 6.21 / 11.50	3.32
90	0.49 / 0.86 / 1.35	3.41 / 5.73 / 9.26	3.07
120	0.57 / 0.82 / 1.19	3.71 / 5.46 / 7.26	2.92
150	0.55 / 0.85 / 1.29	3.69 / 5.66 / 8.68	3.03
180	0.49 / 0.92 / 1.59	3.44 / 6.13 / 11.17	3.28
210	0.46 / 0.96 / 1.75	3.29 / 6.39 / 12.40	3.42
240	0.46 / 0.92 / 1.64	3.27 / 6.18 / 11.52	3.31
270	0.49 / 0.86 / 1.35	3.40 / 5.71 / 9.29	3.06
300	0.56 / 0.82 / 1.20	3.68 / 5.46 / 7.30	2.92
330	0.55 / 0.85 / 1.30	3.66 / 5.68 / 8.71	3.04

In average the satellite would need approx. 3.2 kg propellant (N_2) per year for drag compensation. For attitude control approx. 1 kg per year is estimated empirically. This means in total 46.2 kg of propellant for a life-time of 11 years.

The estimated demand of propellant can be added with a margin of 20% to account for the following imprecissions:

- compensation of neglected disturbing forces and moments,
- efficiency of the thruster configuration,
- safety margin for propellant

Thus the propellant rises to approx. 57 kg for a mission duration of 11 years. This is considered as feasible.

Results for Scenario 2:

The simulation results are summarized in Table 3-5 and the simulation conditions are identical as for scenario 1. As shown in Table 4 the satellite at an altitude of 360 km will need in average 19.1 kg propellant (N_2) per year for drag compensation without margin and attitude control. This means in total 220 kg of propellant are needed at least to guarantee a mission duration of 11 years. Due to other technological constraints (e.g. mass budget, available space on board) this huge amount of propellant is regarded as unfeasible.

Table 3-5: Simulation results for scenario 2 (altitude = 360 km)

LTAN [°]	air density min/mean/max [e-12 kg/m³]	F_{drag} min/mean/max [e-5 N]	annual demand of propellant [kg]
0	3.40 / 5.16 / 7.50	26.02 / 37.11 / 57.56	19.88
30	3.21 / 5.31 / 8.20	24.63 / 38.27 / 62.94	20.50
60	3.20 / 5.13 / 7.63	24.56 / 36.92 / 58.54	19.78
90	3.45 / 4.79 / 6.28	26.38 / 34.36 / 48.17	18.41
120	4.30 / 4.62 / 4.89	30.68 / 33.16 / 37.44	17.77
150	3.88 / 4.80 / 5.88	29.29 / 34.45 / 45.13	18.45
180	3.40 / 5.15 / 7.50	26.04 / 37.02 / 57.56	19.83
210	3.21 / 5.30 / 8.20	24.63 / 38.16 / 62.94	20.44
240	3.20 / 5.12 / 7.63	24.56 / 36.82 / 58.55	19.73
270	3.45 / 4.78 / 6.28	26.35 / 34.30 / 48.17	18.38
300	4.29 / 4.62 / 4.92	30.53 / 33.15 / 37.44	17.76
330	3.88 / 4.80 / 5.88	29.20 / 34.49 / 45.14	18.48

Thus the following propulsion concept for scenario 2 was designed:

- electric propulsion (µRITs) for drag compensation
- cold gas propulsion for attitude control

The electrical power demand for the air-drags of
Table 3-5 was assumed as 82 W – 100 w for compensation (2 thrusters, each approx. 30 W DC + 35 W/mN, plus 20% margin). The average generated solar energy available for each satellite is listed in Table 3-6 (a constant power demand for the satellite of 200 W was assumed disregarding the propulsion system).
This should allow for the power demand for drag compensation. For attitude control approx. 1 kg N_2 per year is needed similar to scenario 1.

Table 3-6: Estimate of the solar energy generation for scenario 2

Power estimate [W]	STO 0	STO 15	STO 30	STO 45	STO 60	STO 75	STO 90
Bender pair 1 @360 km, 89.5°	461	463	473	495	510	615	608
Bender pair 2 @372 km, 72°	461	463	472	492	505	536	615

3.5.4 Summary of Technological Conditions

The results from the feasibility analysis for both scenarios are summarized in Table 3-7 and Table 3-8.

Table 3-7: Summary of the analysis, scenario 1. In the table: configuration, orbit parameter, feasibility, propulsion system, propellant demand, mission lifetime, launcher

configuration	Bender configuration
orbit parameters	satellite pair 1: h = 460 km, I = 89.5°; satellite pair 2: h = 450 km, I = 63°
feasibility	yes
propulsion system	cold gas propulsion system
propellant demand	approx. 43 kg (N_2) for drag compensation approx. 14 kg (N_2) for attitude control
mission duration [years]	11
launcher	Dnepr

Table 3-8: Summary of the analysis, scenario 2

configuration	Bender configuration
orbit parameters	satellite pair 1: h = 360 km, I = 89.5°; satellite pair 2: h = 372 km, I = 72°
Feasibility	Yes
Propulsion system	cold gas/elektric propulsion µRITs for drag compensation, cold gas für attitude control
Propellant demand	approx. 8 kg (Xenon) for drag compensation approx. 14 kg (N_2) for attitude control
mission duration [years]	11
launcher	Dnepr

In summary the following conclusions can be drawn:

The demand of propellant and electric power for drag compensation is an important constraint for the orbit configuration and the expected mission duration:

- For both scenarios a mission duration of 11 years can be expected concerning the drag compensation. Other constraints (e.g. degradation of the batteries) should be investigated in further project phases.
- the cold gas propulsion system is proposed for scenario 1
- a combined propulsion system is proposed for scenario 2 using µRITs for drag compensation and cold gas for attitude control

Note: The current satellite model provides only a first analysis of the technological constraints for both suggested scenarios.

3.6 Conclusions and suggested Constellation/Orbit Parameters

Concerning the geodetic requirements, the sampling distribution and gap evolution behaviour of a mission play important roles in gravity field recovery of satellite missions. It has been discussed that the modified Colombo-Nyquist rule enables higher temporal resolution of gravity solutions, while the high noise level, caused by spatial aliasing of the sub-Nyquist solutions, might be dealt by post-processing methods. That means for a single pair satellite mission, an almost good quality of gravity recovery of 6-day for maximum degree 90 is achievable (provided that the ground-track coverage is homogeneous enough), while even higher quality is achievable for 3-day solutions of Bender formations (two pairs satellite missions).

For the orbit height, several studies suggested at least 300 km and a satellite distance of ρ = 100 km to compromise between geodetic sensitivity and technological feasibility. However, the technical issues within the low altitude missions of around 300 km are still very challenging and lead us to consider higher orbit heights for future missions.

For the double pair missions (Bender formation), and concerning the inclination of the inclined satellite pair, a choice between $I \approx 70°$ and $I \approx 75°$ is suggested.

The results show the superiority of the Bender formation compared to the Pendulum formations with the advantage of reduced demand on the technology (SST range-rate < 1m/s) of Bender formation.

However, for Bender formation, the disadvantage of employing four satellites and hence two launches (meaning an increase in cost) should be considered.

For future gravity satellite missions, it is important to select the orbit in that way that no large resonances occur at low SH orders. Looking for orbits without such large effects up to the highest possible order, one would end up at four altitude bands between 294 and 309 km, 360 and 370 km, 416 and 426 km and 479 and 495 km.

Concerning the technical challenges with the Bender formations, the demand of propellant and electric power for drag compensation is an important constraint for the orbit configuration and the expected mission duration. For both scenarios of Bender formation, with high orbit altitude (around 450 km) and low orbit height (around 360 km), a mission duration of 11 years can be expected concerning the drag compensation. Other constraints (e.g. degradation of the batteries) should be investigated in future. For the Bender scenario of high orbit altitude, this study suggests cold gas propulsion system. A combined propulsion system is then proposed for scenario with lower altitude, using µRITs for drag compensation and cold gas for attitude control.

4 Attitude Determination and Control

4.1 Introduction

For a future gravity field mission (single or double-pair mission), the basic scientific observable is the gravitational acceleration between two reference points on two satellites, separated by approximately 100 km. Ideally, the reference points are assumed to be located at the CoM of the satellites, such that rotations of the satellite do not induce changes to the distance between the reference points. The connecting line between the reference points (coincided with CoMs) is referred as the Line-of-Sight (LoS).

The gravitational accelerations between two reference points is obtained by measuring the non-gravitational accelerations at the reference points with accelerometers and the distance variations between the reference points (along the LoS) with an SST laser interferometer. By combining both measurements one obtains the desired pure gravitational accelerations between the reference points.

An appropriate AOCS system has to be designed for the realization of the described measurement principle. Such an AOCS system should fulfil following key tasks:

- Maintain the orbit height (e.g. by means of drag-compensation)
- Determine the attitude of the satellites
- Perform orbit and attitude control manoeuvres
- Guarantee laser fine pointing
- Guarantee the proposed drag-compensation strategy (e.g. adequate thrust range/resolution/noise level, achievable requirement on the amount of propellant)
- Other related tasks

This section describes the preliminary design for a future gravity field mission taking into account the results obtained in the previous chapters. Chapter 4.2 provides an analysis of the major requirements for the AOCS system, followed by the results of trade-off analyses of the pointing methods (Chapter 4.3) and the propulsion systems (Chapter 4.4). The preliminary AOCS concept is introduced in Chapter 4.5 and the proposed instruments for the AOCS system are listed in Chapter 4.6.

4.2 Identification of Requirements for the AOCS

4.2.1 Drag-Compensation Requirements

A drag-compensation system is required due to following reasons:

- to maintain the orbit height
- to avoid the saturation of the accelerometer
- to fulfil the requirements on the residual accelerations for the accelerometer e.g. as stated in [10].

Correspondingly, the AOCS system should be designed in such a way that it can fulfil the above requirements for the expected mission lifetime of 11 years, under consideration of the technical constraints (e.g. limited amount of propellant on-board, accelerometer performance).

Two drag compensation strategies are considered in the following:

4.2.1.1 High Bandwidth Compensation

One option is to feed back the accelerometer measurement to the AOCS, which minimizes the accelerometer measurement by the thruster. This concept has a higher complexity, since the internal control loop of the accelerometer and the outer AOCS control loop need to work in parallel. This requires for example that the bandwidths of the two control loops are separated to avoid instability (interference or race conditions between the loops). In the case of an infinite control gain, the accelerometer measurement in-orbit would be zero and all information on non-gravitational accelerations are encoded in the control signal for the thrusters. However, for a realistic controller the gain is finite and the accelerometer would measure a value close to zero. Other difficulties may arise from the fact that the accelerometer signal is subject to biases, drifts and jumps. So it cannot be used for very low frequencies. Sensor fusion with GPS or with commands from ground might be required to avoid long-term drifts.

Currently this strategy is proposed and several drag-compensation simulations have been carried out. As a baseline for the drag-compensation strategy, it is proposed to use the measured non-gravitational accelerations caused by disturbing forces in the AOCS control loop and command the thrusters to provide an adequate thrust to counteract the disturbances acting on the satellite. A full-compensation strategy means that it is attempted to counteract all disturbing forces by means of thrusts in opposite directions with (ideally) the same magnitude as the disturbances. The requirement for a drag-compensation system heavily depends on the required noise level and saturation limit of the selected accelerometers, as briefly summarized in Table 4-1.

Table 4-1: Collection of information regarding the accelerometer (Source: STI/IfE/TAS[10])

Missions	ACC noise level ($m/s^2/\sqrt{Hz}$]	ACC saturation limit (m/s2)	Nr. of ACCs per SC
GRACE	1e-10	Ca. 5e-5	1
GOCE	2e-12	Ca. 6e-6	6
e.motion	1e-12 - 1e-11	Ca. 8e-6	1
GeoTech	2e-12	Ca. 6e-6	1
TAS NGGM	1.5 - 5e-12	Ca. 1e-6	4
e^2.motion	4e-11	Ca. 8e-6 – 1e-5	1

Detailed descriptions and results of drag-compensation simulations can be found in chapter 3.5, where the propellant demand for two Bender-configurations at different orbit heights (450 km and 360 km) was analysed. Using the same simulation conditions, an additional analysis has been carried out to find a possible boundary orbit height (in terms of propellant demand) for a mission with purely cold gas propulsion systems. Currently the orbit height of 420 km is considered to be the boundary altitude for a cold gas propulsion system. At this altitude, a propellant demand of about 80 kg cold gas (N_2, Isp = 60 s) has been estimated for the drag-compensation. Taking into account that one would need about another 14 kg for AOCS control, the total amount of propellant would be about 94 kg. Assuming that the tanks would weigh about 56.4 kg (60% of the weight of the propellant), the propellant and tanks together would weigh about 150.4 kg. This weight is considered to be feasible for a mass limit of 800 kg per SC.

The analyses of the proposed drag-compensation concept as well as the behavior of the thrusters are described in section 4.5.3.

4.2.1.2 DC Compensation or Feed Forward Control

Another option for the drag compensation is to use a constant thrust, which might be adopted daily, weekly or monthly. The constant thrust counter-acts the mean non-gravitational forces in along-track direction and therefore avoids an orbital decay of the satellites. This requires that short-term variations of the non-gravitational accelerations do not exceed the dynamic range of the accelerometer. The accelerometer signal contains the full non-gravitational accelerations in the measurement band (e.g. 0.18mHz to 1 Hz) and actuation is performed only out of the measurement band. The thrust level can be determined on ground or in-orbit by accelerometer measurements or by simple models (for air drag and solar radiation pressure). This compensation scheme can be seen as DC compensation or as feed forward control.

4.2.2 Laser Fine Pointing Requirements

4.2.2.1 Beam pointing

The Laser interferometer requires a beam pointing better than a particular threshold to perform phase (distance) measurements and to keep the laser link locked. A value for a requirement for the beam pointing w.r.t. the true line-of-sight is in the order of ±100 µrad (half-cone angle), given by the beam divergence auf a Gaussian beam in TEM00 mode and by the available laser light power. The beam divergence is dependent on the beam size on the satellites, where usually values of a few millimeters are applicable, and the laser light wavelength, where 1064 nm is usually assumed. Since the satellite-to-satellite distance measurement will stop for a pointing error larger than ±100 µrad in the worst-case (link-loss), this requirement should be fulfilled for most of the time (4σ-value or maximum allowable peak-value).

There are two different effects, which might cause a link loss due to pointing errors:

- Too low received light power on a satellite: The transmitted beam on the remote satellite is misaligned w.r.t. the line of sight (see upper panel of Figure 4-1). The beams on the receiver stay aligned.
- Too low interferometric contrast on a satellite: The local/receiver satellite and therefore the received and local beams are misaligned in the interferometer, such that the overlap of the light fields is poor (see lower panel of Figure 4-1).

One should note that Figure 4-1 is a simplified model where only one spacecraft is receiver and the other transmitter. In e^2.motion, however, each satellite is transmitter and receiver at the same time.

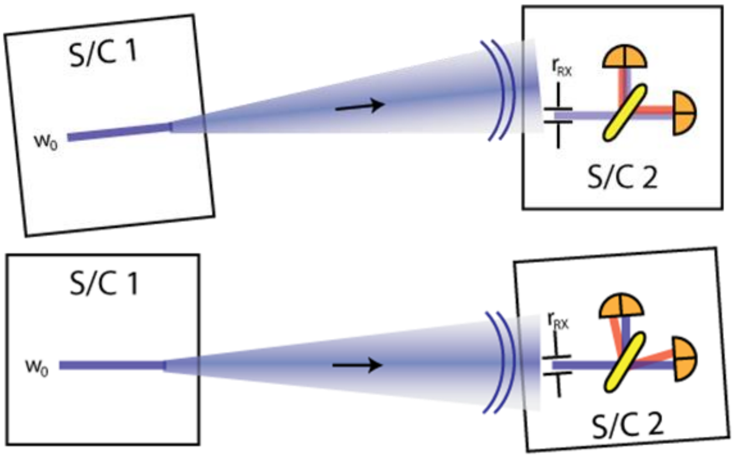

Figure 4-1: Simplified model for interferometer pointing errors. Upper figure: transmitter misaligned, received light power on receiver S/C low, beams on receiver aligned (high contrast); Lower figure: transmitter aligned, receiver misaligned, beams on receiver satellite tilted (low contrast), received light power still high.

4.2.2.2 Attitude Jitter

Next to the beam pointing error, there is also a spacecraft attitude jitter requirement. It is necessary, since a laser ranging interferometer has a rotation-to-length coupling in the order of 100 µm/rad (for yaw and pitch rotations), thus, spacecraft attitude jitter noise of 0.1 mrad/sqrt(Hz) yields directly a distance measurement noise in the order of 10 nm/sqrt(Hz). This requirement limits the degradation of the measurement sensitivity due to attitude jitter. The requirement can be relaxed at low frequencies by the noise shape function (NSF), since the overall instrument sensitivity is relaxed by the NSF. The interferometer is to first order insensitive to rotations in roll-direction, thus both requirements (beam pointing and attitude jitter) can be relaxed by one order of magnitude for the uncritical roll axis.

4.2.2.3 Differential Wavefront Sensing

Although the pointing and attitude requirements are more stringent for the laser ranging interferometer than for a microwave ranging instrument, the laser interferometer is in general capable to measure the pointing, as long as the interferometer is locked. The so-called Differential Wavefront Sensing (DWS) technique can be used to detect the relative wavefront tilt between the received light and the local laser beam, which is ideally proportional to the local spacecraft misalignment (w.r.t. line of sight). A noise in the order of 1µrad/sqrt(Hz) is a feasible assumption for a LEO mission, considering that for LISA a noise below 10 nrad/sqrt(Hz) is envisaged [9].

In contrast to star tracker which provides the attitude of the satellite in an inertial frame, the DWS provides directly the attitude in yaw and pitch w.r.t. the line-of-sight. The DWS signal can be read out with high bandwidth up to several kHz and can be used in a feedback control loop to stabilize the pointing towards the distant satellite and to maximize the interferometric contrast at the same time.

One should note that the DWS is only dependent on the local spacecraft attitude, as long as the beam pointing of the distant spacecraft is sufficient to keep the interferometer locked. Remote spacecraft jitter does not change local DWS signal (to first order), such that each satellite stays an autonomous system. Since DWS is insensitive in the roll-direction, the star trackers have to be used for the roll-information.

4.2.2.4 Pointing Methods

Spacecraft Pointing

For the direct spacecraft pointing method the following requirements should be fulfilled:

- Pointing w.r.t. true line-of-sight is better than
    - Yaw and pitch: ±100 µrad
    - Roll: ±2000 µrad
      (4σ or maximum allowable peak-value, half-cone angle)
- Attitude jitter w.r.t. true line-of-sight is better than
    - Yaw and Pitch: 100 µrad/sqrt(Hz) x NSF(f)
    - Roll: 2000 µrad/sqrt(Hz) x NSF(f)
      in the LRI measurement band (0.18 mHz – 1 Hz)
- The reachability of these values should be assessed in
    - Science Mode, when DWS signal is available
    - Acquisition mode, when DWS is not available
    - Initial Acquisition mode, when DWS is not available and biases are present

Actuation of Component or of Optical Bench

The method of component actuation the following requirements should be fulfilled:

- Pointing w.r.t. true line-of-sight is better than
    - Yaw and pitch: ±2 mrad
    - Roll: ±4 mrad
      (4σ or maximum allowable peak-value, half-cone angle)
- Attitude jitter w.r.t. true line-of-sight is better than
    - Yaw and Pitch: 100 µrad/sqrt(Hz) x NSF(f)
    - Roll: 2000 µrad/sqrt(Hz) x NSF(f)
      in the LRI measurement band (0.18 mHz – 1 Hz)

The trade-off analysis of the pointing methods is described in Chapter 4.3.

4.2.3 Formation Control Requirements

4.2.3.1 Introduction

Beyond the issue of pointing the SST link in the right direction also the formation of the satellites and their orbit altitude needs to be maintained. The formation(s) of the satellites must be controlled sufficiently well that the operational limits are not exceeded for

- SST link distance,
- altitude,
- relative position offset.

Two approaches are conceivable in order to maintain the formation within operational limits. Firstly a manoeuvre could be carried out whenever the operational range is exceeded in order to recover the nominal formation. Alternatively the formation could continuously be maintained within tight limits around the nominal formation. The first option will only require occasional manoeuvres and can be called episodic orbit control. The second option requires very frequent manoeuvres and is most reasonably implemented as continuous orbit control by a low-thrust prolusion system. In the following we analyse the impact of both options on the science operations of the satellites.

In the baseline the preference will be given to a system using drag compensation by a low-thrust electric propulsion system. The reason for this is that a drag compensation system improves that science performance in two ways. Firstly it allows flying at a lower altitude at which the gravity signal is larger, secondly it reduces the acceleration measured by the accelerometer and hence allows to employ a more sensitive accelerometer that is tailored to lower acceleration. Consequently for the baseline only the option of continuous orbit control will be relevant. However for completeness also the topic of episodic orbit control is covered.

4.2.3.2 Episodic orbit control

Episodic orbit control seems attractive because it tends to reduce the operational complexity of the mission. In particular the manoeuvres on the two satellites can be carried out sequentially one after the other.

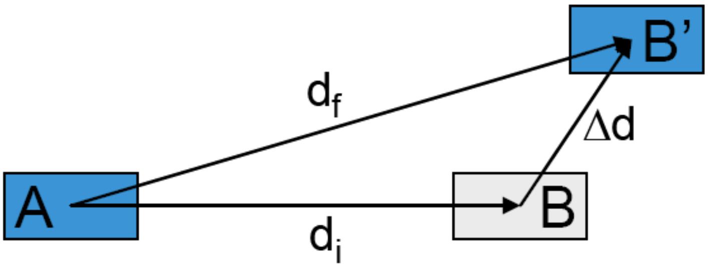

Figure 4-2: Geometry of an orbit manoeuvre for episodic orbit control, initial distance di, final distance df, nominal distance dn

A good rule of thumb for establishing the need for a manoeuvre in order to maintain the link distance is when the link distance differs from the nominal distance by more than half of the nominal distance, Δd > 1/2 dn. While the operational range of the instrument may be larger a large change of distance is not desirable because the response of the SST system to the gravity field changes significantly with the link distance. Obviously no other orbit maintenance manoeuvre must have a final state that exceeds the allowable bounds on the link distance.

As a typical orbit maintenance manoeuvre we consider an orbit raising by a Hohmann transfer, i.e. a change semi-major axis. A Hohmann transfer is particularly relevant for this analysis because it leads to a different semi-major axis for the two satellites during the manoeuvre and hence to a secular drift of the relative position. Such a manoeuvre is hence the worst case for the consideration of changes in the inter-satellite link distance.

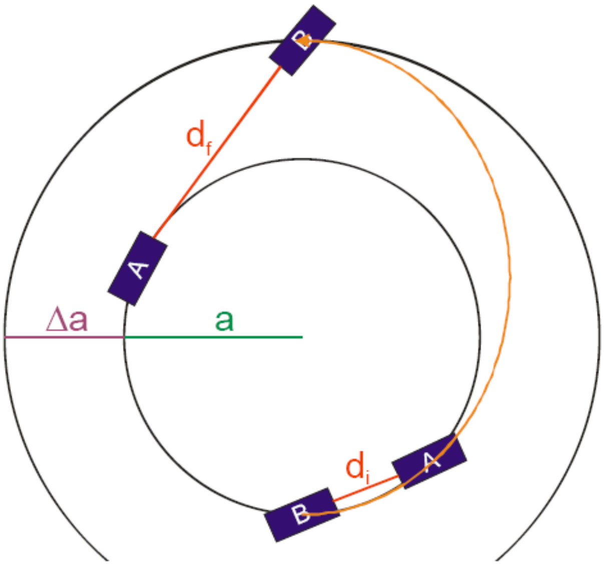

Figure 4-3: Formation behaviour during Hohmann transfer

We consider a maximal orbit raising by Δa = 10 km. Larger manoeuvres are unlikely for mission performance reasons: The ground-track repeat pattern varies drastically with altitude and for changes of more than 10 km the ground-track pattern would be distorted so much that it is no longer acceptable from a science performance point of view. Hence manoeuvres with a change of semi-major axis of more than 10 km are unlikely to be implemented for the mission. A notable exception may be a deliberate large change of altitude that serves to change the science focus or operational conditions of the mission. However such a manoeuvre will be very rare and a loss of the SST link for a longer time span will be fully acceptable. Hence in the following the considerations will be limited to manoeuvres with Δa ≤ 10 km.

If we consider an orbit raising by $\Delta a = 10$ km the following Δv is required: $\Delta v = -\frac{1}{2} n \Delta a \sim 4\sqrt{2}$ m/s, where $n \sim 2\pi/5500$ s is the mean motion of a typical orbit of 400 km altitude. The change of semi-major axis leads to a drift between the satellites. The drift is linear in time and after half an orbit the link distance has changed by

$$\Delta d \sim \Delta v\, P/2 = -\pi/2\, \Delta a\ ,$$

where P is the orbital period. This is less than half of the nominal orbit distance. Consequently, the orbit raising of the satellites in an SST formation can be conducted separately if the manoeuvres are not separated by more than 1.5 orbits.

For a cold-gas system the duration of the orbit raising of one satellite may significantly exceed the above limit of 1.5 orbits. For instance for a propulsion system that provides a thrust of 0.1 N the duration of firing is given by

$$\Delta v = at = F/M_{S/C}\, t = (0.1 \text{ N} / 500 \text{ kg}) \times t = 10\text{-}4 \text{ m/s}^2 \times t,$$

where a spacecraft mass of 500 kg has been assumed. For the orbit raising of 10 km that was considered above the duration of the manoeuvre becomes $t \sim 4\sqrt{2} \times 10^4$ s which corresponds to approximately 10 orbits. Consequently, in this case, orbit raising must be split into several manoeuvres in order to not exceed allowable link distance range. This is achieved if first the altitude of satellite 1 is raised and next the altitude of satellite 2 is raised beyond that of satellite 1. Then again the altitude of satellite 1 is raised beyond that of satellite 2 and so on. The different altitudes and hence semi-major axes of the intermediate orbits lead to secular along-track drifts between the satellites that can be used to reduce the inter-spacecraft distance to its nominal value again. For instance a semi-major axis difference of 350 m leads to a drift of 50 km during one day. A tentative manoeuvre planning is easily conducted using the linearised relation between the along-track drift Δs and the semi-major axis difference Δa,

$$\Delta s = -(3/2)\, n\, \Delta a\, t\ ,$$

where n is the mean motion along of the nominal orbit, and is the duration of the drift. Using an appropriate timing of the manoeuvres and drift phases the SST distance can be kept within operational limits.

For episodic orbit control and a cold-gas propulsion system the allowable distance between the satellites may easily be exceeded during an orbit control manoeuvre. This can lead to significant interruption times for the science operations. In order to avoid these drawbacks three main options exist. Firstly orbit control manoeuvres can be limited in magnitude and instead be conducted more frequently. Alternatively orbit control manoeuvres can be conducted simultaneously for both satellites or can be split into a sequence of alternating manoeuvres on the two satellites that are bundled to accomplish large orbit manoeuvres.

4.2.3.3 Continuous orbit control

For a formation control strategy that foresees continuous orbit maintenance the issues to be considered are of a different nature. In continuous orbit maintenance the magnitude of thrust will be in the order of the drag force onto the satellite due to air drag. As a consequence no large changes in inter-satellite distance will occur. In this case it is sufficient to consider the impact of the continuous variable thrusting due to orbit control on attitude of the satellites. For the thrust level we have

$$a_{thrust} \sim a_{drag} \sim 10^{-5} \text{ m/s}^2 \text{ to } 10^{-6} \text{ m/s}^2\ .$$

The variability of the air drag and hence of the thrust will be roughly by a factor of 2. In order to be highly conservative we assume a maximal thrust of amax ~ 10^{-4} m/s². For a typical control loop period of the AOCS is $t_{AOCS} \sim 1$ s. The maximal angular disturbance due to thrusting can be derived. We assume the following satellite parameters:

- Mass M=500 kg,
- Length l=4m,
- Moment $I=Ml^2/12$ (corresponding to that of a solid slab).

Two effects will lead to angular disturbances:

- Offset of the thrust vector from the centre of mass,
- Thruster misalignment.

The first effect is clearly negligible. Even for a thruster displacement as large as 1 cm the angular disturbance $\Delta\alpha$ is negligible:

$$\Delta\alpha = \tfrac{1}{2}\,(T/I)\,t_{AOCS}^2 \sim 0.4\ \mu\text{rad}\ .$$

Concerning thruster misalignment we consider an orthogonal thrust of 10% of the magnitude used for orbit maintenance. The angular disturbance under this highly conservative assumption is:

$$\Delta\alpha = 5\% \times (a/I)\,t_{AOCS}^2 \sim 7.5\ \mu\text{rad}\ .$$

Also this value for the angular disturbance is significantly below the link pointing knowledge.

Obviously, continuous orbit control does not impair the link pointing between the satellites. On the contrary, under all realistic assumptions the orbit control and attitude control are decoupled in amplitude and cannot interfere.

It is worth noting the coupling between the attitude control and the orbit control is so weak that even for the 0.1 N thrust that has been considered above for episodic orbit control the link pointing will not be affected beyond a negligible disturbance during manoeuvres.

For formation control, the thrust direction will in general not be in the direction of the link. The maximal acceleration in directions different from along-track will be limited to the dynamical range of the accelerometer. This is necessary because, using a low-thrust propulsion system such as electric propulsion, the formation control manoeuvres will have quite long durations. Hence it is not desirable to interrupt science operations during the formation control manoeuvres. The dynamical range of the accelerometer will most likely be less than 10^{-4} m/s² in order to achieve a sufficiently low noise floor for the accelerometer (for the baseline applied it is 5×10^{-6} m/s² in flight and zenith direction and 5×10^{-4} m/s² in sideward direction). Hence the above estimates about disturbances of the link pointing are applicable for formation control as well.

4.2.3.4 Conclusions and Tasks

The control of the formation orbit by episodic orbit control and continuous orbit control have been considered. Episodic orbit control is accomplished by impulsive manoeuvres that are interleaved by large duration coast arcs for science operations. Assuming that episodic orbit control is carried out by a cold-gas propulsion system it turns out that the manoeuvres will typically have durations in the order of the orbital period. If the manoeuvres on the two satellites are carried out sequentially then the drift between the satellites during the manoeuvres may become so large that the SST link can no longer be established. Hence it needs careful consideration if episodic orbit control imposes a significant reduction of the time available for science operations.

For continuous control of the orbit by a low-thrust system the orbit control requires such low levels of thrust that it is fully compliant with continuous science operations even for a very narrow SST beam.

The above analysis of the attitude control concepts has been focussing on the sensors of the attitude control system because commonly the sensors are limiting the performance of the attitude control system. The AOCS will be reconsidered taking into account also torques from atmospheric disturbances and the behaviour of the actuators as part of the AOCS design.

4.3 Trade-Off Analysis of Laser Pointing Methods

4.3.1 Pointing Methods

4.3.1.1 Spacecraft Pointing

In this approach the DWS signal is fed into the AOCS together with conventional attitude information (star tracker, sun / earth sensors). The satellite uses thrusters and magnetic torquer to keep the interferometer beams aligned with the line-of-sight, once the laser link has been established. The interferometer and local laser beams are fixed in the satellite frame, thus, beam pointing and spacecraft attitude are equivalent up to some static offsets. Pointing by AOCS has been studied in the LISA mission for many years [12, 13] and is feasible in a quiet deep-space environment, where the spacecraft can be actuated with low-noise micro-newton thrusters. The application of this concept in a LEO mission with air drag and changing environmental conditions is more challenging, but has been suggested in previous LEO mission proposals [9 and 11]. Keeping the pointing below ±100 µrad requires a tight control, which on the other hand might exceed the propulsion consumption budget or might lead to a higher pointing jitter noise.

4.3.1.2 Actuation of Component

In the case that the S/C pointing error cannot be controlled to be less than ±100 µrad, the direction of the outgoing (transmit) and local oscillator beams can be steered by rotating a mirror or beam splitter on the optical bench of the interferometer. If the component is in the sensitive measurement path, one needs to ensure that the resulting tilt-to-length coupling is sufficient small, which is in general difficult. Therefore the actuation of a component, which is not in the sensitive measurement path, is favored.

The actuator can be used to zero the DWS signal by a feedback control loop, which ensures a beam pointing ideally along the line-of-sight. The residual DWS signal is ideally a measure for the misalignment of the outgoing beam w.r.t. the line of sight and should be close to zero for a control loop with high gain and high bandwidth. Since the laser beams are not fixed in the local spacecraft frame, no direct spacecraft attitude information is available. However, it can be obtained indirectly by an additional sensor in the actuator, which measures the actuator position w.r.t. the satellite frame. This method will be used for the Laser interferometer in the GRACE Follow-On mission (Sheard, et al., 2012). In the Laser Communication Terminal (LCT) missions a similar approach with a set of actuators is used to point the laser beam to the distant spacecraft (Smutny, et al., 2008), however, a phase-stable optical path is not required in these missions.

The actuator decouples the interferometer laser beam from the spacecraft frame, such that larger deviation in spacecraft pointing can be tolerated, since they are compensated by the actuator. Also the spacecraft attitude jitter is still present and couples into the ranging measurement. On GFO this coupling contributes to about 40 nm/sqrt(Hz) to the ranging performance (about 30 % of the total instrument error).

4.3.1.3 Actuation of Optical Bench

This approach is similar to the actuation of the component, whereby not a single component but the whole optical bench is rotated using a DWS control loop. By rotating the optical bench, the beam path of the received light can be held fixed through the optical setup. A varying path through the optical bench usually induces a variation in the optical path length (distance measurement). This coupling can usually be minimized by optimizing the interferometer layout, such that a design sensitivity in the order of nm/sqrt(Hz) is achieved.

A drawback of this method is furthermore the need to move around an object with a mass in the kg region, which might disturb the accelerometer measurements on-board of e^2.motion. The mass also limits the actuation bandwidth to low frequencies.

Due to these drawbacks this method is assumed to be undesirable.

4.3.2 Trade-off Analysis Results

Three different methods as described above have been suggested to achieve interferometer pointing. The following recommendations are identified from this analysis:

Recommendation 1:

At least the following three different modes should be distinguished by/in the AOCS system (see Figure 4-4):

- Science mode, when the interferometer link is established and DWS is available.
- Acquisition mode, when the interferometer is not locked and DWS is not available.
- Initial Acquisition mode, when interferometer is not locked and unknown biases between S/C frame, Star Camera frame and interferometer frame are present.

These modes represent different states of the LRI. It needs to be ensured that the LRI (and satellite) can reach science mode. Initial acquisition is critical, since the instrument (alignment) biases due to launch vibrations, zero-G release, integration tolerances or de-moisturization might be very large.

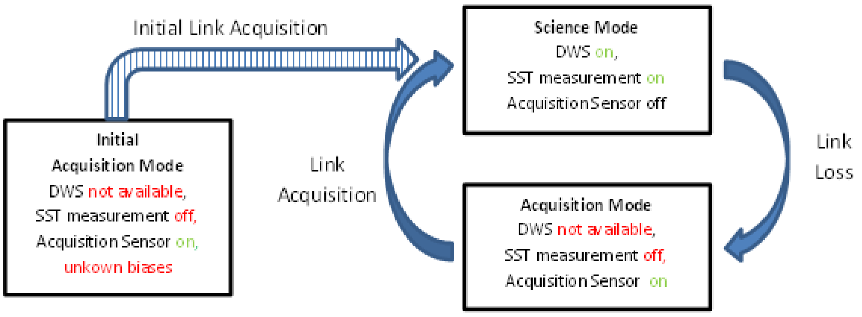

Figure 4-4: Different modes of interferometer and AOCS

Recommendation 2:

The spacecraft pointing method using DWS should be used in the e^2.motion concept if feasible. Actuation of a component is a fallback option if the demands on the satellite are too high. AOCS simulations considering actuator and sensor noise should verify if interferometer pointing by spacecraft can be achieved with an AOCS design for e^2.motion.

The spacecraft pointing method using DWS for the laser interferometer is advantageous against actuation of a component , since

- the main scientific instruments, interferometer and accelerometer, stay aligned more tightly with the line-of-sight axis, which shall be measured by e^2.motion. This is beneficial for the measurement sensitivity.
- a less complex laser ranging instrument can be designed without any moving parts. This leads to increased reliability and lower power consumption of the LRI.
- Direct information on satellite attitude w.r.t. the line-of-sight is available by DWS

Recommendation 3:

AOCS simulations should verify if a dedicated acquisition sensor is required in the LRI. If an acquisition sensor is required, AOCS simulations should provide requirements for an acquisition sensor containing values for sensitivity, allowable bias and dynamic range in yaw and pitch (roll is not measureable). These values can be obtained by performing AOCS simulations with actuator and sensor noise (Star Camera, IMU, GNSS, …) in acquisition mode, but

- without acquisition sensor.
- with different noise levels and biases for the acquisition sensor and observing when the requirement for AOCS Pointing is fulfilled.

Location of the Acquisition Sensor: The tight tolerances on alignment for the instruments and requirements for beam pointing suggest the use of an acquisition sensor on the stable optical bench of the LRI, such that misalignments due to integration and launch are kept small between acquisition sensor and optical axis of interferometer.

Current simulation results of the AOCS suggest that the limiting factor for reaching AOCS pointing might depend on the acquisition sensor. A concept for an acquisition sensor has not been defined, yet. Information and requirements for the design of this sensor would be beneficial.

Recommendation 4:

For AOCS simulations the following DWS sensitivity and bias should be assumed:

$$1\ \mu\text{rad} / \text{sqrt(Hz)} \ \text{ and } 10\ \text{urad offset}$$

The sensitivity requirement is a factor 100 worse than for LISA. A rough estimation for the DWS sensitivity can be obtained by assuming a measurement sensitivity at the photodetector at 10 nm/sqrt(Hz) level, which corresponds to an electric phase noise of 60 mrad/sqrt(Hz). DWS is obtained by a linear combination of four signals of the detector segments, which leads to a factor sqrt(4) in the electrical phase noise. The conversion factor between electrical phase (angle) and geometrical angle is usually in the order of 10.000, yielding 60*sqrt(4)/10000 mrad/sqrt(Hz) = 12 µrad/sqrt(Hz). This estimation completely neglected the high common-mode rejection of e.g. laser frequency noise in the linear combination of DWS signals.

The offset is assumed to consider a misalignment of the transmit and/or receive beam axis w.r.t. the local oscillator (error in optical bench alignment).

Recommendation 5:

If spacecraft pointing is not feasible, a combination of the pointing methods “spacecraft pointing” and “actuation by component” should be considered.

The high-frequency content in the DWS signal can be compensated by the fast component actuator, while the low-frequencies are compensated by the spacecraft. This would still allow a tight control of the satellite attitude w.r.t. to the line-of-sight.

Summary

The trade-off analysis has recommended spacecraft pointing to be the best suitable pointing method, providing far superior ranging performance. The actuation of optical components is less favored and the actuation of the whole optical bench is not considered due to its drawbacks.

4.4 µNRIT System Assessment

4.4.1 Mircopropulsion System Requirements

4.4.1.1 Introduction

Leading on from the Gravity Field and Steady-State Ocean Circulation Explorer (GOCE) mission, the German Aerospace Agency (DLR) has initiated preparatory studies for a Next Generation Gravity Mission (e^2.motion) to measure the temporal variations of the Earth’s gravity field over a longer time span and with higher spatial resolution and temporal resolution than that of the GOCE or GRACE missions. e^2.motion will be based on Low-Low Satellite-to-Satellite Tracking, a technique where one satellite tracks another along orbit in loose formation, with both satellites effectively acting as ‘proof masses’ immersed in the Earth’s gravity field. The variations in distance between the centres-of-mass of the two satellites, resulting from both gravitational and non-gravitational forces, will be measured by laser interferometry. In a scenario utilizing the mini ion engines a higher temporal and spatial resolution is expected. In addition, a higher life time of up to 10 years would be achievable. The drag accelerations produced by aerodynamic forces on the satellites (with the satellites flying at an altitude of 350km or less) will be measured using accelerometers, allowing gravitational accelerations to be extracted from measurements. The mission would provide a relative error on the measured inter-satellite distance of the order 10^{-13} m/√Hz for a typical satellite separation of 100 km, necessitating the need for accurate drag compensation and attitude control.

Miniature gridded ion thrusters have been identified as a candidate technology for actuators on the e^2.motion satellites. The precise, low and variable thrust provided by this type of thruster shall permit the lateral drag forces on the satellites to be compensated and also laser beam pointing control to the accuracy required for the mission. The higher specific impulse achieved by electric propulsion devices over cold gas propulsion also permits total propellant for the mission to be minimised, essential for long duration missions.

In the framework of the NGGM preparatory studies, ESA awarded a contract to the TransMIT and Thales Alenia Space Italia (TAS-I) in 2009 to characterise the performance of a breadboard miniature Radio Frequency Ion Thruster (RIT). Tests performed under this contract included direct thrust measurements of the µNRIT-2.5 thruster at the Thales Nanobalance facility. The thruster was characterised in terms of thrust resolution, noise, linearity and rise/fall time in the range 50µN-1mN, and demonstrated performance approaching that required for e^2.motion. The mini-RIT has therefore been selected for further development with the goal of achieving full compliancy with e^2.motion requirements.

4.4.1.2 Electric Requirements Assessment

A mission utilizing the mini ion engines would provide a higher temporal and spatial resolution. Also a higher life time of up to 10 years would be achievable, however the complexity of the system would be a drawback. In this chapter we will discuss the ion propulsion subsystem for a e^2.motion mission, which would fly in a very low orbit (350km) based on the requirements of ESA’s NGGM.

The In 2010, Thales Alenia Space Italia performed a preliminary study “System Support to Laser Interferometry Tracking Technology Development for Gravity Field Monitoring” which assessed preliminary system requirements relevant to NGGM. The performance requirements for electric propulsion thrusters providing drag compensation and attitude control derived from this study are summarized in Table 4-2.

Table 4-2: Thrust requirements for a e^2.motion

Requirement	Value
Thrust Range	50µN – 2.5mN
Thrust Resolution	0.5µN
Thrust Resolution	<30µN/√Hz for f < 3mHz <1/f increase from 3mHz to 75mHz <1.2µN/√Hz from75mHz to 1 Hz
Thrust Gain Non-Linearity (delivered thrust with respect to commanded thrust)	<2% (whole thrust range) [TBC]
Rise/fall time	<50ms from 10% to 90% of final thrust step
Slew Rate	>0.5mN/s
Specific Impulse	500s – 4000s
Thruster Power	30W – 70W
Lifetime	up to 10 years continuous operation

The mission baseline for e^2.motion consists of two satellites flying in a pendulum formation about either a polar or sun synchronous orbit (the orbital planes of the lead and trailing satellites rotating relative to each other). Such a formation improves the spatial sampling of the gravity field by measuring both in-track and cross-track components of the gravity field. For a given payload mass, a lower orbital altitude increases resolution and therefore the satellites will fly at a low altitude below 350km. Since the payload demands low noise actuators for attitude and orbit control, magnetorquers and electric propulsion thrusters are intended to be used.

The preliminary satellite configuration for e^2.motion is shown in Figure 4-5 together with a schematic highlighting thruster arrangement. A set of eight 2mN class thrusters (four front, four rear) will be used for compensation of the drag forces along the lateral and radial directions (Y,Z), satellite attitude control and pointing control of the laser beams.

A thrust range of 50 µN to 2mN (dynamic range of 40) is specified for the lateral thrusters for e^2.motion due to the expected drag forces and torques acting on the satellite. The requirements on thruster noise, resolution, linearity, rise/fall time and slew rate are related to the final performance requested for the drag acceleration control, attitude acceleration, rate and angle control, and laser beam pointing control.

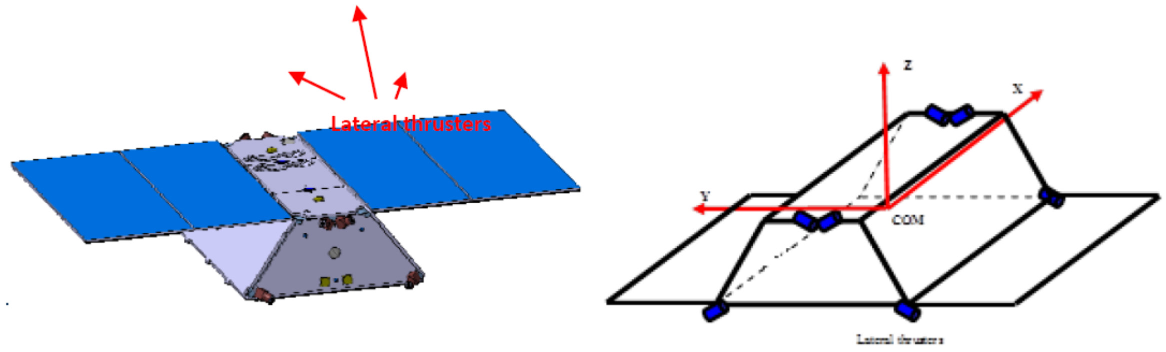

Figure 4-5: Preliminary satellite configuration and thruster arrangements for e^2.motion

A specific impulse between 500s to 4000s across the thrust range and a power consumption between 30W to 70W across the thrust range are specified in order to minimise propellant requirements and the size of the solar arrays and batteries. These design aspects are particularly important to satellites with a long lifetime requirement (~10 years for e^2.motion), and which shall be launched (in pairs) by a small-medium rocket such as Vega.

The miniature RIT was identified as the best candidate thruster for the electric propulsion subsystem based on the measured performance of the µNRIT-2.5 thruster. Thrust resolution, noise, linearity and rise/fall time for µNRIT-2.5 were generally compliant with e^2.motion requirements over the thrust range tested, but maximum thrust for the µNRIT-2.5 (equipped with grids containing 37 apertures) was limited to 1mN.

4.4.2 Radio Frequency Ion Thrusters for Attitude and Orbit Control

4.4.2.1 Thruster Functional Description

Ion thrusters generate thrust by the acceleration of ions via electrostatic fields. The thrust generated by a '*gridded'* ion thruster is a result of the net force acting on grid electrodes used to extract ions from a plasma and then accelerate them out of the thruster.

Radio Frequency (gridded) ion thrusters (RITs) use an electrodeless, inductive discharge for the generation of plasma and their design is based on the standard configuration of an inductively coupled plasma source (ICP). A schematic indicating the general configuration of a Radio Frequency Ion Thruster is displayed in Figure 4-6 and the following sections describe the operating principle of RITs.

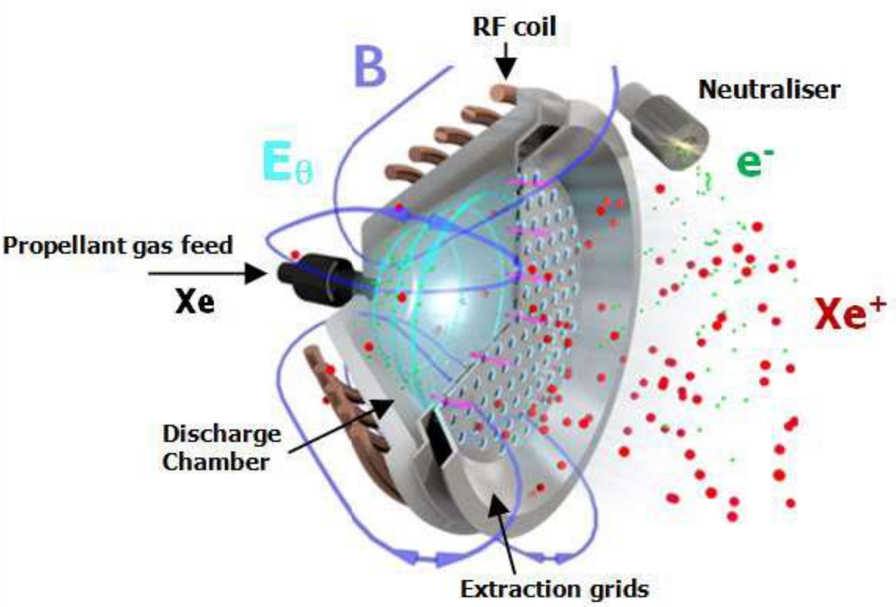

Figure 4-6: Operating principle of a Radio Frequency Ion Thruster

Propellant Ionisation

The discharge chamber of a radio frequency ion thruster consists of a dielectric vessel surrounded by a conducting coil (*termed RF coil or induction coil*) to which an oscillating current (typically at a few

MHz) is applied to generate a RF field. A gas feed system supplies propellant to be ionised; typically the inert gas xenon is used but RF ion thrusters have also been operated on other propellants such as mercury, cesium, argon, nitrogen and oxygen. The RF magnetic field penetrates the vessel inducing an azimuthal electric field according to Faraday's Law:

$$\nabla \times \bar{E} = -\frac{\partial \bar{B}}{\partial t} \tag{4-1}$$

The induced electric field acts to accelerate free electrons present within the discharge chamber to sufficient energies for electron-impact ionizations of the neutral propellant to occur, leading to a self-sustaining discharge. No internal cathodes are required to supply electrons to maintain the discharge, as for Kaufman ion thrusters. A weakly ionized, nonequilibrium plasma is formed, with electron temperature considerably higher than that of the ions and neutral propellant, whose temperatures approximate that of a gas in thermal equilibrium with the walls of the discharge chamber. A stable discharge requires the power absorbed by the plasma to balance the power dissipated.

Thruster Ignition

The ignition of an inductive plasma discharge, as used in the RITs, requires that a sufficient number of impact ionizations occur due to collisions between free electrons and neutral gas atoms. The induced electric field within the discharge chamber is often not sufficient to accelerate electrons to high enough energies within one half period of the RF cycle for ionization to occur. Elastic collisions between electrons and neutrals within the Eθ field region, that reverse the direction of the electron as the direction of the Eθ field changes enables the electrons to accumulate energy from the field. Provided that the electrons undergo enough collisions before being lost to the walls, the electrons can therefore reach energies required for ionization.

Prior to ignition there are not enough free electrons present in the gas to strike the discharge and additional electrons must be supplied. This can be achieved by reversing the polarity of the accelerator grid potential (normally biased to a negative high potential) for a few milliseconds to draw electrons from the neutralizer into the discharge chamber. After ignition, the accelerator grid is once again set to a negative potential.

If high currents exist in the RF coil, a large voltage difference can arise between the ends of the coil due to the resistance of the coil. Capacitive coupling between the RF coil and plasma can therefore lead to radial and axial electric fields in the plasma which can be considerably greater than the induced azimuthal electric field. Capacitive coupling can therefore constitute a significant fraction of the energy coupling to plasma electrons, aiding discharge ignition. However, it is difficult to ignite an inductive discharge by capacitive coupling alone at low neutral pressures. A large impulse can be applied to the gas flow to the thruster to momentarily increase the pressure inside the discharge chamber and allow the discharge to be ignited. This has been demonstrated for miniature RITs (in the frame of μRIT developments for LISA Pathfinder) whereby ignition is achieved by applying a pressure shock whilst a RF pulse is applied to the RF coil to generate a very high voltage spike. This ignition method removes the need of a neutraliser during ignition; however, the pressure shock may affect spacecraft AOCS due the disturbance generated by the pressure pulse. Different ignition methods that have been demonstrated for RITs are summarised in
Table 4-3.

Table 4-3: Ignition methods for miniature RIT's

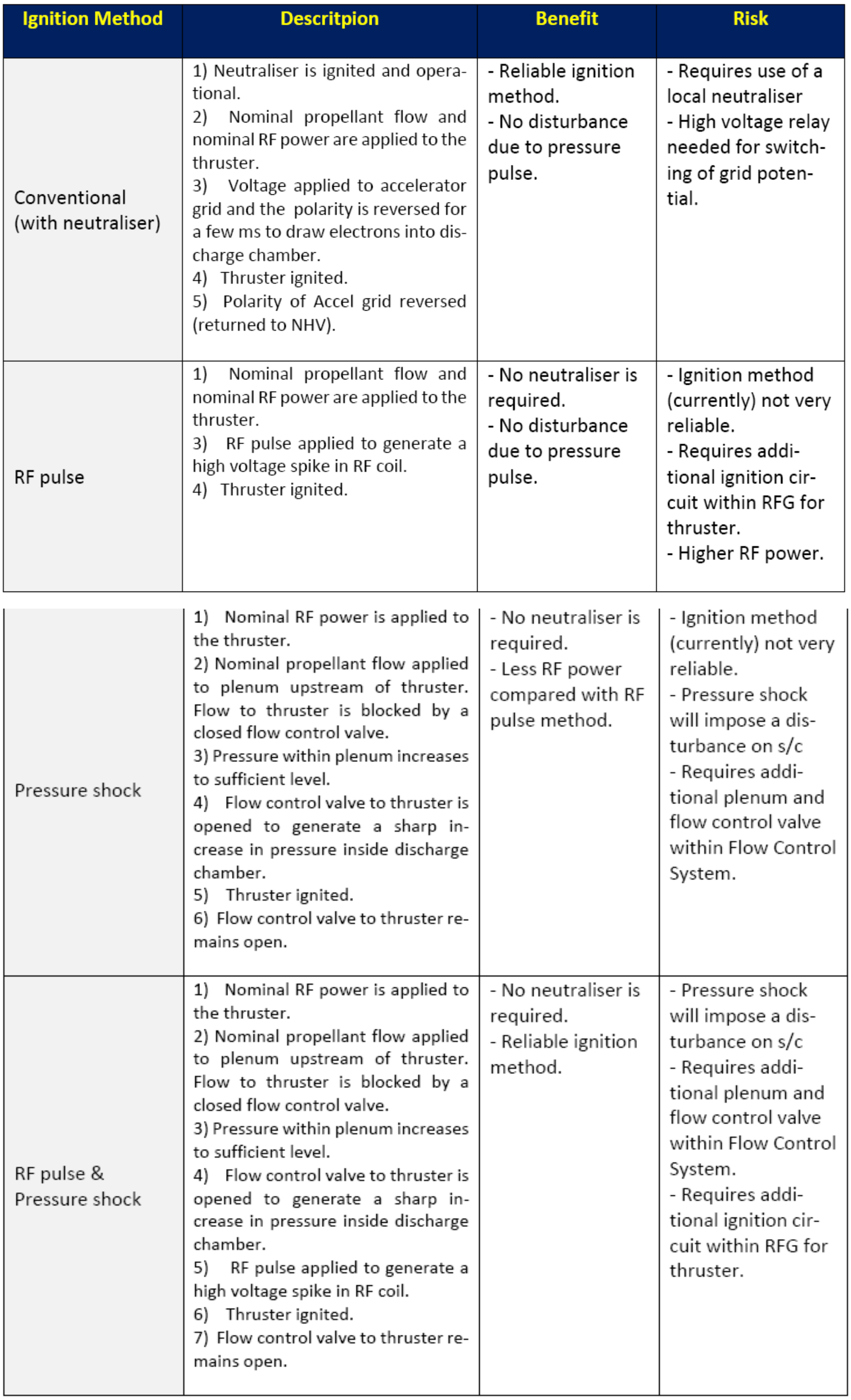

Ignition Method	Descritpion	Benefit	Risk
Conventional (with neutraliser)	1) Neutraliser is ignited and operational. 2) Nominal propellant flow and nominal RF power are applied to the thruster. 3) Voltage applied to accelerator grid and the polarity is reversed for a few ms to draw electrons into discharge chamber. 4) Thruster ignited. 5) Polarity of Accel grid reversed (returned to NHV).	- Reliable ignition method. - No disturbance due to pressure pulse.	- Requires use of a local neutraliser - High voltage relay needed for switching of grid potential.
RF pulse	1) Nominal propellant flow and nominal RF power are applied to the thruster. 3) RF pulse applied to generate a high voltage spike in RF coil. 4) Thruster ignited.	- No neutraliser is required. - No disturbance due to pressure pulse.	- Ignition method (currently) not very reliable. - Requires additional ignition circuit within RFG for thruster. - Higher RF power.
Pressure shock	1) Nominal RF power is applied to the thruster. 2) Nominal propellant flow applied to plenum upstream of thruster. Flow to thruster is blocked by a closed flow control valve. 3) Pressure within plenum increases to sufficient level. 4) Flow control valve to thruster is opened to generate a sharp increase in pressure inside discharge chamber. 5) Thruster ignited. 6) Flow control valve to thruster remains open.	- No neutraliser is required. - Less RF power compared with RF pulse method.	- Ignition method (currently) not very reliable. - Pressure shock will impose a disturbance on s/c - Requires additional plenum and flow control valve within Flow Control System.
RF pulse & Pressure shock	1) Nominal RF power is applied to the thruster. 2) Nominal propellant flow applied to plenum upstream of thruster. Flow to thruster is blocked by a closed flow control valve. 3) Pressure within plenum increases to sufficient level. 4) Flow control valve to thruster is opened to generate a sharp increase in pressure inside discharge chamber. 5) RF pulse applied to generate a high voltage spike in RF coil. 6) Thruster ignited. 7) Flow control valve to thruster remains open.	- No neutraliser is required. - Reliable ignition method.	- Pressure shock will impose a disturbance on s/c - Requires additional plenum and flow control valve within Flow Control System. - Requires additional ignition circuit within RFG for thruster.

The kick-start electronics board for generating a RF pulse consists of a set of capacitors which are charged with a variable voltage. By activating the ignition switch, the stored extra energy is released to the regular RFG supply output. This additional power peak results in a short increase of the RFG-power, which is fed to the coil. The RFG- Supply itself is protected by a diode against the power pulse.

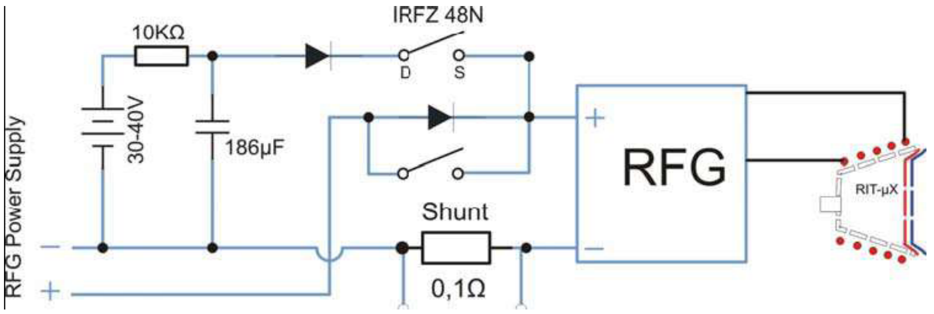

Figure 4-7: Ignition circuit for Radio Frequency Generator

Ion Extraction and Acceleration for Thrust

The ions generated within the discharge are extracted, focussed and accelerated by a set of two (sometimes three) multi-aperture grid electrodes which are biased to high potentials.

A plasma sheath forms upstream to the surface of the first grid (as depicted in Figure 4-8), which is biased to a high positive potential typically between 1-2 kV with respect to 'ground' (or common potential of the spacecraft). This grid is often referred to as the *screen grid*. The second grid is located in close proximity to the first and is termed the *accelerator grid*.

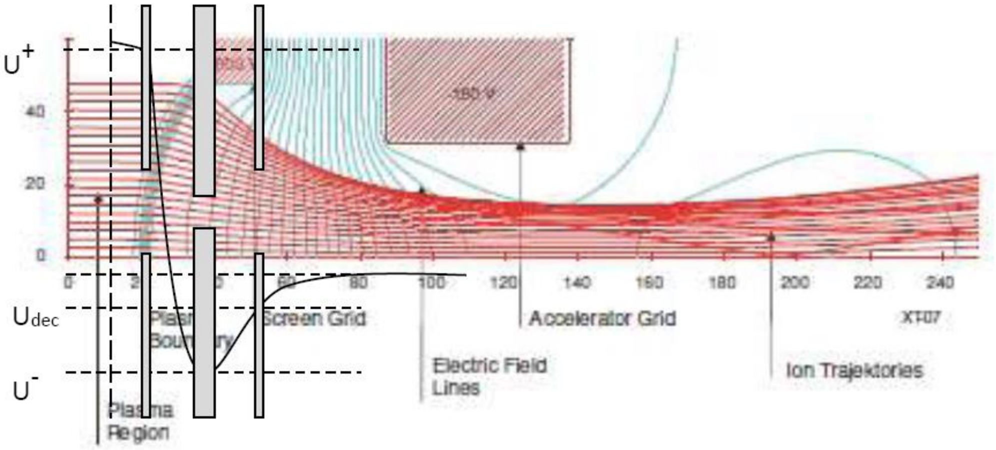

Figure 4-8: Schematics indicating ion extraction through a grid aperture

The accelerator grid is biased to a large negative potential, typically between -100V and -500V with respect to ground (or common potential). Ions that diffuse from the bulk plasma within the discharge chamber to the plasma (sheath) edge upstream of the screen grid are accelerated across the plasma sheath and either impinge on the upstream face of the screen grid or pass through the apertures, where they are then accelerated to high velocity due to the high potential difference between the screen and accelerator grid.

A neutralizer cathode is located outside of the discharge chamber in order to provide an equivalent electron current to 'neutralize' the space-charge of the positive ion beam expelled by the thruster and to prevent spacecraft charging effects. It is important that the negative potential of the accelerator grid be sufficient to prevent electrons external to the thruster from backstreaming towards the grids and into the discharge chamber, which can lead to localised heating and erosion, reduction in thrust, and in some cases, overload of the screen grid supply.

The maximum ion current that can be extracted through each aperture of a gridded ion thruster is limited by the ion space charge in the gap between the screen and accelerator grid, governed by the Child-Langmuir law. The maximum total beam current that can be extracted from a grid set is given by:

$$I_b^{max} = \frac{4\varepsilon_0}{9}\sqrt{\frac{2eU_T^{3/2}}{m_i l_e^2}}A_g T_S \tag{4-2}$$

where m_i is the mean ion mass (which for xenon is m_i= 131.3 AMU), U_T is the acceleration voltage $U_T = U^+ + |U^-|$ being the sum of the PHV and NHV applied to the screen and accelerator grids, A_g is the area of the screen grid, T_s is the transparency of the screen grid to ions, and l_e is the sheath width taking into account the curvature of the sheath. The function A_gT_s can be considered as the open area of the screen grid to a first approximation. The (modified) sheath width is dependent on the geometry of the ion optics, given by:

$$l_e = \sqrt{\left(l_g + t_s\right)^2 + \frac{d_s^2}{4}} \tag{4-3}$$

where l_g is the gap between the screen and accelerator grid, t_s is the thickness of the screen grid and d_s is the diameter of the screen grid apertures.

The ion optics must be designed in order to avoid direct ion impingement on the grids to minimise sputter erosion and prolong grid lifetime. Good focussing of the beamlet ions only occurs over a certain range of plasma conditions and grid potentials however.

At high plasma densities, and too low screen grid potential, the width of the plasma sheath upstream of the screen grid will decrease and become flatter. Ions will be poorly focussed through the grid apertures and may start to impinge directly on the accelerator grid. The onset of direct ion impingement on the accelerator grid in this case defines the '*perveance limit*' of the grids, with perveance being the maximum (total) beam current that can be extracted for a given acceleration voltage.

$$P = \frac{I_b}{U_T^{3/2}} \tag{4-4}$$

At low plasma density, and too high screen grid potential, the sheath width increases and becomes more convex with respect to the surface of the screen grid. The ions will be over-focussed through the apertures, which can lead to the ions crossing over in-between the grids and then impinging on the surface of the accelerator grid. For these conditions, the grids are considered to be operating '*under perveance*'.

Even when the beamlets are properly focussed however, the ions can undergo charge exchange collisions (CEX) with neutrals between the grids and downstream of the exit plane of the grids. These collisions result in a fast neutral being generated and a slow thermal ion. The slow thermal ions generated between the grids tend to be attracted towards the negatively biased accelerator grid, where they are accelerated towards the surface due to the potential difference, often with sufficient energy to sputter the surface when they strike it. Grid erosion by sputtering from CEX ions is the main life-limiting mechanism of the grids.

As stated previously, the thrust generated is equivalent to the net force acting on the grids due to the extraction and acceleration of the ions. Thrust can be approximated by:

$$F = \eta_d \cdot I_{beam} \cdot \sqrt{2\frac{m_i}{q_i}\left(U_+ + V_P\right)} = 50.87\mu N \cdot \frac{I_{beam}}{mA}\sqrt{\frac{U_+ + V_P}{kV}} \tag{4-5}$$

where η_d is a thrust correction factor due to beam divergence, m_i is the mean ion mass for xenon m_i= 131.3 AMU, q_i is the mean ion charge q_i= 1.01e, U_+ is the positive high potential applied to the screen grid and V_P is the plasma potential, which can be assumed to be ~25V.

Thrust Modulation

Thrust generated by gridded ion thrusters can be controlled by varying the beam (grid) potential or the ion flux to the screen grid via the ion density.

In RITs, the ion density within the discharge chamber can be varied by controlling the ionization rate through the RF power and the propellant flow rate applied to the discharge chamber, with thrust increasing linearly with RF power. The thrust accuracy and stability are only dependent on the power supplies and flow controllers used. RF ion thrusters also demonstrate a fast response rate; if RF power is varied, the plasma responds within a few RF periods and therefore reaches a new equilibrium within a few microseconds.

To minimize complexity, RF ion thrusters are typically operated at a fixed beam voltage and only RF power is varied to control thrust about a given throttle point. Varying the beam voltage and/or the propellant flow rate as well as RF power permits a wider throttle range.

Thrust demand is first converted to an equivalent ion current and a required beam voltage. Once the positive high voltage (to the screen grid) is set, only the beam current has to be kept constant at the commanded value. In single closed loop control, the measured beam current is compared to the commanded level and the RF power is adjusted. The accuracy of the thrust control depends primarily on the precision of the PPU with this type of control. Figure 4-9 displays a block diagram of the beam current controller.

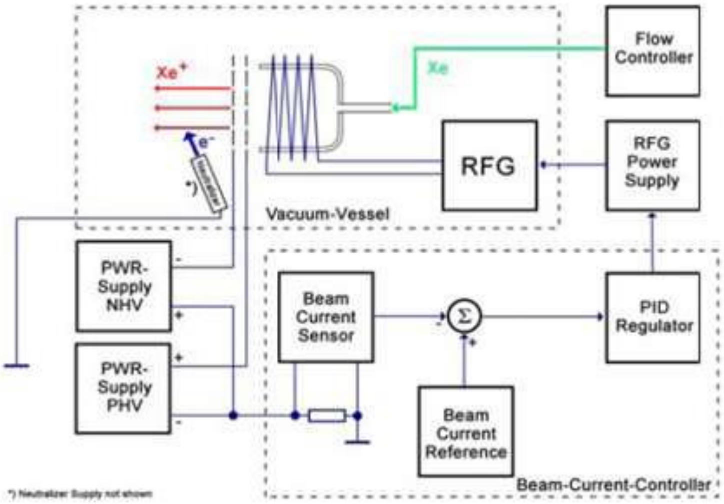

Figure 4-9: Schematic of the beam current controller

<u>Operating Modes</u>

Fundamentally, there are 4 operating modes for a RIT:

(1) Start-up: The start-up mode involves the ignition of the thruster, requiring as minimum, propellant flow and RF power to the thruster. Different ignition options have been investigated for miniature RITs.The thruster may be ignited through the use of a RF voltage pulse and a pressure shock (large impulse in the propellant flow), or at nominal flow and RF power settings using a neutraliser as an electron source.

(2) Standby: During standby mode, a stable plasma discharge is maintained at nominal discharge settings, dependent on desired thrust level, in preparation for the extraction of an ion beam. Propellant flow and RF power are therefore applied to the thruster but no HV is applied to the grids. The neutraliser must be operational prior to beam extraction. If the thruster is to be operated in standby mode for any significant amount of time, propellant flow rate and RF power can be set at minimal values in order to minimise propellant and power consumption.

(3) Thrust: Thrust mode is initiated from standby mode. The propellant flow rate is set and a beam is extracted by applying HV to the grids to provide thrust. The RF power is regulated via the Beam Current Controller (BCC) to control thrust level; wider throttling is enabled by varying the grid voltages and flow rate if necessary, but would require implementation of a more complex control system.

(4) Shutdown: The shutdown mode involves switching off the thruster. The PHV and NHV of the grids are switched off to stop beam extraction. Switching off the RF power then results in the plasma discharge extinguishing, and the propellant flow is stopped by closing flow valves.

The four operating modes are summarised in Table 4-4.

Table 4-4: Summary of operating modes and settings for RITs

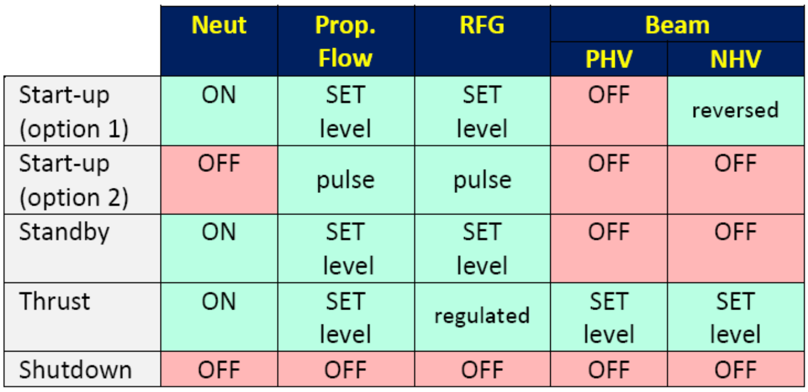

	Neut	Prop. Flow	RFG	Beam	
				PHV	NHV
Start-up (option 1)	ON	SET level	SET level	OFF	reversed
Start-up (option 2)	OFF	pulse	pulse	OFF	OFF
Standby	ON	SET level	SET level	OFF	OFF
Thrust	ON	SET level	regulated	SET level	SET level
Shutdown	OFF	OFF	OFF	OFF	OFF

4.4.2.2 Thruster Concept Heritage

The concept of the radio frequency ion thruster was first developed by Prof. Loeb of the University of Giessen in the 1960’s. The majority of research into radio frequency ion thrusters since that time has also been carried out by the University of Giessen, culminating in the development of the commercial range of RIT thrusters in collaboration with EADS Astrium Space Transportation (Lampoldshausen).

Initial efforts focused on the development of a 10 cm diameter engine, the RIT-10 thruster, which was the first European ion thruster to be demonstrated in space on-board the EURECA spacecraft in 1992. The flight thruster assembly ‘RITA’ was built in collaboration with EADS Space Transportation and was also used to perform rescue operations for the ARTEMIS mission. The RIT-10 thruster has accumulated over 6000 hours operation in space and over 20,000 hours on ground during qualification programs.

In 2004, the University of Giessen initiated a program to investigate the scaling down of the RIT-10 thruster to provide µN thrust levels for micropropulsion applications. This study established a number of scaling laws for RIT thrusters which enabled optimal thruster geometry and working parameters to be identified.

Based on performance data obtained for the RIT-10 thruster and basic theory of plasma physics, the performance of several miniature RIT thrusters with diameters between 1-4 cm were predicted.

In 2008 an optimized 2.5cm diameter miniature RIT with 37 grid apertures was developed by the University of Giessen. The project was supported by funding from the German Aerospace Agency, DLR. The thruster design incorporated a number of modifications compared to earlier miniature RIT prototypes which enabled improvements in performance and efficiency (see Table 4-5). The µNRIT-2.5 thruster incorporated a dome-like discharge chamber to reduce recombination losses at the walls. Tests indicated a reduction in RF power of 15%-25% through the use of a hemispherical discharge chamber compared to a cylindrical one, with a corresponding increase in electrical efficiency. The gas distributor was also redesigned; the gas distributor conventionally at the rear of the discharge chamber was replaced with a distributor ring located near the screen grid, which also acts as part of the main grid holder. The gas is injected axially into the discharge chamber through 12 micro-nozzles machined around the circumference of the ring, close to the walls of the discharge chamber where electron temperature is greatest which helps to improve ionization efficiency. The µNRIT-2.5 was also manufactured to be fitted with either two extraction grids or three. The inclusion of a third, closed decelerator grid reduces neutral losses and shields the accelerator grid from charge exchange (CEX) ions created near the exit plane of the thruster.

Table 4-5: Main design differences between µRIT-2.5 and other miniature RITs

	Conventional MiniRIT	µNRIT-2.5	Advantage of µNRIT-2.5 Design	Disadvantage of µNRIT-2.5 Design
Discharge Chamber	Cylindrical	Hemispherical	Surface area-to-volume ratio is reduced for hemispherical chamber. Ion recombination losses at the walls are decreased compared to a cylindrical chamber and therefore RF power consumption is reduced.	Greater complexity in machining hemispherical discharge chamber from ceramic.
Gas Distributor	Gas injection at rear of discharge chamber	Gas injection from 12 micronozzles around the periphery of the screen grid.	Gas is injected axially into the discharge chamber from the periphery of the screen grid. The residence time of neutrals is increased. Gas is injected close to walls of discharge chamber, where electron temperature (power deposition) is greatest. Ionization efficiency is improved and flow rate demand decreased.	Greater complexity in design and manufacturing.

Preliminary tests on the laboratory model of the µNRIT-2.5 demonstrated a thrust range between 50µN - 500µN, specific impulse between 363s – 2861s and a power consumption of less than 30W. Thrust requirements for e^2.motion demand a thrust range between 50µN – 2mN. Therefore, a contract was awarded to the University of Giessen and Thales Alenia Space Italia (TAS-I) in 2009 to characterise the performance of the µNRIT-2.5 thruster over an extended thrust range on the TAS-I Nanobalance facility. The TAS-I nanobalance is capable of accurately measuring thrust levels up to 1mN, which therefore limited the maximum operating level of the µNRIT-2.5 thruster during the test campaign.

Despite a series of limitations of the NB test set-up, the tests performed on the µNRIT-2.5 demonstrated the robustness and versatility of the thruster and indicated general compliancy with e^2.motion requirements (these are summarised in Table 4-6). Additionally, the tests demonstrated the validity of the thruster ion optics design and of the performance model used to design and operate the thruster. The performance computed from measured electrical parameters and flow parameters were well correlated with the performance measured by the nanobalance. This means that the physics of the thruster and the performance model can be considered validated, and reliable for designing miniature RITs.

Table 4-6: Performance requirement against measurement from the test campaign on the µNRIT-2.5 thruster performed in 2010

Tested parameter	Requirement	Measured Values	Status
Thrust Range	The current prototype of the mini-RIT shall be able to provide continuous thrust with any value in the range 50 µN to 1 mN	From 50 µN up to 1mN.	Fully compliant.
Thrust Resolution	The mini-RIT shall be able to provide continuous thrust in the overall range (50 µN - 1 mN) with a minimum resolution of 0.5 µN	Resolution of 0.5 µN, and in some cases of 0.3 µN, measured in the 50 – 550 µN range. Resolution not measurable above 550 µN due to operational constraints and excessive NB background noise.	Compliant in the tested range.
Thrust gain non linearity	The mini-RIT shall ensure that the gain non-linearity of the delivered thrust with respect to the commanded thrust shall differ by no more than the 2% throughout the whole thrust range.	< 2% from 100µN up to 1mN < 2% from 50 µN to 650 µN < 5.5% from 50µN up to 1mN, with maximum deviation (above 2%) only in the points at 50 µN and 60 µN	Partially compliant over the full thrust range. Compliant on reduced ranges.
Slew rate	The mini-RIT shall be able to change the thrust value at a rate > 0.5 mN/s (50 µN step performed in 100 ms)	Measured thrust rise/fall time < 50 ms over the full thrust range, for any thrust step from 50 µN to 400 µN → slew rate >1 mN/s	Thrust slew rate fully compliant.
Thrust Noise	The thrust noise of the mini-RIT shall be <1.2µN/√Hz for frequencies between 75 mHz and 1 Hz, and not exceed a 1/f increase between 75 mHz and 3 mHz.	Thrust noise measurements limited by the Nanobalance background noise, but lower the requirement from 0.1 to 1 Hz, and close to the requirement from 0.01 to 0.1 Hz. Noise not measurable below 0.01 Hz due to excessive thermal drifts.	Compliant over the frequency range in which the measurements were possible.

4.4.2.3 Development Model Thruster Design

The aim of this activity is to design, manufacture and test a Development Model of a miniature Radio Frequency Ion Thruster in accordance with major e^2.motion requirements. This section describes the design of the DM thruster and outlines assumptions made in the design process.

Design Description

As stated the µNRIT-2.5 thruster (originally designed for a thrust range between 50µN - 500µN but which was characterised up to 1mN) has been shown to have performance generally compliant with e^2.motion requirements. The thruster also features a number of design improvements over other miniature RIT thrusters for improving efficiency; the two most significant design differences reported in Table 4-5.

To meet the extended thrust requirement of e^2.motion, the design of the µNRIT-2.5 thruster was taken as a baseline for the DM thruster but scaled to achieve thrust up to 2mN. Furthermore, in order to move the design towards an Engineering Model several other improvements were made to the DM design compared to the µNRIT-2.5 thruster which shall be detailed in the following sections. Parts and materials were selected as flight representative where possible.

The Thruster Assembly can be considered to comprise the following sub-assemblies:

(1) Ionizer: Consisting of a ceramic discharge chamber and RF coil for generating an inductive plasma discharge.

(2) Gas Inlet: Comprising the propellant gas feedline to the discharge chamber, which incorporates a gas isolator. The gas isolator provides isolation between the high voltage

potential (*being the plasma potential which floats just above the PHV of the screen grid*) within the discharge chamber and the gas feedline connected to S/C ground.

(3) Grid System: Consisting of a three grid extraction system and a grid support and alignment structure. The mounting structure for the screen grid also incorporates a gas distributor that injects gas into the discharge chamber at the periphery of the screen grid.

(4) Thruster Housing and Interface: Consisting of Thruster Housing and support structures, a thruster Back Plate with interface connections for HV, RF and propellant to the Thruster Assembly, and fixings for the HV lines, RF coil and gas inlet.

4.4.2.4 Development Model Thruster Sizing

As explained in Section 4.4.2.1, the maximum ion current that can be extracted through each aperture of a gridded ion thruster is limited by the ion space charge in the gap between the screen and accelerator grid, governed by the Child-Langmuir law.

Equation (4-2) and Equation (4-5) indicate that the maximum thrust that a gridded ion thruster can achieve is directly proportional to the area that ions can be extracted from the plasma. For a given grid geometry and potential, it is directly proportional to the number of beamlets (grid apertures), meaning that a larger diameter thruster can deliver higher thrust as it can be equipped with more grid apertures. Larger dimensions however lead to higher power consumption, as the plasma losses on the walls of the thruster will increase with increasing surface area.

Furthermore, for given plasma discharge conditions the ion current extracted per aperture for a specific accelerating voltage will be constant. In RIT thrusters the radial profile of ion current density can be considered relatively flat, and therefore for the sake of preliminary thruster sizing, the ion current extracted from each aperture can be assumed to be the same. For given discharge conditions, the thrust range is then scalable by the number of apertures and beam voltage, independent of thruster size.

The μNRIT-2.5 thruster equipped with 37 apertures demonstrated a thrust range between 50μN-1mN during characterisation on the TAS-I nanobalance (performance summarised in Table 4-6).

To achieve thrust up to 2.5mN (encompassing the 2mN requirement for e^2.motion), the grids for the DM thruster have been designed with 121 apertures. The geometry of the ion optics will be kept the same as that validated for the μNRIT-2.5 thruster (and other RITs). The number of grid apertures constrains the minimum diameter of the discharge chamber; the internal diameter of the discharge chamber for the DM thruster was selected as 3.5cm, leading to the naming convention of 'μNRIT-3.5'.

4.4.2.5 Predicted Performance

The performance of a 3.5cm diameter RIT thruster with 121 grid apertures has been predicted using a performance model derived from μNRIT-2.5 performance data, RIT scaling laws and basic plasma physics theory.

Performance has been estimated considering two different configurations for propellant flow control:

(1) Variable flow control: Propellant flow to the thruster is controlled by use of proportional flow control valves. This enables specific impulse to be optimised for different thrust levels, and also grid lifetime (via propellant mass utilisation).

(2) Fixed flow control: Propellant flow to the thruster is controlled by use of fixed orifice flow restrictors designed to provide a set, constant flow rate. Three different flow rates have been considered for low, mid and high thrust levels (between 50 μN to 2mN). A fourth gas flow rate was considered for the maximum thrust level of 2.5mN expected for the DM thruster equipped with 121 apertures. Such a configuration would present a less complex flow control system than one utilising proportional flow control valves, but thruster performance and lifetime would be impacted due to the three fixed flows.

Table 4-7 displays predicted performance considering variable flow control and Table 4-8 displays predicted performance considering three fixed flow rates over the required thrust range. The predicted data was calculated over the operational range of the μNRIT-2.5 thruster, which demonstrated thrust down to 50 μN. The impedance of the larger, 3.5 cm diameter, DM thruster will be higher; therefore, operation at lower RF voltages should be possible. It is expected that operation down to approx. 5.5 W

(RF power) will be possible with a corresponding minimum thrust level of ~30 µN. This can only be verified by test.

The relation between RF power and thrust used for the DM thruster was derived from performance data of µNRIT-2.5 and represents operation of the thruster in a non power-optimized regime. Predicted power levels must therefore be considered as conservative estimates.

Thruster power against thrust and specific impulse against thrust predicted for the DM thruster are displayed in the next pages.

Table 4-7: Predicted performance data for a 3.5 cm RIT with 121 apertures considering variable flow control

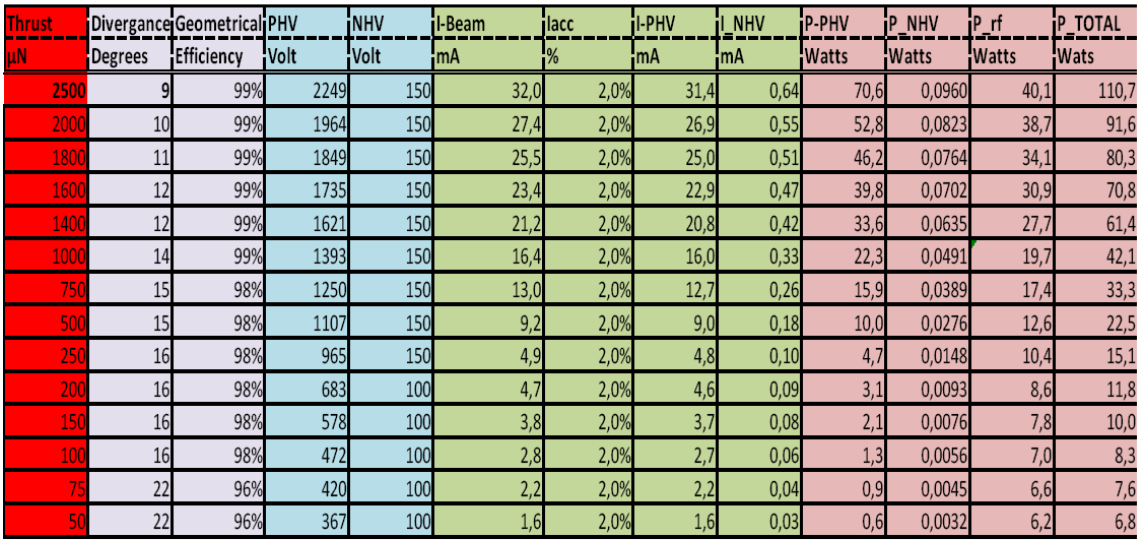

Thrust	Divergance	Geometrical	PHV	NHV	I-Beam	Iacc	I-PHV	I_NHV	P-PHV	P_NHV	P_rf	P_TOTAL
µN	Degrees	Efficiency	Volt	Volt	mA	%	mA	mA	Watts	Watts	Watts	Wats
2500	9	99%	2249	150	32,0	2,0%	31,4	0,64	70,6	0,0960	40,1	110,7
2000	10	99%	1964	150	27,4	2,0%	26,9	0,55	52,8	0,0823	38,7	91,6
1800	11	99%	1849	150	25,5	2,0%	25,0	0,51	46,2	0,0764	34,1	80,3
1600	12	99%	1735	150	23,4	2,0%	22,9	0,47	39,8	0,0702	30,9	70,8
1400	12	99%	1621	150	21,2	2,0%	20,8	0,42	33,6	0,0635	27,7	61,4
1000	14	99%	1393	150	16,4	2,0%	16,0	0,33	22,3	0,0491	19,7	42,1
750	15	98%	1250	150	13,0	2,0%	12,7	0,26	15,9	0,0389	17,4	33,3
500	15	98%	1107	150	9,2	2,0%	9,0	0,18	10,0	0,0276	12,6	22,5
250	16	98%	965	150	4,9	2,0%	4,8	0,10	4,7	0,0148	10,4	15,1
200	16	98%	683	100	4,7	2,0%	4,6	0,09	3,1	0,0093	8,6	11,8
150	16	98%	578	100	3,8	2,0%	3,7	0,08	2,1	0,0076	7,8	10,0
100	16	98%	472	100	2,8	2,0%	2,7	0,06	1,3	0,0056	7,0	8,3
75	22	96%	420	100	2,2	2,0%	2,2	0,04	0,9	0,0045	6,6	7,6
50	22	96%	367	100	1,6	2,0%	1,6	0,03	0,6	0,0032	6,2	6,8

Table 4-8: Predicted performance data for a 3.5 cm RIT with 121 apertures considering three (four) fixed flow rates

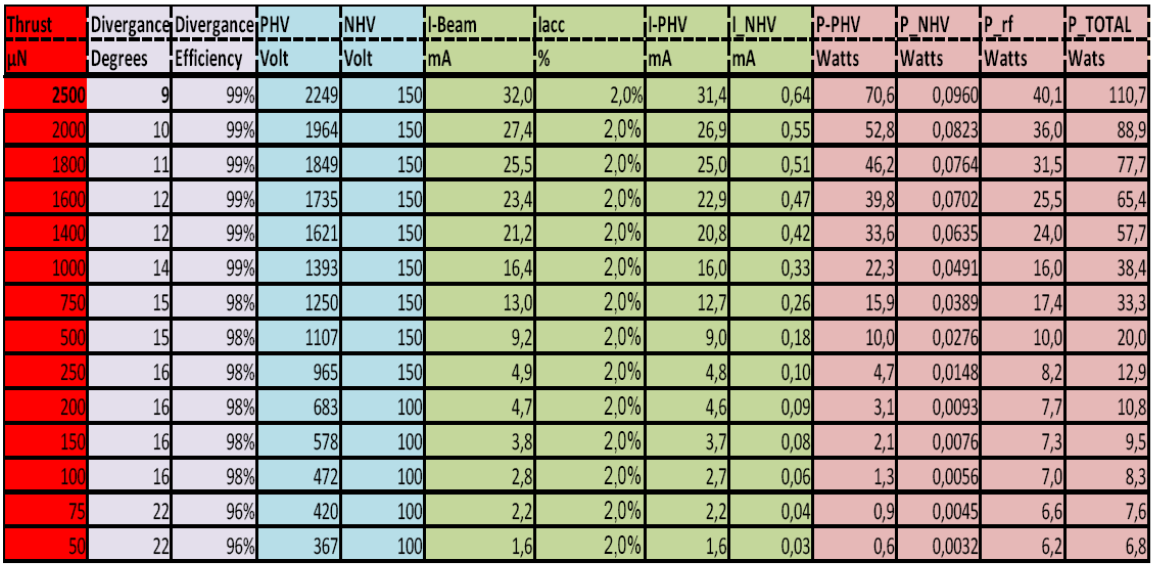

Thrust	Divergance	Divergance	PHV	NHV	I-Beam	Iacc	I-PHV	I_NHV	P-PHV	P_NHV	P_rf	P_TOTAL
µN	Degrees	Efficiency	Volt	Volt	mA	%	mA	mA	Watts	Watts	Watts	Wats
2500	9	99%	2249	150	32,0	2,0%	31,4	0,64	70,6	0,0960	40,1	110,7
2000	10	99%	1964	150	27,4	2,0%	26,9	0,55	52,8	0,0823	36,0	88,9
1800	11	99%	1849	150	25,5	2,0%	25,0	0,51	46,2	0,0764	31,5	77,7
1600	12	99%	1735	150	23,4	2,0%	22,9	0,47	39,8	0,0702	25,5	65,4
1400	12	99%	1621	150	21,2	2,0%	20,8	0,42	33,6	0,0635	24,0	57,7
1000	14	99%	1393	150	16,4	2,0%	16,0	0,33	22,3	0,0491	16,0	38,4
750	15	98%	1250	150	13,0	2,0%	12,7	0,26	15,9	0,0389	17,4	33,3
500	15	98%	1107	150	9,2	2,0%	9,0	0,18	10,0	0,0276	10,0	20,0
250	16	98%	965	150	4,9	2,0%	4,8	0,10	4,7	0,0148	8,2	12,9
200	16	98%	683	100	4,7	2,0%	4,6	0,09	3,1	0,0093	7,7	10,8
150	16	98%	578	100	3,8	2,0%	3,7	0,08	2,1	0,0076	7,3	9,5
100	16	98%	472	100	2,8	2,0%	2,7	0,06	1,3	0,0056	7,0	8,3
75	22	96%	420	100	2,2	2,0%	2,2	0,04	0,9	0,0045	6,6	7,6
50	22	96%	367	100	1,6	2,0%	1,6	0,03	0,6	0,0032	6,2	6,8

It should be noted that all power levels given are those at thruster level and not bus level. For calculating the bus level powers, the electrical efficiencies of the high voltage power convertors, high frequency convertors and the auxiliary power needed for the whole subsystem should be taken into account.

The conservative performance estimates for the DM thruster indicate that the thruster shall be able to achieve thrust from 50 µN to 2mN within a power range of approx. 7W to 90W. The specific impulse is estimated to be of the order 260s at 50 µN, and 4000s at 2mN. The values are calculated without margin but must be considered conservative. It is expected that power levels could be reduced by 20% by operating in a power-optimized regime. The impact of power and flow rate levels on thruster lifetime are being assessed in an extended grid lifetime study.

4.4.2.6 Testing of NRITs

Performance mapping for µNRIT2.5 was conducted over this operating envelope by varying the RF power and xenon flow rate to generate a given beam current. Figure 4-10 displays the hyperbola-like curves for extracted beam currents of 2,3,5,7 and 8mA.

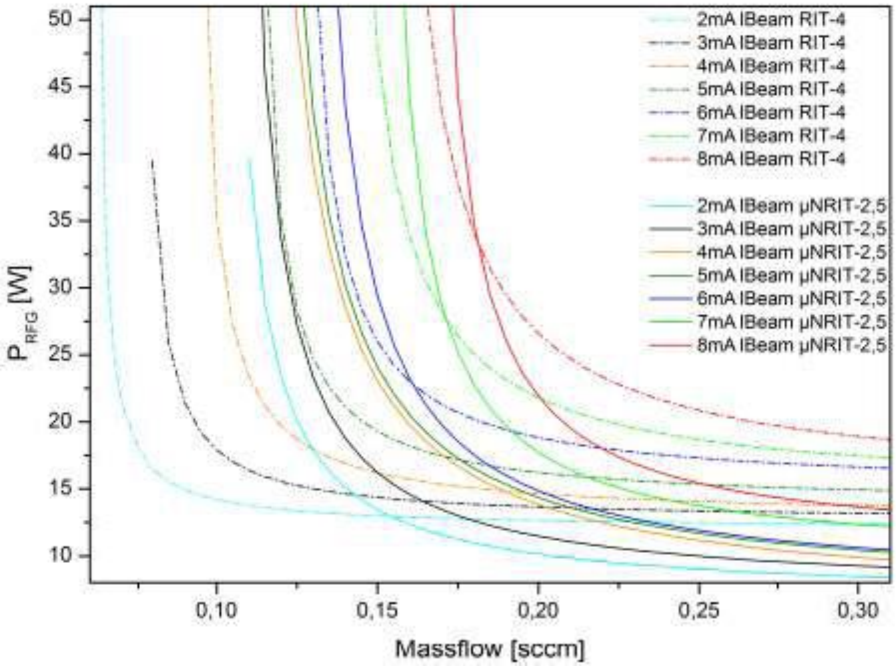

Figure 4-10: Discharge characteristic $I_{beam}(P_{rf}, \dot{V})$ of the µNRIT-2.5 micro-thruster for 5 beam currents between 2mA and 8mA

Thrust was calculated from equation (4-5). The specific impulse then was calculated from:

$$I_{sp} = \frac{n_m}{g_0} \cdot \sqrt{2\frac{q_i}{m_i}\left(U_+ + V_P\right)} = 3927.6s \cdot \eta_m \cdot \sqrt{\frac{U_+ + V_P}{kV}} \tag{4-6}$$

where g_0 is the standard acceleration due to gravity

Note, the beam divergence and ratio of doubly charged to singly charged Xenon ions for the µNRIT-2.5 thruster have not been measured but the following assumptions can be made based on other miniature RIT data:

α=16° or a divergence efficiency $\eta_d = \left(1 + \cos\alpha\right)/2 = 0.98$
and a ratio of 1% of Xe^{++}, i.e. q_i=1.01e.
The plasma potential may be estimated to be V_P= 25V.

The positive high voltage U_+ was chosen (together with the negative high voltage U_-= 100...125V) in such a way that optimum focusing of the grid system was always maintained. The necessary beam current to generate the required thrust was then estimated by Equation (4-5).

The RF power and propellant flow rate were taken from Figure 4-10 (by interpolation) in such a way that the total efficiency obtained a maximum, i.e. the apex-points of each curve were connected by a straight line.

It should be noted that fast throttling of any RIT-engine must be done in a different manner; the propellant flow rate should be kept constant (due to the long adjustment time) along with the grid voltages, and the RF power adjusted using a beam current control loop. The beam current, and therefore thrust, can be varied within milliseconds in this way. In this case however, the throttling range is limited to 4:1 to avoid beamlet defocusing.

A wider throttling range of 11.5:1 can be achieved for the µNRIT-2.5 thruster with 37 apertures by varying all of the control parameters. The minimum thrust is determined by discharge losses, with the plasma extinguishing at low RF powers and flow rates.

Direct thrust measurements of the µNRIT-2.5 were performed on the TAS-I nanobalance. The µNRIT-2.5 was capable of thrust from 50µN to 1mN by variation of the RF power, flow rate and grid voltage.

The thrust measured by the nanobalance (NB) against the nominal (commanded) thrust is displayed in Figure 4-11. The scale factor (or thrust correction factor) between the measured thrust and commanded thrust deviates from unity by 3.05% over the full thrust range from 50µN to 1mN.

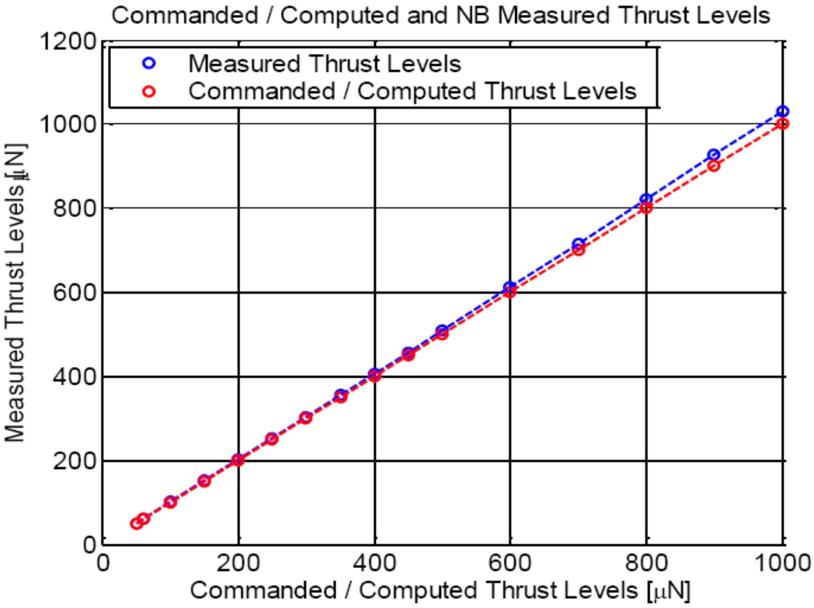

Figure 4-11: NB measured thrust characteristic against nominal thrust

Thrust resolution tests indicated that the µNRIT-2.5 thruster and control electronics can be commanded with a resolution of ~0.1µN. This value was determined by the thrust computed from the thruster electrical parameters. The excessive background noise of the NB test facility prevented the direct verification of the thrust resolution. The minimum steps detectable from the NB measurements were ±0.3µN (Figure 4-12) and ±0.5µN (Figure 4-13).

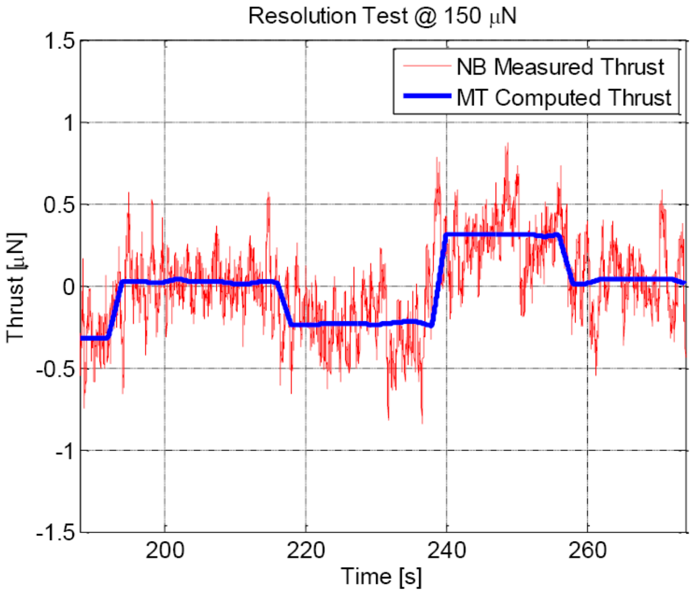

Figure 4-12: NB measured and MTCU thrust

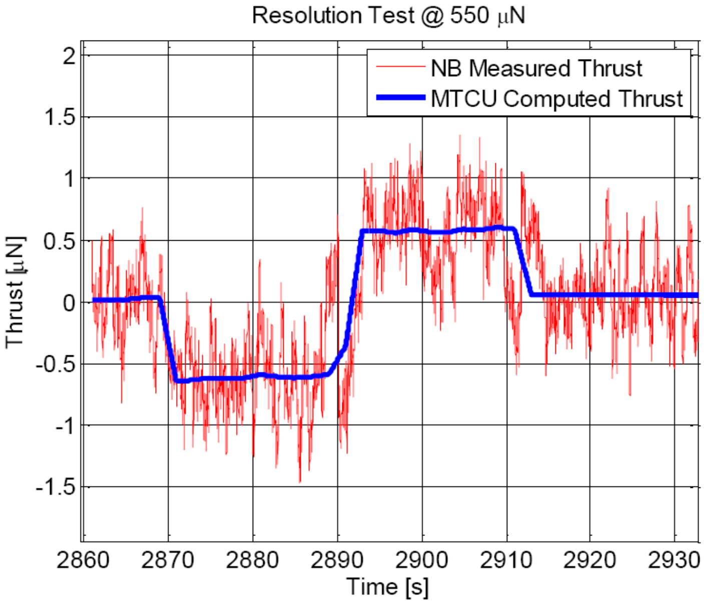

Figure 4-13: NB measured thrust and MTCU recorded thrust

Thrust rise/fall time (the time required to switch from 10% to 90% of the final thrust step) was verified to be <100ms. This is shown in Figure 4-14 to Figure 4-17 in which the red line (measured thrust filtered of the test facility resonance) rises and falls in ~100ms, independent of the amplitude of the thrust step and thrust level. Filtering the NB measurement with a higher bandwidth filter (and unfortunately introducing more noise on the thrust measurement) resulted in a rise/fall time less than 50ms over the full thrust range.

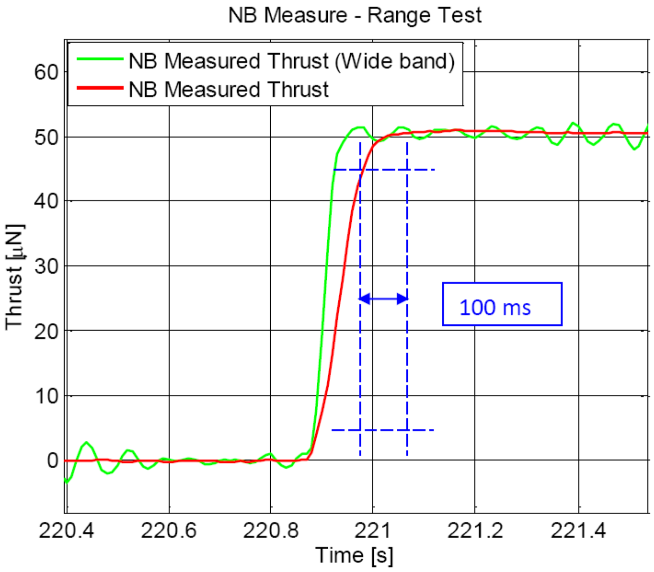

Figure 4-14: Measured thrust step from 100 to 150 μN. Width between the two vertical lines is ~100ms

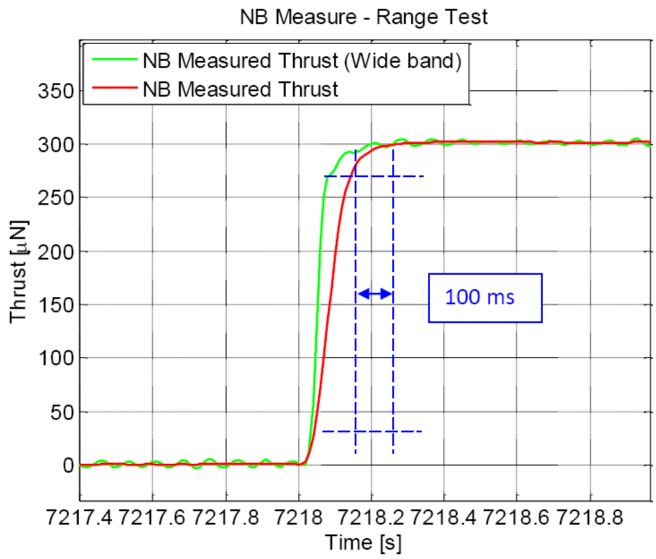

Figure 4-15: Measured thrust step from 200 to 500 µN. Width between the two vertical lines is ~100ms

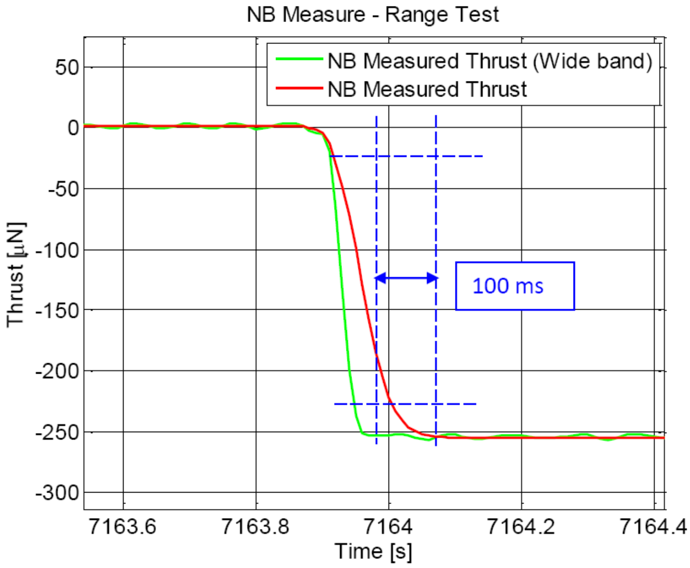

Figure 4-16: Measured thrust step from 450 to 200 µN. Width between the two vertical lines is ~100ms

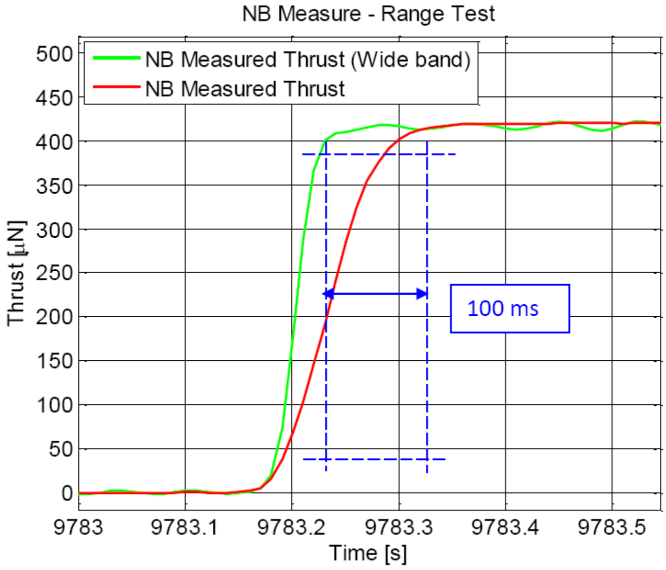

Figure 4-17: Measured thrust step from 500 to 900 µN. Width between the two vertical lines is ~100ms

The thruster noise was measured at different thrust levels up to 650 µN. Above this level, noise tests were not possible due to thermal issues affecting the behaviour of the NB and the thruster itself (the thruster being adiabatically isolated). In all tests, the measured noise was very close to the test facility background noise, which therefore represents an upper limit to the thrust noise. From 0.1 Hz to 1 Hz the measured thrust noise was always below <1.2µN/√Hz. At frequencies less than 0.1 Hz it is very close to requirement as shown in Figure 4-18. The thrust noise computed by the thruster control unit using the electrical parameters was, as expected, much less than requirement.

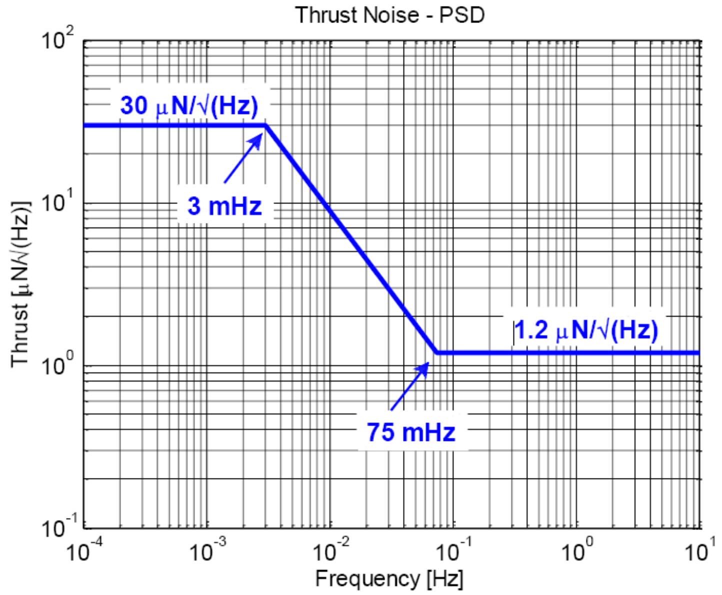

Figure 4-18: Thrust noise requirement

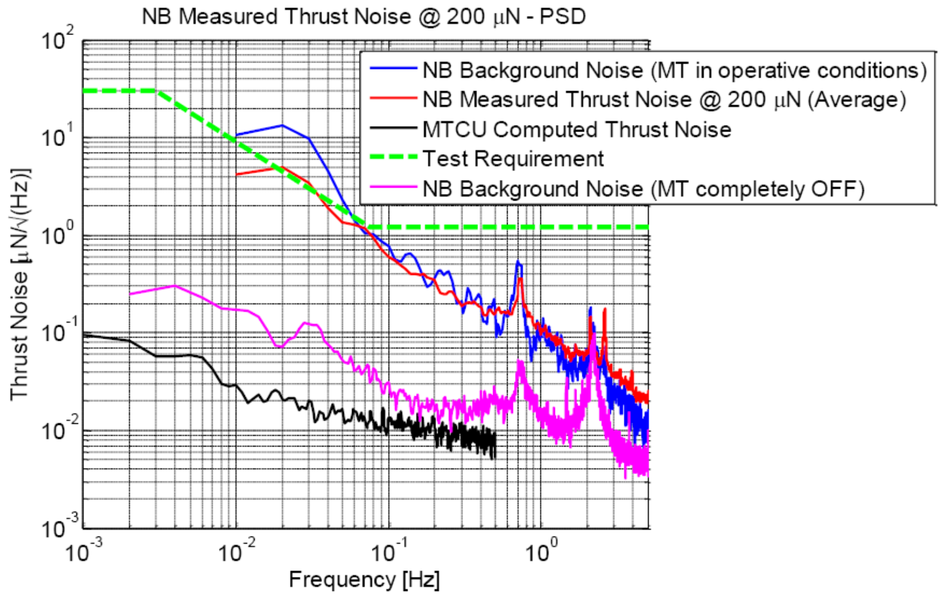

Figure 4-19: Measured and computed thrust noise PSD @ 200 µN

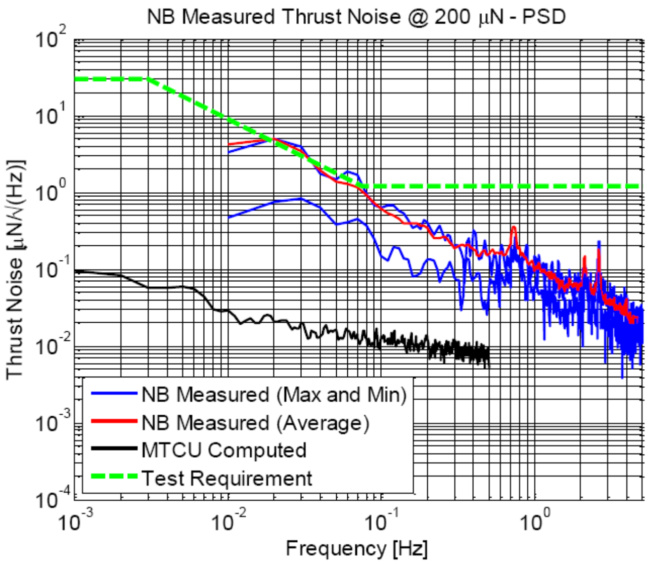

Figure 4-20: Measured thrust noise PSD, best and worst PSD of all the valid data segments

The performance of the µNRIT-2.5 thruster measured is summarised in Table 4-9.

Table 4-9: Performance requirement versus measurement of the test campaign on the µNRIT-2.5 prototype performed in 2010

Tested parameter	Requirement	Measured Values
Thrust Range	The current prototype of the mini-RIT shall be able to provide continuous thrust with any value in the range 50 µN to 1 mN	From 50 µN up to 1mN.
Thrust Resolution	The mini-RIT shall be able to provide continuous thrust in the overall range (50 µN - 1 mN) with a minimum resolution of 0.5 µN	Resolution of 0.5 µN, and in some cases of 0.3 µN, measured in the 50 – 550 µN range. Resolution not measurable above 550 µN due to operational constraints and excessive NB background noise.
Slew rate	The mini-RIT shall be able to change the thrust value at a rate > 0.5 mN/s (50 µN step performed in 100 ms)	Measured thrust rise/fall time < 50 ms over the full thrust range, for any thrust step from 50 µN to 400 µN → slew rate >1 mN/s
Thrust Noise	The thrust noise of the mini-RIT shall be <1.2µN/√Hz for frequencies between 75 mHz and 1 Hz, and not exceed a 1/f increase between 75 mHz and 3 mHz.	Thrust noise measurements limited by the Nanobalance background noise, but lower than the requirement from 0.1 to 1 Hz, and close to the requirement from 0.01 to 0.1 Hz. Noise not measurable below 0.01 Hz due to excessive thermal drifts.

The µNRIT-3.5 Thruster

In the frame of preparatory studies for ESA's Next Generation Gravity Mission (NGGM), the TransMIT GmbH is developing a miniature RIT to provide a thrust range from low µN level to 2.5mN. The performance of the µNRIT-2.5 thruster (originally designed for a thrust range 50µN – 500µN but tested up to 1mN) has been shown to be generally compliant with e^2.motion requirements.

In order to meet the extended thrust range up to 2.5mN, the design of µNRIT-2.5 has been taken as baseline but scaled up to a 3.5cm diameter thruster with 121 grid apertures.

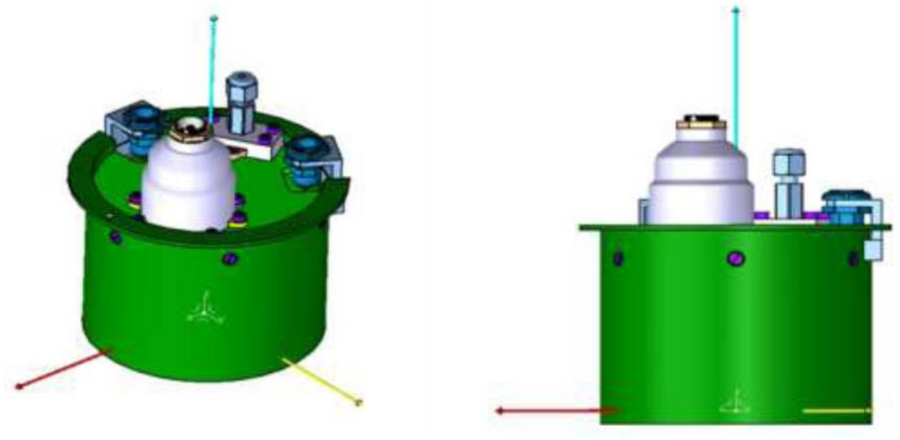

Figure 4-21: Drawings of the µNRIT-3.5 thruster

4.4.3 Proposed Subsystem Architecture

4.4.3.1 Top Level Subsystem Architecture

A RIT thruster requires propellant and electricity for operation. The propellant flow to the thruster is controlled by a flow control unit (FCU). The required electric power is provided by a power processing and control unit (PCU). A neutraliser is used to provide an equal electron current to compensate the positive ion beam extracted. The PCU powers and controls the Radio Frequency Generator (RFG) for each thruster, the FCU and the neutraliser assembly (NA).

A top level subsystem block diagram (for a single thruster chain) is displayed in Figure 4-22.

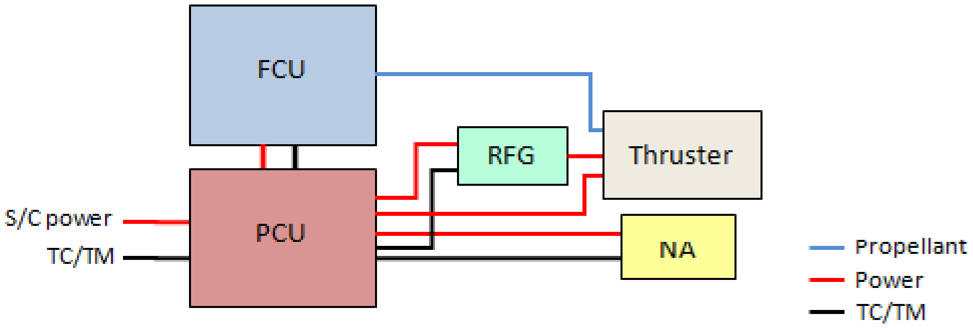

Figure 4-22: System functional block diagram for a single µNRIT

4.4.3.2 Thruster

The slew and dither manoeuvres will require a maximum thrust of at least 2mN per axis, provided by either a single thruster or two thrusters firing at 1mN. Additionally, thrusters will be required to operate at the 50µN - 100µN level to compensate disturbance torques.

Thruster Sizing

The maximum thrust that a gridded ion thruster can achieve is directly dependent on the area that ions can be extracted from the plasma. For a given grid geometry, it is therefore directly proportional to the number of beamlets (grid apertures).

For given discharge conditions, the ion current extracted per aperture for a specific beam voltage will be constant. In RIT thrusters the radial profile of ion current density is relatively flat, and therefore, the ion current extracted from each aperture can be assumed to be approximately the same. For given discharge conditions, the thrust range is then scalable by the number of apertures and beam voltage, independent of thruster size.

The µNRIT-3.5 thruster under development in the frame of NGGM is designed to achieve a thrust range from low µN level to 2.5mN. It will be taken as the baseline design for e^2.motion but different configurations of the thruster will be considered;

- RIT-3.5/13: thruster fitted with extraction grids containing 13 apertures to achieve thrust levels between 50µN – 100µN.
- RIT-3.5/60: thruster fitted with extraction grids containing 60 apertures to achieve thrust levels between 50µN – 1 mN.
- RIT-3.5/120: thruster fitted with extraction grids containing 120 apertures to achieve thrust levels between 100µN – 2 mN.

The geometry of the ion optics will be kept the same as that validated for the µNRIT-2.5 (and other RIT thrusters).

Thrust Modulation

As can be seen by Equation (4-5), at a fixed flow rate, thrust can be controlled by varying the beam potential (PHV), which provides slow thrust variations, or by regulating the RF power to control I_{beam}, with the plasma (and therefore thrust) responding within a few ms to changes in the RF power.

Performance for a 3.5cm diameter thruster equipped with different grid sets has been predicted. It is assumed that the thrusters will be operated at different fixed flow rates; one for the low thrust regime and one for high thrust. The flow rates assumed for the different configurations of thruster are:

- µNRIT-3.5/13: low thrust, 5 µg/s
- µNRIT-3.5/60: low thrust, 20 µg/s high thrust, 33 µg/s
- µNRIT-3.5/120: low thrust, 25 µg/s high thrust, 50 µg/s

Thrust demand is converted to an equivalent ion current and required beam voltage. Once the positive high voltage is set, only the beam current has to be kept constant at th commanded value. In closed loop control, the measured beam current is compared to the commanded level and the RF power is adjusted. The accuracy of the thrust control depends primarily on the precision of the PCU. Figure 4-23 displays a block diagram of the beam current controller.

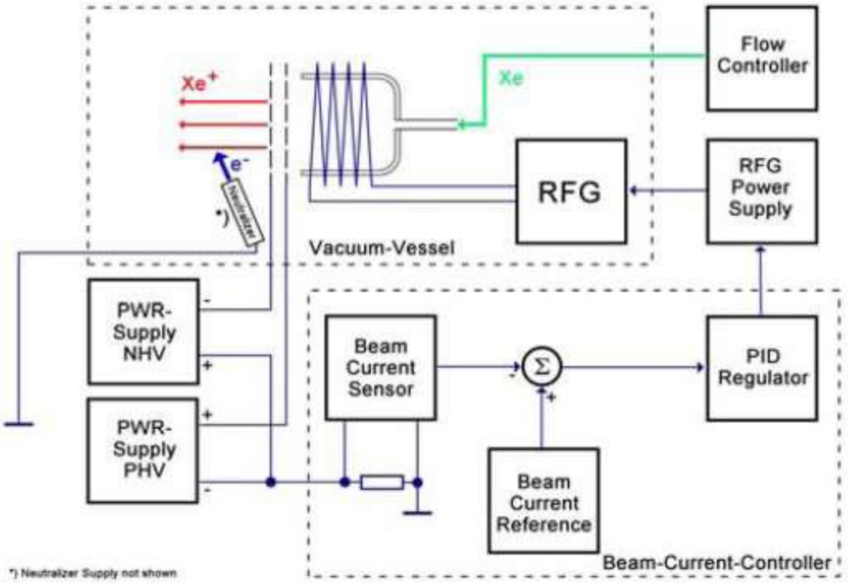

Figure 4-23: Block diagram of µNRIT beam current controller

Thruster Lifetime

Preliminary estimates of grid lifetime for RIT-3.5 are available for thrust levels 100µN and 2mN. The simulations were performed using the 2D ion optics code of IOM, which simulates the erosion of the second (accelerator) grid over time due to primary (beamlet) ions and secondary (charge-exchange) ions created in collisions between the primary ions and neutral gas. The simulations were run for 10,000 hours. Grid erosion by CEX ions is the main life limiting factor and is dependent on ion (beamlet) current and neutral gas flow. The end-of-life is defined when the aperture diameter of the second (Accel) grid reaches the same diameter as the first (screen) grid (1.9mm).

The simulations were performed considering a constant gas flow of 0.38 sccm at 100µN and 0.7 sccm at 2mN. The results at low thrust indicate a linear erosion of the second grid of the order 10-20µm after 10,000 hours at different points along the aperture bore. Extrapolation of the erosion rate would indicate a grid lifetime over 200,000 hours at low thrust. Figure 4-24 shows the evolution of the Accel grid aperture diameter against time for the thruster running at 100µN. At high thrust (2mN), erosion is more significant and lifetime is estimated around 16,000 hours (Figure 4-25).

These simulations represent worst case as much higher flow rates are used (40% and 80%) than those expected for nominal operation of RIT-3.5, thus leading to lower lifetimes than expected. However, these predicted lifetimes comply with requirements for the different thrust regimes for e^2.motion.

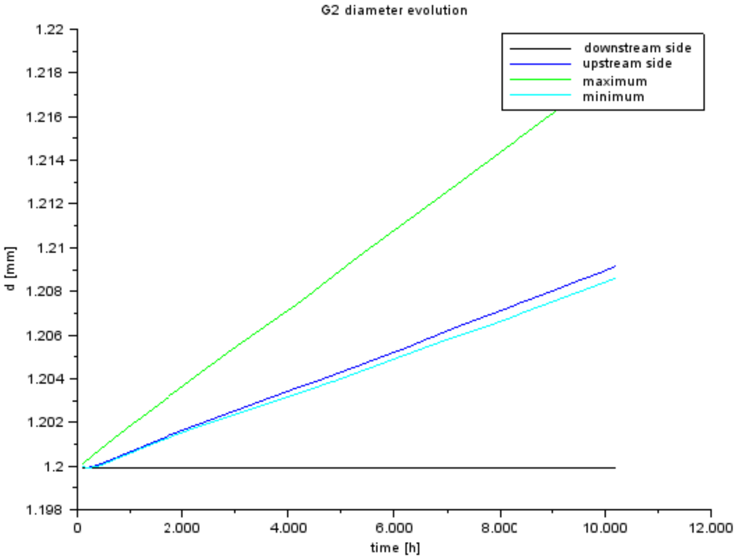

Figure 4-24: Accel grid aperture diameter with time for low thrust (0.38 sccm at 100 µN)

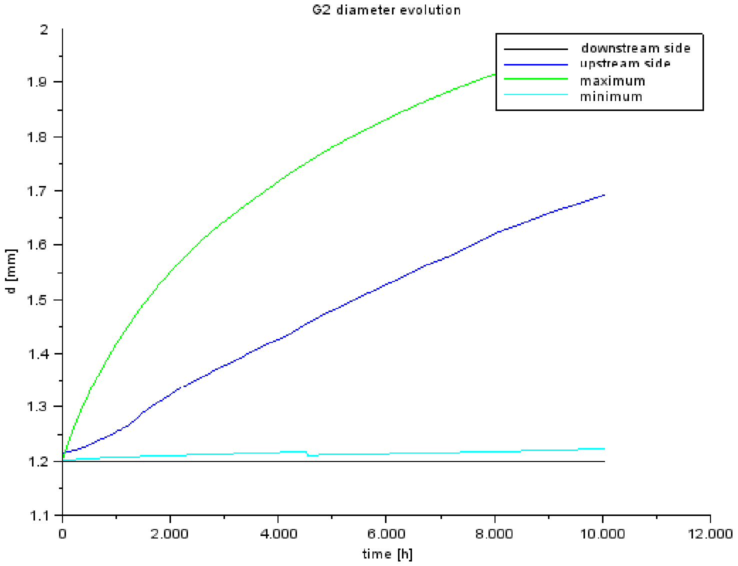

Figure 4-25: Accel grid aperture diameter with time for high thrust (0.7 sccm at 2 mN)

4.4.3.3 Xenon Storage and Flow Control System

The Xenon storage and flow control system feeds the Xenon propellant from a high pressure storage tank to a low pressure flow regulation stage, which provides a fixed flow to each thruster.

Common to each of the thruster architectures will be a high pressure stage comprising:

- Xenon pressurant tank; the size or number of tanks required depends on volume of propellant to be stored.

- A high pressure feeding system, separated into parallel regulating branches to provide redundancy and which comprises:
    - 1 off manual 3-way valve
    - 1 off fill and drain valve (FDV)
    - 1 off high pressure inlet filter (to protect from particulate contamination)
    - 1 off high pressure transducer (HPT)
    - 2 off high pressure latching isolation valves (HPLV)
    - 2 off pressure regulators (PR)

The low pressure regulation stage will differ for each configuration as follows:

Architecture 1:

The regulating branches from the high pressure stage will feed into a common low pressure section containing:

- 1 off fill and drain valve (FDV)
- 1 off plenum and filter assembly
- 2 off low pressure transducers (LPT)

Xenon will be supplied at a fixed flow rate, or blocked, to each of the thrusters (6N and 6R) as required using low pressure latching isolation valves (LPLV) and fixed orifices (flow restrictors). The 4N and 4R thrusters that may be used for performing the slew and dither manoeuvres (about X and Y) will need to operate at high thrust/high flow rate, but also low thrust/low flow rate. The remaining 2N and 2R thrusters (about Z-axis) are only required to operate at low thrust/low flow rate. The following number of isolation valves and flow restrictors will be required:

- 20 off low pressure latching isolation valves (LPLV)
- 12 off fixed orifice flow restrictors for 25µg/s (*operation at 50µN-100µN*)
- 8 off fixed orifice flow restrictors for 50µg/s (*operation at 2mN*)

The complete flow control system for architecture 1 is shown schematically in Figure 4-26.

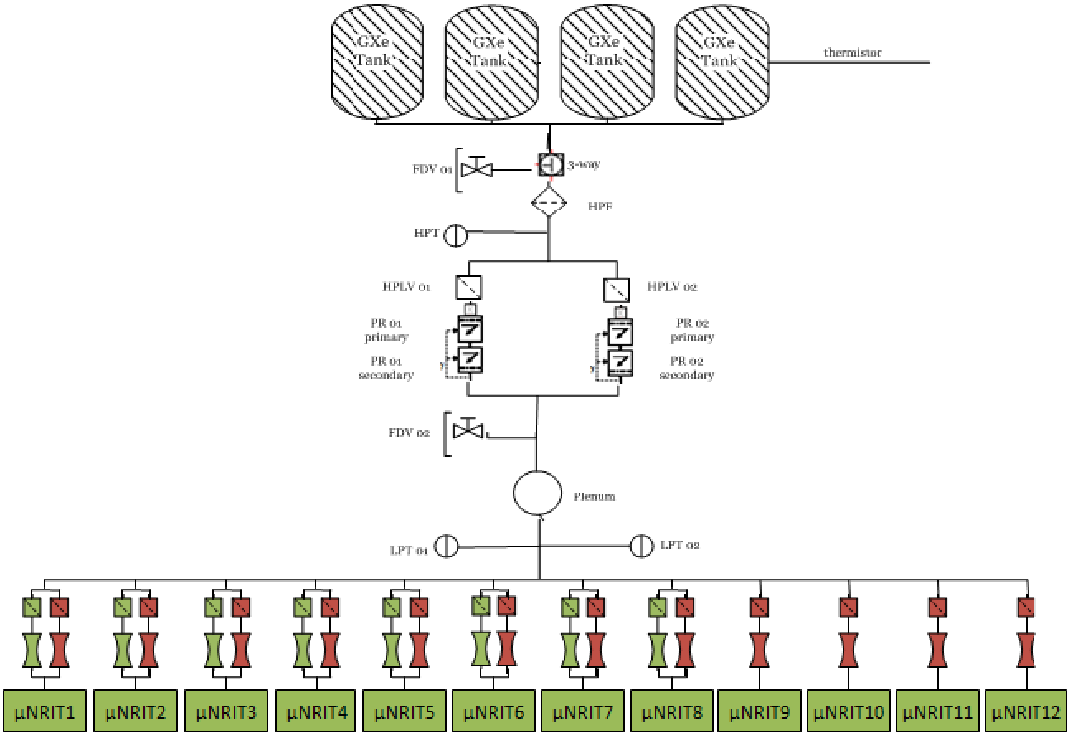

Figure 4-26: Flow control schematic for architecture 1

Architecture 2:

The flow control system for architecture 2 will be similar to that of architecture 1 (as shown in Figure 4-27) but will use the following isolation valves and flow restrictors:

- 36 off low pressure latching isolation valves (LPLV)

- 20 off fixed orifice flow restrictors for 20µg/s (*operation at 50µN-100µN*)
- 16 off fixed orifice flow restrictors for 33µg/s (*operation at 1mN*)

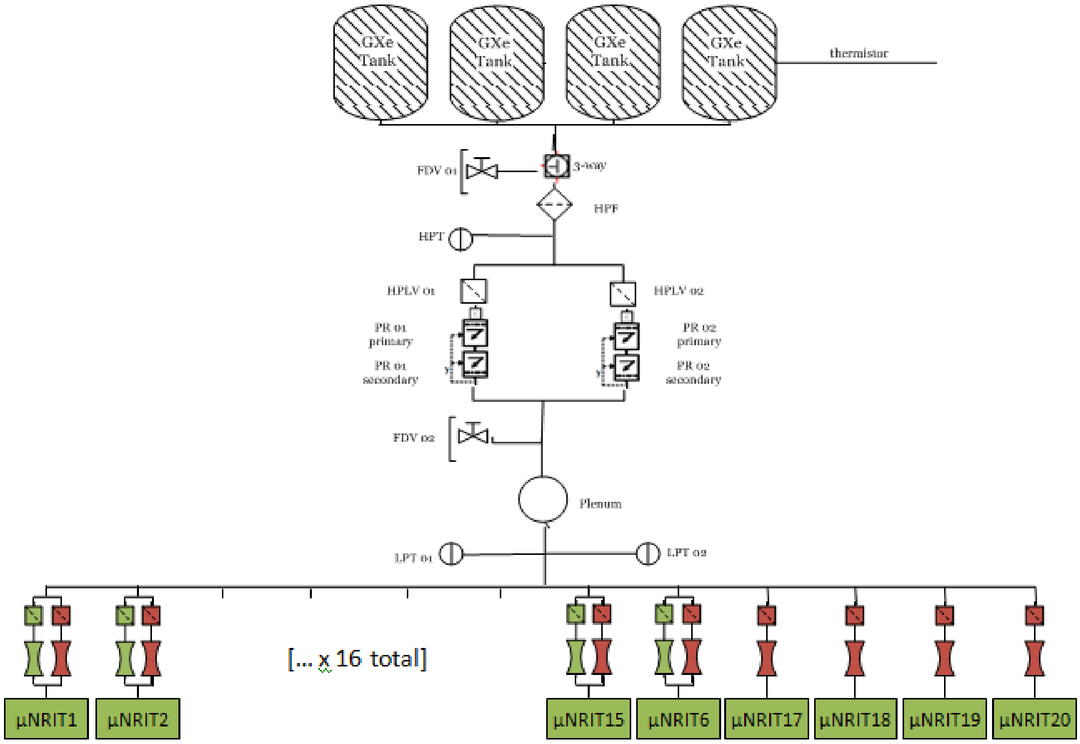

Figure 4-27: Flow control schematic for architecture 2

Architecture 3:

The use of dedicated sets of thrusters, one for the slew/dither manoeuvres and one for compensating disturbance torques, will reduce the number of isolation valves and flow restrictors required. During the slew/dither manoeuvres, the thruster opposite to that firing will be switched to standby mode (discharge ON, beam extraction OFF) and the flow rate dropped to a minimal value to maintain the discharge. The total propellant will be minimised with this configuration, and therefore, also the size or number of propellant tanks required. The flow control system for architecture 3 is displayed in Figure 4-28 and will use the following isolation valves and flow restrictors:

- 30 off low pressure latching isolation valves (LPLV)
- 2 off fixed orifice flow restrictor for 5µg/s (*operation at 50µN-100µN*)
- 8 off fixed orifice flow restrictor for 20µg/s (standby mode)
- 8 off fixed orifice flow restrictor for 50µg/s (*operation at 2mN*)

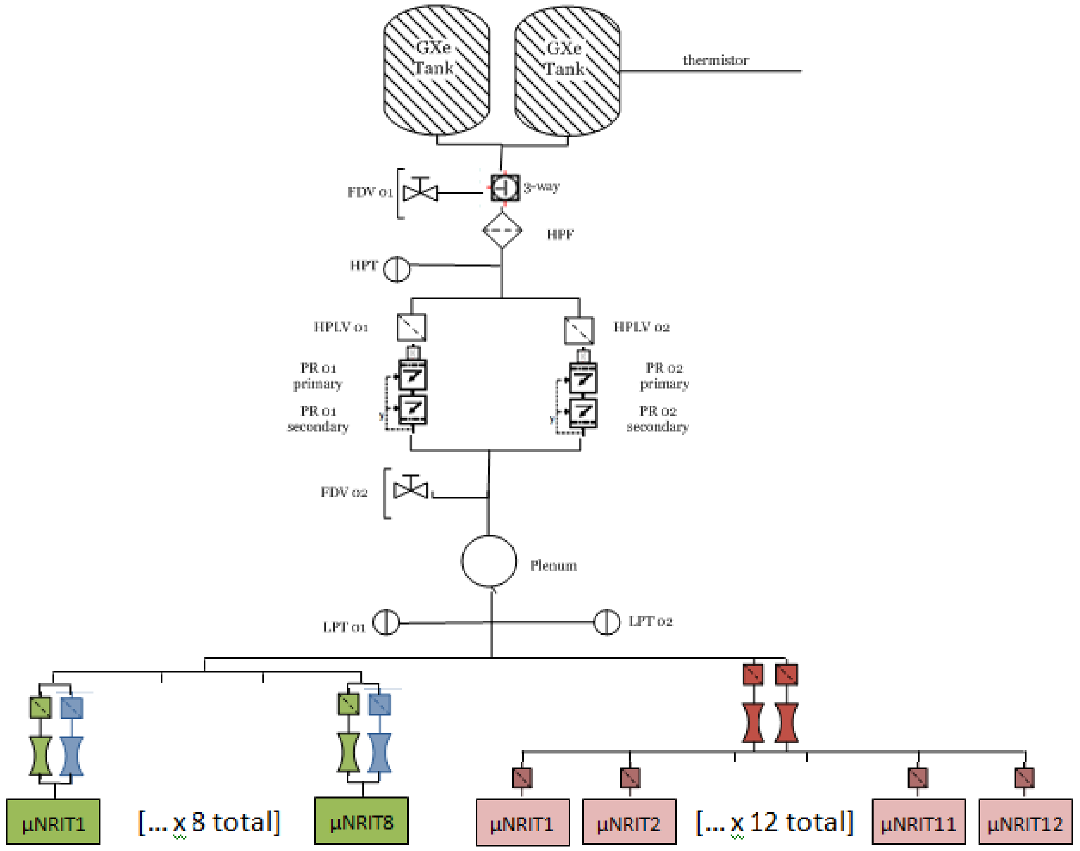

Figure 4-28: Flow control schematic for architecture 3

Architecture 4:

The flow control system for architecture 4 will be the same as that of architecture 1 (as shown in Figure 4-26) but will use different sized flow restrictors:

- 20 off low pressure latching isolation valves (LPLV)
- 12 off fixed orifice flow restrictors for 20µg/s (*operation at 50µN-100µN*)
- 8 off fixed orifice flow restrictors for 33µg/s (*operation at 1mN*)

4.4.3.4 Neutralizer

A neutralizer is required to provide an equivalent electron current to compensate the ion beam current extracted from the RIT thrusters. A gas-free neutralizer device based on travelling wave tube technology has been developed by THALES Electron Devices GmbH for the Lisa Pathfinder mission. Currents above 10mA have been demonstrated during qualification tests; for this study a current of ~11mA is assumed per neutralizer, with a power of ~8W (bus).

The thrust levels and equivalent beam current assumed for each thruster configuration are:

- µNRIT-3.5/13: I_{beam} = 1.45 mA @ 50 µN
- µNRIT-3.5/60: I_{beam} = 14.5 mA @ 1 mN
  I_{beam} = 1.45 mA @ 50 µN
- µNRIT-3.5/120: I_{beam} = 29.1 mA @ 2 mN
  I_{beam} = 2.91 mA @ 100 µN

The thruster opposite to that being fired to perform a slew or dither manoeuvre will be switched to stand-by mode (discharge ON, beam extraction OFF) or switched OFF completely (depending on thruster re-ignition capability).

4.4.3.5 Subsystem Architecture

Figure 4-29 shows the functional block diagram for the proposed architecture.

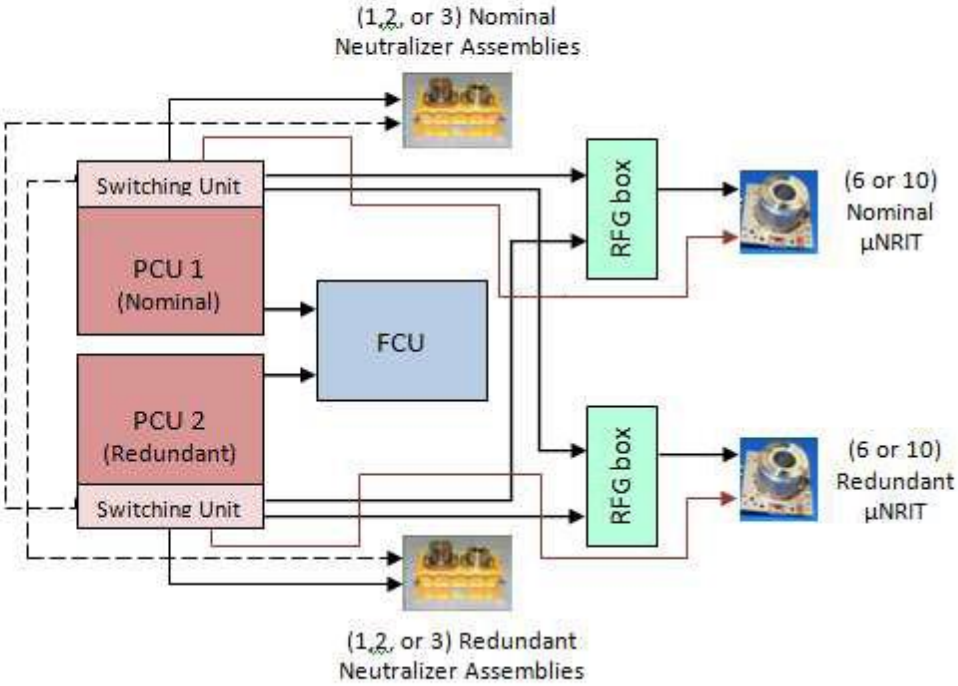

Figure 4-29: Subsystem functional block diagram

4.4.3.6 Subsystem Mass and Power Budgets

Propellant Budget

The amount of Xenon required for each manoeuvre for the different slew and dither options is based on the following assumptions:

- µNRIT-3.5/13: low thrust (50µN), $\dot{m}$ = 5 µg/s
- µNRIT-3.5/60: high thrust (1mN), $\dot{m}$ = 33 µg/s; low thrust (50µN), $\dot{m}$ = 20 µg/s
- µNRIT-3.5/120: high thrust (2mN), $\dot{m}$ = 50 µg/s; low thrust (100µN), $\dot{m}$ = 25 µg/s; standby (archt. 3) $\dot{m}$ = 20 µg/s

The imaging sequence is repeated 41888 times; therefore, 41888 slews, 125664 dithers and 167552 observation periods shall be performed. The mission duration is specified as 6.25 years; therefore, an additional commissioning period is assumed with a nominal or redundant set of thrusters operating at low thrust.

Considering worst-case, the propellant flow to a thruster will not be switched off when it is not firing; it will be operated in standby mode (discharge ON, beam extraction OFF) at low flow rate. Switching the flow rate off will depend on thruster re-ignition capability (and the effect on AOCS).

A 100% margin is applied to the propellant calculated for thrusters operating at the very low flow rate of 5µg/s; a 20% margin is applied for all other flow rates. Propellant mass for a given manoeuvre can be calculated as per the following example:

Example: Option A:

Xe mass for Low Thrust Manoeuvring = (2 x 50µg/s x 66s x 125664) + (4 x 25µg/s x 66s x125664) = 1.659 kg

Xenon must be stored above critical temperature (Tc ~17oC), so the propellant tank should be kept above 20oC (between 20-50oC) by use of heaters.

Several COTS pressurant tanks for xenon are available from Ardé Inc. with fill pressures of 150 bar. Assuming the compressibility of xenon is approximately:

Z ~ 0.5 (at P = 150 bar, T = 323 K)

then xenon density can be assumed to be:

$$\rho = \frac{P}{Z\frac{R}{M}T} \sim 1.47\mathrm{kg}/\mathrm{l} \qquad (4\text{-}7)$$

with $R = 8.315 \times 10^{-2}$ L.bar.K^{-1}mol^{-1} and $M_{Xe} = 131.293$ gmol-1.

Subsystem Mass Budget

The overall subsystem mass budget for option 1 is displayed in Table 4-10.

Table 4-10: Subsystem mass budget for µNRIT-3.5/120, simultaneous dithers along x and y directions

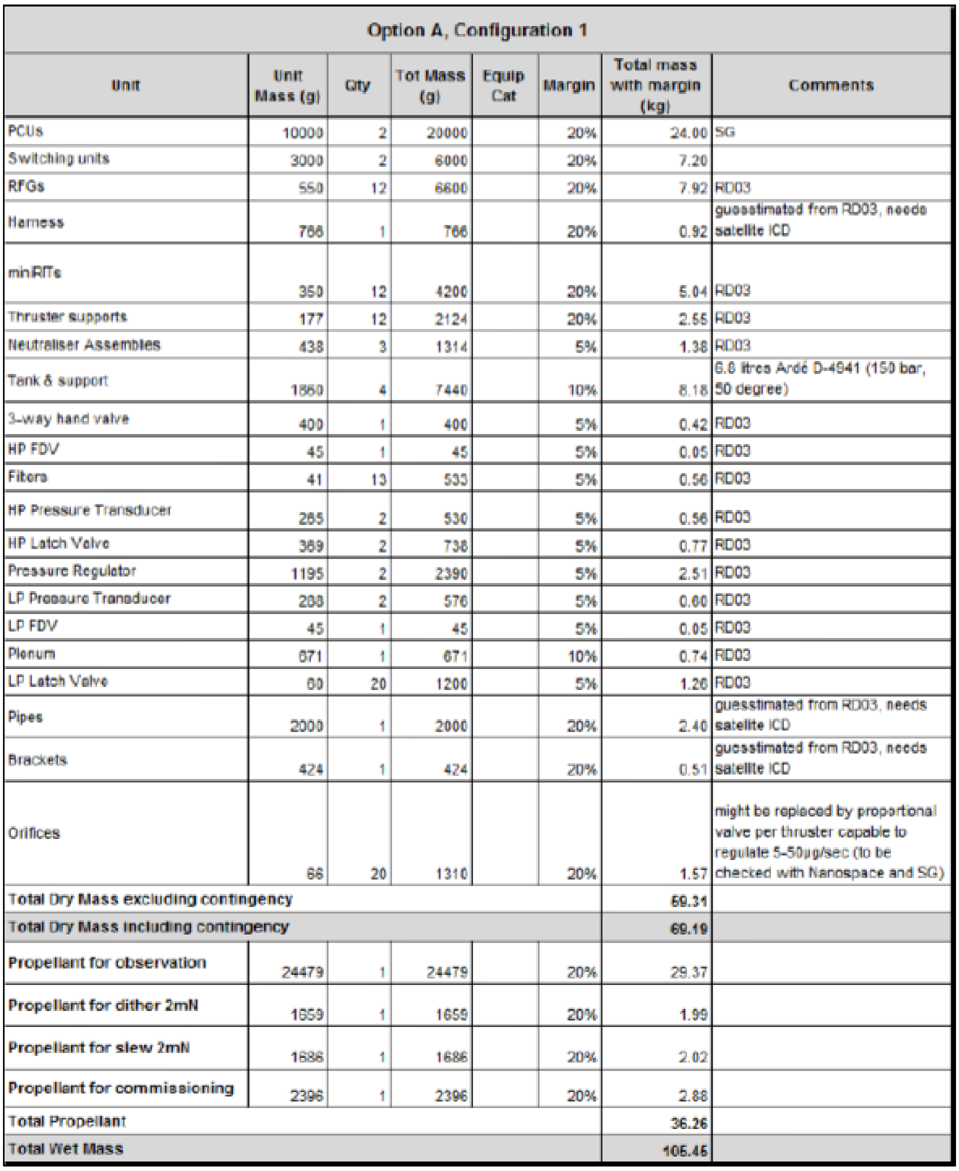

Option A, Configuration 1							
Unit	Unit Mass (g)	Qty	Tot Mass (g)	Equip Cat	Margin	Total mass with margin (kg)	Comments
PCUs	10000	2	20000		20%	24.00	SG
Switching units	3000	2	6000		20%	7.20	
RFGs	550	12	6600		20%	7.92	RD03
Harness	766	1	766		20%	0.92	guesstimated from RD03, needs satellite ICD
miniRITs	350	12	4200		20%	5.04	RD03
Thruster supports	177	12	2124		20%	2.55	RD03
Neutraliser Assemblies	438	3	1314		5%	1.38	RD03
Tank & support	1860	4	7440		10%	8.18	6.8 litres Ardé D-4941 (150 bar, 50 degree)
3-way hand valve	400	1	400		5%	0.42	RD03
HP FDV	45	1	45		5%	0.05	RD03
Filters	41	13	533		5%	0.56	RD03
HP Pressure Transducer	265	2	530		5%	0.56	RD03
HP Latch Valve	369	2	738		5%	0.77	RD03
Pressure Regulator	1195	2	2390		5%	2.51	RD03
LP Pressure Transducer	288	2	576		5%	0.60	RD03
LP FDV	45	1	45		5%	0.05	RD03
Plenum	671	1	671		10%	0.74	RD03
LP Latch Valve	60	20	1200		5%	1.26	RD03
Pipes	2000	1	2000		20%	2.40	guesstimated from RD03, needs satellite ICD
Brackets	424	1	424		20%	0.51	guesstimated from RD03, needs satellite ICD
Orifices	66	20	1310		20%	1.57	might be replaced by proportional valve per thruster capable to regulate 5-50µg/sec (to be checked with Nanospace and SG)
Total Dry Mass excluding contingency						**59.31**	
Total Dry Mass including contingency						**69.19**	
Propellant for observation	24479	1	24479		20%	29.37	
Propellant for dither 2mN	1659	1	1659		20%	1.99	
Propellant for slew 2mN	1686	1	1686		20%	2.02	
Propellant for commissioning	2396	1	2396		20%	2.88	
Total Propellant						**36.26**	
Total Wet Mass						**105.45**	

Subsystem Power Budget

The subsystem power budget is calculated based on the following assumptions:

Thruster Power: $P_T = P_{RFG} + P_{HV}$

- µNRIT-3.5/60: $P_{HV} = 0.6$ W $P_{RFG} = 8.72$ W @ 50 µN
- µNRIT-3.5/60: $P_{HV} = 28.2$ W $P_{RFG} = 16.95$ W @ 1 mN
  $P_{HV} = 0.6$ W $P_{RFG} = 8.72$ W @ 50 µN
- µNRIT-3.5/120: $P_{HV} = 56.4$ W $P_{RFG} = 26.86$ W @ 2 mN
  $P_{HV} = 1.2$ W $P_{RFG} = 8.72$ W @ 100 µN

Neutraliser Power: $P_{neut} = 6.8$ W @ 11 mA

PCU efficiency: $\eta_{PCU} = 85\%$

Losses:	PCU 5 W (harness, connectors etc.) 3 W $P_{loss} = 8W$

Subsystem (bus) power: $P_{SYS} = ((P_T + P_{neut})/ \eta_{PCU}) + P_{loss}$

Sequence duration: $t_s = 4*t_m$ (obs) + $3*t_m$ (dither) + t_m (slew)

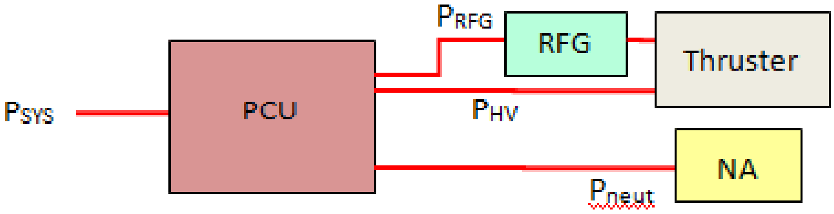

Figure 4-30: Breakdown of power for subsystem (showing single thruster chain)

<u>Summary:</u>

If the longer manoeuvre times resulting from performing the slew/dithers at 1mN are not acceptable, then architectures 1 and 3 should be considered (summarised in Table 4-11).

Table 4-11: Subsystem mass and power budgets for architecture 1

Architecture 1	Subsystem Mass		Subsystem Power	
	Dry	Wet	Mean Power	Peak Power
Option A	69.2 kg	105.5 kg	108.6 W	295.8 W

4.5 Preliminary AOCS Design

4.5.1 Concept for Initial Link Acquisition

4.5.1.1 STI Proposal for Initial Link Acquisition

As stated above in GFO a beam steering mirror is used to ensure the required beam co-alignment of less than 100 µrad in science mode. Furthermore this mirror is used to enable initial acquisition. In the following a more detailed discussion is shown to explain the challenges and drawbacks of such an approach and to justify why for e^2.motion another approach is favored.

The challenges for the initial link acquisition for the current GFO mission are mainly:

- The on orbit alignment uncertainty between the star tracker reference frame and the laser interferometer LoS is in the range of 2 mrad for the initial link acquisition. This error exists on both SCs after launch (due to setting effects, 1g-0g effects, temperature effects etc.). After initial acquisition and in-flight calibration and temperature stabilisation of the optical bench, this error is reduced to about 150 µrad (see [9]), which is still larger than the 100 µrad pointing requirement.
- Before laser interferometer information is available, the pointing performance is dependent on the static error of the star trackers, assuming sufficient accuracy of the actuators (discussed in section 4.5.3). The performance of the star tracker is conservatively assumed as following for this document (and also for simulations in section 4.5.3): bias = 300 µrad (1 σ), noise = 240 µrad (1 σ). After in-flight calibration an accuracy of about 50 µrad should be possible.
- To reduce the approx. 2-2.5 mrad uncertainty a 5-dimension searching loop has to be performed. The laser interferometer can only start to work if fine pointing performance (< 100 µrad) in pitch/yaw of both SCs and the laser frequency offset lock-on can be guaranteed simultaneously.

A possible solution to the above mentioned challenges could be a 5-dimensional scanning algorithm consisting of a spatial scan of both steering mirrors and a frequency scan on one laser. Both SCs should scan with a certain step size (constrained by the accuracy of star tracker) over a broader area (e.g. 3 mrad*3 mard), trying to align the laser beams w.r.t. LoS of the laser interferometers. The remaining uncertainty of about 150 µrad should be eliminated by a spatial scan with smaller step size to ensure the final link acquisition. The coherent signal data of both S/Cs should be sent to ground and the corrected pointing information should be uploaded to the S/Cs to assist the acquisition process. Meanwhile, the frequency scanning loop should try to lock the frequency offset between the transmitter and receiver lasers. The initial acquisition process is only finished if at some point all three scanning loops can succeed simultaneously.

The described scanning procedure has a significant drawback that the scanning algorithm is complex and the whole process is quite time consuming (current assumption for GFO: up to 16 hours). After a possible loss of link, a similar (but significantly accelerated) procedure has to be repeated again.

For the e^2.motion mission, a spacecraft pointing strategy is proposed (see section 4.3) where no steering mirror is planned, not only to avoid the complex acquisition, but also to improve the instrument ranging performance. Thus the above mentioned scanning algorithm is not considered suitable.

STI proposes a tailored and advanced strategy for the e^2.motion mission concerning the initial link acquisition. It is planned to implement a dedicated acquisition sensor and (optionally) a dedicated acquisition laser source. This concept is illustrated in Figure 4-31.

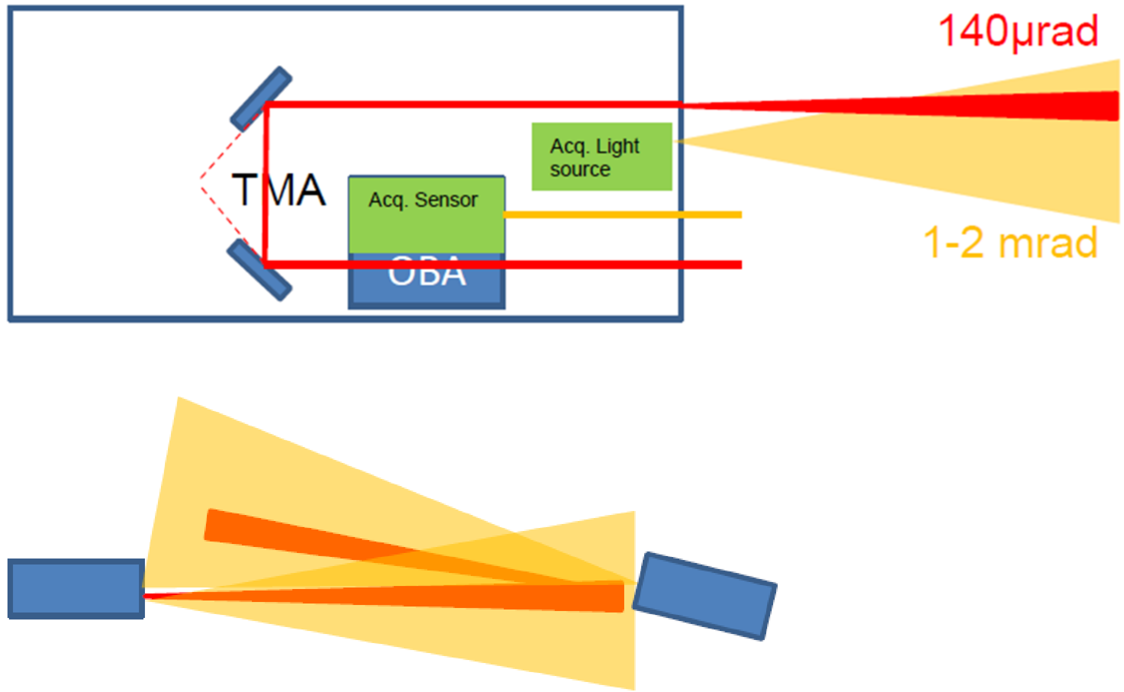

Figure 4-31: Simplified conceptual sketch of the acquisition sensor and laser source. TMA: Triple Mirror Assembly, OBA: Optical Bench Assembly

The science laser (e.g. Tesat NPRO with 25 mW power) is collimated to a half cone beam divergence of about 140 µrad (as a result of a heterodyne signal contrast optimisation) and the laser power drops quickly with the distance to the center of the beam. In order to guarantee sufficient power and acceptable wavefront tilt arriving at the receiver and thus enabling a detection of the DWS signal, a pointing accuracy of about 100 µrad is required. This accuracy is, however, challenging for the initial acquisition and (without a dedicated acquisition sensor for incoherent signals) requires a complex scanning algorithm, as discussed above. The idea of introducing a dedicated acquisition sensor is to relax the pointing requirement for the initial acquisition phase. The acquisition sensor could be a CCD sensor inherited from the star sensor with e.g. 0.5 -1 Mega pixel. The major advantages of implementing a dedicated acquisition sensor are:

- The acquisition sensor has a broad Field of View (FoV) of approximately 3 mrad (half-cone angle) enabling detection of incoherent signals in its FoV. For the assumed 25 mW of laser power this allows a tilting of the transmitter to about 300 µrad and the tilting of the receiver up to 3 mrad w.r.t LoS between two laser interferometers. As a comparison, for the case without the acquisition sensor, both transmitter and receiver have to point with an accuracy of 100 µrad w.r.t. LoS.

- The acquisition sensor would reduce the time-consuming 5-dimension searching loop to a coarse spatial scan of one S/C over 3 mrad with a step size of e.g. 600 µrad, since the sensor provides directly tilting information of the receiver w.r.t. LoS and no laser frequency lock-on is needed simultaneously in this case. This significantly reduces the complexity of the pointing algorithm and the laser frequency search can be done after completion of the pointing process with required accuracy.
- The acquisition sensor can provide tilting measurements w.r.t. LoS with an accuracy of down to several µrad, which is more accurate than the star camera. Thus it is possible to command the actuators more precisely and accurately.

The initial acquisition procedure can be further relaxed by introducing a dedicated acquisition laser source. This could be a commercial inexpensive laser diode which has a much higher output power and larger beam divergence than the science laser. A laser with 1 W of output power and a beam divergence of e.g .about 4 mrad brings the following key advantages:

- The transmitter and receiver would be able to detect each other immediately after switching on the acquisition sensor. The combination of high power and large beam divergence allows both transmitter and receiver to tilt up to 4-8 mrad, which should be large enough to cover all uncertainties during the initial acquisition phase. In comparison: without the acquisition laser, the transmitter has to point better than 300 µrad so that the acquisition sensor of the receiver can detect the incoming beam.
- This laser simply serves as a focused light source and is therefore not necessary to be thermal/frequency stabilized. Thus it is not necessary to accommodate the acquisition laser on the optical bench, where thermal environment should be actively stabilized.
- The acquisition laser can be placed on a convenient location on the panel facing the other SC and a very precise alignment to the science laser is not required, as long as the cone angle is larger than the alignment error.

In conclusion, with the dedicated acquisition laser and sensor, the time-consuming 5-dimensional searching loop can be eliminated and the initial acquisition process can be considerably simplified and accelerated. It is to notice that a precise alignment between acquisition sensor and the science laser in the range of 100 µrad is required.

The acquisition laser may be spared if a science laser with higher power is available, but the overall complexity and cost is reduced with the implementation of a dedicated acquisition light source. Therefore, a trade-off analysis between a high-power single frequency science laser (also used for LRI) and a separated laser source (only for acquisition) without frequency stability requirements is suggested for further project phases. It is also not necessary to implement the additional laser source if the pointing procedure with the acquisition sensor alone is considered to be sufficient and efficient enough. Such a trade-off analysis is recommended in further project phases.

4.5.1.2 ASG Proposal for Initial Link Acquisition

ASG discussed the following 3 options for the initial link acquisition:

- The desired direction is determined in inertial space using the real-time exchange of GPS data between the satellites and translated into the spacecraft pointing using the star trackers measurements.
- The desired direction is determined in inertial space using the GPS position of the satellite and an orbit propagator uploaded from the ground to infer the position of the other satellite. The direction is translated into required spacecraft pointing using the star trackers.
- The differential wave front sensor is used to determine the relative pointing between the satellites. No information with respect to the inertial frame is required for link pointing.

The second solution requires the least hardware and processing capabilities on the spacecraft. Hence it is preferable if a sufficient performance of this solution can be verified.

Also for the first solution the required performance needs to be verified. However since this solution eliminates the error originating from the orbit prediction it will by design have a better performance than the second option. The first option requires the real-time exchange of GPS data. Options for this data exchange are analysed and a spacecraft-to-spacecraft S-band link is found to form a suitable solution. However it has the disadvantage to require additional hardware.

The use of the SST instrument as a pointing sensor as considered in option 3 has the undesirable consequence that it makes the attitude control system reliant on the SST instrument. This is not of operational concern since the fine-pointing mode is required only when the instrument is operated. It may however complicate the verification of the AOCS during AIT. Furthermore, a sensor within the instrument cannot in general be used during link acquisition because it relies on the presence of the link for its operation. The latter shortcoming may be circumvented at the expense of a more complicated instrument design: The LISA system is an example for a concept with an SST link that provides angular information already during acquisition. For LISA the SST laser beam is widened up during acquisition such that the direction finding sensor can operate over a broader angular range during the stage. Such an enhancement of the instrument is however expected to have a higher complexity than the option to exchange real-time GPS data. Alternatively the link acquisition could be carried out a scanning procedure and no modifications in the instrument.

In the following we will first consider the attitude determination performance of the first two options. Afterwards the third option including a possible acquisition procedure will be consider. Finally the results will be compared in terms of feasibility, and complexity and a preferred solution will be selected.

Link pointing based on inertial information

A good impression of the capabilities of the exchange of real-time GPS data is obtained if one assumes the GPS performance of the PRISMA mission. The setting of the PRISMA mission is relevant to this mission in the sense that it uses real-time GPS based navigation for formation flying. The 1σ real-time three-dimensional navigation accuracy from the absolute and differential GPS according to simulations for PRISMA mission is:

- real-time GPS, 2 m (1σ),
- real-time differential GPS, 0.04 m (1σ).

Over a distance of 200 km this corresponds to angular errors of

- real-time GPS 40 μrad (1σ),
- real-time differential GPS, 0.8 μrad (1σ).

The information provided by both, GPS and differential GPS is in an inertial reference frame. It can be tied to the satellite reference frame by means of star tracker measurements. The typical absolute pointing knowledge provided by a set of two high quality star trackers is about 15 μrad (1σ). Since the star tracker errors and the GPS errors are uncorrelated one arrives at the following pointing knowledge for the direction towards the other satellite.

- GPS: $\Delta\alpha = \sqrt{(\Delta STR^2 + \Delta GPS^2)} \approx 43$ μrad (1σ),
- Differential GPS: $\Delta\alpha = \sqrt{(\Delta STR^2 + \Delta\Delta GPS^2)} \approx 15$ μrad (1σ).

The PRISMA simulations have been performed assuming spacecraft distances of ~1 km. Hence the performance of the differential GPS may be inferior. However the accuracy cannot degrade below the absolute GPS accuracy. Hence assuming a 43 μrad (1σ) knowledge of the direction towards the other satellite is conservative as soon as GPS data between the satellites are being exchanged in real-time. Even for a baseline of 200 km spacecraft distance some benefit from differential GPS is expected and hence a pointing knowledge error below 100 μrad (3σ) will be reached by the real-time exchange of GPS data. However care has to be taken if the pointing knowledge noise consumes large part of the allowable pointing range. In this case a high level of actuator activity may be triggered that may be unacceptable for other reasons.

If no GPS data are exchanged between the satellites and no instrument data are used then the knowledge about the direction towards the other satellite has to rely on information that is provided by the ground. This information will typically be updated twice per day if one assumes the use of a single ground station. The worst case pointing knowledge will occur just before the next ground station contact. The growth of satellite position uncertainty with respect to an on-board orbit propagator that is updated once per day based on the orbit data of the previous day has been analysed for the GRACE orbit. Only the along track error can reach a magnitude of 500 m (1σ) whereas the errors vertical to the velocity vector are more than one order of magnitude smaller. The prediction errors considered are absolute prediction errors. Common mode effects may further reduce the relative orbit prediction error.

Assuming a baseline length of 200 km between the satellites the knowledge of the direction towards the other satellite after 1 day is given by:

$$\Delta\alpha = \sqrt{[\Delta STR^2 + (\Delta c/l)^2]} \approx 80\ \mu\text{rad}\ (1\sigma),$$

where Δc is the position knowledge vertical to the baseline after one day and l is the length of the baseline. Depending on the orientation of the SST baseline with respect to the orbit we have for the situation of high solar activity approximately

- for a baseline that is oriented along-track (like GRACE), $\Delta c \approx 20$ m, $\Delta\alpha \approx 100$ µrad (1σ);
- for a baseline that is oriented crosstrack, $\Delta c \approx 500$ m, $\Delta\alpha \approx 2500$ µrad (1σ).
- for a pendulum with 15° amplitude, $\Delta c \approx 500$ m, $\Delta\alpha \approx 650$ µrad (1σ).

From the above numbers it is obvious that the link pointing for any formation cannot be based purely on orbit propagator knowledge. Instead any formation will either require the exchange of GPS data between the satellites or directional information provided by the instrument.

Link pointing based on instrument information

The performance of a differential wavefront sensor is about 1 µrad (1σ). Hence relying for the fine pointing on the knowledge of the DWS is clearly feasible once the link has been acquired with lots of margin. The critical aspect for using the instrument in the loop is the link acquisition. If a special acquisition mode of the instrument in which the beam is widened up shall be avoided it is necessary to resort to inertial information for the acquisition. Hence it is important to analyse this critical aspect of attitude control based on the instrument in the loop. The full set of options for the link acquisition are summarised and evaluated in Figure 4-32.

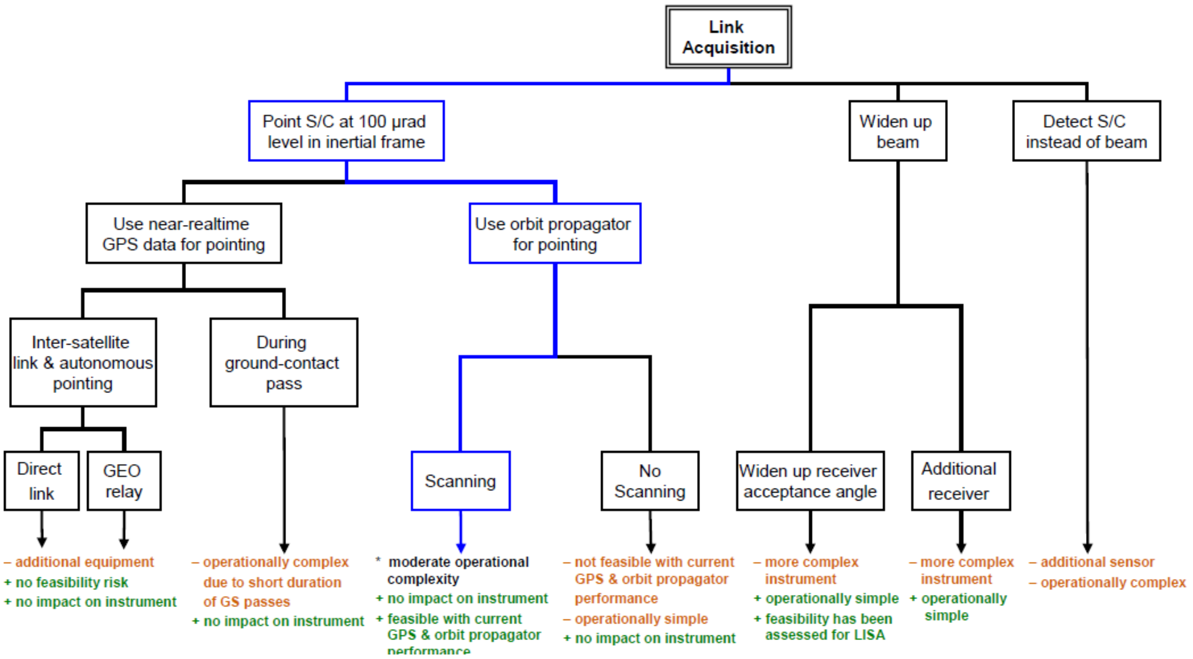

Figure 4-32: Systematic review of link acquisition options and their appraisal

Amongst the options listed in Figure 4-32 the most attractive one it the use of the information of an orbit propagator previously uploaded from ground because this option requires no special hardware on-board the satellites. The operational procedure underlying the use of an orbit propagator for acquisition is illustrated in Figure 4-33 . In a first ground contact the GPS data of the satellites are downloaded. The downlinked data are processed on the ground to generate an orbit prediction for both satellites spanning at least 24 h. For the two orbit prediction also a prediction of the inertial direction from each satellite to the other is generated. This prediction is uplinked to the satellites at the next ground contact together with a timeline for the acquisition. After that contact both satellites are equipped with the knowledge of inertial direction towards the other satellites valid for at least 12 h. Based on the pointing knowledge they can follow the acquisition timeline and carry out a successful acquisition.

In general only one satellite of an SST pair will be in view of a single ground station. Hence two ground stations would be needed if instead of autonomous acquisition after the contact based on a mission timeline acquisition should be conducted during the contact. Assuming that a single ground station is used and that contacts are conducted twice per day the orbit prediction and pointing prediction will have propagation error corresponding to a propagation over 12 h to 24 h at the time of link acquisition.

The critical issue for in this procedure is if the pointing prediction is supplied with a sufficient accuracy such that the acquisition can be carried out in an acceptable timespan. From the analysis in Figure 4-35 it is already clear that the acquisition cannot be accomplished by simply pointing the beam in the right direction because the pointing knowledge will not be sufficiently precise. Hence a scanning procedure needs to be devised that allows the link acquisition taking into account the available pointing knowledge.

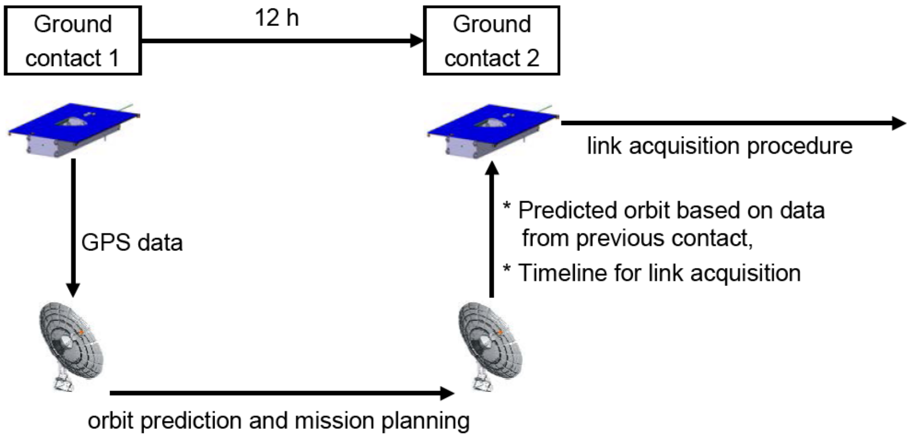

Figure 4-33: Operational concept for update of orbit propagator for link acquisition

In order to derive a link acquisition procedure the pointing knowledge is again estimated from the orbit prediction errors for GRACE. For the application of the orbit prediction errors to e^2.motion the case of high solar activity will be considered because acquisition must be possible at any time during the mission. In addition it is assumed for simplicity that the position and pointing errors on the spacecraft since any correlation would rather tend to reduce the uncertainty in relative pointing. The orbit propagation uncertainty over 24 h is considered. In order to ensure a high probability of success 3 times the 1σ uncertainty is considered as the boundary of the uncertainty. To summaries the following assumptions are made:

- 1σ position uncertainty ellipse of the other satellite along track: 528 m, cross track: 16 m, radial: 1 m
- Star tracker errors: ~ 15 µrad (1σ),
- GPS errors: < 10 m (1σ)

Considering all of these errors the pointing uncertainty ellipse for each satellite is determined to:

- cross track axis: 399 µrad
- radial axis: 215 µrad

This error ellipse assumes that the nominal laser direction is along track as is the case through-out the orbit for the pearl string. However also for any other formation this situation will occur twice per orbit. Hence the uncertainty estimate holds for any other formation if acquisition opportunities twice per orbit are considered sufficient and the duration of the acquisition procedure is short compared to the orbital period.

Since this uncertainty ellipse is larger than acceptance angle of the laser instrument a scanning procedure is required to accomplish acquisition. In order to derive an acquisition scheme it is important to notice that each acceptance area direction needs to be paired with every acceptance direction on other satellite in order to have laser source and receiver oriented to each other. The uncertainty ellipse that has been determined above can be completely covered by 4 beam diameters as is depicted in Figure 4-34. Hence the acquisition can be accomplished in 4 x 4 = 16 steps. The acquisition time will be dominated by the time that the instrument requires for interferometer locking. This has been estimated to 30 s per step. Adding a margin of 100% for the attitude motion, de-synchronisation between the satellite timelines and other potential effects the acquisition procedure will be accomplished within 16 mins.

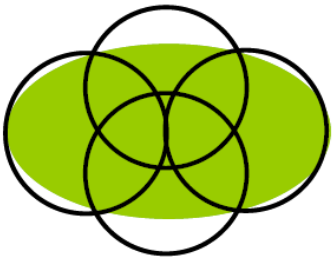

Figure 4-34: Acquisition pattern: circle - instantaneous beam spots, green ellipse - 3σ angular uncertainty of direction of other spacecraft

In conclusion a scanning procedure has been established that is based on pointing predictions obtained by on-ground processing. The procedure is compliant with present-day orbit prediction accuracy and the locking time of the laser interferometer. This procedure is possible without any additional hardware on the satellites and will be considered as the baseline for acquisition of the laser link.

The differential orbit prediction error between the two GRACE satellites has been analysed for a certain data set. The differential prediction errors are about one order of magnitude smaller than the absolute prediction errors. If this could also be accomplished for this mission, then the scanning procedure could be omitted altogether. It is however worth noting that the analysis has been carried out for medium solar activity and that the mission will fly at a significantly lower altitude. Hence it seems wise to retain the above conservative estimates until a dedicated simulation of the orbit prediction error for e^2.motion has been carried out.

Conclusion on link pointing

The options for the link pointing have been considered: Link pointing based on the real-time exchange of GPS data between the satellites, link pointing based on pointing predictions that are uplinked to the satellites and link pointing based on the differential wavefront sensor in the SST instrument. The latter solution was found to yield the best performance. Since the DWS data are only available after the lasers on the two spacecraft have locked to each other the use of the DWS must be augmented by an acquisition procedure using other information. This acquisition procedure has been successfully established based on pointing predictions generated on ground. Due to its superior performance the use of the DWS will be considered as the baseline for the attitude determination in the science mode.

Potential interference between attitude and orbit control

The above discussion has not considered the potential interference between attitude control and orbit control. However in order to maintain link pointing throughout the operations it will be essential that the orbit control does not impair the link pointing during science operations - or if unavoidable only leads to negligible outage times compared to the overall duration of science operations.

Two routes exist in order to avoid or at least minimise such interference:

- Temporal separation of (short) periods of orbit control from long period of science operations
- Separation in amplitude by ensuring that the effect of the orbit control on link pointing is small enough such that it does not affect the link pointing by the attitude control system

If the first option leads to the concept of episodic orbit control where the short orbit maintenance manoeuvres are interspersed into long periods of science operations without orbit manoeuvres. The second option leads to continuous orbit control applying a sufficiently small thrust to the spacecraft that does not disturb the pointing. As the baseline a drag compensation concept will be adopted. In this case the external disturbances along the drag compensation direction will be reduced. In the AOCS analysis the full disturbances by air drag are considered. Hence the performance demonstrated will also be achieved for the baseline with drag compensation.

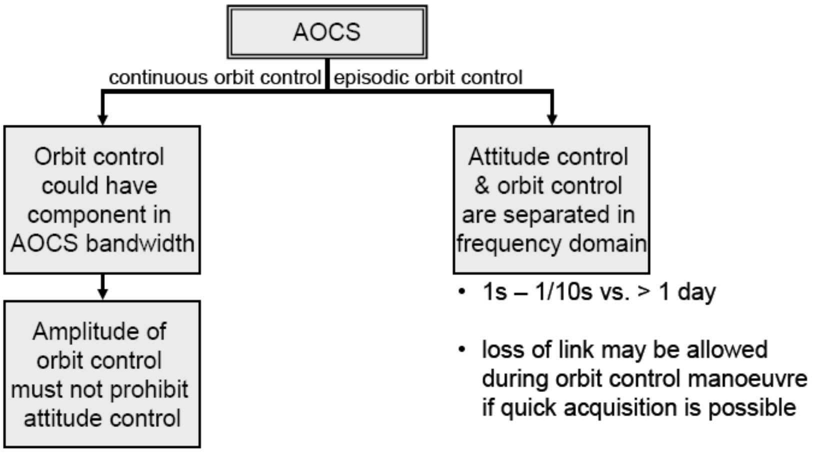

Figure 4-35: Options for avoiding interference between attitude control (link pointing) and orbit control (formation maintenance)

4.5.2 Definition of AOCS Modes

Earth oriented safe mode

The spacecraft is in Earth oriented safe mode after separation and de-spin, using the Coarse Earth and Sun Sensor (CESS) for attitude determination. The aim is to maintain coarse earth pointing as well as S/C X-axis in flight direction (LVLH).

Initial acquisition mode

The spacecraft switches into the initial acquisition mode after completion of the Earth oriented safe mode. The star trackers as well as GPS receivers will be switched-on and calibrations will be carried out with ground support. Meanwhile, the dedicated acquisition sensor as well as the acquisition laser source will be switched-on and the initial acquisition will take place as described in section 4.5.1. This mode is a transition and fall-back mode.

Nominal mode / science mode

The spacecraft switches into the science mode (or nominal mode) after the laser link has been established. The LRI will be switched-on, where the DWS sensor will take over the attitude determination for pitch and yaw directions. The roll direction remains being determined from the star tracker. The accelerometer is switched-on and the drag-compensation system works with the acceleration measurements. Once the laser link is lost, the spacecraft will automatically switch back to the acquisition mode.

The attitude controls in different modes will be performed with the cold gas thrusters and magnetic torquers.

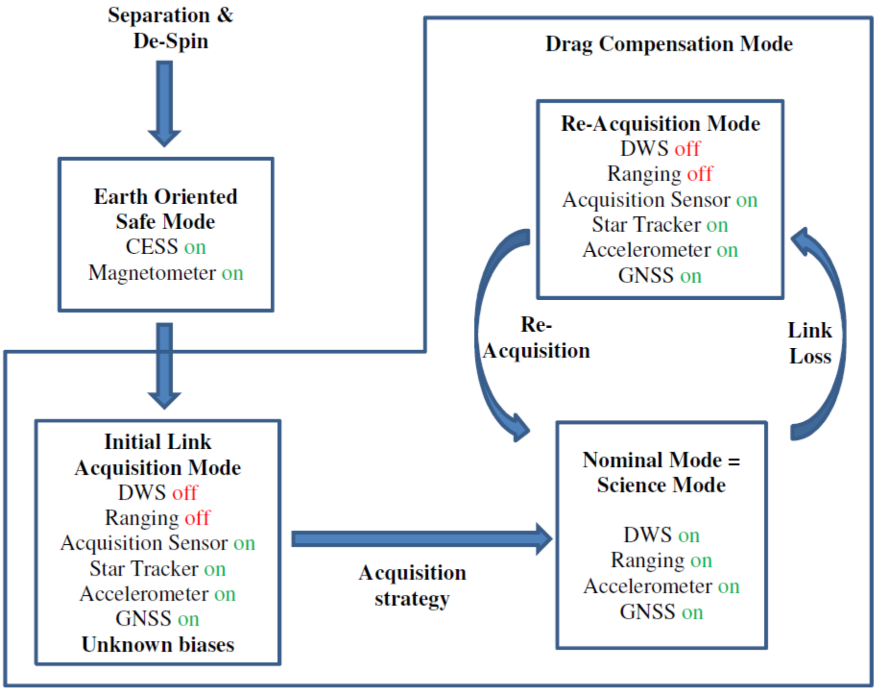

Figure 4-36: AOCD modes

4.5.3 Preliminary AOCS Performance Analysis

Simulations have been carried out at STI in order to preliminarily assess AOCS performance concerning pointing and drag-compensation. The simulations cover the science mode only, where, besides the star tracker, the DWS signal is available for attitude determination of the pitch and yaw axes. Table 4-12lists the sensor performance parameters that have been assumed. The DWS is modeled as a nearly perfect sensor, whereas the bias and noise value of the star tracker are taken from the units used on the CHAMP and GRACE missions.

Table 4-12: Sensor parameters used for the simulations

Sensor	Bias (1 σ)	Noise (1 σ)	Dead band	Respective altitude axes
DWS	0 µrad	1 µrad	10 µrad	Pitch, Yaw
Star Tracker	300 µrad	240 µrad	500 µrad	Roll

The only AOCS actuators in the simulations are cold gas thrusters that operate in a quasi-linear manner, called Pulse-Width Modulated mode (PWM). While linear thrusters can fire continuously with various thrust levels, PWM thrusters feature only one nominal thrust level. However, it is possible to vary the pulse duration within the time window that is defined by the inverse update frequency of the thruster. For example, assuming a update frequency of 1 Hz, a requested thrust of 100 µN would cause a linear thruster to fire one second with a thrust of 100 µN. The PWM thruster with a nominal thrust of 400µN, however, fires only 250 ms with its nominal thrust, thereby applying the same impulse bit to the spacecraft. Considering a mission lifetime of 11 years and one thruster cycle each second, a thruster that can cope with at least 350 Million cycles is required. Advanced Space Technologies in Bremen and STI have been currently developing and space qualifying new cold gas thrusters, where a lifetime of at least 700 Million cycles were proven in an accelerated wear test. Moreover the thruster response time is less than 1 ms resulting in a minimal openning time of 10 ms. Theoretically a shorter minimal open time is possible, but may result in an irregular gas flow that decreases the I_{sp}.

The SCs are differently modelled in the simulations. The leading satellite is modelled as a point mass which only experiences gravitational forces, therefore flying perfectly drag-free. The second satellite features the proposed e^2.motion configuration and is exposed to air drag and solar pressure. The atmospheric environment is modelled with JB2006. The used atmospheric indices comply with the ECSS values for mean solar activity (F10.7 = 140, Ap = 15). The thruster configuration is based on the one used for GRACE and is extended to meet the requirement of drag-compensation in radial and out-of-plane directions. At the rear side of the spacecraft a cluster of PWM thrusters is accommodated. A cluster is mandatory, since the nominal thrust of each thruster has to be within the range of the accelerometer, while the maximum possible drag would exceed this thrust level. The simulation starts with the two satellites perfectly pointing at each other. During the simulation the following satellite must stay locked on the leading one. After initial oscillations, three orbits have been simulated and data have been recorded with a sampling frequency of 1 kHz.

It is to note that the analysis only serve as a preliminary assessment of the AOCS concept and is not optimized for e.g. fuel consumption. Similarly, the AOCS control loops are not optimized either. The optimization as well as a detailed design of the AOCS concept should be carried out in further project phases.

4.5.3.1 Pointing Performance Analysis

The requirements for pointing performance were described in section 4.2.2. Figure 4-37 shows the time series of the pointing error in pitch, yaw and roll in comparison with the peak value requirements. It can be seen that pointing errors remain below the requirements (100 µrad for pitch/yaw and 2 mrad for roll). Figure 4-38 shows the LSDs of the pointing errors in pitch, yaw and roll in comparison with the jitter requirements. Similarly, the pointing error LSDs stay below the jitter requirements, which are 100 µrad/√Hz*NSF for pitch/yaw and 2 mrad/√Hz*NSF for roll with the Noise Shape Function defined as NSF(f) = $\sqrt{1 + (\frac{10mHz}{f})^2}$. Attention should be paid that the simulations didn't cover all error sources (only major error sources were included) and thus the results should be considered as preliminary at this stage. The results of the analyses, however, do suggest that the impulse behaviour of the PWM cold gas thrusters should not cause specific problems (due to pulsed thrust) that would violate the pointing requirements. The PWM cold gas thrusters are therefore, in principle, considered to be suitable for the laser fine pointing for a e^2.motion.

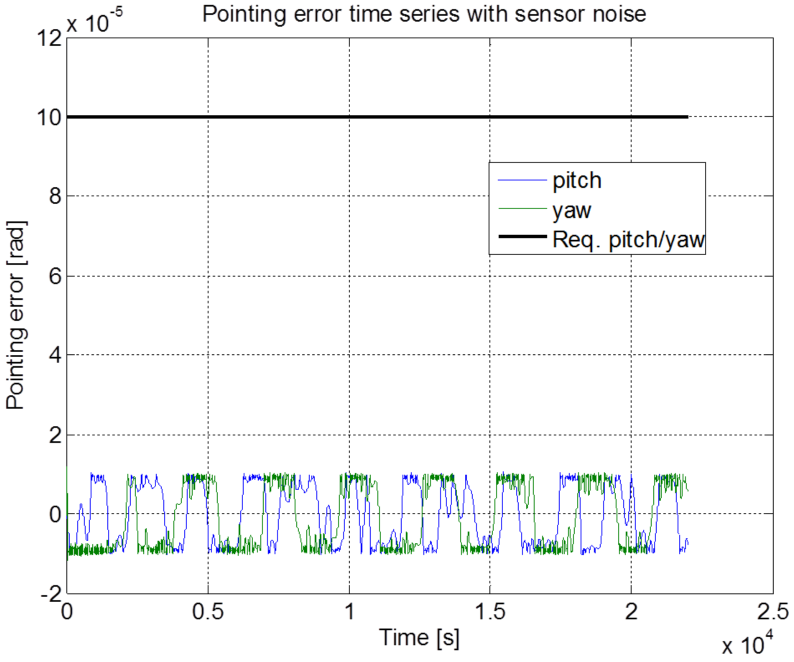

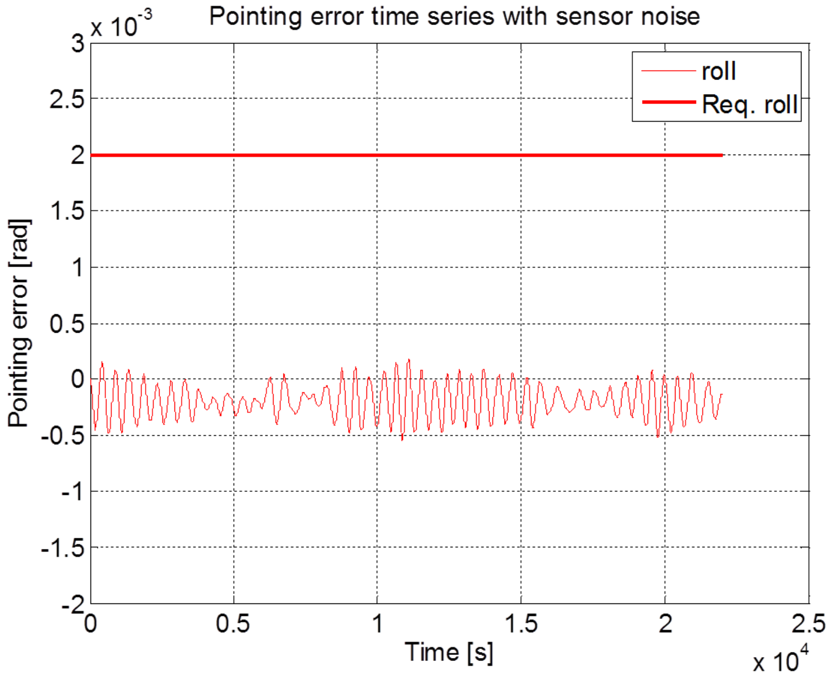

Figure 4-37: Time series of pointing error. Upper panel: pitch and yaw, lower panel: roll

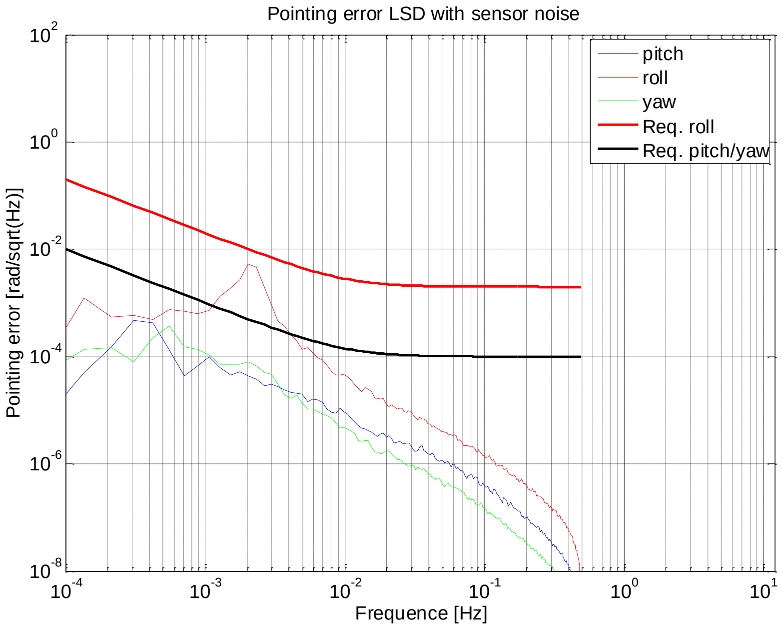

Figure 4-38: Pointing errors in comparison with the pointing jitter requirements

4.5.3.2 Drag-Compensation Analysis

A full drag-compensation scenario has been simulated to preliminarily assess the possibility of using the PWM cold gas thrusters for the drag control. As discussed in section 4.2.1, it is required to keep the accelerometer from being saturated. Figure 4-39 shows the simulated air drag accelerations in x, y and z directions, while Figure 4-40 shows the acceleration residuals in comparison with the saturation limit of 8e-6 m/s^2. The detailed behaviour of the drag-compensation is demonstrated in Figure 4-41, where the drags before and after compensation are plotted for a period of 10 s. It can be seen that the thrusters fire with a 1 Hz frequency. The thrust duration is modulated in such a way that it is attempted to control the integrated air drag over 1 second to 0. This is illustrated for the first period of 1 second, where the blue-dashed area and red-dashed area attempt to cancel each other.

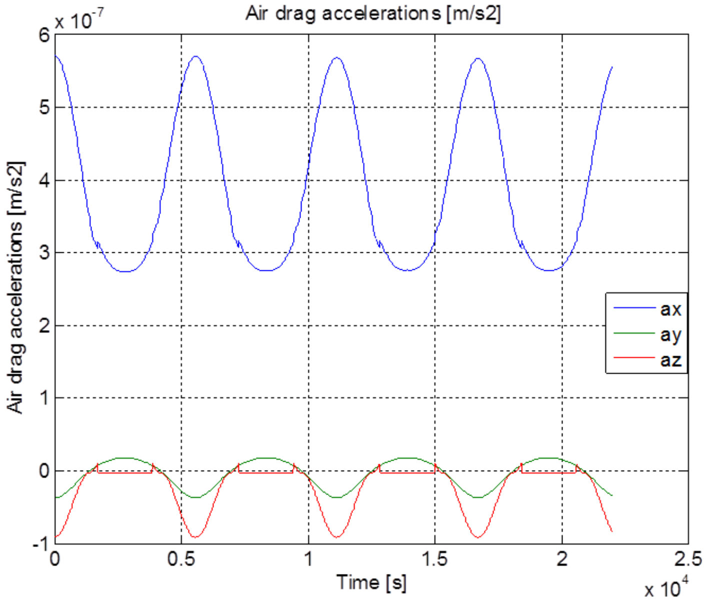

Figure 4-39: Simulated air drag accelerations for 420 km orbit height

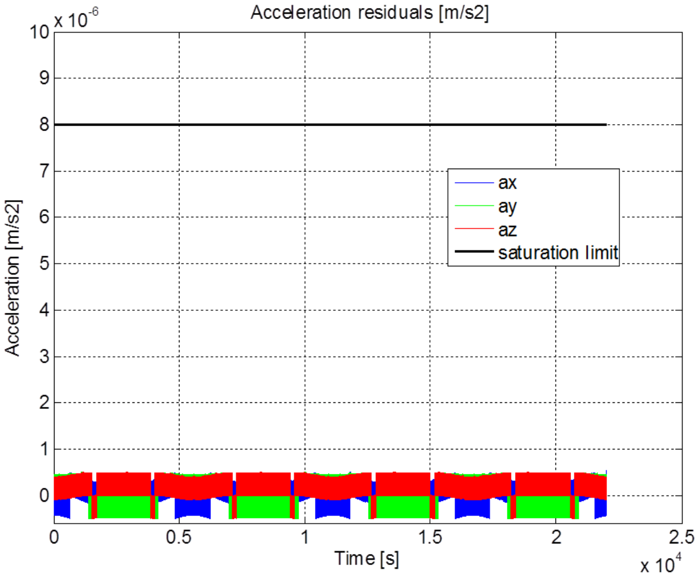

Figure 4-40: Acceleration residuals in comparison with the saturation limit

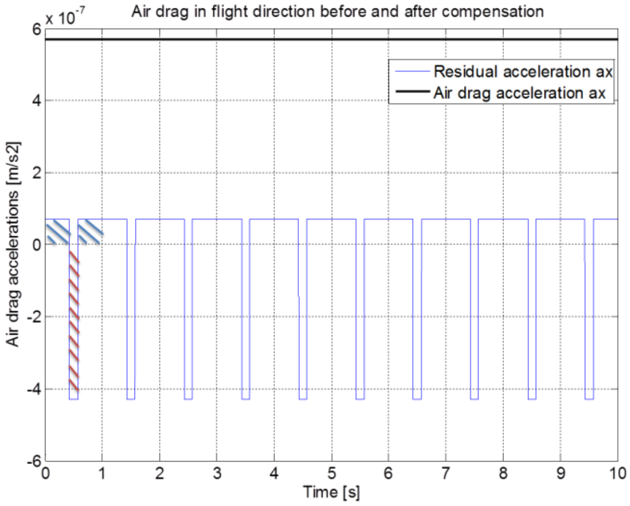

Figure 4-41: Behavior of PWM cold gas thruster for drag-compensation. Plotted are air drag accelerations before and after compensation for the x direction.

Since there is no PSD requirement defined for the residual drags for the e^2.motion mission, a PSD requirement from [10] has been selected, which defined the stability of the linear accelerations. Taking into account that [10] proposed to use an accelerometer assembly consisting of 4 accelerometers and considered in general a more challenging requirement on the accuracy (1.5 - 5e-12 m/s2) than the e^2.motion mission, this PSD requirement can be seen as a strict reference requirement. The requirement is illustrated in Figure 4-42 (black curve), where the air drags without and with drag-compensation are plotted for x, y, z directions. While it is debatable if such a strict requirement is necessary for the NGGDM-D project, the effect of drag-compensation is clearly visible. The drag-compensation suppressed the amplitude of the air drag accelerations so that their LSDs stay below the TAS requirement in the measurement bandwidth of [1 mHz, 100 mHz]. It is also notable that peaks appear at multiple of 1 Hz with relatively high amplitudes. However, these peaks are located fairly outside the science measurement bandwidth so that it encourages making an assumption that they would not lead to degradation of the scientific performance. Currently this assumption has not been proven yet and it should be clarified in further project phases.

In general it can be stated that the proposed drag-compensation concept with PWM cold gas system is preliminarily considered to be suitable for the e^2.motion mission.

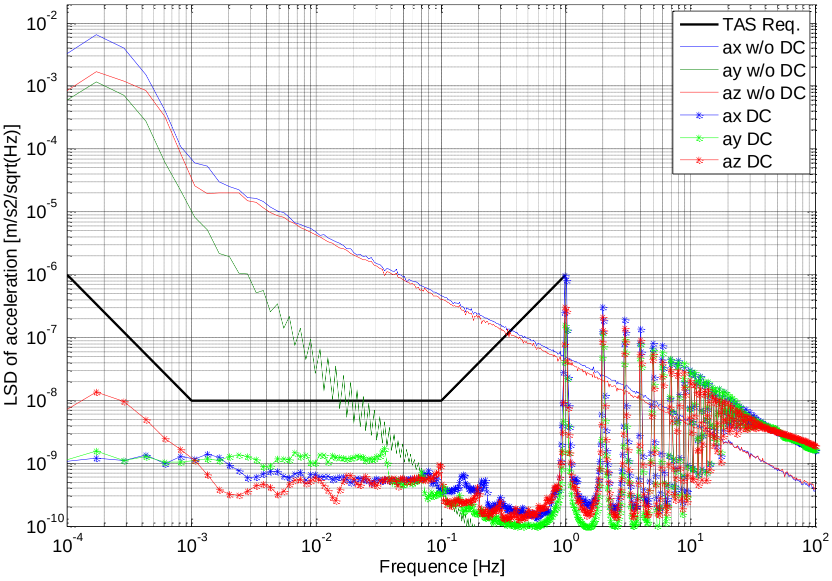

Figure 4-42: LSDs of the accelerations without drag-compensation (w/o DC) and with drag-compensation (DC) in comparison with the TAS requirement as stated in [10]

4.6 Preliminary AOCS Instrumental Concept

Based on the information from ASG and considering the required lifetime of 11 years, some recommended AOCS instruments are briefly summarized in Table 4-13. Attention should be paid that at this stage of the project, the requirements for the individual instruments have not been analyzed in details and thus the selection of the hardware is not fixed. It is more appropriate to understand the table below as a collection of information rather than a fixed instrument concept. The latter should be developed and optimized with in-depth analyses in further project phases.

Table 4-13: List of selected AOCS instruments

Unit	Name	Manufacturer	Mass (kg)	Power (W)	Key performance	Flight heritage	Lifetime (years)
Star tracker	Hydra	Sodern	1.37 (OH) 1.85 (EU)	11 W (1 EU + 3 OH)*	See HYDRA CMOS Star Tracker Product Information	Spot-6	10
GPS receiver	Mosaic	Airbus DS	3,9	10	Accuracy < 10m	Since 2006	15
Magnetometer	FGM Analogue	ZARM	0,25	<1	Range = ± 64 µT, Accuracy < ± 1 %	Many	> 11**
Magnetorquer	MT-140-2	ZARM	5,3	1,9	140 Am²	Many	> 7
Safe-mode sensor	Advanced-CESS	STI	Ca. 70 g	-	Earth-vector error peak value ca. 9.4°	Many***	7
Cold gas thruster	PWM cold gas propulsion system	AST	45 g per thruster	3.5 W pull, 0.5 W hold	thrust range: 400 µN - 8 mN; response time: <1 ms; resolution: 1 µN	Formosat 5, launch in 2015	12

* OH = optical head, EU = Electronic Units

** estimated based on radiation tolerance of 50 krad

*** Advanced-CESS is based on CESS from Airbus DS. Performance improvements have been demonstrated with improved algorithm and hardware developed at STI.

5 Instrument Concept

5.1 Introduction

The aim of the e^2.motion satellite gravimetry mission is the measurement of Earth's gravitational field and its temporal and spatial variations. Different concepts exist to determine Earth's gravity field by remote satellite sensing. In this study a GRACE-like configuration was selected as baseline, which is described in the following as "single axis long baseline gradiometer". The design of the payload is based on experience from GOCE, GRACE and GRACE Follow-On.

Based on analysis in the previous chapters a Bender configuration consisting of two identical satellite pairs, each equipped with a ranging link forming a single axis long baseline gradiometer, has been selected. The orbit parameters are:

- Pair 1: ~420 km orbit height, incl. 89.5°, spacecraft separation: 100 km, in-line formation (no pendulum)
- Pair 2: ~430 km orbit height, incl. 70.0°, spacecraft separation: 100 km, in-line formation (no pendulum)

The mission duration shall be 11 years. A fallback option is the use of only one polar satellite pair.

5.1.1 Measurement Principle: Single Axis Long Baseline Gradiometer

The e^2.motion measurement principle is based on a high-low and low-low satellite-to-satellite tracking (SST) approach, which utilizes a single axis long baseline gradiometer. This means, the differential (pure) gravitational acceleration is measured along the connection line of the satellites (LOS, line of sight) with a baseline length according to the spacecraft separation. The high-low SST is established by means of Global Navigation Satellite Systems (GNSS).

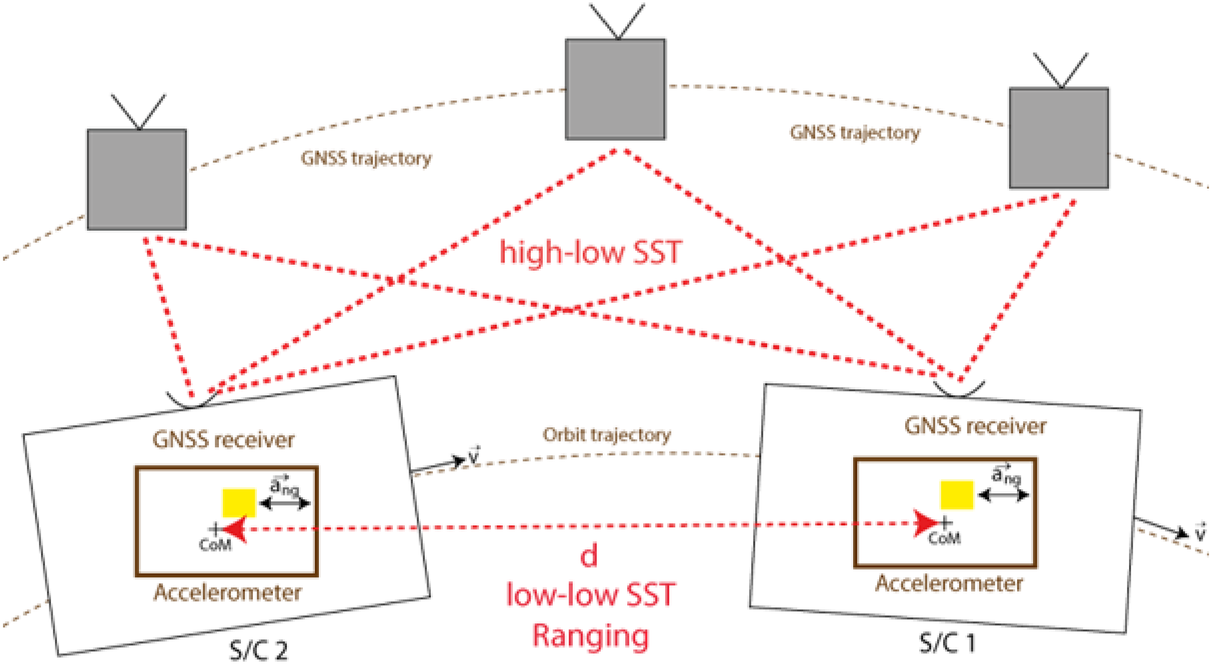

Figure 5-1: Measurement principle of a single e^2.motion pair. Ranging provides the distance (variations) between center of mass (CoM) of S/C 1 to the center of mass (CoM) of S/C 2. The accelerometer measure the non-gravitational accelerations of a test mass within each satellite.

The information about Earth's gravitational field is encoded in the satellite range (distance), which contains gravitational and non-gravitational contributions. Accelerometer on-board of each satellite measure the non-gravitational contributions, such that combination of ranging information and accelerometer data yields pure gravitational acceleration along the LOS.

The differential gravitational acceleration Δa_g between the two satellites can be written in a co-rotating frame as

$$\Delta a_g(t) = \ddot{\rho}(t) - a_{ng,x,1}(t) - a_{ng,x,2}(t) \tag{5-1}$$

where $a_{\mathrm{ng},x,1}$ and $a_{\mathrm{ng},x,2}$ are the non-gravitational accelerations along the LOS, as measured by the accelerometer, and $\ddot{\rho}$ is the second time derivative of the S/C to S/C distance, as measured by the ranging instrument. The differential gravitational acceleration Δa_g is a function of the two satellite positions and time, as well as of the underlying Earth gravity field. Since the satellite positions and time are known from high-low SST, the gravity field can be deduced from these measurement.

5.1.2 Earth's Gravity Field Signature

Earth's gravity field is usually expressed as spherical harmonic expansion of the potential V, which has the form:

$$V(r,\theta,\lambda) = \frac{GM}{R}\sum_{l=0}^{l_{max}}\sum_{m=0}^{l}\left(\frac{R}{r}\right)^{l+1}\cdot P_{lm}(\sin\theta)\cdot\left(C_{lm}\cdot\cos m\lambda + S_{lm}\cdot\sin m\lambda\right) \tag{5-2}$$

where (r,θ,λ) are the spherical coordinates of the point, where the potential is evaluated. For simplicity we assume a static gravity field.

The differential gravitational acceleration Δa_g between the satellites in an inertial frame is given by:

$$\Delta a_g(t) = \left(\nabla V\left(\vec{P}_1(t)\right) - \nabla\left(\vec{P}_2(t)\right)\right)\cdot\vec{l}(t) \tag{5-3}$$

where $\vec{l}$ is the LOS direction and $\vec{P}_1(t), \vec{P}_2(t)$ are the trajectories of S/C 1 and 2, respectively. Earth's gravity field signature within the single axis gradiometer can be written in a Fourier series as:

$$\Delta a_g(t) = \sum_{l=0}^{l_{max}}\sum_{m=0}^{+1}\sum_{q=0}^{q_{lmq}}\left(C_{lm}\cdot c_{lmq}\cdot\sin\left(2\pi\cdot f_{lmq}\cdot t + \alpha_{lmq}\right) + S_{lm}\cdot s_{lmq}\cdot\sin\left(2\pi\cdot g_{lmq}\cdot t + \beta_{lmq}\right)\right) \tag{5-4}$$

which means each spherical harmonic coefficient C_{lm} and S_{lm} produces a comb of sinusoidal signals in the differential gravitational acceleration (see Figure 5-2). The amplitudes (c_{lmq}, s_{lmq}), frequencies (f_{lmq}, g_{lmq}) and phases $(\alpha_{lmq}, \beta_{lmq})$ depend on the orbits of the satellites, which are measured by GNSS.

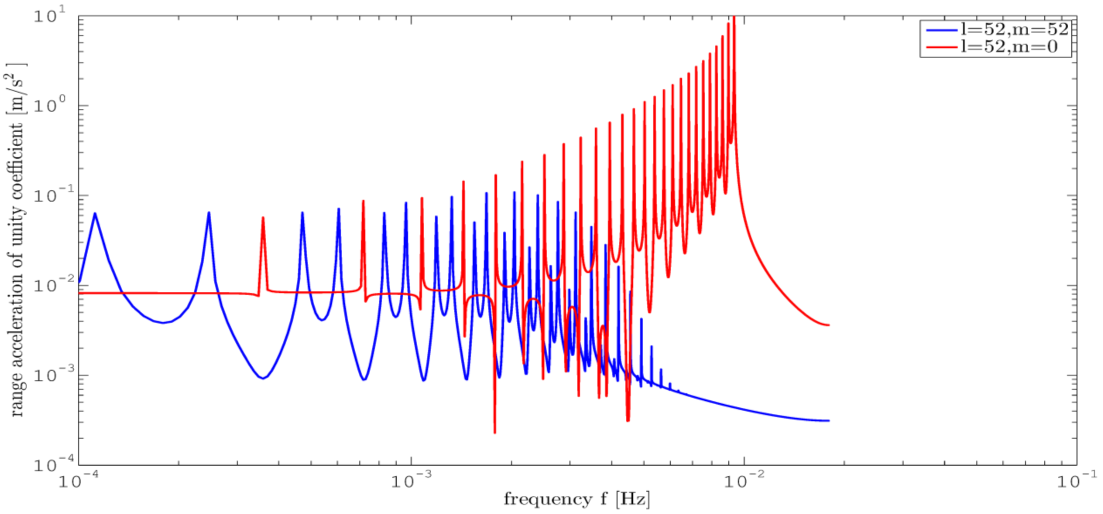

Figure 5-2: Effect of single coefficients of degree 52 with unit magnitude on the differential gravitational acceleration between two satellites for a polar e^2.motion pair (L = 100 km, incl. = 89.5°, h = 420 km). The final measurement consists of a superposition of ten-thousands coefficients.

For a sufficiently long time-series $\Delta a_g(t)$ the effect of each spherical harmonic coefficient C_{lm} and S_{lm} of the geopotential can be separated and the amplitude of each coefficient can be fitted, for example in a least-squares sense.

5.1.3 Instrument Sensitivity

The main scientific measurement in e^2.motion is the differential gravitational acceleration along the LOS $\Delta a_g(t)$. As in all physical measurements stochastic noise sources are present, which limit the sensitivity of the measurement. The sensitivity is usually measured in terms of power spectral densities (PSD) or amplitude spectral densities (ASD=√PSD). We can assume that the stochastic noise sources within the accelerometer and the ranging instrument are uncorrelated, such that the noise of the single-axis long baseline gradiometer is given by:

$$\mathrm{ASD}[\Delta a_g](f) = \sqrt{2\cdot \mathrm{ASD}[\mathrm{ACC}_x]^2(f) + (2\pi f)^2 \cdot \mathrm{ASD}[\rho]^2(f)}\ \left[\frac{\mathrm{m}}{\mathrm{s}^2\sqrt{\mathrm{Hz}}}\right] \qquad (5\text{-}5)$$

where $ASD[ACC_x]$ is the noise amplitude spectral density of one accelerometer in LOS direction with units of $\frac{\mathrm{m}}{\mathrm{s}^2\cdot\sqrt{\mathrm{Hz}}}$ and $ASD[\rho]$ is the noise amplitude spectral density of the ranging instrument (single path) with units $\frac{\mathrm{m}}{\sqrt{\mathrm{Hz}}}$.

The measurement of non-gravitational accelerations shall be performed with a noise level of:

$$\mathrm{ASD}[\mathrm{ACC}_x] = 4\cdot 10^{-11}\,\frac{\mathrm{m}}{\mathrm{s}^2\sqrt{\mathrm{Hz}}}\cdot\sqrt{\left(\frac{1\mathrm{mHz}}{f}\right)^4 + 1 + \left(\frac{f}{0.1\mathrm{Hz}}\right)^4} \qquad (5\text{-}6)$$

for frequencies between 0.1 mHz up to 0.3 Hz, while the ranging performance requirement is:

$$\begin{aligned} \mathrm{ASD}[\rho] &= 25\frac{\mathrm{nm}}{\sqrt{\mathrm{Hz}}}\cdot\sqrt{\left(\frac{10\mathrm{mHz}}{f}\right)^2 + 1}, \qquad 0.1\mathrm{mHz} < f < 0.1\mathrm{Hz} \\ \mathrm{ASD}[\rho] &= 25\frac{\mathrm{nm}}{\sqrt{\mathrm{Hz}}}\cdot\sqrt{\left(\frac{0.1\mathrm{mHz}}{f}\right)^4}, \qquad 0.1\mathrm{Hz} < f < 0.3\mathrm{Hz} \end{aligned} \qquad (5\text{-}7)$$

Equation (5-5)provides the top-level requirement of the single axis long baseline gradiometer based on sub-allocations ((5-6) and (5-7)) for the instruments and is expressed as an acceleration amplitude spectral density. The noise levels have been defined in an iterative process, such that the science requirements can be met under consideration of technical feasibility. As one can see in Figure 5-3, the accelerometer is limiting the sensitivity of the single-axis gradiometer link for frequencies below 7 mHz, which has contributions for SH coefficients up to degree ~35, while higher frequencies are limited by the noise of the ranging instrument. Detailed analysis of the instruments and justification of the instrument allocations is provided in subsequent sections.

The frequency band between 0.2 mHz and ~30 mHz is of special interest, since it contains the signal information for the SH coefficients up to degree ~150.

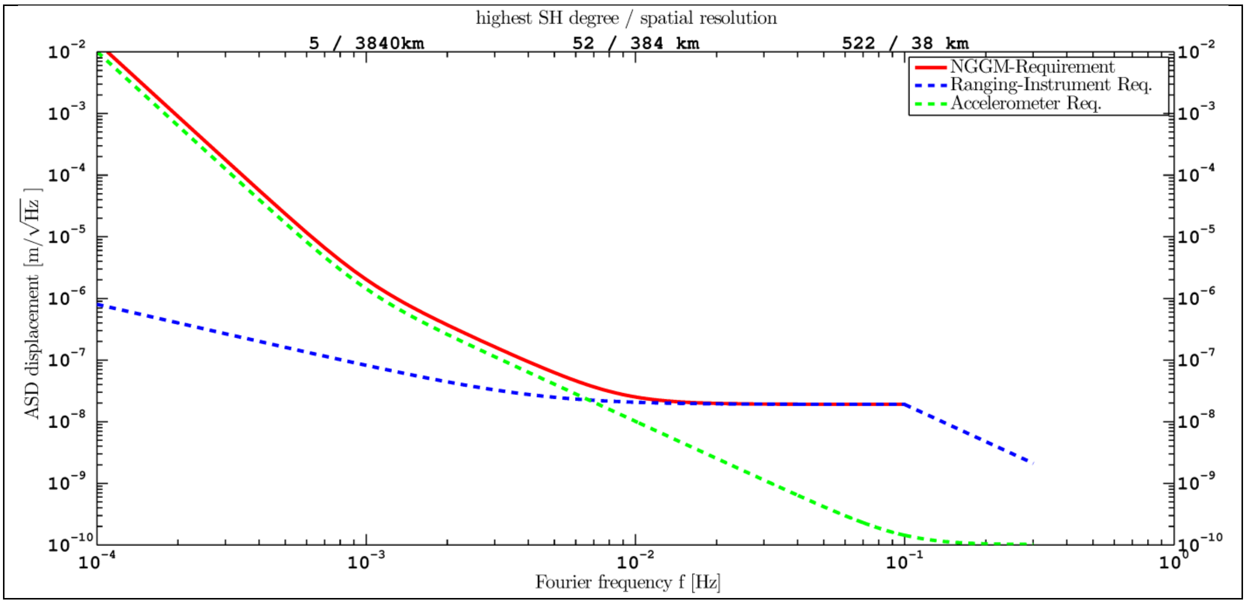

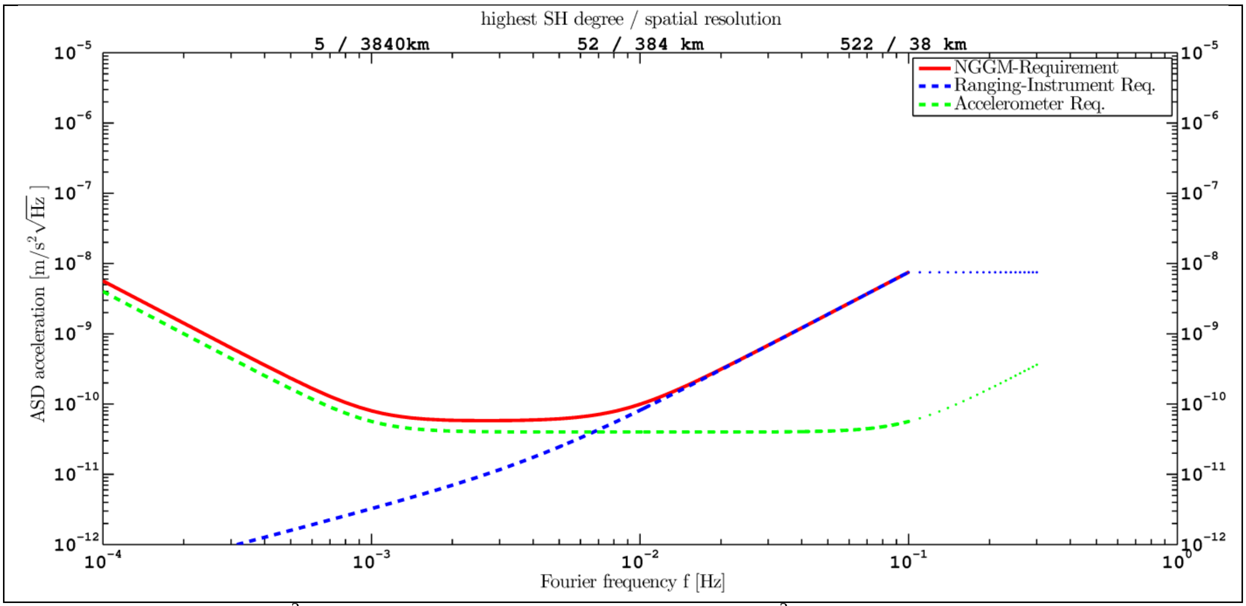

Figure 5-3: Top-level e^2.motion sensitivity requirement for a single e^2.motion pair. Upper plot shows the requirement in the displacement domain (range), while lower plot shows the requirements in the acceleration (range acceleration) domain.

5.1.4 Frequency Bands

The scientific measurement band, which contains the signal of spherical harmonic coefficients of degrees 2…520 and where the single-axis long baseline gradiometer shall perform measurements, is defined as

Science Measurement Band: $0.18\ \text{mHz} < f < 0.1\ \text{Hz}$.

An additional calibration band is defined as

Calibration Band: $0.1\ \text{Hz} < f < 0.3\ \text{Hz}$,

where the accelerometer is calibrated with the LRI using the drag compensation loop. For further details it is referred to section 5.2.4.

Higher frequencies (1 Hz to 50 Hz) will show a comb of thruster peaks, which are caused by the pulse-width-modulation scheme. It is currently not planned to record this frequencies.

5.1.5 Instrument Tone Errors

In addition to stochastic noise sources, which are described by spectral densities, deterministic (sinusoidal) errors also appear in measurements. These errors are called tone errors and are driven by periodic perturbations at the satellites, e.g. by

- Temperature variations due to regular transitions from sun illuminated to shadow regions
- Magnetic field variations (geomagnetism).

These errors appear mainly at integer multiples of the orbit frequency (1/rev, 2/rev, …) and cannot be described with spectral densities, since the amplitude of the peaks is dependent on the integration time. In addition tone errors mimic the same behaviour as (zonal) spherical harmonic coefficients in the differential gravitational acceleration measurement.

To ensure that the baseline sensitivity for gravity field determination is met, it is necessary to set properly tone requirements for the single axis of the long baseline gradiometer and to flow-down these requirements onto instrument level (see also section 6.4.2.1).

An error model in the time-domain is given by

$$e\left[\Delta a_g\right](t)=\sum_{i=1}^{\dots} a_i \cdot \sin\left(2\pi f_{orb} t \cdot i+\delta_i\right) \tag{5-8}$$

where a_i are the tone amplitudes in units of m/s² and δ_i are phases of the tone errors. The effect of tones on the inter-satellite acceleration (or range) mimics the effect of some spherical harmonics coefficients. As pointed out in section 6.4.2.1, tone errors affect mainly low-degree coefficients as expected for low-frequency tones. Requirements have been derived based on simplified (quick-look tool) simulations and on the assumption that tone errors shall contribute less than 10% total geoid error.

The requirements given in chapter 6.4.2.1 are very tight and difficult to fulfill, especially for the accelerometer. We assumed here a relaxation by a factor of 5 of the values given in section 6.4.2.1, since the first full-scale simulations indicated that the errors in gravity field retrieval are dominated by far by background model errors (like ocean and atmosphere) and not by instrument noise.

We note that the single-axis long-baseline gradiometer (GRACE like low-low SST) does not allow proper recovery of some low-degree SH coefficients due to tone errors. However, these coefficients are usually accessible via pure orbit observations or by other means. Therefore it might be beneficial to exclude these coefficients from benchmarks, if these single coefficients become driving factors.

The e^2.motion tone requirements for the first six tones (6x orbit frequency) are shown in Figure 5-4. For example, the permissible tone error at twice per orbit frequency is $101 \cdot 10^{-12}$ m/s² or equivalently 20 µm in half-way round-trip ranging. This value is divided into an accelerometer error of $25.5 \cdot 10^{-22}$ m/s² per spacecraft and a ranging error of 10 µm (half-round trip or single way).

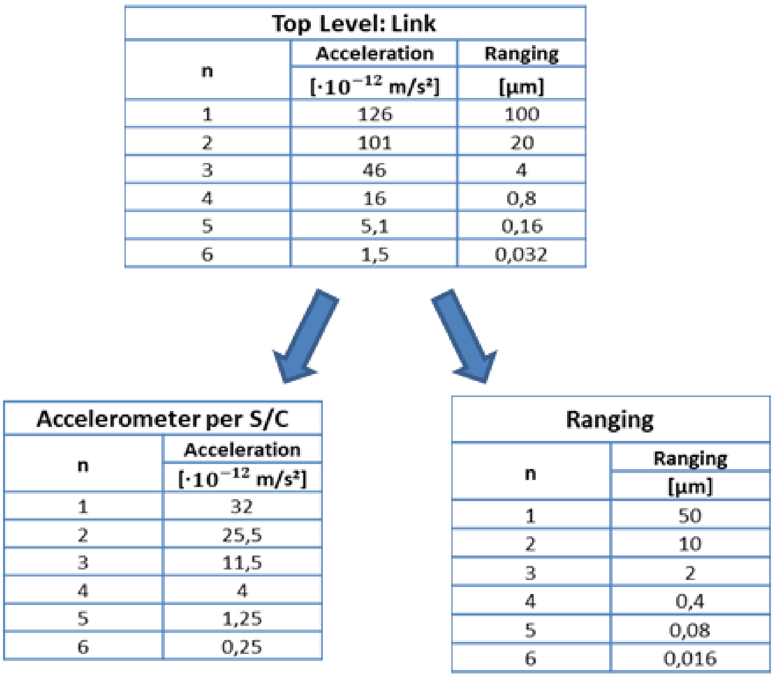

Top Level: Link

n	Acceleration [$\cdot 10^{-12}$ m/s²]	Ranging [µm]
1	126	100
2	101	20
3	46	4
4	16	0,8
5	5,1	0,16
6	1,5	0,032

Accelerometer per S/C

n	Acceleration [$\cdot 10^{-12}$ m/s²]
1	32
2	25,5
3	11,5
4	4
5	1,25
6	0,25

Ranging

n	Ranging [µm]
1	50
2	10
3	2
4	0,4
5	0,08
6	0,016

Figure 5-4: e^2.motion requirement of tone amplitudes (zero-peak) for the single-axis gradiometer link (top) and break-down onto instrument level (bottom). 'n' indicates the integer multiple of the orbit frequency. Numbers relaxed by factor 5 as specified in section 6.4.2.1.

5.2 Satellite and AOCS Concept

The satellite concept shall ensure that the required sensitivity of the differential gravitational acceleration measurement can be met. This requires that the environmental conditions for the accelerometer and the ranging instruments are within certain boundaries, namely,

- Ranging instrument: satellite pointing accuracy and precision sufficient, relative satellite velocity is smaller than threshold.
- Accelerometer: Non-gravitational accelerations are sufficient small to avoid saturation and avoidance of aliasing.

In addition orbital decay due to residual atmospheric drag should be avoided, such that no deficiencies in gravity field recovery appear due to resonances or short ground-track repeat cycles.

In order to meet these requirements a dedicated AOCS concept needs to be developed and implemented. Details for this are shown in chapter 4. Here some items of the AOCS concept, which have impact on the instruments and their performance are repeated and summarized again.

5.2.1 Drag Compensation

Drag compensation is required in e^2.motion to avoid orbital decay. Different concepts for the implementation exists (see Table 5-1), which are

- DC compensation: Only the average (DC) drag force is compensated by applying a constant thrust. The DC drag force can be computed in-orbit or on-ground from orbit determination, which might include also ranging information to keep the satellite distance within a nominal range. The accelerometer data is in general less accurate at very low frequencies and biased, which would lead to a continuous drift of the satellites.
- DC+MBW compensation: In addition to the DC compensation, the on-board accelerometer measurements are fed into AOCS and are used to suppress the fluctuations of the drag forces within the measurement bandwidth (MBW).
- Drag Free: This concept does not use electro-static actuation of a proof mass within the measurement band, but only capacitive sensing of the proof mass position. The proof mass motion is free-falling within the accelerometer housing, which means it is influenced only by gravitational forces and not by electro-static or drag forces. The satellite acts as a shield for non-gravitational forces. Usually only a few degrees of freedom can be kept free-falling, while the others need to be controlled e.g. by electro-static actuation. Accelerometers in a drag-free concept are often called “Inertial Sensors”.

The difference between drag free and DC+MBW drag compensation is the control of the accelerometer proof mass. Former one has no electro-static actuation within the MBW and requires that the satellite AOCS is capable to keep the free-falling proof mass centered within the housing. An ideal drag compensation with infinite gain and without sensor noise cannot be distinguished physically from a drag free system. The feasibility of such a concept in a noisy Low-Earth Orbit (LEO) has not been shown yet. As the analysis in the following sections will show, e^2.motion can reach the required sensitivity for the measurement of non-gravitational accelerations with DC+MBW drag compensation. Therefore, it has been selected as baseline.

Table 5-1: Trade-off analysis between different drag compensation concepts for e^2.motion like missions

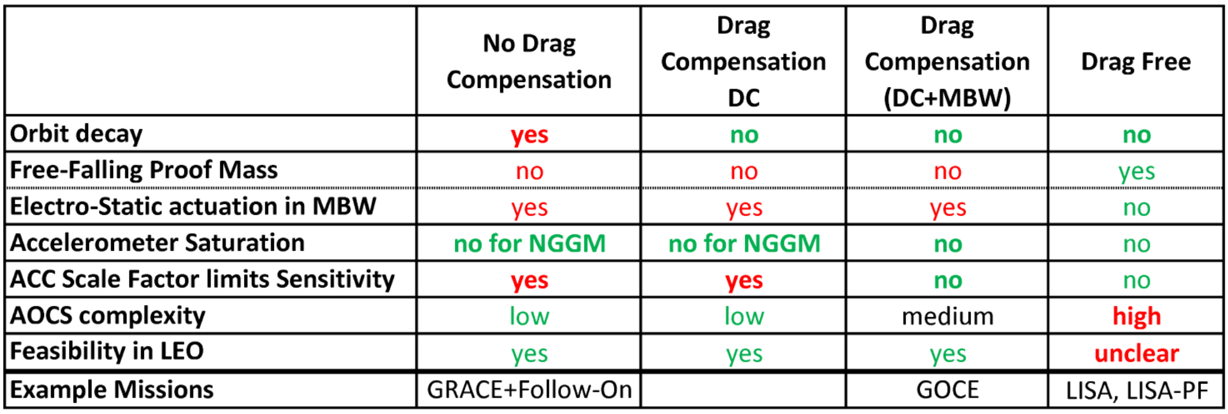

	No Drag Compensation	**Drag Compensation DC**	**Drag Compensation (DC+MBW)**	**Drag Free**
Orbit decay	**yes**	**no**	**no**	**no**
Free-Falling Proof Mass	no	no	no	yes
Electro-Static actuation in MBW	yes	yes	yes	no
Accelerometer Saturation	**no for NGGM**	**no for NGGM**	**no**	no
ACC Scale Factor limits Sensitivity	**yes**	**yes**	**no**	no
AOCS complexity	low	low	medium	**high**
Feasibility in LEO	yes	yes	yes	**unclear**
Example Missions	GRACE+Follow-On		GOCE	LISA, LISA-PF

5.2.1.1 Accelerometer Saturation

Due to the limited dynamic range of the accelerometer measurements (zero-peak amplitude: $4 \cdot 10^{-6}$ m/s^2) the necessity for drag compensation needs to be assessed. The measured peak values of non-gravitational accelerations should stay within the dynamic range of the accelerometer for most of the time.

The analysis was performed by evaluating 11 years of GRACE accelerometer data. The along-track direction shows as expected the highest non-gravitational signals. The data has been scaled by a factor of 6 to account for the slightly lower orbit height and for an increased solar activity in e^2.motion. Figure 5-5 shows the minimum, maximum and mean value of accelerations within one day over the 11 year period. Except for some single days, the maximum and minimum values are within the dynamic range of the accelerometer. The exceptions can be explained by spurious spikes in the GRACE accelerometer data, which are several magnitudes higher than the continuous atmospheric drag. The physical origin of these spikes is not (fully) understood and appearance in future missions is likely to be suppressed by design improvements.

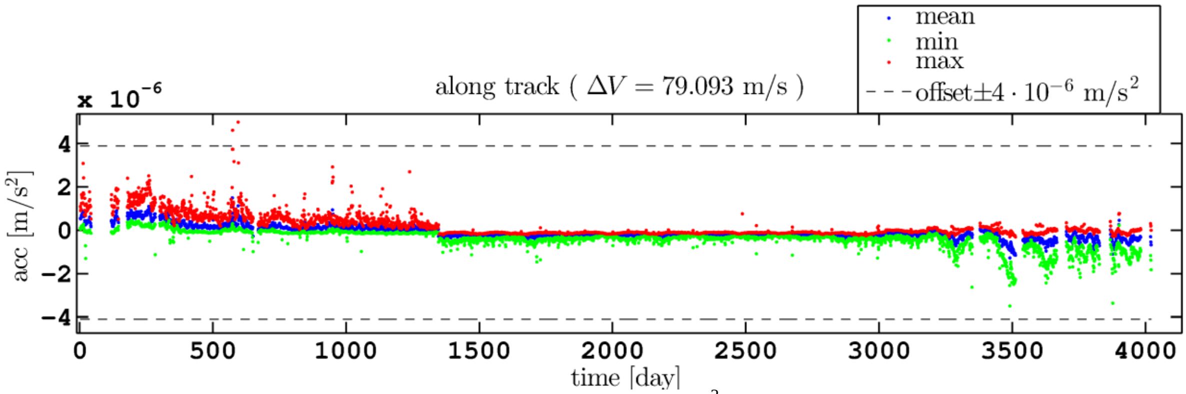

Figure 5-5: Assessment of non-gravitational accelerations for a e^2.motion satellite based on 11-year GRACE accelerometer data. Noisy periods at days >3300 can be explained by low battery capacity and reduced heater usage.

Based on analysis of real data, drag compensation is not required to avoid accelerometer saturation. It was also assessed using atmosphere model. The dynamic range of the accelerometer corresponds to a maximum allowable drag force of 3.2 mN for a satellite with 800 kg mass. The expected drag force during high solar activity was found to be below 0.65 mN. Although the number is referred to an orbit height of 450 km, it has still sufficient margin to remain below the limit for 420 km orbit height. In addition, the values provided by atmosphere models are mean values and can be avoided by simple DC compensation.

5.2.1.2 Accelerometer Scale Factor

The dynamic range of the accelerometer, which describes the saturation limit, provides an upper limit for the accelerometer signals in the time domain.

The scale factor knowledge of the accelerometer provides a limit on the maximum allowed signal height of the accelerometer in the frequency domain or in the measurement band. For e^2.motion a scale factor knowledge of 0.2% is assumed in the x-direction (line-of-sight). If the sensitivity or noise of the accelerometer measurement is denoted as spectral density $ASD[ACC_x]$ (see (5-6), the maximum allowed signal height is given by:

$$\mathrm{ASD}\left[s_{\max}\right](f) = \frac{1}{2} \cdot \frac{\mathrm{ASD}\left[\mathrm{ACC}_x\right](f)}{0.002} = 1 \cdot 10^{-8} \frac{\mathrm{m}}{\mathrm{s}^2\sqrt{\mathrm{Hz}}} \cdot \sqrt{\left(\frac{1\mathrm{mHz}}{f}\right)^4 + 1 + \left(\frac{f}{0.1\mathrm{Hz}}\right)^4} \qquad (5\text{-}9)$$

where $ASD[ACC_x]$ is the sensitivity from (5-6) and a ‘margin’ or safety factor of ½ was used.

5.2.1.3 Drag Compensation Requirements

Non-gravitational accelerations acting on the satellites in the line-of-sight direction (along track) are mainly induced by residual atmospheric drag. They shall be suppressed by the AOCS drag compensation system to a level defined by (5-9), which is shown in Figure 5-6.

For comparison GRACE accelerometer data is included in Figure 5-6 (black trace), which was magnified by a factor 10 to serve as worst case assumption for a slightly lower flying e^2.motion satellite. The dashed light blue trace is an upper limit on the maximum level of non-gravitational forces. The control bandwidth for the drag compensation is between 0.18 mHz (or orbit frequency) up to 30 mHz. For frequencies higher than 30 mHz the non-gravitational disturbance forces are so small such that no compensation is required.

The variations of non-gravitational accelerations in cross-track and radial direction are comparable in magnitude with the along track direction (DC offsets excluded). It is beneficial for later data analysis (e.g. transformation of accelerations from accelerometer frame to line-of-sight) to have also drag compensation in these axes, such that cross-coupling can be minimized.

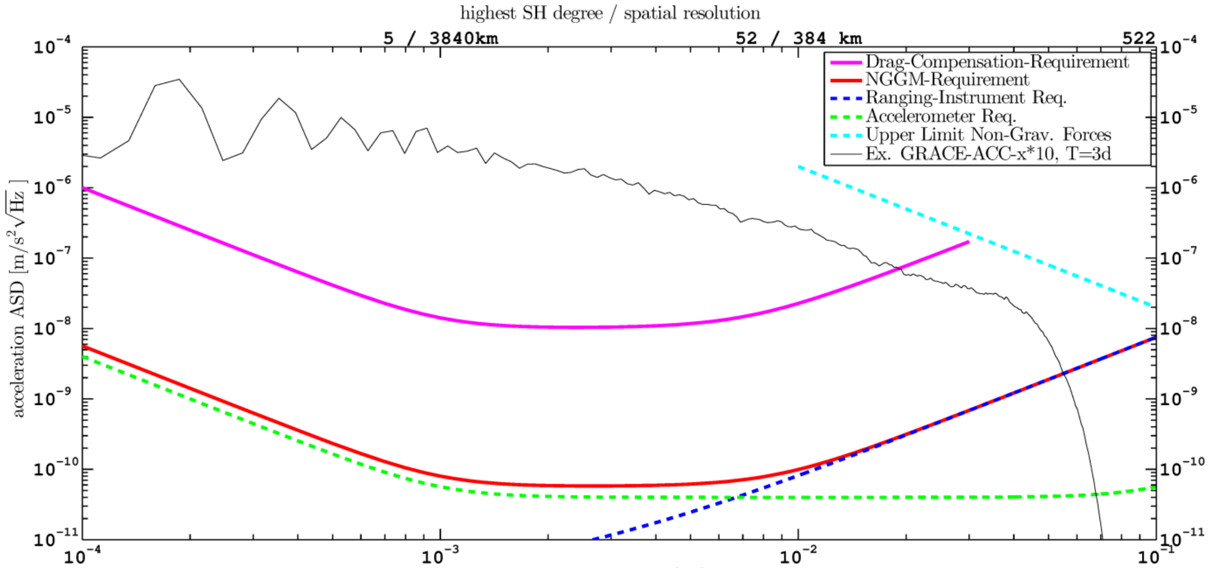

Figure 5-6: Drag compensation requirement (magenta) shown in comparison to the e^2.motion link requirements (red), consisting of accelerometer (dashed green) and ranging instrument (dashed blue). The light-blue trace shows the maximum (worst-case).

In addition the drag compensation shall ensure that the measured accelerations in the time-domain after low-pass filtering (with corner-frequency at 0.5 mHz) are smaller than

$$a_{\max,DC} = \pm 1 \cdot 10^{-8}\,\frac{m}{s^2} \tag{5-10}$$

in all three axes of the accelerometer. This requirement is necessary to suppress the effect of accelerometer scaling factor fluctuations within the measurement bandwidth.

5.2.2 Ranging Instrument Technology

The Ranging Instrument consists in the GRACE mission of a dual-way K/Ka microwave band ranging (KBR) system (sensitivity $\sim 10^{-6}\frac{\mathrm{m}}{\sqrt{\mathrm{Hz}}}$). The successor GRACE Follow-On mission (planned launch 2017) has a KBR and an additional Laser Interferometer as technical demonstrator.

Laser interferometry is a well-established technique for measuring small displacements on ground, e.g. ground-based gravitational wave detectors reach easily sensitivities of $10^{-16}\frac{\mathrm{m}}{\sqrt{\mathrm{Hz}}}$ at high frequencies (> 10 Hz). The space-based gravitational wave detector LISA based on laser interferometry has been studied since several decades and LISA Pathfinder (planned launch 2016) will demonstrate measurements with a displacement noise between two test masses on one satellite with $\sim 10^{-12}\frac{\mathrm{m}}{\sqrt{\mathrm{Hz}}}$ sensitivity in the mHz regime. The GRACE Follow-On Laser Ranging Interferometer (LRI) will show the applicability of this technique also for gravimetric inter-satellite ranging with an aimed sensitivity of $80 \cdot 10^{-9}\frac{\mathrm{m}}{\sqrt{\mathrm{Hz}}}$.

The advantage of Laser interferometry is the increased sensitivity due to the 10,000 times smaller wavelength. Additionally, it allows to retrieve very precise spacecraft attitude information w.r.t. the LOS with a technique called Differential Wavefront Sensing.

A disadvantage is that tighter satellite pointing is needed with current laser technology. However, since satellite pointing jitter is a major contributor to the overall noise of the differential gravitational acceleration measurement, a tighter control of satellite pointing using DWS is beneficial, anyway.

The baseline for e^2.motion foresees the use of a laser interferometer as primary ranging instrument.

5.2.3 AOCS Concept

The AOCS concept of e^2.motion is demanding, since it does not allow the traditional separation between payload and AOCS. In operational science mode a feedback control loop shall minimize the along-track non-gravitational accelerations as measured by the accelerometer to a level defined in sec. 5.2.1.3. Two nested feedback control loops shall minimize the yaw and pitch DWS signal of the LRI, such that the LRI interferometer axis of each satellite is pointing along the LOS. Most of the error signals shall be zeroed by the AOCS system, since a tight spacecraft pointing along the LOS increases the measurement sensitivity. An additional steering mirror within the LRI can be used if the gain of the AOCS loop is not sufficient.

The interferometer misalignment in yaw and pitch direction, as measured by the DWS signals, shall be kept smaller than

$$y_{max} = p_{max} = \pm 100 \mu rad \tag{5-11}$$

(4σ or maximum allowable peak value).

The S/C attitude in roll is controlled using conventional star-tracker information and has relaxed requirements of a permissible error of

$$r_{max} = \pm 2 mrad \tag{5-12}$$

(4σ or maximum allowable peak value).

The roll axis cannot be measured with the interferometer.

At least three star-tracker shall be used per spacecraft in hot redundant mode, to ensure operation even if two instruments are blinded by sun and moon.

Next to the maximum permissible pointing error there are spacecraft attitude jitter requirements to avoid degradation of the phase measurement sensitivity. These are defined for the science measurement band (see sec. 5.1.4) for the yaw (y), pitch (p) and roll (r) as

$$\begin{gathered} ASD[y](f) = ASD[p](f) = 100 \frac{\mu rad}{\sqrt{Hz}} \cdot \sqrt{\left(\frac{10mHz}{f}\right)^2 + 1} \\ ASD[r](f) = 1000 \frac{\mu rad}{\sqrt{Hz}} \cdot \sqrt{\left(\frac{10mHz}{f}\right)^2 + 1} \end{gathered} \tag{5-13}$$

For the calibration band between 0.1 and 0.3 Hz the requirements are tightened to

$$\begin{gathered} ASD[y](f) = ASD[p](f) = 10 \frac{\mu rad}{\sqrt{Hz}} \\ ASD[r](f) = 100 \frac{\mu rad}{\sqrt{Hz}} \end{gathered} \tag{5-14}$$

but are not considered challenging, since disturbances at these high frequencies are very low.

After orbit injection of the satellites, the on-board instruments have usually alignment biases in the order of a few milliradian, which are caused by the launch vibrations and settling effects. A crucial step is the first locking of the interferometer (acquiring signal), which requires that the interferometer optical axes of both satellites are pointing along the line-of-sight (LOS) without DWS signals. The line-of-sight is not known a-priori and needs to be estimated on-board using data and information from

- Star Cameras
- GNSS
- On-board orbit prediction (two-line elements including corrections).

Once a LoS estimation is available, the acquisition strategy shall provide autonomously interferometer lock and science mode. Therefore, the e^2.motion baseline foresees the use of a dedicated LRI acquisition sensor. It shall be located on the optical bench to avoid misalignments between LRI optical axis and acquisition sensor optical axis. The acquisition sensor provides yaw and pitch misalignment of the local satellite w.r.t. to the LOS. Further description of acquisition can be found in section 5.3.5.

5.2.4 Instrument Calibration and Validation

The main payload e^2.motion instruments are GNSS receiver, star cameras, accelerometer and interferometer. Many inter-dependencies and correlations exist between the measurements of these instruments, such that an integrated data analysis approach is required to minimize errors and uncertainties in the post-processed data and to achieve an unprecedented accuracy in the final gravity field retrieval. For example the satellite attitude is measured by star cameras w.r.t. inertial space, by the LRI w.r.t. to the line-of-sight and in terms of angular rates also potentially by the accelerometer. A proper sensor fusion and data analysis allows estimation of the precise attitude state, which can be used for corrections of interferometer (rotation-to-pathlength coupling, see section 5.3.7.2) and GNSS receiver (phase center offsets), and for the determination of the LOS non-gravitational accelerations.

A novelty in e^2.motion is the capability to calibrate the accelerometer measurements by the interferometer along the sensitive line-of-sight. This allows in particular measuring the accelerometer scaling factor (see section 5.4.5).

As pointed out in section 5.2.1 e^2.motion uses drag compensation (compensation of non-gravitational accelerations) of the average DC part as well as of the fluctuations within the science measurement band. The DC part of the non-gravitational acceleration along the line-of-sight is dominated by air drag. Precise predictions of the magnitude of the DC part are difficult due to dependency on solar and geomagnetic activity and on the underlying air density model. We assume an average DC drag for e^2.motion along the line-of-sight of 50 μN, which corresponds to an acceleration of $6.25 \cdot 10^{-8}$ m/s² for a e^2.motion S/C mass of 800 kg and to an integrated thruster action of $\Delta V = 21$ m/s over 11 year mission lifetime.

This non-gravitational acceleration can be compensated by continuous thrust or by periodic thrust varying sinusoidally between 0 μN and 100 μN with a mean value of 50 μN. The frequency of the sinusoidal thrust can be selected to be within the calibration band of 0.1 Hz to 0.3 Hz, such that signals in the science measurement band are unaffected.

The electronic injection of this calibration signal into the AOCS control loop can be implemented at several locations (e.g. between accelerometer and AOCS controller or between AOCS controller and thruster). The optimal solution has to be identified at later stages of the mission.

The calibration signal does not increase the propellant consumption, since it contributes to the DC drag compensation. However, the advantage of such a calibration signal is that it can be measured simultaneously by the accelerometer and by the interferometer. Within the calibration band the accelerometer has a measurement noise below 10^{-9} m/s²$/\sqrt{\text{Hz}}$ and the interferometer noise is below 10^{-8} m/s²$/\sqrt{\text{Hz}}$ as shown in Figure 5-3.

Since the interferometer scaling factor is well known (see section 5.3.7.5), the ratio of the measured amplitudes of the calibration signal C yields the scaling factor s_{ACC} of the accelerometer:

$$s_{\text{ACC}} = \frac{\text{LRI}[\text{C}]}{\text{ACC}[\text{C}]} \tag{5-15}$$

The sensitivity in the scaling factor measurement is dominated by the interferometer noise and can be computed by the inverse signal-to-noise density

$$\text{ASD}[s_{\text{ACC}}](f) \approx \frac{\text{ASD}[\text{LRI}]}{C_{\text{rms}}} = \frac{\text{ASD}[\text{LRI}]}{C_{\text{pk-pk}}} \cdot \sqrt{2} = \frac{10^{-8}\,\frac{\text{m/s}^2}{\sqrt{\text{Hz}}}}{6.25 \cdot 10^{-8}\,\text{m/s}^2} \cdot \sqrt{2} = 0.22 \cdot \frac{1}{\sqrt{\text{Hz}}} \tag{5-16}$$

If the accelerometer scaling factor would show fluctuations, they could be measured with such sensitivity. However, the overall e^2.motion accelerometer sensitivity requires knowledge or stability of the scaling factor to $\frac{10^{-3}}{\sqrt{\text{Hz}}} \cdot NSF(f)$ within the science measurement band, which is a separate requirement on the intrinsic stability of the accelerometer scale factor (see section 5.4.5).

Although fluctuations of the scaling factor (at short time scales) cannot be measured precisely, the error in the scaling factor at low frequencies depends on the integration time. For an integration time T of approx. 3 hours (2 orbit periods), the relative scaling factor error is below

$$\delta s_{\text{ACC}} \approx \frac{\text{ASD}[s_{\text{ACC}}](f)}{\sqrt{T}} \approx 0.2\% \tag{5-17}$$

which is a significant improvement to current gravimetric missions, where the scale factor is fitted (see section 5.4.5). If different frequencies for the calibration peaks are used on each satellite, the calibration of both accelerometers in a e^2.motion link can be performed continuously and in parallel as shown in Figure 5-7.

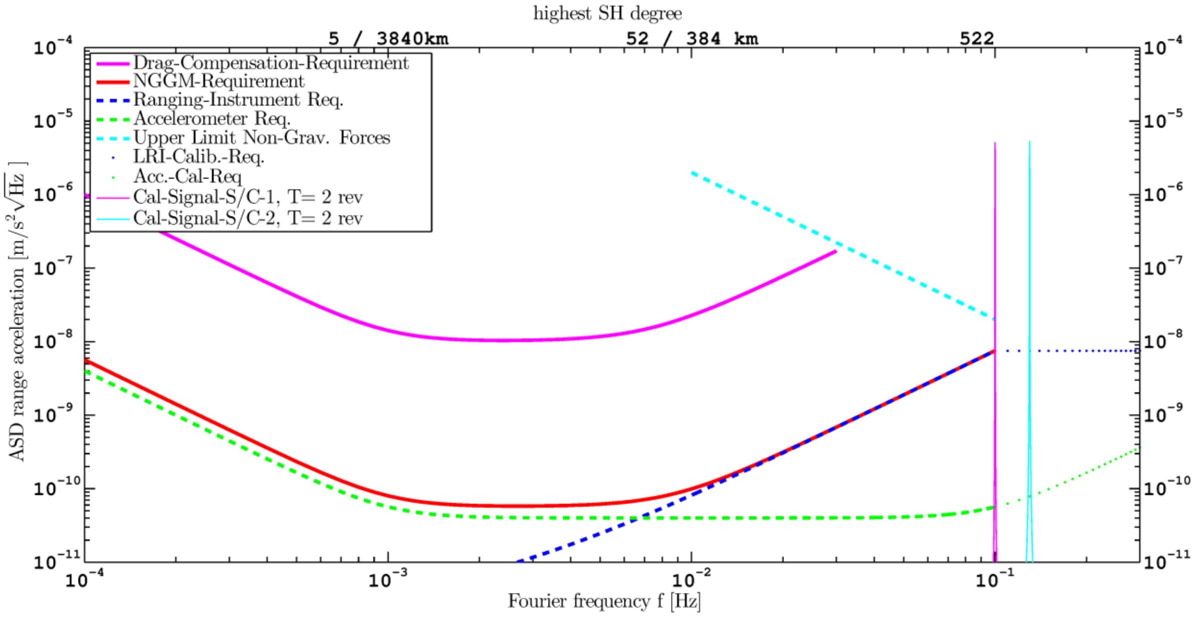

Figure 5-7: Calibration peaks of S/C 1 in magenta at 0.1 Hz and of S/C 2 in light blue at 0.13 Hz, which are measured by the laser link and by the accelerometer of each satellite. The integration time is two orbit revolutions.

5.3 Laser Ranging Instrument (LRI)

5.3.1 Measurement Principle

Interferometry exploits the fact that small changes (Δx) in the pathlength of a light beam change the phase of the light by

$$\Delta\varphi = \Delta x \cdot \frac{2\pi}{\lambda} \tag{5-18}$$

where λ is the wavelength of the laser light (e.g. 1 micrometer for a near-infrared laser). Phase changes in the light field cannot be resolved directly, since the frequency of 282 THz for 1 micrometer wavelength light is far too high for all detectors which thus respond only to the averaged power over many cycles (“square law” detection). However, interference of the light field with a phase stable reference field (local oscillator) allows resolving the phase with a photodetector. Two different techniques are widely used:

- homodyne interferometry: The local oscillator has the same frequency as the measurement beam. The photodiode current I_C changes sinusoidally with the phase of the measurement beam $I_C = A + B \cdot \sin(\Delta\varphi)$

  The photodiode current is usually stabilized to a working point using control loops, and the actuator signal is used to deduce the phase and ranging information.

- heterodyne interferometry: The local oscillator has a slightly shifted frequency, which produces a beatnote at the difference frequency on the photodetector and a current of the form $I_C = A + B \cdot \sin(2\pi f_b t + \Delta\varphi)$

  where f_b is the beatnote frequeny. The oscillatory part of the current and therefore the phase $\Delta\varphi$ can be tracked continuously by a phasemeter.

Heterodyne interferometry is advantageous for inter-satellite ranging, since it allows measuring a higher dynamic range (maximum relative velocity) between the satellites and the measurement signal can be in a convenient frequency region, such that it is robust against omnipresent low-frequency noises. Current technology allows to use homodyne schemes only with Doppler rates up to cm/sec in laboratory setups, which would require well matched satellite orbits and control of the relative velocity. Therefore heterodyne interferometry has been selected as baseline technology fore^2.motion.

5.3.1.1 Ranging Phase

Ranging interferometers exploit the fact that the phase change of light is proportional to a path length change. If a transmitter emits phase-stabile light, the phase measured by a receiver will represent the optical pathlength. If the receiver or transmitter is in linear motion with relative velocity $v(t)$, the received light will be Doppler shifted in frequency by

$$f_D(t) = \lambda \cdot v(t) \tag{5-19}$$

with λ being the laser light wavelength.

Since frequency is the time-derivative of the phase, a frequency shift corresponds to a ramp in the phase domain. The frequency and phase pictures are equivalent.

It is important to notice that interferometers are in general not capable to measure absolute distances, but only distance changes from a zero-position (defined by the measurement start). This is often called “biased ranging”, since an unknown bias is present in the data. For gravimetric satellite missions this constant bias is usually fitted from other observations, like GNSS.

5.3.1.2 Attitude: Differential Wavefront Sensing DWS

If the reference light field is fixed w.r.t. the satellite, one can obtain the tip and tilt of the measurement beam (received light) by using a segmented photodetector (e.g. Quadrant-Photodiode). Such a detector provides 4 photocurrents, whereby the phase of each current depends on the average wavefront tilt on each segment.

As shown in Figure 5-8, the phase of the left segments has a different sign than the phase of the right segments. Appropriate linear combinations of the 4 phases provide a measure for the tip and tilt of the measurement beam:

$$DWS_{tilt} = \frac{\varphi_B + \varphi_D - \varphi_A - \varphi_C}{2} \qquad DWS_{tip} = \frac{\varphi_A + \varphi_B - \varphi_C - \varphi_D}{2} \tag{5-20}$$

It turns out that the DWS combinations (with units of radian, electrical phase) provide a high gain of the geometrical wavefront / beam tilt in front of the detector. The DWS signals are a good measure of the local spacecraft tilt w.r.t. an incoming light field, which can be read out with high bandwidth.

One should note that small DWS signals usually mean small relative wavefront tilts, which maximizes the wavefront overlap and the interferometric contrast or visibility, which is proportional to the signal-to-noise ratio of an interferometer.

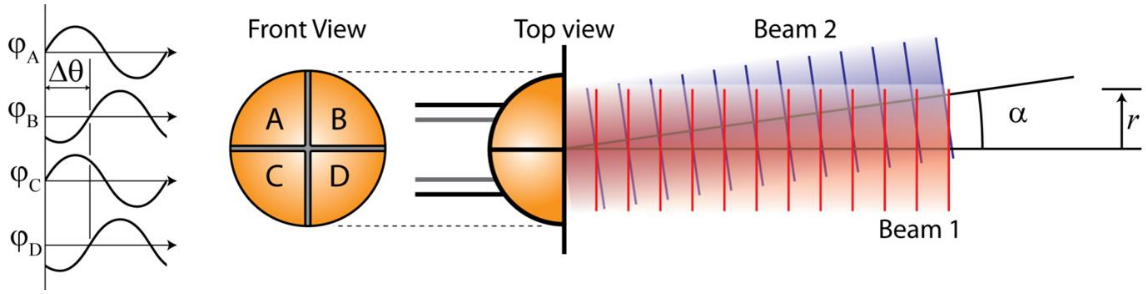

Figure 5-8: Working principle of Differential Wavefront Sensing. A circular Quadrant-Photodiode with segments (A,B,C,D) is used to detect the interference of tilted wavefronts. A phase difference $\boldsymbol{\Delta\theta}$ of the electric current between the left (B, D) and right (C, D) segments is present, which is proportional to the wavefront/beam tilt $\boldsymbol{\alpha}$ in front of the detector. The ranging information is given by the average of the four phases

5.3.2 Interferometer Concepts

The following technical constraints and challenges need to be considered when designing an interferometer.

1. A phase-stable reference light field (reference oscillator) is required to obtain interference and to provide a reference phase.
2. The resulting beatnote frequency needs to be within the photodetector bandwidth, considering that the relative satellite velocity introduces time-variable sinusoidal frequency shifts.

3. The resulting beatnote frequency needs to be within the phasemeter bandwidth, such that the phase can be tracked continuously.

Due to (1) the use of single-way interferometers is in general very difficult, since a phase stable light source is needed on each satellite. In case of heterodyne interferometry, the sources have to have slightly different frequencies, but need to be phase stable at the same time. To avoid this problem usually a round-trip measurement is performed.To avoid this problem usually a round-trip measurement is performed.

Figure 5-9 shows the general setup, where the master (satellite 1) emits some light. This light gains some Doppler shift and time delay, due to finite speed of light, and is received by the slave (satellite 2). The same effect is observed in the reverse direction.

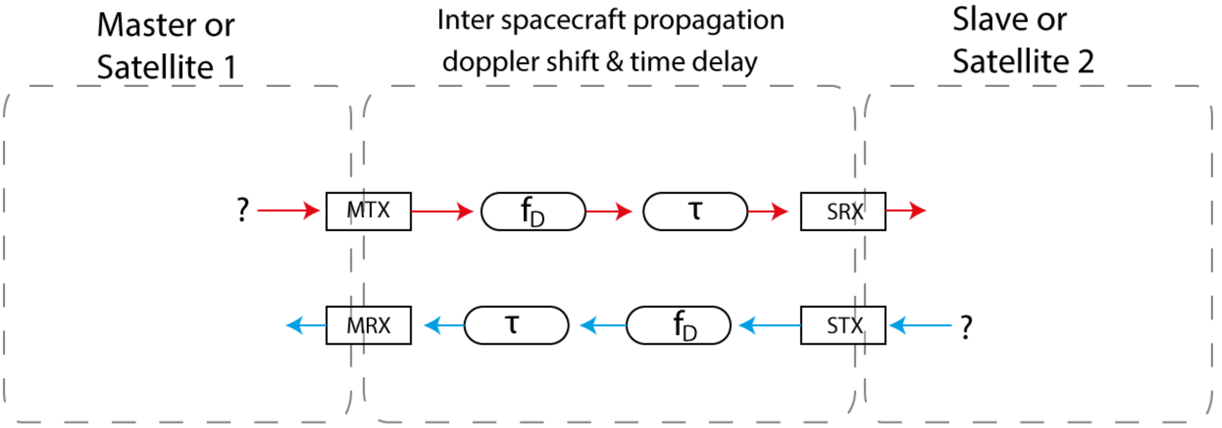

Figure 5-9: MTX: Master-Transmit, MRX: Master Receive; SRX: Slave Receive, RTX: Slave Transmit

5.3.2.1 Passive Retro-Reflector

The use of a passive retro-reflector has been suggested in [3], which is depicted in Figure 5-10. The master satellite is equipped with a frequency stabilized laser (e.g. NPRO with cavity). A small fraction of the light is used as local oscillator (MLO), but most of the light is send out to the distant slave satellite. The slave satellite retro-reflects the light to the master, such that the light gains a second time a Doppler shift (and delay). On the master satellite the received light (MRX) is interfered with the local oscillator and the interference is measured on the photodetector (MQPD).

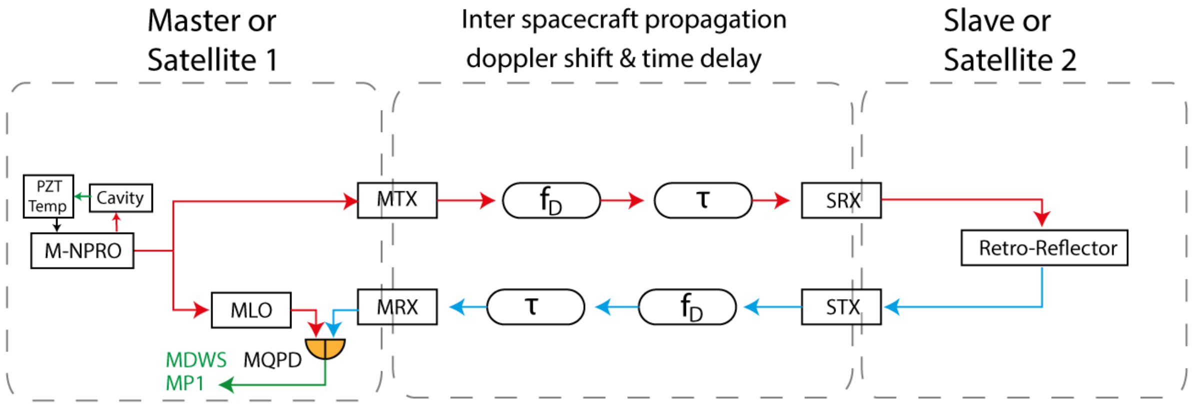

Figure 5-10: Block diagram of a passive retro-reflector concept for a satellite-to-satellite ranging interferometer. Slave satellite is purely passive without phase measurement. Green arrows indicate electrical signals, while red and blue arrows indicate optical paths.

The disadvantage of this layout is the limitation to only short inter-satellite distances ($d < 10$ km), since the retro-reflector at the distant satellite can only reflect a small fraction of the light and the received light power on the master is again only a small fraction of the retro-reflected light. Other difficulties are the zero-crossings of the beatnote frequency on the master photodetector (MQPD), such that a heterodyne readout with a (phase-tracking) phasemeter is not possible without interruptions (link-loss). The phase of a beatnote is not well-defined for signals with zero beatnote frequency. Also the optical design with low satellite attitude jitter to pathlength coupling is harder, since the retro-reflector vertex has to be placed close to the center-of-mass, but the aperture should be as large as possible.

5.3.2.2 Transponder System with Offset Frequency

The limitation of short baseline can be evaded by the use of an active transponder system, as shown in Figure 5-11. . In this concept the master satellite emits most of the frequency stabilized light to the slave satellite. The laser of the slave satellite is not locked to a cavity, but to the phase of the incoming light using a Phase-Lock Loop (PLL). This is achieved by measuring the beatnote phase on SQPD and providing a feed back to the laser, which can shift the frequency and phase with a piezoelectric actuator and with the temperature of the laser crystal. The beatnote frequency on SQPD is the frequency difference between SRX and SLO, which is kept to the reference frequency (Sfo) with the control loop. The reference frequency (Sfo) is also called the offset frequency and can be chosen such that the beatnote frequency is in the detection band of the photodetector and appropriate for a phasemeter (e.g. 5..25 MHz). The (beatnote) frequency is in general the time derivative of the (beatnote) phase, however, in the context of phase tracking usually a linear trend (ramp) is subtracted in case of a fixed offset frequency.

In the infinite gain limit (of the control loop) the measured phase on the slave satellite is zero (or constant) and the frequency of the light at STX (and SLO) is

$$\mathrm{f_{STX}} = \mathrm{f_{MTX}} + \mathrm{f_D} + \mathrm{f_{Sfo}} \tag{5-21}$$

The measured beatnote on the master satellite is

$$\mathrm{f_{MQPD}} = 2 \cdot \mathrm{f_D} + \mathrm{f_{Sfo}} \tag{5-22}$$

which contains twice the Doppler shift and is equivalent to the round-trip pathlength in the phase domain. The frequency offset (Sfo) on the slave satellite has to be selected such that the beatnotes on both satellites are within the detection band.

If one assumes a detection band of 5..25 MHz on both satellites, one can allow a maximum Doppler shift of ±5 MHz, which is equivalent to ±5 m/s relative satellite velocity if laser light with a wavelength of 1064 nm is used. With an offset frequency of f_{Sfo}=15 MHz, the beatnote on the master satellite varies between 5..25 MHz, while the slave satellite would measure constantly 15 MHz. In other words, the beatnote frequency is distributed in a ratio of 100% to 0 % between master and slave satellite.

The maximum allowable relative velocity can be increased by a factor of 2 with a time-dependent frequency offset, since the Doppler shift can be distributed equally between master and slave satellite.

Both satellites are capable to measure DWS and phases. In the infinite gain-limit the complete ranging information is measured at the master satellite, while the slave satellite measures zero. In case of finite gain, the ranging information has to be obtained by combining the phase measurement of slave and master.

The transponder concept is used in the GRACE Follow-On LRI and has also been intensively studied in the LISA context. Since the relative velocities in e^2.motion are in the region of a few m/s as well, this concept has been selected as baseline due to its maturity and simplicity.

By making both satellites identical and equipping both satellites with a frequency stabilization, the role of master and slave can be swapped between the satellites in case of failures of one frequency stabilization providing redundancy.

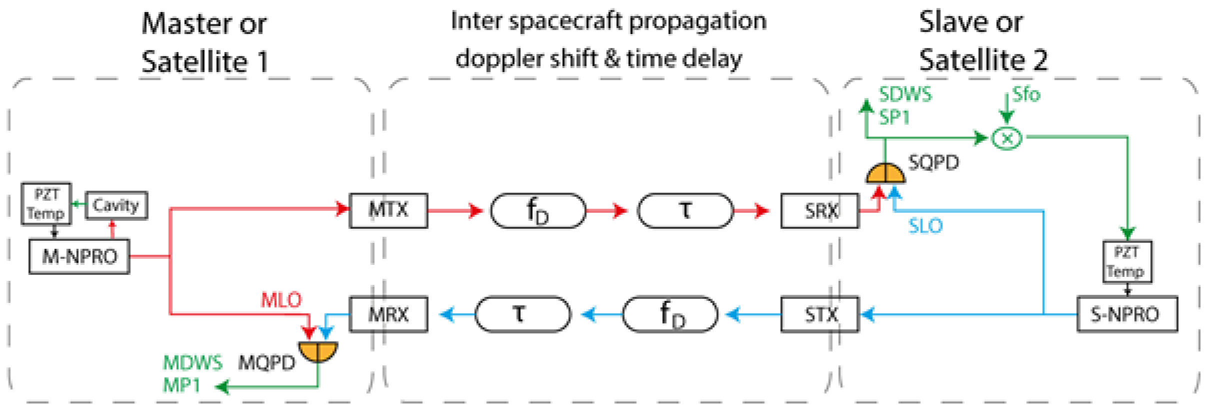

Figure 5-11: Block diagram of a transponder concept for a satellite-to-satellite ranging interferometer. Green arrows indicate electrical signals, while red and blue arrows indicate optical paths.

5.3.2.3 Enhanced Dynamic Range

If future gravimetric missions require higher Doppler rates, e.g. if pendulum orbits are used, one can distribute the Doppler shifts on several photodiodes (see Figure 5-12). Small Single-Element Photodiodes have usually higher bandwidth than large Quadrant-Photodiodes, so they can measure higher Doppler shifts. The Quadrant-Photodiodes are in general still required to obtain the attitude measurements using DWS. Acousto-optical modulators (AOMs) can serve as frequency shifter. The illustrated concept would allow Doppler rates up to 20 m/s for a detection band of 5..25 MHz (for all photodetectors) with variable offset frequencies. However, such concept has significantly increased complexity, requires more phasemeter channels and needs to be studied in more detail.

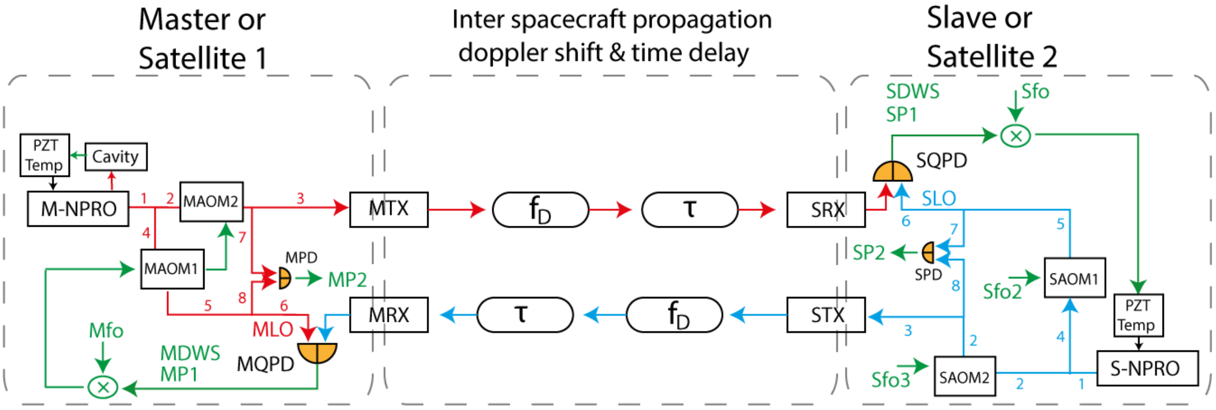

Figure 5-12: Block diagram of a transponder concept for a satellite-to-satellite ranging interferometer with several photodiodes (and phase-lock loops). The Doppler shift of the light is distributed onto several photodiodes. Green arrows indicate electrical signals, while red and blue arrows indicate optical paths.

5.3.3 Optical Layout

So far different concepts have been discussed on abstract block diagram level. The actual optical implementation of the interferometer can be accomplished in various ways. In general one can distinguish two different types: on-axis or off-axis layouts.

5.3.3.1 On-axis Layout

An on-axis interferometer has a common optical path for the receive and transmit beam along the line-of-sight. Since the main measurement is the distance variation between the CoM of the satellites, it seems a natural choice to use this axis for the interferometric measurement. In principle an on-axis interferometer can be realized with only a few components, however, it turns out that these simple concepts do not allow to obtain sensible power ratios between local oscillator beam, transmit beam and received beam. This drawback can be avoided by exploiting different polarization states of the light. With polarizing beam splitters (PBS) and waveplates a sensible ratio between local oscillator power and transmit beam power can be selected and the received light can be separated from the local light on the optical bench (if required).

However, this increases the complexity of the interferometer and the amount of optical components. The introduction of additional components in interferometers should be minimized, because additional optical components might yield negative side effects, which need to be analyzed (see Table 5-2). It is beneficial to keep space interferometers as simple as possible.

An on-axis layout is in particular useful if a common telescope for the received and transmit beam is envisaged. It increases the received light power and magnifies the transmit beam, which yields a smaller beam divergence in the far field. This allows using less laser power or allows to increase the satellite separation as in the LISA mission concept.

An examplary on-axis layout with telescope is depicted in Figure 5-13. One major challenge is the determination of the laser interferometer point of minimal coupling (POMC), which minimizes the rotation-to-pathlength coupling. The POMC is usually dependent on the optical layout, beam parameters, component misalignments etc. For ideal interferometers the POMC might have zero rotation-to-pathlength coupling for rotations around all axes (yaw, pitch and roll). However, in general there are three different axes (lines) of zero coupling for each rotation axis (yaw, pitch and roll). In an ideal interferometer the axes (lines) intersect in one point, which is the zero coupling point for all rotations at the same time. In general in non-perfect interferometers the three axes (lines) do not intersect and therefore the POMC is determined as the point with least distance to all three axes (lines) or else as the point with minimum total coupling from all 3 axes. It is often useful to apply even some weighting between the axis, therefore the POMC might depend on definitions and weighting parameters.

For on-axis layouts the POMC is in general located close to the optical axis, whereby the longitudinal position is dependent on the parameters like wavefront curvatures (waist location) and imaging systems. It may be laterally shifted, if the optical bench show some linear tilt-to-length couplings, which should be avoided by sensible optical design. It is therefore required to measure the optical axis precisely w.r.t. the interferometer housing for the determination of the POMC, which is non-trivial since it is not directly physical accessible (by probing). Often the POMC is also just called Reference Point (RP).

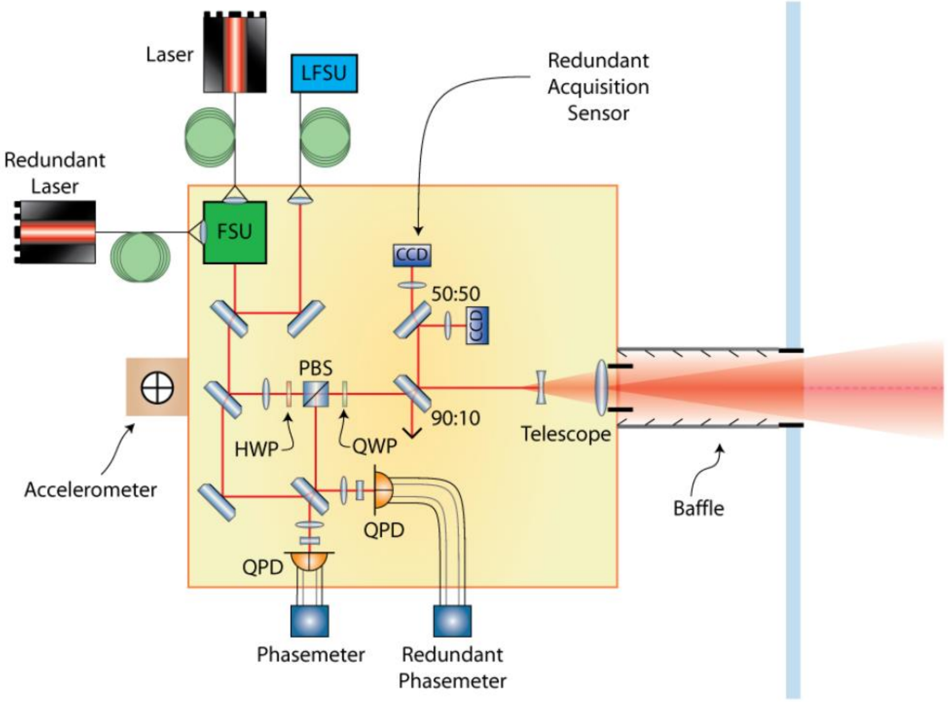

Figure 5-13: e.motion on-axis interferometer concept [9]. The POMC of this interferometer coincides with the accelerometer center.

Table 5-2: Potential negative side effects of (additional) optical components. Some effects may cancel in an interferometric measurement, if both interference beams are affected in the same way.

Effect	**Description**	**Counteraction / Mitigation**
Temperature coupling	Mainly transmissive optics; Optical phase changes due to temperature variations; Two effects: dn/dT value and thermal expansion of component;	Optimization of thermal stability of optical bench; glass substrates with low temperature coupling; Thin components
Attitude coupling	Transmissive optics induce a optical pathlength variation dependent on the light incidence angle; light incidence angle might change to due to spacecraft attitude (jitter), beam steering or jitter of laser beam	Compensation plates can help to reduce linear coupling, but increase quadratic coupling; Optimization of optical layout might reduce linear coupling (alternating orientation of 45° components)
Power loss	Absorption within component or due to contaminant on the optical surfaces (in-orbit contamination); non-perfect coating reflectivity/transmissivity	glass substrates with low absorption; optimization of design (Ifo, S/C) to minimize contamination; use of high-quality coatings; sufficient margin in optical power link budget
Ghost beams	Imperfect AR coatings produce parasitic reflections at surfaces, which might propagate into the sensitive path	Optimization of optical layout, beam dumps, use of wedged components
Wavefront errors	planarity or quality of surfaces influences wavefront of transmitted and reflected light	Use of high quality optics
Polarization changes	Some combination of optical components (periscopes) might rotate the polarization; polarization purity decrease due to reflection (e.g. metals)	Use of additional polarizer components; use of high quality coatings; Analysis of polarization
Beam overlap / co-alignment	Parasitic wedges on components change direction of light (static offset): Increased complexity in manufacturing (interferometer alignment)	Use of high quality substrates
Mass increase	Especially large components (telescopes) increase total optical bench mass	-

5.3.3.2 Off-axis Layout

In an off-axis layout the transmit and receive beams are separated spatially, as illustrated in Figure 5-14. It is evident that such a concept can be realized with significant less complexity, since the use of polarizing components is not required. Often (in ideal) interferometers the POMC for the full round-trip pathlength measurement can be determined as arithmetic mean of a POMC in the transmit path (TX-POMC) and of a POMC in the receive path (RX-POMC). The TX-POMC is given by the waist position of the transmit beams (or more precisely by the center of wavefront curvature at the distant spacecraft), while the RX-POMC is close to the receive beam axis. The axis is defined by the center of the portions of the received wavefront, which interfere later with the local oscillator (in Figure 5-14) it is the flat top beam directly at the receive aperture). The longitudinal position of the POMC along the axis is determined by quadratic couplings measured with the photodetectors on one satellite, while lateral offsets may be induced by linear tilt-to-pathlength couplings. In general each photodetector has its own POMC, however, the points can usually be co-located by adjusting some distances (as done in

Figure 5-14). Ideally the interferometer would be placed within the spacecraft, such that POMC and satellite CoM coincide. This minimizes the rotation-to-pathlength coupling. However, for NGGM-like gravimetric missions usually an accelerometer (accelerometer reference point) needs to be located at the satellite CoM, therefore the optical layout has to ensure that the POMC is outside the interferometer housing and that it can coincide physically with satellite CoM and accelerometer RP. One should emphasize, that the precise measurement of beam axes and of TX- and RX-POMC is challenging.

Another drawback of the layout shown in Figure 5-14 is the lack of an easy way of implementing a beam steering mechanism, which allows compensating spacecraft rotations by minimizing the local DWS signal (=maximizing interferometer signal level) and ensuring thereby pointing of the TX beam to the distant satellite. The mirror M1 can be used for the purpose in case of yaw-rotations, however, pitch rotations are “compensated” in the opposite direction and therefore misalignments would be doubled.

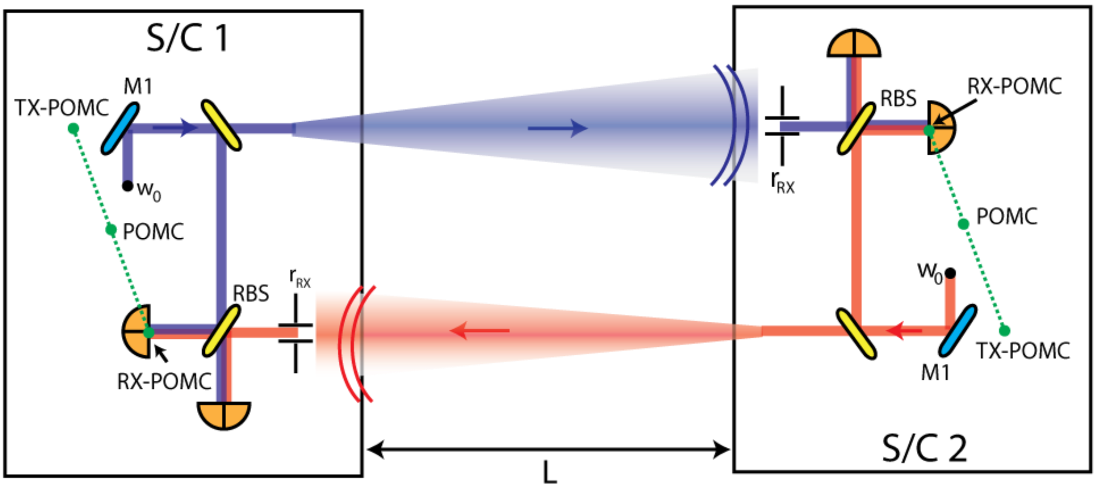

Figure 5-14: Simple off-axis concept. TX-Point of Minimal Coupling (POMC) is the center of wavefront curvature (measured in the far-field at the distant satellite), RX-POMC is given as intersection point of local-oscillator beam (axis) with the recombination beamsplitter (RBS). The total interferometer POMC is given by the arithmetic mean (center of gravity) of both points.

5.3.3.3 Off-axis Racetrack Layout

The racetrack layout is a special type of an off-axis layout, which utilizes an additional retro-reflector. It has initially been suggested by William Folkner (JPL – NASA) and further elaborated by the AEI for the GRACE Follow-On Laser Ranging Interferometer. It was born out of necessity, since the GRACE Follow-On mission uses an on-axis Microwave Ranging Instrument and propellant tanks, which occupy the line-of-sight. It turned out that it has several attractive properties, which make the design also suitable for future spacecraft-to-spacecraft interferometers. Namely,

- A beam steering mechanism can be implemented easily, which allows to simultaneously maximize the interferometer contrast and signal-to-noise ratio (minimize DWS signal) and to compensate local spacecraft jitter, such that the transmit beam is sent out always in the direction of the distant satellite.
- No polarization optics are required: only 2 transmissive optics on the optical bench and 3 reflective components of the hollow corner-cube are within the sensitive measurement path for each satellite (see Figure 5-15)
- Off-racetrack pathlength fluctuations are suppressed by a high factor (dashed lines in Figure 5-15). The sensitive measurement path is the racetrack with solid red/blue lines in Figure 5-15.
- A two-lens telescope on the optical bench images the receive aperture and the steering mirror onto the photodetector. This suppresses beamwalk on the detector, if the satellite or the steering mirror rotates. In addition diffraction rings introduced by the receive aperture disappear in the image plane.

- The interferometer POMC coincides with the TMA (corner-cube) vertex (see Figure 5-16) in the ideal case. Misalignments or motion of the optical bench do not change the colocation of both points due to the special properties of corner-cubes. In addition offsets in x-direction between POMC and CoM influence the measurement only in second order.
- The POMC can be placed outside physically present interferometer hardware, e.g. into the accelerometer

A small fraction of the received light on each satellite is transmitted through the beamsplitter and does not propagate to the photodetector, which slightly decreases the signal-to-noise ratio. For Signal-to-Noise or Carrier-to-Noise-density limited interferometers like LISA, which are dominated by noise due to the low received power, this might be an argument against a racetrack configuration.

However, as pointed out later, the sensitivity of satellite-to-satellite interferometry in LEO is not dominated by the carrier-to-noise density with current mission proposals and therefore a small loss in the received power is uncritical.

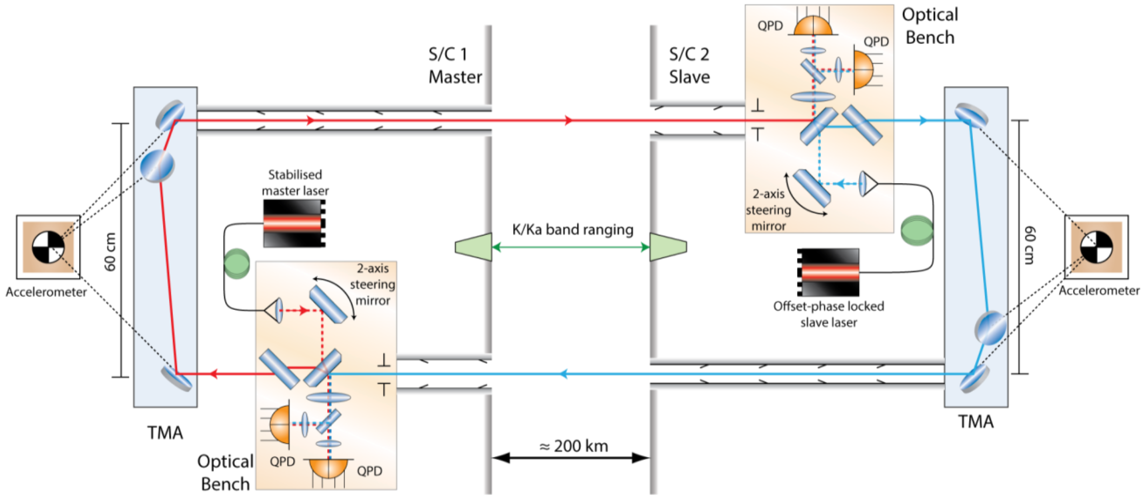

Figure 5-15: GRACE Follow-On Laser Ranging Interferometer with offset phase-locked transponder and corner-cube retro-reflector (Triple Mirror Assembly, TMA) on each satellite.

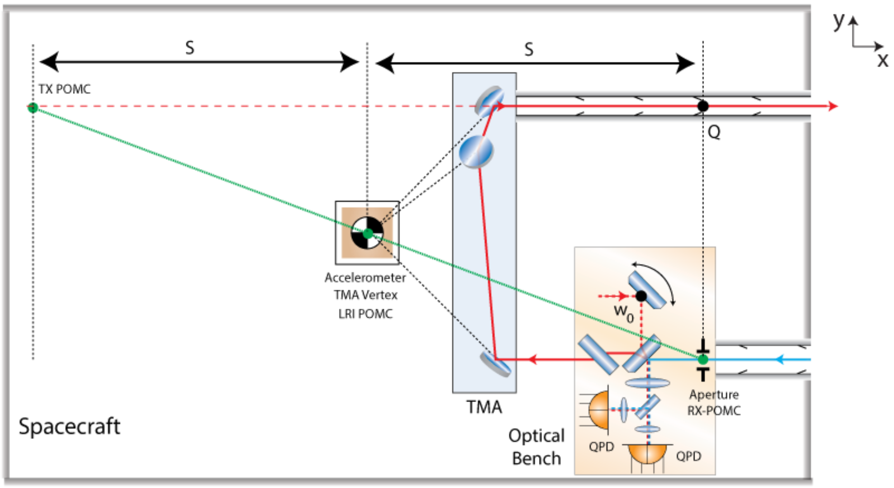

Figure 5-16: POMC in GRACE Follow-On LRI is collocated with the TMA vertex. Due to the special properties of corner-cubes, the geometrical pathlength between RX-POMC and point Q is $\boldsymbol{2 \cdot s}$, as well as between $\boldsymbol{w_0}$ and Q. Effects in beamsplitter and compensation plate are omitted.

5.3.4 Pointing Methods and Satellite Attitude

In satellite-to-satellite interferometry each spacecraft simultaneously receives and transmits laser light. In the presence of spacecraft attitude jitter it is important that each satellite is capable to send out the light to the direction, where the distant satellite is located. For current proposals of gravimetric satellite missions a compensation of the point-ahead angle, which is caused by the finite speed of light, is not necessary. The point-ahead angle can be computed as shown in (Sheard, et al., 2012).

$$\theta_{pa} \approx \frac{2\upsilon_\perp}{c} \tag{5-23}$$

where $v_\perp$ is the relative transverse velocity between the satellites (perpendicular to the line-of-sight). The magnitude of the point ahead angle is in the order of 2 μrad for currently proposed gravimetric missions (Sheard, et al., 2012). The effect of transmitter (TX) misalignment is shown at the top of Figure 5-17. The laser beam does not hit the receive aperture on the central axis, where the intensity is maximal, but at the side. The power P_{AP} in the receive aperture with units of optical Watt decreases.

If the local (receiver) satellite is misaligned, it leads to a poor overlap of the laser beams in the interferometer, a misalignment between local oscillator (LO) and received (RX) beam (see bottom Figure 5-17). The overlap of both interfering beams is described by the so-called heterodyne efficiency η, which is a number between 0 (no interference) and 1 (perfect interference). For the usual case of a sufficient strong local oscillator, the signal amplitude (strength) of an interferometer is dependent on the effective received power P_{eff}, which is the product of heterodyne efficiency η and received light power P_{AP},

$$P_{\mathrm{eff}} = P_{AP} \cdot \eta \tag{5-24}$$

Next to the signal strength also the actual signal, which is the measured inter-satellite distance variation, is influenced by local spacecraft rotations. Static pointing deviations are included in ε for receiver misalignments and in P_{AP} for transmitter misalignments, wheras fluctuations called *attitude jitter* or *pointing jitter* contribute a significant amount of noise to the overall noise budget, as will be discussed later. The attitude jitter can be described by a (frequency dependent) spectral density with units of $\mathrm{rad}/\sqrt{\mathrm{Hz}}$, which couples mostly linearly with a coupling factor with units of m/rad into the pathlength. The product of attitude jitter spectral density and coupling factor directly yields directly the contributed measurement noise.

These effects as seen on the receiver (RX) satellite are summarized in Table 5-3. The TX misalignments have only a small influence on the measured pathlength, since the phasefronts are almost spherical in the far field and hence rotationally symmetrical. The phasefront normal vector (=local propagation direction of wavefront) as seen by the receiver satellite is (to first order) parallel to the line-of-sight.

Table 5-3: Effect of spacecraft misalignments w.r.t. the line-of-sight as seen by the receiver (RX) satellite. SNR: Signal-To-Noise ratio, DWS: Differential Wavefront Sensing (signal)

Cause	**Received power (in Aperture)**	**Heterodyne efficiency**	**SNR**	**DWS**	**Linear coupling of attitude jitter into pathlength**
RX misalignment	const.	decrease	decrease	non-zero	~ 100 um/rad (yaw & pitch)
TX misalignment	decrease	const	decrease	~const./ zero	< 1 um/rad

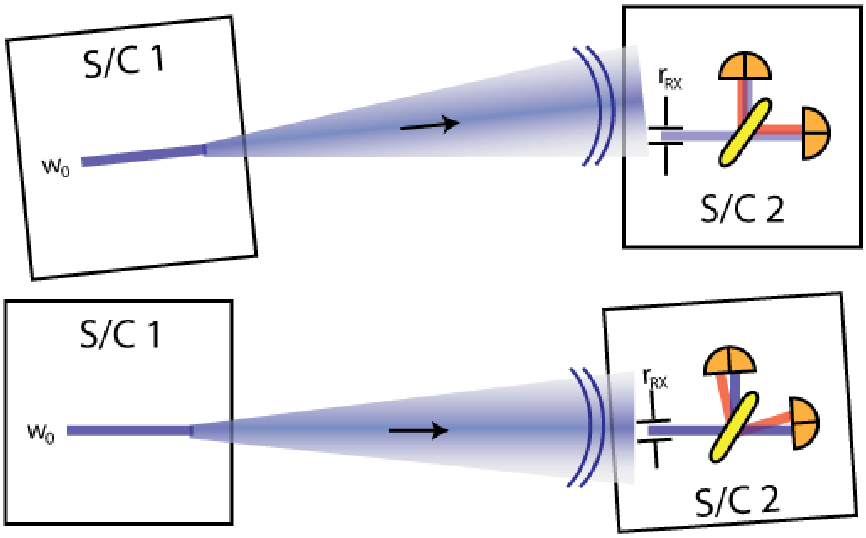

Figure 5-17: Transmitter misalignment (top) yields a drop of received light power due to the Gaussian beam nature. Receiver (local spacecraft) misalignment leads to poor overlap between the beams in the interferometer.

The maximum tolerable RX-LO misalignment is dependent on the detection limit of the phasemeter and on beam parameters on the optical bench. For a wide range of usual parameters it has to be better than (roughly) ±100µrad. The TX pointing requirement is highly dependent on the beam divergence of the exiting beam and on the available laser power.

In general the transmit beam and the local oscillator beam, which is interfered with the received light, can be made independent. For example, a beam pointing mechanism can be used for the transmit beam, such that the light propagates always to the distant satellite, and a second beam steering mechanism can be used to compensate RX-LO misalignments and to keep the SNR high.

However, in practice a constant phase relation between TX and LO beam is required[1], which is complicated to achieve with additional beam steering mechanisms. Such mechanisms introduce non-negligible pathlength variations in addition to the deflections, and they increase the complexity of the interferometer. In addition a sensitive measurement of the TX pointing error is not directly available, which would be necessary to control the TX beam pointing.

For gravimetric missions it is advantageous that point-ahead angle compensation is not required. Therefore, the TX light can be sent in the direction of the RX light, which is equal to the line-of-sight.

In the following three different pointing mechanisms are described and a trade-off is provided.

5.3.4.1 Spacecraft Pointing

In this approach the DWS signal is fed into the AOCS together with conventional attitude information (star tracker, sun / earth sensors). The satellite uses thrusters and magnetic torquers to minimize misalignments between RX and LO and between TX and the line-of-sight, once the laser link has been established. The interferometer and LO beams are fixed in the satellite frame, thus, beam pointing and spacecraft attitude are equivalent up to some static offsets. As a consequence, the beams travel always on the same path within the satellite and on the optical bench. Pointing by AOCS has been studied in the LISA mission for many years and is feasible in a quiet deep-space environment, where the spacecraft can be actuated with low-noise micro-newton thrusters. The application of this concept in a LEO mission with air drag and changing environmental conditions is more challenging, but has been suggested in previous gravimetric LEO mission proposals [9,10]. Keeping the pointing below ±100µrad requires a tight control, which might consume excessive propellant or might lead to a higher pointing jitter noise.

5.3.4.2 Pointing by Component

The direction of the outgoing TX and LO beam of an interferometer can usually be changed by rotating a mirror or beamsplitter on the optical bench of the interferometer. If the component is in the

---

[1] Either TX and LO beam have constant phase relation, or the phase variations are measured

sensitive measurement path, one needs to ensure that the residual tilt-to-pathlength coupling is sufficient small, which is in general difficult. Therefore the actuation of a component, which is not in the sensitive measurement path, is favored.

The actuator can be used to zero the DWS signal by a feedback control loop, which ideally simultaneously ensures TX beam pointing along the line-of-sight. The residual DWS signal is ideally a measure for the misalignment of the outgoing beam w.r.t. the line of sight and should be close to zero for a control loop with high gain and high bandwidth. Since the DWS signal is zeroed and thus 'used up' by the control loop, no direct spacecraft attitude information is available. However, it can be obtained indirectly by an additional sensor in the actuator, which measures the actuator position/orientation w.r.t. the satellite frame. This method will be used for the laser interferometer in the GRACE Follow-On mission (Sheard, et al., 2012).

The actuator decouples the interferometer laser beams from the spacecraft frame, such that larger deviations in spacecraft pointing can be tolerated, since they are compensated by the actuator. However, the resulting beam pointing with the actuator in closed-loop operation still has to be better than ±100 µrad. Although larger spacecraft pointing errors can be tolerated, one should keep in mind, that the spacecraft attitude jitter is not compensated and does still contribute measurement noise.

5.3.4.3 Actuation by Optical Bench

This approach is similar to the actuation of the component, whereby not a single component but the whole optical bench is rotated using a DWS control loop. By rotating the optical bench, the beam path of the received light can be held fixed through the optical setup. A varying path through the optical bench usually induces a variation in the optical pathlength (distance measurement). However, this coupling can usually be minimized by optimizing the interferometer layout, such that a design sensitivity in the order of $\mathrm{nm}/\sqrt{\mathrm{Hz}}$ is achieved as required for current gravimetric missions.

A drawback of this method is furthermore the need to move around an object with a mass in the kg region, which might disturb the accelerometer measurements on-board of e^2.motion. The mass also limits the actuation bandwidth to low frequencies.

Due to these drawbacks this method is assumed to be undesirable for a e^2.motion mission. *Pointing by spacecraft* shifts the problem of achieving good pointing to the satellite AOCS and allows a less complex interferometer, without moving parts, for the sake of a more complex AOCS. In addition one obtains direct readout of the spacecraft attitude variations w.r.t. LOS from DWS. In general a better spacecraft pointing reduces measurement errors due to tilt-to-pathlength coupling and is assumed to be beneficial against *pointing by component*. Most laser interferometer studies and preliminary AOCS simulations for e^2.motion suggest that *spacecraft pointing* is feasible. However, there is still some risk that more realistic simulations considering thruster imperfections (delay times, noise) and simulations of the whole AOCS chain reveal difficulties in achieving the required pointing performance.

Therefore, as risk mitigation, concepts with capability of accommodation of a steering mirror are favored for the e^2.motion laser interferometer design.

5.3.5 Laser Link Acquisition

Acquisition is the process of initializing an interferometric connection between the satellites, which allows the phasemeter to track the beatnote and to obtain DWS and longitudinal (ranging) signals. This requires that both satellites receive sufficient high light power levels (depending on TX beam pointing) and that the interferometric contrast (depending on receiver S/C pointing) is high enough, such that the signal-to-noise-ratio is above a detection and tracking threshold. In addition the laser frequency difference between both satellites has to be below a certain limit, which allows measuring the beatnote with photodetectors and phasemeter.

In general the very first *initial acquisition* is more difficult, since unknown biases in the orientation and position of all instruments are present due to the vibrations and shocks during launch, de-moisturization or zero G-effects. Once the biases are calibrated and known, a *re-acquisition* needs to cover a smaller uncertainty cone in the parameter space and is therefore less time consuming.

In both cases a line of sight estimation (LOS-estimation) is required on both satellites, which can be obtained by sensor fusion of attitude and position information (star cameras, GPS and other sensors via AOCS) and orbit prediction. The LOS-estimation is an estimation for the direction to the distant satellite and serves as starting point for the acquisition search. The difference between LOS-estimate and true LOS is the pointing error, which is dominated by the static bias.

The acquisition process is additionally complicated due to the fact that the interferometers on both satellites need to detect a parameter match at the same time, in general without exchanging information due to the lack of real time communication.

Since the GRACE Follow-On concept has a fixed dependency between orientation of the local oscillator beam and orientation of TX beam, the acquisition is a five dimensional search: two angular degrees on each satellite and the frequency difference need to be matched simultaneously. The current acquisition baseline strategy for GRACE Follow-On foresees that the steering mirror on each satellite performs a fast spatial scanning pattern, while the laser frequency on one satellite is swept (see Figure 5-18). For the *initial acquisition* or *calibration* a non-autonomous scheme is used, where both satellites record the events of received light and on-ground data processing is used to derive bias values between laser interferometer and LOS estimation, which includes the instrument misalignments.

Once the bias values are uploaded to the satellites, an autonomous *re-acquisition* is started with much smaller angular uncertainties to establish the link. Extended studies have been performed on the optimal search strategy, including different spatial scan patterns, coherent and incoherent detection methods of the photodetector segment signals.

The *initial acquisition* or *calibration* in GRACE Follow-On will take several hours, while *re-acquisition* might need up to a few minutes, although most *re-acquisition* events are assumed to be finished within a few seconds, since short interruptions of the laser link connection should not induce large pointing errors or laser frequency offsets.

A GRACE Follow-On like acquisition is based on a complex five dimensional search, which requires a complex and well tested on-board software and fast beam steering capabilities. Advantageous is the detection of light from the remote satellite with the photodetectors, which also perform the measurement of the optical phase (ranging), since less optical and electrical components are required.

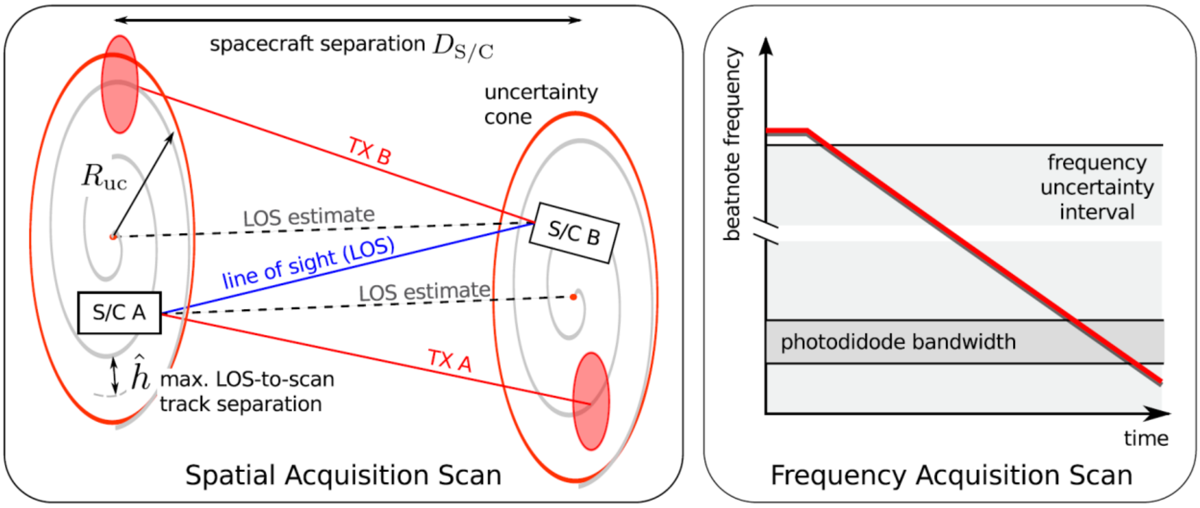

Figure 5-18: Laser Link Acquisition for GRACE Follow-On (Source: V. Müller, AEI). *Left:* Geometric parameters of the spatial/angular acquisition scan. Shown are the LOS estimates for each satellite (dashed black), and the true LOS (blue). TX A and TX B denote the actual pointing directions of the laser beams. The red (filled) circles are the areas, where a satellite can detect the laser power. *Right:* Frequency scan of the free-running slave laser. The laser link can be established, if the beatnote frequency is within the photodiode (and phasemeter) band (right figure) and if at the same time both red filled circles hit the distant satellite.

5.3.5.1 Acquisition Sensor Concept

An alternative is the use of an additional incoherent acquisition sensor with a wide field of view, which only receives light from the distant satellite and images it onto a multi-pixel array. This sensor detects only the weak received (DC) light power and is more sensitive at DC than the ranging photodiodes, since no strong local oscillator beam is present. If the acquisition sensor axis is aligned with the interferometer RX axis, the acquisition sensor provides the local spacecraft misalignment w.r.t. the LOS, if the distant satellite is pointing 'roughly' to the right direction. It provides a measurement of the LOS direction for the local satellite. It is independent of the laser frequency and thus reduces the 5 degree of freedom to only two (TX angles of distant S/C).

An additional acquisition sensor reduces significantly the complexity of the acquisition, since it breaks down the multi-dimensional parameter space into disjoint subsets, which can be matched (searched) in parallel.

To reduce misalignments of the acquisition sensor axis with the interferometer axis due to spacecraft launch vibrations and zero-G effects it is beneficial to locate the sensor directly at the optical bench close to the interferometer RX axis.

The pointing of the distant transmitter satellite influences only the received light power, but not the position of the spot on the local detector or the measurement of the LOS due to the almost spherical phasefronts at the receiver. Based on the sensor sensitivity, transmitter laser power and beam divergence two cases of transmitter visibility can be distinguished: a) transmitter is visible permanently b) transmitter is visible impermanent, meaning that the transmitter needs to perform some kind of spatial scan pattern, such that the receiver can detect the transmitter for a short time and measure the LOS direction.

If the beam parameters of the laser interferometer allow only a low transmitter visibility for the acquisition sensor, the use of a dedicated acquisition light source with high power and optimal beam divergence can be envisaged. Such a light source does not need to provide any coherence criteria, since the acquisition sensor measures incoherent DC power. Even a light source in the visible spectrum might be used, where common silicon CCD sensors with high responsivity are available.

5.3.6 Design Justification

The e^2.motion mission is conceived from the beginning to accommodate a laser interferometer. Environmental boundary conditions important for the interferometer design are provided by the mission design:

- Lifetime: 11 years
- Nominal spacecraft separation: 100 km
- Maximum relative velocity: < 5 m/s

A *transponder system with fixed offset frequency* has been selected as e^2.motion baseline in section 5.3.2 due to its maturity (e.g. from the GRACE Follow-On LRI and LISA) and compliance with the environmental e^2.motion boundary conditions. In addition it allows the use of simple and robust optical layouts with low risk and high measurement precision.

As discussed in section 5.3.2, the interferometer on each satellite has in general at least three types of laser beams: local oscillator beam (LO), received beam (RX) and transmit beam (TX). The phase between LO and RX is measured with photodetectors on each satellite, and the phase relation between LO and TX should be fixed, or least measured using an additional readout. The combination of the phase measurements on both satellites leads to a round-trip or ranging measurement, which is proportional to the satellite distance (variations).

The pointing of the TX beam is important to achieve sufficient light power in the receive aperture at the distant satellite. On the other hand the alignment between LO and RX is important to achieve sufficient wavefront overlap (heterodyne efficiency). The combination of both effects determines the signal-to-noise ratio of a phase measurement. Different pointing methods have been discussed in section 5.3.4 *Spacecraft pointing* and *pointing by component* are suitable options for e^2.motion like missions, whereby *actuation of the optical bench* is assumed to be unfeasible.

Use of a steering component on a single beam has the disadvantage that actuator translations couple into the ranging measurement (last three columns in Table 5-4). Therefore steering of two beams at the same time is advantageous, since the actuator translation is measured with the ranging photodetector (and cancels out in the round-trip measurement). The second column in Table 5-4 denotes a GRACE Follow-On LRI scheme, where LO and TX beam are steered with a steering mirror. The beam overlap between LO and RX is maximized, as well as the TX beam pointing is along the line-of-sight, as required, if the DWS is zeroed. The control loop ensures pointing and maximal signal-to-noise ratio of the phase measurement by a single actuator.

The third column in Table 5-4 is based on a Racetrack like scheme, where the recombination beamsplitter is rotated instead of a steering mirror. Since the local oscillator is transmitted, it does not change the direction, but the reflected TX beam does. Rotation of a beamsplitter might be more difficult to achieve, since the central part (of the beamsplitter) cannot be blocked by the actuator, in contrast to a reflecting steering mirror.

The fourth column assumes beam steering to maximize the interferometric contrast, but the TX beam is fixed in the spacecraft, meaning that the TX beam is pointed by the satellite attitude.

The first column in Table 5-4 shows pure spacecraft pointing without any actuator, which is possible since the point-ahead angle in e^2.motion is sufficient small (see section 5.3.4). The difficulty of interferometer pointing is shifted to the satellite AOCS. A stricter control of the satellite attitude is in general beneficial, since it reduces the tilt-to-length coupling (attitude jitter noise) in the ranging measurement. However, the signal-to-noise ratio of the interferometer is completely dependent on the attitude control of the satellite.

Although preliminary simulations of the AOCS and other future gravity mission studies suggest that pure spacecraft pointing is feasible, it is assumed here as potential risk, in particular it cannot be excluded that more realistic AOCS simulations reveal difficulties in achieving the required pointing accuracy and precision. A steering mirror as auxiliary pointing method is selected as baseline for the e^2.motion interferometer, if the S/C pointing accuracy is not sufficient.

The capability of maximizing the overlap between LO and RX beam and correcting the TX beam direction at the same time requires the use of a retro-reflector. Solid corner-cubes or cat’s eye retro-reflectors are less suitable, due to the additional optical pathlength coupling upon rotations, but hollow corner-cube retro-reflectors provide the correct properties.

If a mirror at normal incidence is used instead of the retro-reflector, the DWS zeroing control loop ensures correct TX pointing for rotations around one direction (e.g. yaw), but in general not for the orthogonal direction (e.g. pitch).

Since corner-cube retro-reflectors induce a lateral shift between incidence and exiting beams, an off-axis racetrack concept seems to be the natural choice.

The selection of beam parameters induces other restrictions on the optical layout. In the off-axis racetrack configuration the TX beam and the LO beam have equal beam parameters, since they originate from the same fiber beam. This reduces degrees of freedom in the design of the optical layout. Additional beam shaping optics (lenses) might be introduced in the TX or RX path, however, they do not allow closed-loop TX beam steering, since a change in the beam size by a factor m corresponds in general to an inverse change in beam tilt by a factor $1/m$.

Table 5-4: Beam steering of different beams (first row) and effects on interferometer design and performance. SAS: (Beam) Steering Actuator Sensor, SM: Steering Mirror, LOS: Line-Of-Sight, CL: Closed-Loop, SCA: Spacecraft attitude

		e^2.motion Baseline					
Received Beam (RX)			**x**	**x**		**x**	
Local Oscillator (LO)		**x**		**x**	**x**		
Transmit beam (TX)		**x**	**x**				**x**
Actuation of		SM	Recomb. BS	Recomb. BS	SM	SM	SM
Steering control		feed-back	feed-back	feed-back	feed-back	feed-back	feed-forward
DWS measures	LOS	CL: ~zero	CL: ~zero	CL: ~zero	CL: ~zero	CL: ~zero	LOS
SAS measures		LOS	LOS	LOS	LOS	LOS	TX direction
TX beam pointing	SCA	SM, CL	SM, CL	SCA	SCA	SCA	SM
TX Pointing Accuracy	SCA	CL DWS, SAS, Retro-Refl.	CL DWS, SAS, Retro-Refl.	SCA	SCA	SCA	SM, DWS
Actuator pathlength coupling	no	no	no	no	yes	yes	yes
LO-RX overlap	SCA dep.	maximized	maximized	maximized	maximized	maximized	SCA dep.
Comment	S/C pointing	Retro-Reflector required	Retro-Reflector required				

As pointed out in section 5.3.5, a dedicated acquisition sensor can significantly reduce the complexity of the acquisition process, and it should be foreseen in an e^2.motion interferometer. As shown in Table 5-5 (first row), the GRACE Follow-On LRI requires matching of 5 degrees of freedom at the same time, while the use of an acquisition sensor in e^2.motion allows to match the two angular degrees (of local spacecraft misalignment) in parallel, while the frequency is scanned.

The size of the parameter space in acquisition reduces to a few points, which are given by the frequency points (number N in Table 5-5) and by a small number of points, which are required to achieve guaranteed transmitter visibility.

An interferometer with a small TX beam with high light power can achieve all-time transmitter visibility, which further reduces the acquisition problem (column 4 and 5 in Table 5-5). However, such a concept requires beam shaping optics which would not allow an closed-loop TX beam steering by zeroing the DWS signal.

Table 5-5: Comparison of e^2.motion and GRACE Follow-On LRI with alternative concepts with unequal beam parameter interferometer.

	GFO LRI	**e^2.motion**	**Alternatives (non-optimal)**		
		equal beam parameter (LO, TX)		**unequal beam parameter (LO, TX)**	
		Off-axis	**On-axis**	**Off axis**	**On-axis**
Acquisition Sensor	No	Assumption: Yes			
Corner-Cube	60 cm	30 cm	no	not required	no
Curved Surface in Measurement Path	No	No	No	Yes	Yes
Acquisition[1]	{2+2+1}	{2},{2},{1}	{2},{2},{1}	{1}	{1}
Acquisition Degrees	All degrees	TX beam scan + Frequency scan	TX beam scan + Frequency scan	Frequency Scan	Frequency Scan
Initial Acquisition Parameter Space	e.g. {60x60xN}	e.g. {5}, {5}, {N}	e.g. {5}, {5}, {N}	{N}	{N}
Laser TX Power Demand	Low	Low	Low	≳ 400 mW	≳ 400 mW
S/C pointing accuracy sufficient[3]	No, > 1 mrad	Yes in e^2.motion, ≲ 100 urad	S/C pointing of ≲ 100 urad required!		
LO+TX SM capability if S/C pointing not available	SM used	yes	No without retro-reflector	No closed-loop TX beam steering	No closed-loop TX beam steering
Max. RX/LO misalignment[2]	SM: ≲ 5 urad	SC ≲ 100 urad; SM: ≲ 5 urad	SC ≲ 100 urad	SC ≲ 100 urad	≲ 100 urad (x Magnification)
Dedicated Acquisition Light source	No	Possible	Possible	Not required	Not required
Number of transmissive optical components	Low	Low	High	Low	High

[1]: {n} number of parameters to be matched simultaneously; [2]: values for different interferometer pointing methods, [3]: based on preliminary simulations, SM = Steering Mirror

5.3.6.1 Optical Layout

The e^2.motion LRI optical layout is based on an off-axis racetrack configuration, similar to the GRACE Follow-On LRI. The laser beam is launched at a fiber coupler in a nearly Gaussian beam mode with radius of 1.7 mm (see Figure 5-19). The beam is routed via a steering mirror to the 97:3 beamsplitter. 97% of the light power is reflected, and routed via a compensation plate and a corner-cube retro-reflector to the TX-baffles and to the distant satellite. The other 3% transmitted light (at the beamsplitter) propagate to the quadrant photodetectors.

The weak light from the distant satellite is traveling through the RX baffle, where ring apertures shall suppress undesired ghost reflections. The center region of the light is clipped at the 3 mm radius receive aperture and most of the light propagate to the photodetectors. A two-lens beam compressor in front of each photodiode de-magnifies the beams, such that they fit onto the photodetector’s active area with 0.5 mm radius. The beam compressor images the receive aperture and at the steering mirror onto the photodetector, which reduces beam walk on the detector and suppresses diffraction rings induced by the clipping at the receive aperture.

The acquisition sensor is located on a separate light path with separate baffle to keep the number of optical components in the sensitive ranging path small. An imaging system focuses the light in the 10 mm acquisition aperture onto the active area of the sensor and increases the spot displacement upon wavefront tilt.

The laser power to be delivered to the optical bench on each satellite by the optical fiber is 100 mW over the full mission duration. e^2.motion was designed to make use of the e^2.motion-High Stability Laser, which is being developed for the future geodesy missions.

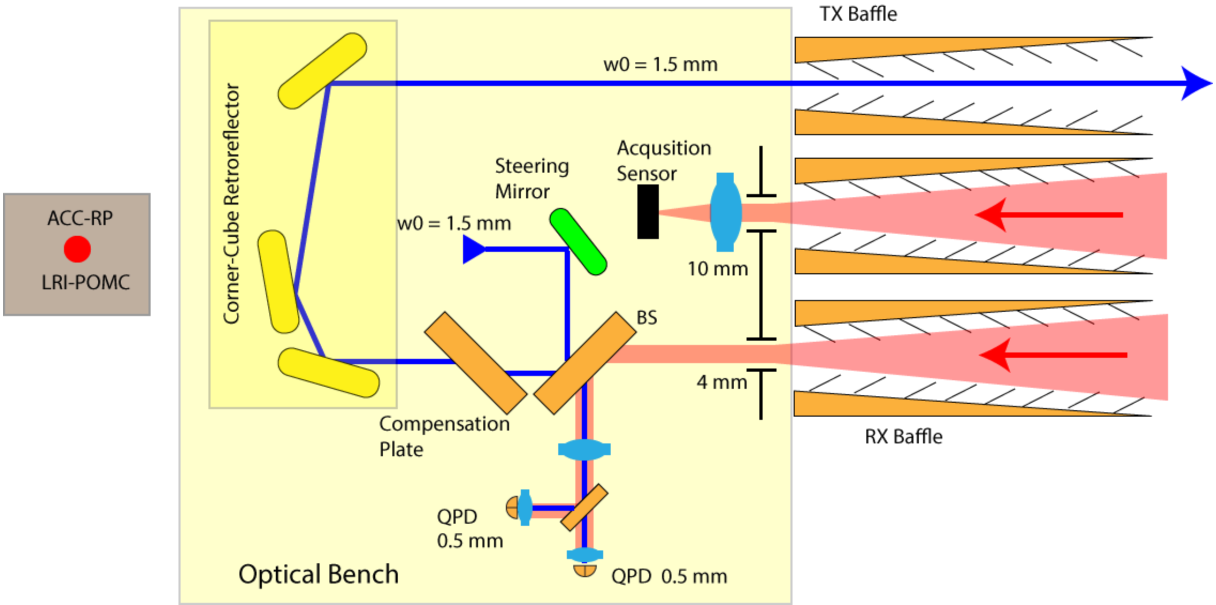

Figure 5-19: Optical layout of e^2.motion interferometer. BS: Beamsplitter, QPD: Quadrant-Photodiode

The 30cm hollow corner-cube retro-reflector is a central part of the interferometer. The parallelism of incident and reflected light has to be within a few (ten) µrad to a) guarantee pointing towards the distant satellite with sufficient light power and b) to reduce rotation-to-pathlength coupling. The vertex point, which is defined by the intersection point of the three mirror planes, can be derived from measurements of the mirror surfaces with a coordinate measurement machine. The vertex is to first order the reference point of the interferometer, which needs to coincide with the accelerometer reference point and the S/C center of mass. The interferometric distance measurement is ideally invariant under rotations around the vertex.

The changes of the e^2.motion interferometer compared to the GRACE Follow-On inter-ferometer are summarized and justified in Table 5-6.

Table 5-6: Majors changes between the GRACE Follow-On interferometer and e^2.motion interferometer

Acquisition Sensor	An additional acquisition sensor reduces the complexity and duration of the laser link acquisition process. It is located on the optical bench, such that misalignments of the acquisition sensor w.r.t. the interferometer axis are minimal when satellites are launched.
High Power Laser	e^2.motion assumes usage of the NGGM-High Stability Laser, which shall provide up to 500mW. Only 100 mW are required for the e^2.motion interferometer, however, due to contamination of optics and degradation of laser power over the mission duration (11 years) sufficient margin is available.
Beam Size	The beam size was reduced to 1.7mm to provide a higher beam divergence and thereby to improve transmitter visibility during acquisition. In addition beam properties can be determined easier at small beams, which fit onto commercially available sensors.
Corner-Cube size	The lateral displacement of the laser beams is assumed to be in the order of 30cm (compared to 60 cm in GRACE Follow-On). This allows a more compact and robust retro-reflector design with increased stability. Testing of the corner-cube properties like co-alignment is simplified due to the potential use of COTS devices.

5.3.6.2 Optical Link Power Budget

The e^2.motion layout assumes a laser source which can provide between 100 mW and 400 mW optical laser power to the optical bench. 100 mW are sufficient to operate the interferometer at the beginning of the mission. Due to the long mission lifetime of 11 years sufficient margins need to be incorporated to account for contamination of optical components (contaminant from spacecraft, corrosion in space due to atomic oxygen etc.), laser power and photodetector responsivity degradation.

The laser beams have been selected of smaller size (1.7 mm waist radius), compared to GRACE Follow-On LRI to simplify determination of beam properties, and to increase transmitter visibility in acquisition. The corresponding TX beam divergence is 200 µrad, which is equivalent to a Rayleigh range of 8.5 meter. The transmitted beam has a $1/e^2$ radius of approx. 20m at the receiver satellite, where only a small fraction is cut-out by the apertures.

A power level of 100 fW (1 fW = 10^{-15} W) in the acquisition receive aperture is assumed as detection limit for the acquisition sensor, which uses incoherent DC detection. For the e^2.motion beam parameter a transmitter misalignment of 500 µrad is tolerable to guarantee transmitter visibility by the acquisition sensor (see Figure 5-20). Since the uncertainty cone at *initial acquisition* is in the order of 2 mrad, the transmitter satellite needs to scan only a few spatial points achieve a high probability of detection by the receiver satellite during *initial acquisition*.

For the determination of the (ranging) phase with the quadrant photodiodes the so-called effective power, the product of overlap (heterodyne efficiency) and light power level is of importance. The e^2.motion dependency of the effective power for a single segment of the photodetector upon simultaneous transmitter & receiver is shown in Figure 5-21.

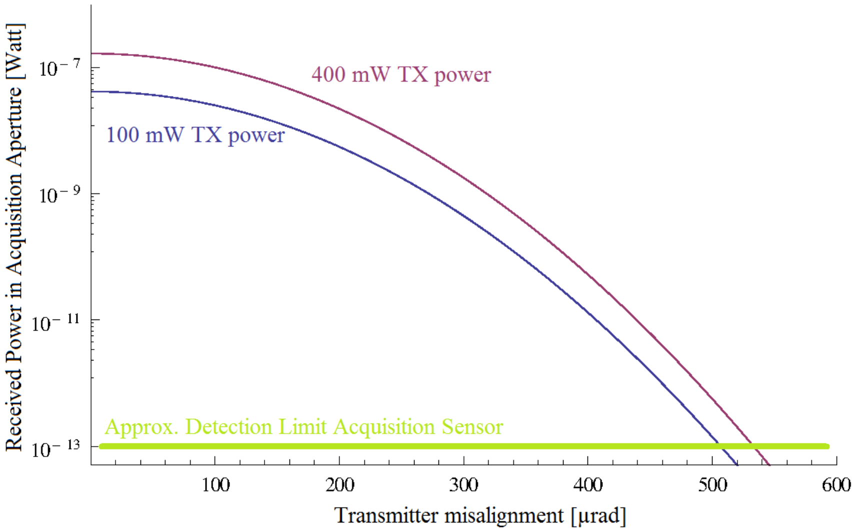

Figure 5-20: Received optical power in the acquisition aperture with 10 mm radius plotted as function of the transmitter tilt.

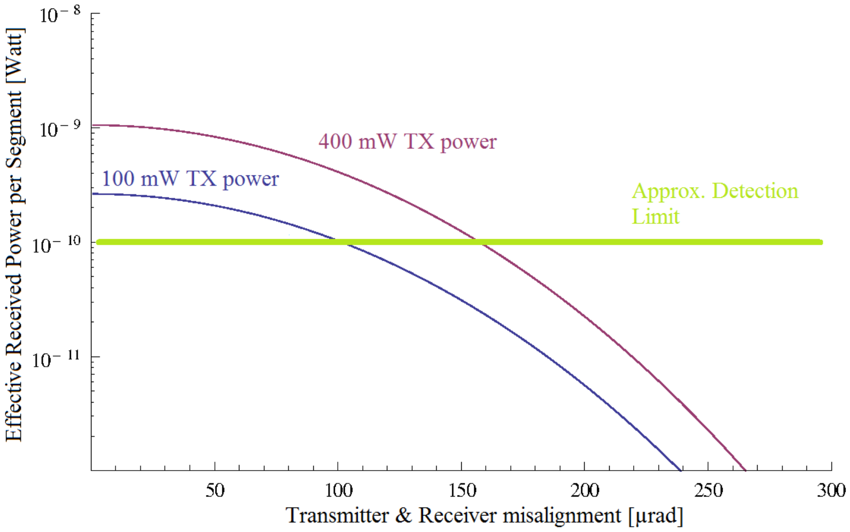

Figure 5-21: Effective received power per photodiode segment as a function of simultaneous transmitter & receiver misalignment.

A misalignment of 100 µrad of the transmitter and receiver satellite (w.r.t. the LOS) leads to a drop in the signal-to-noise ratio close the detection limit. The effective power is slightly more sensitive on receiver misalignment than on transmitter misalignment, as shown in Figure 5-22.

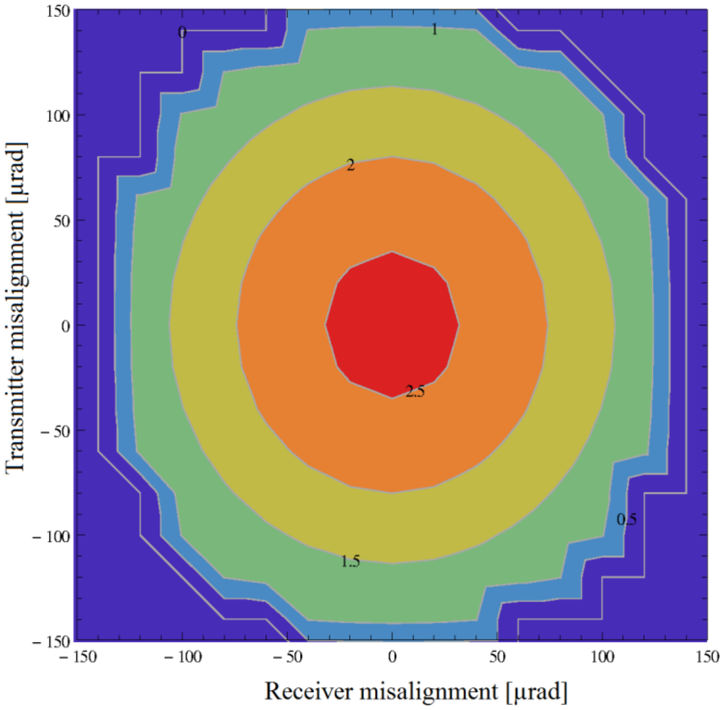

Figure 5-22: Effective receiver power per photodiode segment in units of 100 pW (contour plot) as function of transmitter and receiver misalignment.

A power link budget for three different scenarios is given in Table 5-7. The 3rd column shows the result for a perfectly aligned interferometer. The Carrier-To-Noise density is well above 75 dB-Hz, which is the detection limit of the e^2.motion phasemeter (see section 5.3.7.2 and 5.3.8.5). In the 4th column the interferometer was misaligned by 100 µrad on both satellites. The 5th column assumes End-Of-Life conditions, where the photodiode responsivity and maximum laser power is significantly degraded. In addition contamination of optical surfaces was considered (Contamination Loss). In all cases the Carrier-To-Noise density is sufficiently above the detection limit.

Table 5-7: Link power budget for e^2.motion

Quantity/Property/Parameter	**Unit**	**Nominal, aligned**	**Nominal, Misaligned**	**End Of Life, Misaligned**
Laser Wavelength	m	1,064E-06	1,064E-06	1,064E-06
Electron Charge	C	1,609E-19	1,609E-19	1,609E-19
Number of Photodiode segments		8	8	8
Initial AR coating transmission		0,999	0,999	0,999
Initial Beamsplitter Reflectivity		0,97	0,97	0,97
Initial Corner-Cube-Reflectivity		0,95	0,95	0,95
Receiver + Transmitter misalignment	µrad	0	100	100
Laser Power (adjusted to account for degradation)	W	0,1	0,1	0,3
Contamination per Interface	%	0,00%	0,00%	5,00%
Photodiode responsivity	A/W	0,8	0,8	0,4
Photocurrent AC per Segment	A	4,79E-07	3,01E-07	2,09E-07
Photocurrent AC rms per Segment	A	3,39E-07	2,13E-07	1,48E-07
Photocurrent DC per Segm.	A	2,98E-04	2,98E-04	2,67E-04
Relative Intensity Noise of Laser	$1/\sqrt{Hz}$	3,00E-08	3,00E-08	3,00E-08
	$dBc/\sqrt{Hz}$	-150,46	-150,46	-150,46

Photoreceiver noise per Segm.	pA/√Hz	5	5	5
PSD of Shot Noise per Segm.	A²/Hz	9,58E-23	9,58E-23	8,60E-23
PSD of Intensity Noise per Segm.	A²/Hz	7,97E-23	7,97E-23	6,43E-23
PSD Photoreceiver Noise per Segm.	A²/Hz	2,5E-23	2,5E-23	2,5E-23
Total Noise PSD per Segm.	A²/Hz	2,00E-22	2,00E-22	1,75E-22
Carrier-To-Noise Density per Segm.	Hz	5,72E+08	2,26E+08	1,25E+08
	db-Hz	**87,57**	**83,55**	**80,97**
Readout Noise per Segm.	rad/√Hz	4,18E-05	6,65E-05	8,95E-05
	m/√Hz	7,08E-12	1,13E-11	1,51E-11

5.3.7 Sensitivity, Noise and Error Contribution

The e^2.motion laser interferometer measures the distance variations $\rho(t)$ between two satellites by means of a round-trip pathlength $\rho_{RT}(t)$, which is obtained from phase measurements on both satellites ($\Psi_m(t)$ and $\Psi_s(t)$). The relation is given to first order as

$$\rho(t) = \frac{\rho_{RT}(t)}{2} = \frac{\lambda}{4\pi}\cdot\left(\Psi_m(t)+\Psi_s(t)\right)+\text{bias} \tag{5-25}$$

where a bias is introduced explicitly to remind that an interferometer is in general not capable to measure absolute distances, since an unknown constant bias is present. λ is the wavelength of the used laser light which relates the measured phase to an distance. The knowledge and errors in this scaling factor are discussed in section 5.3.7.5.

The measured inter-satellite distance $\rho(t)$ is subject to stochastic noise and deterministic errors. The sensitivity defines the maximum allowable stochastic noise in an instrument, while deterministic errors are described as tones.

The design sensitivity of the e^2.motion interferometer for the science measurement band is

$$\text{ASD}[\rho] = 25\frac{\text{nm}}{\sqrt{\text{Hz}}}\cdot\sqrt{\left(\frac{10\text{mHz}}{\text{f}}\right)^2+1} \quad 0.1\text{mHz} < \text{f} < 0.1\text{Hz} \tag{5-26}$$

while the measurements in the calibration band should and can be performed with lower noise, since at such frequencies the pointing jitter and laser frequency noise are significantly lower

$$\text{ASD}[\rho] = 25\frac{\text{nm}}{\sqrt{\text{Hz}}}\cdot\sqrt{\left(\frac{0.1\text{Hz}}{\text{f}}\right)^4} \qquad 0.1\text{Hz} < \text{f} < 0.3\text{Hz} \tag{5-27}$$

Many of the noise sources are uncorrelated, such that a simplified noise model of the interferometer can be written as sum of power spectral densities (PSD = ASD²)

$$\text{PSD}[\rho] = \text{PSD}[\text{LFN}](\text{f}) + \text{PSD}[\text{P}](\text{f}) + \text{PSD}[\text{T}](\text{f})\cdot c_t^2 + \text{PSD}[\text{I}](\text{f}) + \text{PSD}[\text{U}](\text{f}) \tag{5-28}$$

The major contributors are the laser frequency noise and attitude jitter noise. A description of the individual terms is given in the next four subsections.

5.3.7.1 Laser Frequency Noise

We remind that the e^2.motion interferometer is based on a transponder system, where the 'master' satellite emits frequency (and phase) stabilized light, while the slave satellite uses a phase-locked loop (PLL) with offset frequency to zero the measured phase ($\Psi_s(t) = 0$ in infinite gain limit of PLL, see section 5.3.2.2), omitting the linear phaseramp due to the offset frequency. The measured phase on the master satellite $\Psi_m(t)$ contains a term of the form

$$\varphi_m(t-\tau)-\varphi_m(t) \tag{5-29}$$

where φ_m is the phase of the frequency stabilized laser light and τ is the round-trip propagation time ($\tau = 100\frac{km}{c} \approx 0.66$ ms). Recall that the frequency is the time derivative of the phase and that a linear trend (ramp) induced by a constant frequency offset is usually subtracted for the phase measurement.

If the frequency stabilization is perfect, the phase does not change over time and the term (5-29) vanishes. If residual phase (frequency) fluctuations are present, they can be related to pathlength fluctuations $ASD[LFN](f)$ with units of m/$\sqrt{\text{Hz}}$ by the equation

$$\text{ASD}[\text{LFN}](f) = \frac{\text{ASD}[\nu](f)}{\nu}\cdot L \tag{5-30}$$

where L is the satellite separation (e^2.motion: L=100 km), $\nu = 281$ THz is the nominal laser frequency (for 1064 nm laser light), and $ASD[\nu](f)$ is the amplitude spectral density of the laser frequency fluctuations (unit: Hz/$\sqrt{\text{Hz}}$). (5-30) holds as long as the Fourier frequency f is much smaller than $1/(2\pi\cdot\tau) = 240$ Hz, which is true for gravimetric interferometer missions (the interesting frequencies are < 1 Hz, see section 5.1.4.

For e^2.motion a laser frequency stability requirement has been defined as

$$\text{ASD}[\nu](f) = \frac{20\text{Hz}}{\sqrt{\text{Hz}}}\cdot\sqrt{1+\left(\frac{10\text{mHz}}{f}\right)^2} \tag{5-31}$$

which corresponds to a pathlength noise of $ASD[LFN](f) = 8$ nm/$\sqrt{\text{Hz}}\cdot$NSF(f). Such a frequency stability is already difficult to achieve on LEO satellites and significant improvements within short timescales are not assumed (see section 5.3.8.4).

Remark: The laser frequency noise can also be seen as noise in the laser wavelength (or scaling factor). Thus, fluctuations of the laser wavelength within the interesting science measurement bandwidth do not need to be considered a second time, since they are covered by the laser frequency noise. The stability of the scaling factor within the measurement bandwidth, as discussed in section 5.4.5 for the accelerometer, is given by the relative frequency noise $ASD[\nu](f)/\,\nu$. The static error in the scaling factor knowledge is discussed in section 5.3.7.5.

5.3.7.2 Pointing Jitter Noise

Next to the laser frequency noise, the most important error contribution is the tilt-to-pathlength coupling. Pure rotations of a satellite should ideally not change the measured inter-satellite distance, but several effects induce a coupling. If $y(t), p(t), r(t)$ denote the yaw, pitch and roll attitude angles of a satellite w.r.t. to the nominal LOS pointing direction, the effect can be expanded to second order as series

$$\rho(t) \approx \begin{pmatrix} y(t) & p(t) & r(t) \end{pmatrix}\cdot\begin{pmatrix} c_y \\ c_p \\ c_r \end{pmatrix} + \begin{pmatrix} y(t) & p(t) & r(t) \end{pmatrix}\cdot\begin{pmatrix} c_{yy} & c_{yp} & c_{yr} \\ c_{yp} & c_{pp} & c_{pr} \\ c_{yr} & c_{pr} & c_{rr} \end{pmatrix} \tag{5-32}$$

The linear coupling terms can be written as

$$\begin{pmatrix} c_y \\ c_p \\ c_r \end{pmatrix} = \begin{pmatrix} V_x - SCoM_x \\ V_y - SCoM_y \\ 0 \end{pmatrix} + \overrightarrow{CC} + \overrightarrow{CO} \tag{5-33}$$

where the first term is dominating and denotes an offset between corner-cube vertex and spacecraft center-of-mass. The y- and z-directions are orthogonal to the line-of-sight (yaw rotation axis along y-axis, pitch rotation axis along z-axis). The second term $\overrightarrow{CC}$ accounts for imperfections of the corner-cube. $\overrightarrow{CO}$ denotes linear couplings due the optical bench. Some tilted or wedged components on the optical bench may introduce such couplings, e.g. a single tilted slab like the beamsplitter in e^2.motion yields a linear coupling in the order of mm/rad, while the compensation plate yields the same coupling with opposite sign, since it is tilted in the opposite direction (w.r.t. the transmitted beam). The residual remaining effect as the sum is in the order of a few µm/rad.

The dominating quadratic coupling factors are the yaw and pitch coupling factors

$$c_{yy} \approx c_{pp} \approx \frac{1}{2}\Delta z_{off} + \frac{1}{2}\left(V_x - \mathrm{SCoM}\ \right) \tag{5-34}$$

Δz_{off} is an offset in the waist location of the TX beam, or more general, of the center-of-wavefront curvature as measured at the distant satellite. Nominally the beam waist should be located on the steering mirror, but may vary by a magnitude of a (few) meters. Thus, the coupling has an approximated magnitude of 1 m/rad² and is usually dominating compared to the offset between corner-cube vertex and spacecraft center-of-mass along the line-of-sight $(V_x - SCoM_x)$. Also the optical bench and imperfections of the corner-cube induce quadratic effects, which are less important due to a magnitude of a few mm/rad².

Quadratic couplings cannot be treated with linear Fourier analysis (and spectral densities). Therefore one usually approximates the quadratic coupling by a linear coupling around a working point (here: $50\ \mu\text{rad} =\ 5 \cdot 10^{-5}$ rad) which yields the effective coupling factors:

$$\begin{pmatrix} c_{y,eff} \\ c_{p,eff} \\ c_{r,eff} \end{pmatrix} = \begin{pmatrix} V_x - \mathrm{SCoM}_x \\ V_y - \mathrm{SCoM}_y \\ 0 \end{pmatrix} + \overline{C}\vec{C} + \overline{C}\vec{O} + 5 \cdot 10^{-5} \cdot \begin{pmatrix} \Delta z_{off} + \left(V_z - \mathrm{SCoM}_z\right) \\ \Delta z_{off} + \left(V_z - \mathrm{SCoM}_z\right) \\ 0 \end{pmatrix} \tag{5-35}$$

The working point of $50\ \mu$rad corresponds to a static interferometer misalignment, which might be caused by corner-cube or optical bench imperfections.

The stochastic fluctuations of the satellite attitude, the so-called pointing jitter, induces a noise in the ranging measurement, which is approximated by linear effective coupling factors

$$\mathrm{PSD}\left[P\right]\left(f\right) = \sqrt{2} \cdot \sqrt{\mathrm{PSD}\left[y\right]\left(f\right) \cdot c_{y,eff}^2 + \mathrm{PSD}\left[p\right]\left(f\right) \cdot c_{p,eff}^2 + \mathrm{PSD}\left[r\right]\left(f\right) \cdot c_{r,eff}^2} \tag{5-36}$$

Which assumes a simplified model with uncorrelated yaw, pitch and roll rotations.

The factor of $\sqrt{2}$ is applied since two spacecraft need to be considered and the attitude jitter of both spacecraft is assumed to be uncorrelated. For e^2.motion a co-location between corner-cube vertex and S/C CoM of $70\ \mu$m is assumed (in transverse directions), a waist offset of $\Delta z_{off} = 0.5$m and additional corner-cube and optical bench contributions of 5 µm. Thus, the rotational coupling per S/C as linear sum yields

$$c_{y,eff} = c_{p,eff} = 100 \mu\mathrm{m} / \mathrm{rad} \tag{5-37}$$

A relaxation of one order of magnitude is assumed for the less sensitive roll-axis

$$c_{r,eff} = 10 \mu\mathrm{m} / \mathrm{rad} \tag{5-38}$$

The e^2.motion attitude jitter is assumed to be (cf. section 5.2.3)

$$\begin{aligned} \mathrm{ASD}\left[y\right]\left(f\right) &= \mathrm{ASD}\left[p\right]\left(f\right) = 100 \mu\mathrm{rad} / \sqrt{\mathrm{Hz}} \cdot \mathrm{NSF}\left(f\right) \\ \mathrm{ASD}\left[r\right]\left(f\right) &= 1000 \mu\mathrm{rad} / \sqrt{\mathrm{Hz}} \cdot \mathrm{NSF}\left(f\right) \end{aligned} \tag{5-39}$$

which yields ranging noise of

$$\mathrm{ASD}\left[P\right]\left(f\right) = \frac{24\mathrm{nm}}{\sqrt{\mathrm{Hz}}} \cdot \mathrm{NSF}\left(f\right) \tag{5-40}$$

Although the interferometer is designed to fulfill the sensitivity requirement with jitter noise, one should note that this noise can be subtracted partly in post-processing. Correlations between ranging data and satellite attitude data from interferometer (DWS) and star cameras can be used to estimate the coupling coefficients in orbit. Another option might be a special calibration maneuver, where the satellites are deliberately rotated to induce pathlength changes. A reduction of these errors by a factor of 10 is assumed to be achievable. In addition we assumed for the sake of simplicity in this derivation the same attitude jitter noise shape function as for the LRI, which over-estimates the noise at high frequencies. With a more realistic attitude jitter model the noise is sufficiently below the requirement given by equation (5-26).

5.3.7.3 Temperature Noise

The ranging measurement can be influenced by temperature fluctuations on the optical path and on the electrical path. The optical contributions are dominated by temperature induced refractive index change (dn/dT) and by linear thermal expansion (coefficient of linear thermal expansion α or CTE). The optical pathlength (OPL) temperature coupling for glass substrates in vacuum is

$$\frac{\mathrm{ds}}{\mathrm{dT}} = \alpha(\mathrm{n}-1) + \frac{\mathrm{dn}}{\mathrm{dT}} \tag{5-41}$$

The light paths through the beamsplitter and the compensation plate are sensitive to temperature fluctuations, while other paths benefit from high common mode rejection, since both RX and LO beam are affected. The thickness of both components is approx. $d = 10$ mm. The coupling coefficient for BK7 glass is in the order of $\frac{ds}{dT} \approx\ 10^{-5} \cdot 1/\mathrm{K}$, thus the temperature OPL coupling into the round-trip pathlength is roughly

$$\frac{\mathrm{dOPL}}{\mathrm{dT}} = \frac{\mathrm{ds}}{\mathrm{dT}} \cdot 2 \cdot \mathrm{d} = 200\frac{\mathrm{nm}}{\mathrm{K}} \tag{5-42}$$

A much higher coupling is due to the mechanical stability of the corner-cube retro-reflector. A design with CFRP structure like in GRACE Follow-On requires some engineering effort in terms of CTE matching and thermal modelling. For e^2.motion the use of a smaller corner-cube likely improves the situation. Additional usage of low CTE materials like Zerodur ($< 10^{-6} \cdot 1/\mathrm{K}$) can be envisaged.

The optical round-trip pathlength coupling of the corner-cube is assumed to be in the order of 300 nm/K, such that the total round-trip coupling per S/C is 500 nm/K.

A target thermal stability of $ASD[T](f) = 0.01\ K/\sqrt{\mathrm{Hz}} \cdot \mathrm{NSF(f)}$ at the compound of accelerometer, optical bench and corner-cube in e^2.motion yields to a ranging noise of

$$\mathrm{ASD}[\rho](\mathrm{f}) = 0.01\frac{\mathrm{K}}{\sqrt{\mathrm{Hz}}} \cdot \mathrm{NSF}(\mathrm{f}) \cdot 500\frac{\mathrm{nm}}{\mathrm{K}} \cdot \frac{1}{2} \cdot \sqrt{2} \approx 4\mathrm{nm}/\sqrt{\mathrm{Hz}} \cdot \mathrm{NSF}(\mathrm{f}) \tag{5-43}$$

where the factor ½ converts round-trip values to one-way, while $\sqrt{2}$ accounts for uncorrelated thermal noise on both spacecraft.

The electrical coupling is less critical, since a phase dependency of 10 mrad/K corresponds to a pathlength noise of only

$$\mathrm{ASD}[\mathrm{T}](\mathrm{f}) = 0.5\frac{\mathrm{K}}{\sqrt{\mathrm{Hz}}} \cdot \mathrm{NSF}(\mathrm{f}) \cdot 10\frac{\mathrm{mrad}}{\mathrm{K}} \cdot \frac{\lambda}{2\pi} \cdot \frac{1}{2} \cdot \sqrt{2} \approx 6\mathrm{nm}/\sqrt{\mathrm{Hz}} \cdot \mathrm{NSF}(\mathrm{f}) \tag{5-44}$$

if a thermal stability of more relaxed $0.5\frac{K}{\sqrt{Hz}} \cdot NSF(f)$ is assumed at the electronic boxes.

Recall that the noise-shape functions for temperature fluctuations are highly dependent on the thermal shielding of the components and on the structure design of the satellite. The thermal noise shape functions will have different dependencies than the noise shape function of the LRI sensitivity defined in (5-26).

Detailed thermal analysis of the spacecraft is beyond the scope of this report and especially $0.01\ K/\sqrt{\mathrm{Hz}}$ is assumed to be a tight requirement for a LEO satellite.

5.3.7.4 Readout Noise and Detection Limit

The readout noise is of minor importance for gravimetric missions, since the magnitude is far below other noise contributions.

The e^2.motion phasemeter shall be capable to acquire beatnote tracking for signals with higher carrier-to-noise-density than the minimal threshold

$$\mathrm{CND_{min}} = 75\mathrm{dB-Hz} = 10^{7.5}\,\mathrm{Hz} \tag{5-45}$$

which is a relaxed requirement compared to GRACE Follow-On and LISA levels (cf. section 5.3.8.5). The theoretical phase readout noise is given by the reciprocal CND, which can be related to a pathlength noise by

$$\mathrm{PSD}[P](f) = \frac{1}{\sqrt{\mathrm{CND_{min}}}}\frac{\lambda}{2\pi} \approx 30\frac{\mathrm{pm}}{\sqrt{\mathrm{Hz}}} \tag{5-46}$$

Thus, for all cases where the phasemeter can track the beatnote signal, the theoretical readout noise is sufficient small compared to other noise contributions like attitude jitter noise. A readout sensitivity better than 1 nm/√Hz for e^2.motion, which is equivalent to a phase noise of less than 6 mrad/√Hz, is easily achievable and was shown in several laboratory experiments as well as for the LISA phase readout system.

5.3.7.5 Scaling Factor

The scaling factor is a critical parameter for the e^2.motion accelerometer and the overall e^2.motion performance, in particular the knowledge of the absolute value (accuracy) as well as fluctuations within the science measurement band. In case of the accelerometer the scaling factor relates measured voltages to forces.

In case of the LRI the scale factor relates phases to distances (optical pathlengths). This factor is the wavelength (or equivalently the absolute laser frequency). The fluctuations of the LRI scale factor is the laser frequency noise (cf. section 5.3.7.1), which is stabilized to a macroscopic distance, well isolated and controlled in the frequency stabilization unit (cavity). From on-ground calibration of the laser crystal, in particular measurements of the dependency between crystal temperature and absolute laser frequency, one obtains absolute scaling factor knowledge of approx. 1 ppm:

$$\frac{\lambda_{\mathrm{true}}}{\lambda_{\mathrm{knowledge}}} \approx 1 \pm 10^{-6} \tag{5-47}$$

which corresponds to a knowledge of the absolute laser frequency of approx. 2 GHz. A typical temperature dependency is in the order of ~2 GHz/K, meaning that the crystal temperature needs to be measured to about 1 Kelvin.

5.3.7.6 Tone Errors

The tone errors are deterministic sinusoidal signals, which are driven by periodic external disturbances. The susceptibility of the LRI phase to magnetic field changes is assumed to be sufficiently small. However, the periodic transitions from sunlight illuminated to shadowed regions induce periodic temperature variations within the spacecraft, which are dependent on the spacecraft structure and thermal shielding. The thermal coupling coefficient of 440 nm/K from section 5.3.7.3 suggests that for periodic variations of the temperature of 1 K, the induced tones are sufficient small (440 nm) compared to the requirements from section 5.1.5.

The satellite CoM is assumed to be less stable w.r.t. to the LRI and ACC reference points, in particular, it will show periodic variations at integer multiples of the orbit frequency due to thermal expansion of the satellite structure and fluctuations e.g. due to propellant distribution changes. In contrast to the accelerometer measurement (cf. section 5.4.3), the LRI measurement is not directly dependent on the distance between LRI reference point (corner-cube vertex) and S/C center-of-mass. It is nevertheless affected indirectly via the attitude jitter coupling.

5.3.7.7 USO Phase Noise

The e^2.motion payload instruments use a common clock (ultra-stable oscillator) to sample the acceleration or ranging measurement. Since the LRI measures a phase of a MHz signal, small variations in the sampling time directly couple into the phase measurement. The corresponding displacement noise contribution with units of m/√Hz can be computed from the (single-sided) amplitude spectral density of USO phase variations (ASD[USO] with units of rad/√Hz) via

$$\mathrm{ASD}[\mathrm{U}](\mathrm{f}) = \frac{\mathrm{ASD}[\mathrm{USO}](\mathrm{f})}{2\pi \mathrm{f}_{\mathrm{USO}}} \cdot 2\pi \mathrm{f}_{\mathrm{het}} \cdot \frac{\lambda}{4\pi} \tag{5-48}$$

where f_{USO} is the frequency of the oscillator and f_{het} is the (maximum) heterodyne frequency of the beatnote. The stability of clocks is usually given in terms of Allan variations. We assume for e^2.motion a GRACE-like USO stability shown in Table 5-8.

Table 5-8: Specified stability of ultra-stable oscillator for GRACE

Integration time τ in sec	Allan deviation $\sigma_y(\tau)$
2	$2 \cdot 10^{-13}$
10	$2 \cdot 10^{-13}$
100	$3 \cdot 10^{-13}$
1000	$5 \cdot 10^{-13}$

We assume an USO phase noise model with units of rad²/Hz of the form

$$\mathrm{PSD}[\mathrm{USO}](\mathrm{f}) = \mathrm{h}_0 + \frac{\mathrm{h}_1}{\mathrm{f}^1} + \frac{\mathrm{h}_2}{\mathrm{f}^2} + \frac{\mathrm{h}_3}{\mathrm{f}^3} + \frac{\mathrm{h}_4}{\mathrm{f}^4} \tag{5-49}$$

The spectral density phase noise $PSD[USO](f)$ is defined here for positive frequencies f (single-sided) and contains the power contributions for negative frequencies (fold-over). The relation to the IEEE preferred single-sideband (SSB) phase noise (without fold-over) is $PSD[USO](f) = 2 \cdot \mathcal{L}(f)$. Typical values for high-frequency noise are in the order of $\mathcal{L}(f > 1\text{kHz}) \approx -155$ dBc/Hz, which yields $h_0 = 6.4 \cdot 10^{-16}$ rad²/Hz. From the well- known relationship between Allan variance and power spectral density

$$\sigma_y^2(\tau) = \frac{2}{(\pi \nu_0 \tau)^2} \int_0^{\mathrm{f}_\mathrm{h}} \mathrm{PSD}[\mathrm{USO}](\mathrm{f}) \cdot \sin^4(\pi \mathrm{f} \tau)\, \mathrm{df} \tag{5-50}$$

we derived based on GRACE USO specification the following low-frequency phase-noise formula, which serves as e^2.motion USO phase noise requirement

$$\mathrm{PSD}[\mathrm{USO}](\mathrm{f}) = \left(6.4 + \frac{7000}{\mathrm{f}^3} + \frac{80}{\mathrm{f}^4}\right) \cdot 10^{-16}\, \mathrm{rad}^2 / \mathrm{Hz} \tag{5-51}$$

where a USO frequency of $\nu_0 = 5$ MHz was assumed. The corresponding noise in the ranging measurement derived by (5-48) is below the e^2.motion LRI ranging sensitivity, as shown in Figure 5-23. A high performance USO as used in GRACE is required for e^2.motion to reach the ranging sensitivity.

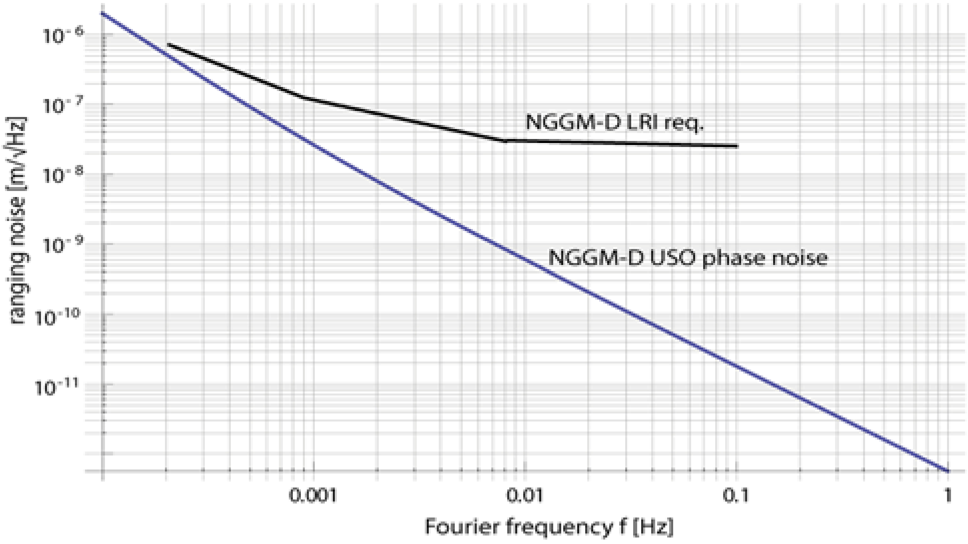

Figure 5-23: USO phase noise induced ranging error (blue) and e^2.motion LRI sensitivity (black).

5.3.8 Components

In this section some key components of the LRI are discussed and they technical readiness is assessed.

The redundancy scheme suggested for e^2.motion consists of cold-redundant optical benches and corner-cube retro-reflectors on each satellite, which are located on the front and back side of the accelerometer. The satellites can swap the ram direction (180 degree yaw rotation) such that the interferometer remains functional in case of failures e.g. of optical bench or of corner-cube retro-reflector due to micrometeorites or premature aging e.g. from space corrosion (atomic oxygen) or contamination.

5.3.8.1 Optical Bench

The optical bench accommodates the photodetectors with imaging system, a steering mirror, as well as the beamsplitter and a compensation plate. A fiber collimator is used to inject light onto the optical bench. An acquisition system consisting of CCD sensor and imaging system is also placed on the optical bench in case of e^2.motion (see Figure 5-19).

The racetrack configuration rejects many disturbances on off-axis paths, like from the imaging system or steering mirror. This allows designs based on conventional, easy machinable metals with low to medium coefficient of thermal expansion.

In Figure 5-24 an optical bench breadboard for the GRACE Follow-On interferometer is shown, which is based on an aluminum baseplate.

For high-precision interferometers also designs based on ultra-low CTE materials can be envisaged (cf. Figure 5-25), in particular a technique called hydroxide-catalysis bonding allows to produce quasi-monolithic connections between optical components (substrates) and baseplate. It has been elaborated for LISA Pathfinder and LISA optical benches and enables significantly higher stability e.g. against vibrations and temperature, but is probably unnecessary here.

The optical bench of e^2.motion benefits form heritage of the GRACE Follow-On LRI. For example, the use of wedged components for beamsplitter and compensation plate is advantageous to suppress signals from parasitic ghost reflections. The differential wedge angle of beamsplitter and compensation plate is of importance, since it directly influences the beam co-alignment. However, the overall design is robust against misalignments as Monte-Carlo simulations have shown.

Due to the long mission duration some effort is required to decrease and control contamination of optical surfaces. This topic needs to be addressed in early stages of mission design.

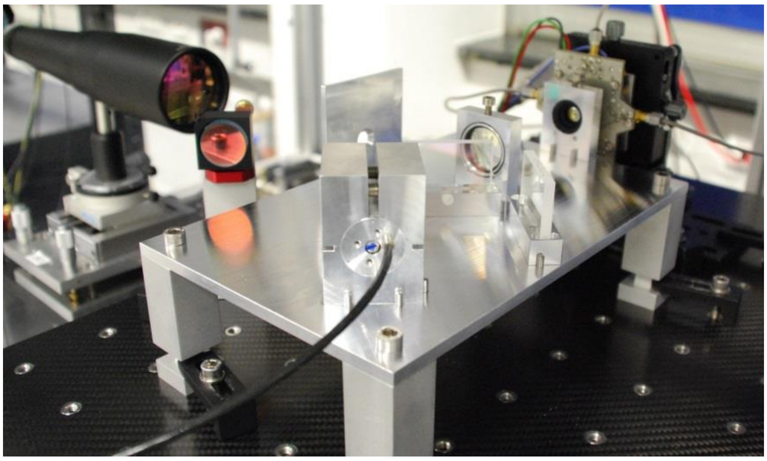

Figure 5-24: Aluminum breadboard of GRACE Follow-On optical bench with steering mirror (front) and non-redundant photodetector (back, right). Source: AEI Hannover

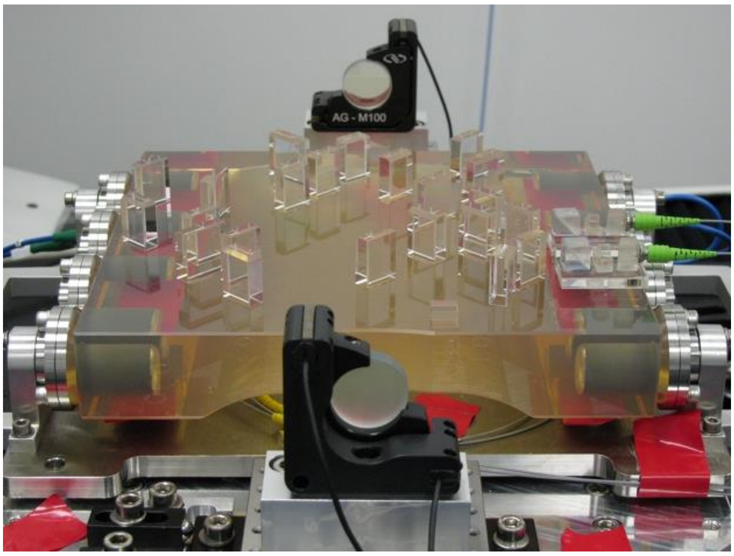

Figure 5-25: Zerodur® optical bench of LISA Pathfinder with fiber collimators (right) and two mirrors (front and back) acting as test mass simulator. Source/Copyright: University of Glasgow (http://sci.esa.int/jump.cfm?oid=51960)

5.3.8.2 Corner-Cube Reflector

Retro-reflectors, in particular corner-cubes, are commonly used for ground-based tracking of satellites and are usually mounted at the nadir face of the satellite. They also function as calibration devices for optical instruments and are commercially available with co-alignments in the arcsecond region (e.g. by PLX Inc.).

For GRACE Follow-On LRI the design and manufacturing of a corner-cube with 600mm lateral beam offset required some effort. In particular verification of the co-alignment over such large separation is non-trivial. For e^2.motion a lateral offset of 300mm can significantly decreases complexity, since commercial large aperture interferometer can be used to determine wavefront planarity and co-alignment. The separation between the lateral frame axis and vertex point is roughly $300\text{mm}/\sqrt{2} \approx 210\text{mm}$, defining also the required position of the accelerometer reference point and S/C center-of-mass.

The main requirements of the passive component concern the reflectivity (>95%), wavefront distortion, polarization change and co-alignment (< 50 µrad). The optimal design for a 300mm e^2.motion corner-cube needs to be determined. The GRACE Follow-On LRI is based on a CFRP tube frame (cf. Figure 5-26), while also a ceramic bar has been considered (cf. Figure 5-27). Although significant heritage from GRACE Follow-On exists, the long mission duration requires analysis and risk mitigation of optical surface contamination and space corrosion due to atomic oxygen.

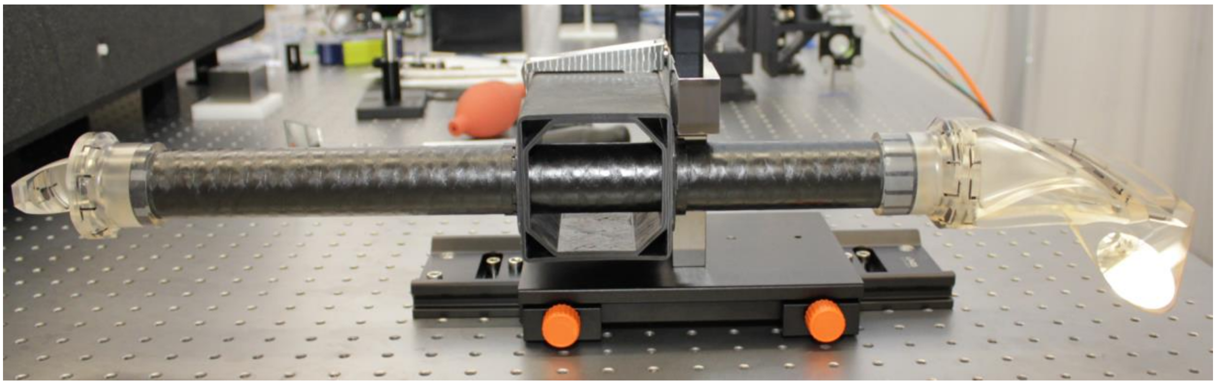

Figure 5-26: GRACE Follow-On LRI Triple-Mirror-Assembly (corner-cube retro-reflector) consisting of 600mm CFRP tube with approx. 40 mm diameter. Light is reflected at the mirror on the left side, into the tube. On the right side light is reflected by two other mirrors. Manufactured by STI Immenstaad and Cassidian-Zeiss.

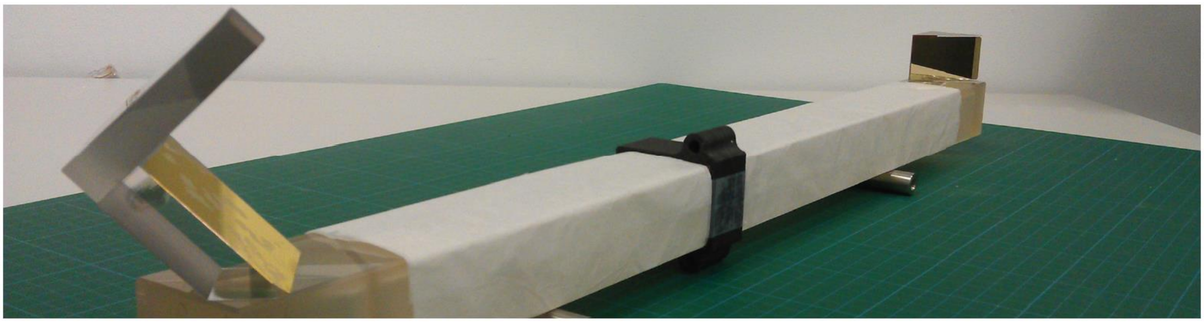

Figure 5-27: A 600 mm lateral offset corner-cube retro-reflector developed by a consortium led by Centre for Gravitational Physics, Australian National University (ANU). The bar is based on a light-weight ceramic structure. Two mirrors are on the left side, while another mirror is on the right side. Source: “Retroreflector for GRACE follow-on: Vertex vs. point of minimal coupling”, D. Schütze et al, Opt Express. 2014 Apr 21;22(8):9324-33. doi: 10.1364/OE.22.009324.

5.3.8.3 Laser

Satellite laser interferometer missions like LISA Pathfinder and GRACE-Follow-On use solid-state Nd:YAG lasers configured as a non-planar ring oscillator (NPRO), which generate 1064 nm light with up to a few tens milli-Watts of optical power. The advantages of NPRO lasers are a high mechanical stability, a narrow linewidth of a few kHz and a high free spectral range of a few GHz. The laser frequency can be tuned mechanically by inducing stress with a piezoelectric transducer, by changing the crystal temperature or by adjusting the pump power. A NPRO laser is usually pumped with laser diodes and offers a low noise in terms of intensity and frequency.

The e^2.motion laser is based on the currently developed e^2.motion High Stability Laser, which can deliver approx. 500 mW optical power at a wavelength of 1064nm. It is based on a NPRO laser and a fiber amplifier. Similar concepts have been analyzed also for the LISA mission with promising results.

A well-known issue is the reliability of pump diodes for the fiber amplifier and NPRO, especially considering the long e^2.motion mission duration. Bars or arrays of pump diodes have been commercially developed over the last two decades, providing high optical power (55W) and reliability (e.g. Coherent © 55W 870-890 nm CCP, MTTF > 20,000 hours ~ 2.3 yrs). Diodes operated at low loads show in general increased lifetime, such that multiple devices operated in cold redundancy can provide the desired pump light over 11 years.

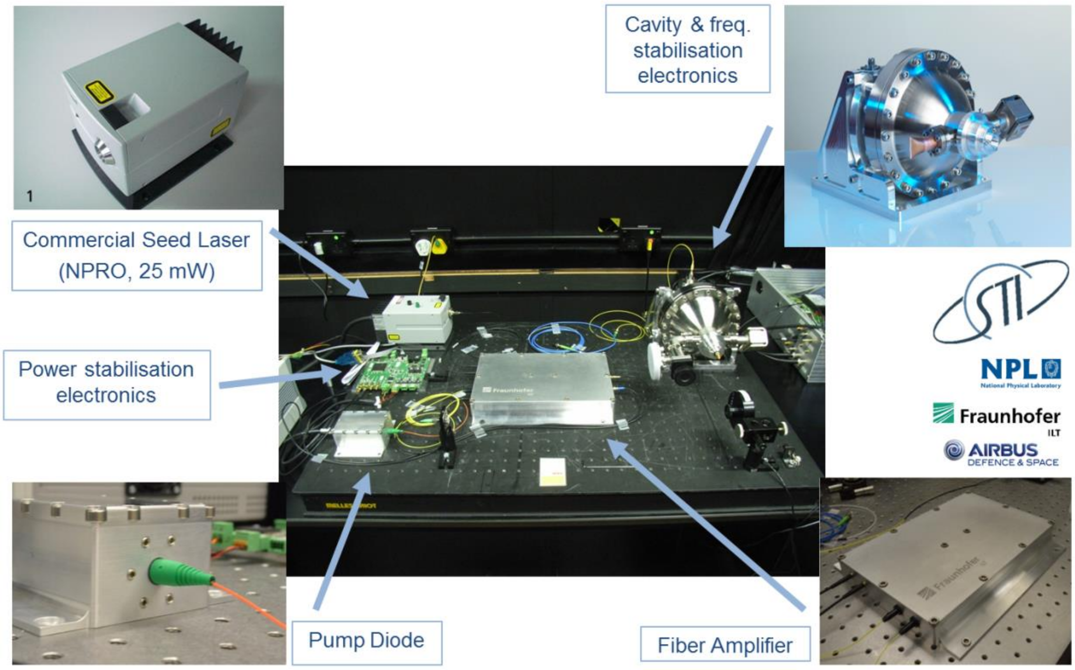

Figure 5-28: Breadboard setup of the e^2.motion High Stability Laser (picture from SpaceTech GmbH Immenstaad, Germany).

5.3.8.4 Frequency Stabilization

The laser wavelength or frequency defines the relation between the (laser) phase measurements and optical pathlengths. It must be stabilized because (1) it defines the scale and (2) frequency noise couple into the length measurements. A common approach is to apply a weak phase modulation onto the light, which is sent into an optical cavity of a few (ten) centimeter size (see Figure 5-29, left). The cavity is usually made out of ultra-stable materials and is well controlled in temperature. The reflected light can be used to generate a feedback signal to keep the light resonant in the cavity by shifting the laser frequency e.g. with the NPRO piezo-electric actuator (Pound-Drever-Hall technique).

Such a scheme is the baseline for the GRACE Follow-On mission, where a frequency stability of approx. 30 Hz/$\sqrt{\text{Hz}}$, 40 Hz/$\sqrt{\text{Hz}}$, and 700 Hz/$\sqrt{\text{Hz}}$ at 1 Hz, 10 mHz and 1 mHz, respectively, has been reached. This corresponds to a relative stability of $1 \cdot 10^{-13}\ 1/\sqrt{\text{Hz}}$, $1.4 \cdot 10^{-13}\ 1/\sqrt{\text{Hz}}$ and $2.5 \cdot 10^{-12}\ 1/\sqrt{\text{Hz}}$ for light with a wavelength of 1064 nm. Such stability is already close to fundamental limits like thermal noise (see Figure 5-29, left) and is difficult to achieve with thermal conditions in laboratories. Significant improvements for e^2.motion with low-earth orbit thermal variations cannot be expected.

Alternatively, a frequency can be stabilized to an atomic or molecular energy transition (absorption line). In particular a Iodine cell offers the opportunity to lock the second harmonic (532 nm) of a Nd:YAG laser to a transition and promising results have been achieved on breadboard level (cf. Figure 5-30). However, to reach the stability of a cavity, such systems show comparable complexity.

The e^2.motion requirement of 20 Hz/$\sqrt{\text{Hz}} \cdot \text{NSF}(f)$ is demanding and only slightly tighter than the GRACE Follow-On LRI requirement. The laser system NGGM-HSL has currently a requirement of 40 Hz/$\sqrt{\text{Hz}} \cdot \text{NSF}(f)$. By the time of the writing final experimental results of the frequency stability of NGGM-HSL were not available, but it is expected that the performance will be close to the values required for e^2.motion.

Recall that a e^2.motion link only requires one frequency stabilization unit on the master satellite, while the slave satellite has a phase-locked laser to the incoming beam. By accommodation of laser frequency stabilization units on both satellites they can be operated in cold redundant mode, since the role of master/slave can be swapped.

The frequency stability of the laser ranging instrument corresponds to the USO phase stability for the GRACE microwave ranging instruments or to the scale factor stability of the accelerometer.

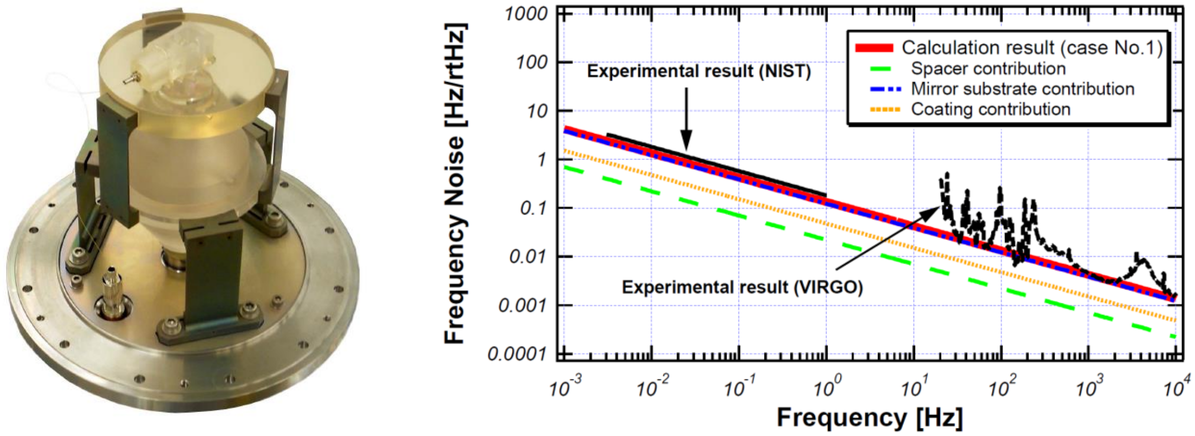

Figure 5-29: (Left) ULE cavity of a GRACE Follow-On LRI Prototype Frequency Stabilization (without housing). Source: "A Flight-Like Optical Reference Cavity for GRACE Follow-on Laser Frequency Stabilization", R. Thompson et al., 2011, Frequency Control and the European Frequency and Time Forum (FCS), 2011 Joint Conference of the IEEE International, vol., no., pp.1,3, 2-5 May 2011 doi: 10.1109/FCS.2011.5977873; (Right): Thermal noise limit in rigid cavities for 563 nm light (532 THz). In case of 1064 nm light with same relative frequency stability the frequency noise needs to be multiplied by a factor of approx. 2, Source: "Thermal-Noise Limit in the Frequency Stabilization of Lasers with Rigid Cavities", Kenji Numata et al., 2004, Phys. Rev. Lett. 93, 250602.

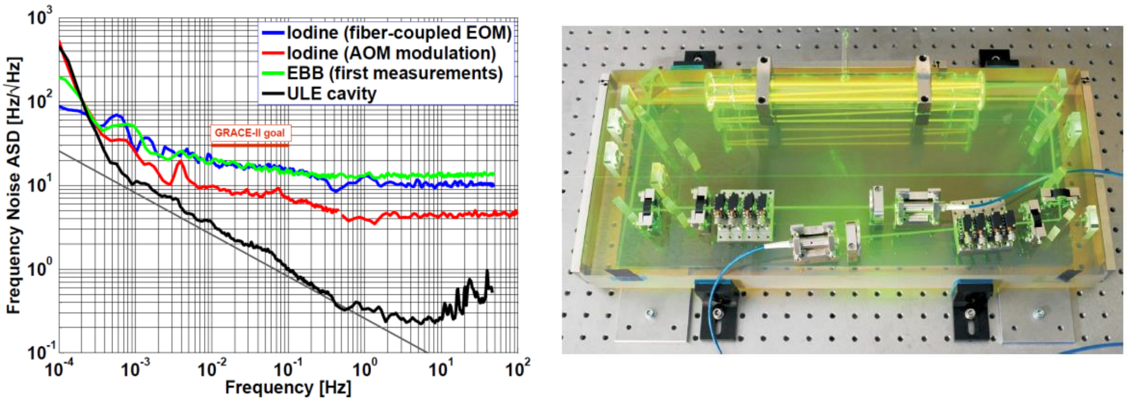

Figure 5-30: Results of a laser frequency stabilization based on an iodine cell on breadboard level, Source: “Iodine based optical frequency reference with 10^{-15} stability”, Dohringshoff K., European Frequency and Time Forum (EFTF), 2012 , vol., no., pp.419,421, 23-27 April 2012 doi: 10.1109/EFTF.2012.6502415

5.3.8.5 Phasemeter

The phasemeter is an essential part of the LRI. It has to track the phase of the MHz signals of each photodiode segment. Fast electronics based on Field-Programmable-Gate-Arrays (FPGAs) has proven to be s suitable. FPGAs have been used for space applications many times. Additional front-end electronic like Digital-to-Analog and Analog-to-Digital converter (DAC/ADC) are required to control the steering mirror, the laser and frequency stabilization, and to read in several signals like AC and DC channels of the photoreceiver, steering mirror and laser sensors. It can also be used to read out high performance temperature sensors.

The GRACE Follow-On LRI Phasemeter has been developed by JPL/NASA. A European study for the LISA Metrology System developed a phasemeter up to TRL 4. Such a LISA like phasemeter offers additional features to reach the desired $\mathrm{pm}/\sqrt{\mathrm{Hz}}$ in a deep-space environment, e.g. corrections for USO drifts and ADC timing jitter subtraction and capability for data transfer via modulations of the laser light. A reduced subset of the LISA phasemeter fulfills all requirements of the e^2.motion mission. Reaching $\mathrm{nm}/\sqrt{\mathrm{Hz}}$ without corrections is easily achievable at high frequencies, whereby low frequencies are dominated by ADC timing jitter noise induced by USO phase noise.

The latter noise source is in general not visible in laboratory setups where a common clock (USO) is used for the whole setup and no other reference with higher stability in terms of frequency (e.g. clock, USO) or distance (e.g. ultra-low-expansion optical cavity) is present. The e^2.motion phasemeter can be based on the LISA metrology system, however, with substantial reduction in complexity since “only” $\mathrm{nm}/\sqrt{\mathrm{Hz}}$ sensitivity is required for e^2.motion. Some effort is still required to reach TRL 6 or higher, in particular decrease in power consumption and dissipation as well as thermal stability.

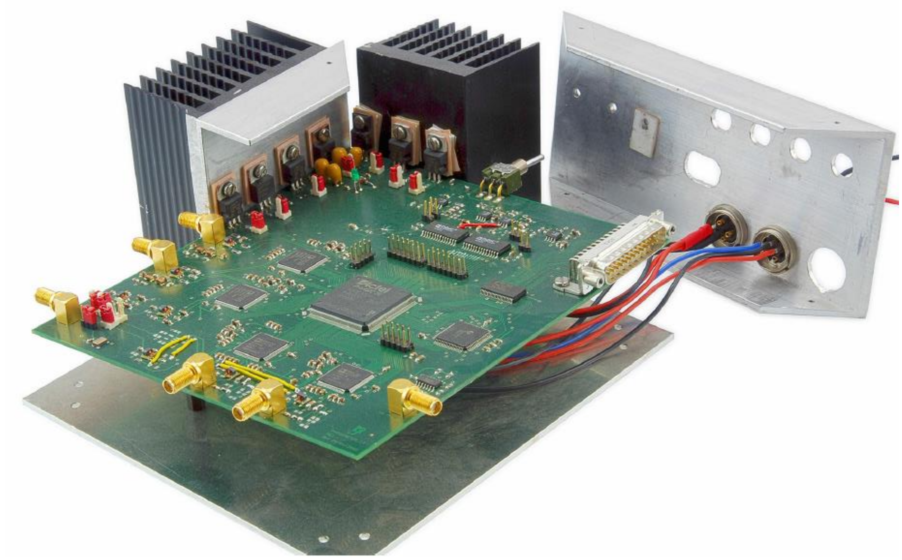

Figure 5-31: A typical 4 channel FPGA based phasemeter developed at AEI Hannover.

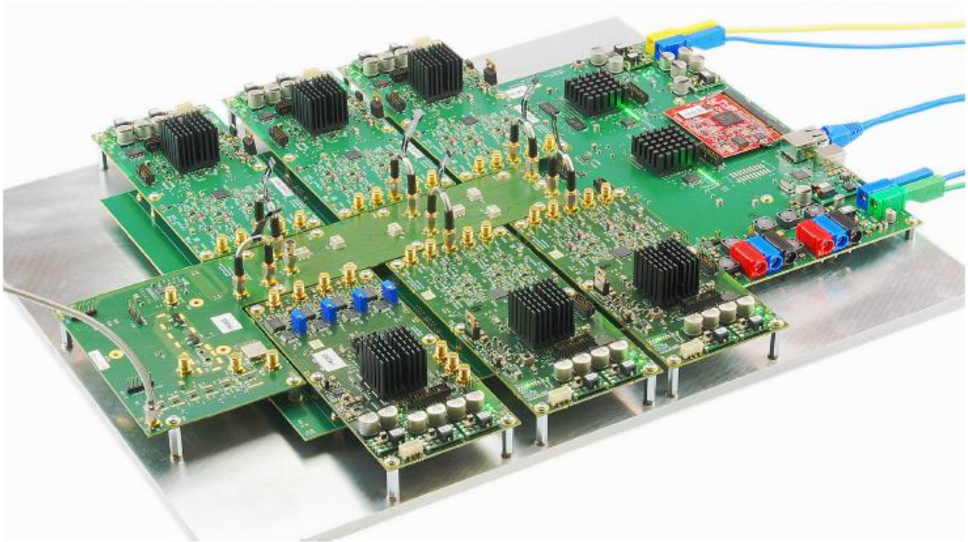

Figure 5-32: Engineering Breadboard of LISA-like phasemeter developed by DTU Space (Denmark), Axcon ApS (Denmark) and AEI (Germany). It is based on a FPGA and on a modular design. The main module is equipped with a clock module, an ADC module (4 channels) and a DAC module (4 channels).

5.3.8.6 Acquisition Sensor

CCD sensors for interferometer link acquisition have been studied for the LISA mission on laboratory breadboard level. A two lens system is suitable to focus the light in the acquisition aperture onto a few pixel of the sensor and to convert at the same time a wavefront tilt into a spot displacement. A COTS device like the InGaAs sensors *Goodrich SU320* with 320x256 pixels should be capable to detect 100 fW on 2x2 pixels with a signal-to-noise ratio >50 for integration times around 1 second (see Figure 5-33). The determination of the LOS with approx. ±30 µrad is sufficient for e^2.motion. The LISA mission requires an accuracy of ±8 µrad, but has a light level of at least 1 pW and a bandwidth requirement of 10 Hz.

The acquisition sensor for e^2.motion is less mature than other interferometer components, since flight hardware heritage is not available from GRACE Follow-On or LISA Pathfinder. In addition the background illumination in a LEO orbit needs to be assessed in detail.

Figure 5-33: InGaAs CCD sensor ‘Goodrich SU320KTSX’ (source: product data sheet, Goodrich)

5.3.8.7 Photodiodes

Photodiodes convert an optical power into an electric current exploiting the inner photoelectric effect. The absorption of photons takes place in an active region based on a semiconductor material. Different materials yield a different responsivity w.r.t. light wavelength. Commercially available detectors out of InGaAs offer the highest effective responsivity of approx. 0.8 A/W for 1064nm light. Silicon sensors usually achieve only approx. 0.4 A/W or less for such a wavelength.

Next to the responsivity, which is limited for interferometer applications to approx. 0.862 A/W due to the quantum efficiency, the other important property is the bandwidth of the detector. It is usually limited by the capacitance of the sensor, since the cut-off frequency is proportional to the inverse capacity. The capacity is dependent on the size of the detector, which limits the active area size to less than 1 mm², if signals up to 20 MHz shall be detected. Typical capacities are in the region of a few ten pico-Farads for satellite interferometric applications.

The LISA Pathfinder mission utilizes heterodyne interferometry with beatnotes in the region of 1 kHz, therefore, also larger photodiodes are sufficient and only indirect heritage (e.g. of handling) can be provided. However, for the GRACE Follow-On mission several small Quadrant-Photodiodes have been space qualified. A typical diode is the commercially available InGaAs-Q1000 by OSI Opotoelectronics Inc., which offers low cross-talk between neighboring segments and low dark current. In combination with low-noise photoreceiver an equivalent input current noise of approx. 5 $\text{pA}/\sqrt{\text{Hz}}$ has been shown on laboratory and engineering model level, which is sufficient for e^2.motion.

A concern is the degradation of responsivity and increase in dark current due to LEO radiation, which needs to be addressed e.g. by additional shielding if applicable. The degradation in responsivity or quantum efficiency is in general not distinguishable from a decrease in laser power, and sufficient margin should be provided in the power link budget.

Figure 5-34: InGaAs Quadrant-Photodiodes with housing by OSI Opotoelectronics Inc. Source: Product data sheet.

5.4 Accelerometer

The accelerometer is a main scientific instrument. It shall measure the non-gravitational accelerations acting on the satellite induced by

- Residual atmospheric drag
- Satellite thruster
- Solar radiation pressure
- Earth’s albedo radiation pressure
- Lorentz force due to interaction of charged satellite with geomagnetic field
- other (unexpected) disturbances

The accelerations shall be measured in three orthogonal directions.

5.4.1 Measurement Principle

An accelerometer consists usually of an cuboid conductive mass, called ‘proof mass’ (PM) or ‘test mass’, located within an evacuated electrode housing, which is only a few tens micrometer larger than the PM. The PM can be charged using a thin (5 micrometer) gold wire. Its position within the housing can be measured using capacitive sensing by the electrodes. The position within the housing can be changed by applying an electro-static force using the electrodes. In closed-loop mode the capacitive sensing signal is fed back into a controller, which centers the position of the PM with high gain and high bandwidth (‘levitation of the proof mass’).

If the PM is centered within the housing, the center of mass of PM and housing coincide, and the proof mass stays centered under free fall conditions, where only gravitational accelerations are acting on the PM and housing. No electro-static force needs to be applied. If non-gravitational forces like drag are acting on the housing, the control loop applies electro-statically the same force with opposite sign to keep the PM centered. The control signals are therefore the measurement of the non-gravitational accelerations.

If the accelerometer housing is mounted rigidly into a satellite, the trajectory of the housing is defined by the center-of-mass of the whole satellite. The e^2.motion baseline foresees that the accelerometer proof mass is located close to the satellite center of mass. An offset between CoM of PM and S/C induces a constant acceleration proportional to the gravity gradient. In addition pseudo-forces depending on the rotation of the satellite couple into the measurement. Therefore the use of a mass trim unit is envisaged, such that the offset can be kept smaller than 30 µm by periodic calibrations.

5.4.2 Available Instruments

Accelerometers (ACCs) are commonly used in gravimetric satellite missions and are also widely used in other missions (e.g. SWARM). The French company ONERA has built the ACCs for the gravimetric missions CHAMP (STAR), GRACE (SuperSTAR), GOCE (GRADIO) and GRACE Follow-On and was also involved in the prequel NGGM study. The nominal accuracy levels of these instruments within a dedicated measurement bandwidth (ACC-MBW) are $10^{-9}\ \frac{\mathrm{m}}{\mathrm{s}^2\sqrt{\mathrm{Hz}}}$ (CHAMP), $10^{-10}\ \frac{\mathrm{m}}{\mathrm{s}^2\sqrt{\mathrm{Hz}}}$ (GRACE) and $10^{-12}\ \frac{\mathrm{m}}{\mathrm{s}^2\sqrt{\mathrm{Hz}}}$ (GOCE).

The ACC-MBW is the frequency band with white instrument noise floor and should not be confused with the much wider science measurement bandwidth (MBW). These ACC accuracies hold for the two high-sensitive axes respectively. Each ACC typically has one less-sensitive axis.

For e^2.motion the less-sensitive axis is worse by a factor of 10. It is not trivial to determine the real accuracies of these sensors, which are reached in orbit. For GRACE there are several significant disturbing effects in the observations, e.g. due to heater switches. For GOCE the situation is better as there are six ACCs implemented on three orthogonal axes around the center of mass of the satellite. By analyzing the differences of these sensors several correlated error contributions can be reduced. Figure 5-35 shows the ASD of different accelerometer noise models in comparison with the e^2.motion requirement for the accelerometer and the laser ranging instrument (LRI) and with a possible e^2.motion target signal, a monthly mean hydrology and ice signal (computed up to spherical harmonic degree and order 150 for the polar pair of the baseline scenario).

The $1/f^2$ part below the ACC-MBW ($f < 1$ mHz) might be more realistic than the assumptions for the GRACE and e.motion noise model. One critical parameter could be the lowest limit of the MBW at 1 mHz compared with the other models. The total observation noise is dominated by the ACC noise for $f < 7$ mHz, and by the LRI noise for $f > 7$ mHz.

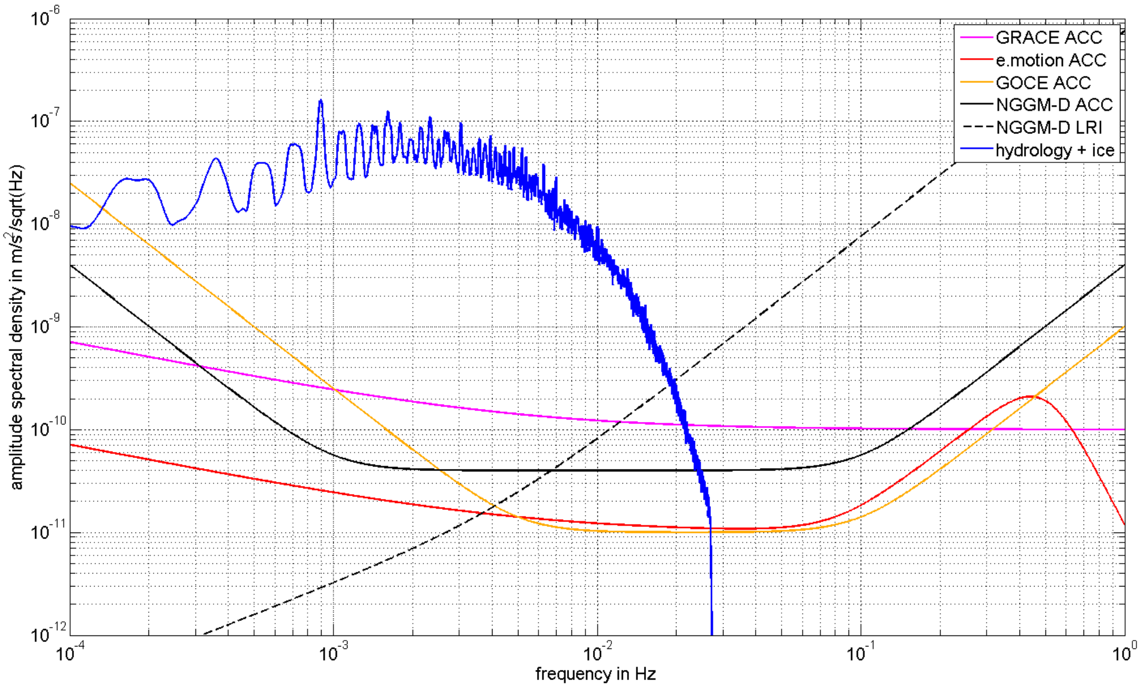

Figure 5-35: Amplitude spectral densities (ASDs) in $\frac{\mathbf{m}}{\mathbf{s^2\sqrt{Hz}}}$ of different ACCs in comparison with the e^2.motion requirement for the ACC and the laser ranging instrument and with a possible e^2.motion target signal, a monthly mean hydrology and ice signal (computed up to spherical harmonic degree and order 150 for the polar pair of the baseline scenario). The e^2.motion LRI trace does not consider a slightly increased sensitivity in the calibration bandwidth (0.1 Hz to 0.3 Hz).

There are several previous NGGM studies dealing with a low-low SST concept defining requirements for ACC and LRI. Table 5-9 shows the requirement values within the ACC-MBW together with the proposed altitudes and formations.

Table 5-9: Instrument requirements (within the ACC-MBW) of selected previous future low-low SST studies together with altitudes and formations

Study (Ref.)	**Altitude in km**	**Formation**	**ACC req. in $\mathbf{10^{-12}\ \frac{m}{s^2\sqrt{Hz}}}$**	**LRI req. in nm/√Hz**
e^2.motion	420	Bender	40	20
e.motion [9]	370	Pendulum (15° maximum yaw angle)	10	50
NGGM-TAS [10]	330 and 420	Bender and Pendulum (45°, 4 ACC)	10	20
NG2 [11]	315 and 360	Bender and Pendulum (15°)	2	20
BMBF study (Reubelt, et al., 2014)	300 and 335	Pendulum (24° and 45°)	2	50

5.4.3 Sensitivity

The measurement sensitivity of non-gravitational accelerations has been defined in equation (5-6). This top-level requirement contains intrinsic accelerometer noise sources (e.g. electronic noise), but also extrinsic contributions from the spacecraft or environment. A simplified model for the measurements with the accelerometer in all 3 dimensions is given by:

$$\vec{a}_{meas}(t) = \hat{S}\cdot\hat{R}_{ACC}\cdot\left(\hat{G}\cdot\vec{r} - \hat{w}^2\cdot\vec{r} - 2\hat{w}\cdot\frac{d}{dt}\vec{r} - \frac{d}{dt}\hat{w}\cdot\vec{r} + \hat{R}_{SC}\cdot\vec{a}_{ng}\right) + \vec{b} + \vec{n} \qquad (5\text{-}52)$$

where $\vec{a}_{ng}$ is the non-gravitational acceleration given in inertial space frame, $\vec{r}$ the offset between S/C and PM center of mass in the local spacecraft frame, $\hat{G}$ the gravity gradient in local spacecraft frame, $\hat{w}$ the angular velocity tensor in local spacecraft frame, $\vec{b}$ accelerometer bias, $\hat{R}_{ACC}$ accounting for misalignments of the accelerometer axes w.r.t. the local spacecraft frame, $\hat{R}_{SC}$ the rotation matrix from inertial frame to local spacecraft frame, $\hat{S}$ a diagonal scaling factor matrix and $\vec{n}$ is the instrument sensor noise.

The components of the vector $\vec{a}_{\text{meas}}(t)$ refer to the signals along the accelerometer axes (accelerometer frame).

Based on equation (5-52) it is obvious that the accelerometer proof mass shall be co-located as close as possible with the satellite center of mass to avoid coupling of gravity gradient and satellite attitude variations (pseudo-forces) into the accelerometer measurements. The use of a Mass-Trim-Unit (MTU), as in GRACE, is desired for e^2.motion to adjust the co-location of both points to better than 30 μm in orbit (mean over several days). The structural stability of the whole satellite (S/C CoM) as well as the stability of the accelerometer reference point (ACC-RP) needs be optimized to keep the variations as small as possible.

In particular the effects induced by the offset between S/C CoM and ACC RP (pseudo accelerations) shall not limit the accelerometer sensitivity, namely,

$$\mathrm{ASD}\left[\hat{G}\cdot\vec{r}-\hat{w}^2\cdot\vec{r}-2\hat{w}\cdot\frac{d}{dt}\vec{r}-\frac{d}{dt}\hat{w}\cdot\vec{r}\right](f)<\frac{1}{4}\cdot\mathrm{ASD}\left[\mathrm{ACC}_x\right](f) \qquad (5\text{-}53)$$

for all three accelerometer axes.

The accelerometer instrument sensor sensitivity (intrinsic noise) is defined in the ultra-sensitive directions (x – along-track, z - radial) as given in equation (5-6) and one order of magnitude worse in the less sensitive axis y (cross track). A less sensitive axis is usually present due to deficiencies in on-ground calibration due to 1g conditions. The instrument noise levels assumed for e^2.motion seem to be feasible and realistic, considering that the previous NGGM studies with industry partners claimed to reach sensitivity levels in the region of $10^{-12}\ \frac{\mathrm{m}}{\mathrm{s}^2\sqrt{\mathrm{Hz}}}$.

5.4.4 Saturation

The dynamic range of the accelerometer is limited, e.g. to due to maximal applicable force on the proof mass, or electronic constraints (e.g. range of the analogue-to-digital converter). This saturation limit is assumed to be for a e^2.motion mission at $\pm 4\cdot 10^{-6}\,\mathrm{m/s^2}$.

The environmental conditions or the drag compensation should ensure the measured signal with the accelerometer in science mode does not exceed the maximum level (in time domain). Short and infrequent periods of saturation may be acceptable (e.g. during orbit maintenance maneuvers or unexpected events) and should not harm the accelerometer. Since the measurement sensitivity is degraded during saturation, periods of accelerometer saturation should be marked or flagged in the data streams.

As discussed above accelerometer saturation due to residual atmospheric drag is not expected in e^2.motion. In addition equation (5-10) imposes a similar requirement on the maximum allowable amplitude for the low-frequency part of the data, when the drag compensation loop is closed.

5.4.5 Scale Factor and Bias

The accelerometer measures voltages, which produce an electro-static force. If the mass of the proof mass (m) is known, the force can be related to an acceleration (a). The transfer function T, which relates voltages u to an acceleration a is defined by:

$$T=\frac{F}{m\cdot u}=\frac{a}{u} \qquad (5\text{-}54)$$

The transfer function is in general not constant and may be influenced by changes of the 'proof mass' mass due to contamination, bias voltage fluctuations of the proof mass, reference voltage fluctuations within the instrument, temperature of electronics and electrode housing, aging effects and so on.

The relative deviation of the nominal transfer function from the true transfer function is the so-called scaling factor and it is usually close to unity.

$$s = \frac{T_{true} - T_{nom}}{T_{nom}} = 1 + \varepsilon \tag{5-55}$$

If an acceleration (x) is measured with a scaling factor s_{true} and noise $n(t)$, the accelerometer provides a value:

$$a(t) = s_{true} \cdot x(t) + n(t) = (1 + \varepsilon_{true}) \cdot x(t) + n(t) \tag{5-56}$$

We assume the scaling factor is known, e.g. form a measurement, as value s_{know}.

Then the true error of the measurement, which is given by $a(t)/s_{know} - x(t)$, has an amplitude spectral density of:

$$\mathrm{ASD}\left[\frac{a(t)}{s_{know}} - x(t)\right] \approx \mathrm{ASD}[x](f) \cdot (s_{true} - s_{know}) + \mathrm{ASD}[n](f) \tag{5-57}$$

If the signal level is too high compared to the noise level, the measurement sensitivity (noise level) is dominated by the product of scaling factor term $\Delta s = (s_{true} - s_{know}) = \Delta\varepsilon$ and the signal and not by the noise term.

Note: For particular measurements, where the absolute magnitude of a value does not matter, the scaling factor knowledge and stability might be unimportant. However, since e^2.motion *combines ranging measurements with accelerometer measurement, which have different scaling factors, the issue cannot be neglected.*

We identified the scaling factor as a critical parameter for the overall e^2.motion sensitivity. The knowledge for previous missions and studies is shown in Table 5-10. Currently the scale factor is estimated to 1% accuracy, however, various studies for future geodesy missions assume a significantly improved scaling factor knowledge, without providing technical details how to reach the accuracy. For e^2.motion a scaling factor knowledge of 0.2% is assumed, which directly implies requirements on the drag compensation level.

The scaling factor for the x-direction (close to line-of-sight direction) will be measured in e^2.motion using a calibration scheme. For the y (~cross-track) and z (~radial) direction the requirement can be relaxed to 5%, since these accelerometer axes are almost orthogonal to the line-of-sight.

Table 5-10: Comparison of different missions and studies regarding scale factor knowledge and stability

Mission / Concept / Study	**Scale Factor Knowledge DC**	**Stability in MBW**
Alenia study [3]	0.02 %	$5 \cdot 10^{-8}\ 1/\sqrt{\mathrm{Hz}}$
FGM simulations (Reubelt, et al., 2014)	0.01 %	$1 \cdot 10^{-6}\ 1/\sqrt{\mathrm{Hz}}$
NGGM [9]	-	-
NG2 by Astrium [11]	0.001 %	$1 \cdot 10^{-6}$
GRACE/CHAMP	1%	unknown
GOCE-simulation	1%	$1 \cdot 10^{-2}$
GOCE-diff-measured	0.01%	$1 \cdot 10^{-5}$

So far the scaling factor has been assumed as time-independent. However, this is of course only an approximation. We assume that ε_{DC} is the constant part of the scaling factor, which is known up to 0.2% using the continuous calibration scheme. It corresponds to the average over several orbit revolutions and is therefore out of the interesting measurement band. The time-dependent part with higher frequency contributions is denoted as $\varepsilon_{AC}(t)$ such that:

$$s_{true}(t) = 1 + \varepsilon_{true,DC} + \varepsilon_{true,AC}(t) \tag{5-58}$$

In the same manner we expand an acceleration (x), which is measured by an accelerometer as:

$$a(t) = s_{true}(t) \cdot x_{AC}(t) + s_{true}(t) \cdot x_{DC} + n(t) \tag{5-59}$$

The measurement error expressed as amplitude spectral density is

$$\begin{aligned} ASD\left[\frac{a(t)}{s_{know}(t)} - x(t)\right] &\approx \Delta\varepsilon_{DC} \cdot ASD[x_{AC}](f) + ASD[\Delta\varepsilon_{AC}](f) \cdot x_{DC} + \\ &+ ASD[\Delta\varepsilon_{AC}(t) \cdot x_{AC}(t)] + ASD[n](f) \end{aligned} \tag{5-60}$$

The first term was already encountered in equation (5-57), while the second term provides the noise due to scale factor fluctuations (also in the interesting measurement band). We assume for e^2.motion that the drag compensation loop can suppress the (DC) accelerations to levels below 10^{-8} m/s² (see equation (5-10)), which corresponds to $8\,\mu$N force for satellite with 800 kg mass. This implies in particular that the accelerometer biases are below 10^{-8} m/s² in magnitude along each axis (vector $\vec{b}$ in equation (5-52). The offset between accelerometer reference point and S/C center of mass induces also an accelerometer bias, however, it is in the order of 10^{-11}m/s² and therefore uncritical for the scale factor.

The stability of the accelerometer scaling factor (in each axis) needs to be better than

$$ASD[s](f) = 1 \cdot 10^{-3} \frac{1}{\sqrt{Hz}} \cdot \sqrt{\left(\frac{1mHz}{f}\right)^4 + a}, \quad 0.1mHz < f < 0.1Hz \tag{5-61}$$

to achieve an accelerometer sensitivity in the order of $10^{-11} \frac{m}{s^2\sqrt{Hz}}$. Tthe sensitivity of the measurement of the scaling factor is not sufficient, therefore equation (5-61) is a requirement on the intrinsic stability of the accelerometer.

5.4.6 Axes Alignment

The alignment of the accelerometer axes is covered by the matrix $\hat{R}_{ACC}$ in equation (5-52), which can be decomposed as:

$$\hat{R}_{ACC} = \left\{ \hat{R}_y(\alpha_x) \cdot \hat{R}_z(\beta_x) \cdot \begin{pmatrix} 1 \\ 0 \\ 0 \end{pmatrix}, \hat{R}_x(\alpha_y) \cdot \hat{R}_z(\beta_y) \cdot \begin{pmatrix} 0 \\ 1 \\ 0 \end{pmatrix}, \hat{R}_x(\alpha_z) \cdot \hat{R}_y(\beta_z) \cdot \begin{pmatrix} 0 \\ 0 \\ 1 \end{pmatrix} \right\} \tag{5-62}$$

forming a 3x3 matrix, which describes the misalignments of each axis with angles (α_x, β_x) for the x-axis, (α_y, β_y) for the y-axis and (α_z, β_z) for the z-axis. $\hat{R}_x, \hat{R}_y, \hat{R}_z$ are the fundamental rotation matrices around the *x,y,z* axes, respectively. We require for e^2.motion that all angles are smaller than 2 mrad, meaning that the accelerometer axes are aligned to better than 2 mrad to the satellite axes – in orbit. If the satellite pointing is perfect, the x-axis of the satellite shall be parallel with the line-of-sight, which is the connection line of both satellites.

5.4.7 Line-of-Sight Acceleration

The important quantity for the retrieval of Earth's gravity field is the non-gravitational acceleration along the line-of-sight, which can be computed using:

$$a_{LOS}(t) = \vec{L} \cdot \hat{R}^{-1}_{ACC,ext} \cdot \hat{S}^{-1}_{est} \cdot \vec{a}_{meas}(t) \tag{5-63}$$

where $\hat{R}^{-1}_{ACC,est}$ is the estimation of the accelerometer axes w.r.t. to the spacecraft frame, $\hat{S}^{-1}_{est}$ the estimation of the accelerometer scaling factor and $\vec{L}$ is the measured or estimated direction of the line-of-sight in the spacecraft frame.

For e^2.motion we assume that the acceleration can be transformed to the LOS to better than 0.1%. This number accommodates the knowledge of the accelerometer axes w.r.t. the spacecraft frame (to better than 1 mrad) and cross-coupling terms of accelerometer axes (non-orthogonality, e.g. caused by imperfections of the proof mass or electric cross-talk). Mathematically the off-diagonal terms of the 3x3 matrix $\hat{R}_{ACC,est}^{-1} \cdot \hat{R}_{ACC}$ shall be smaller than 0.001 and the diagonal terms shall be close to unity.

In addition the accuracy of the LOS estimation in the spacecraft frame needs to be better than 1 mrad, which is easily achievable considering the tight pointing requirements of the interferometer.

Finally, Figure 5-36 contains a stack-up of the individual noise contributions discussed in the previous sections. The result is a worst-case noise of $4.16 \cdot 10^{-11} \frac{\mathrm{m}}{\mathrm{s}^2\sqrt{\mathrm{Hz}}} \cdot \mathrm{NSF(f)}$ for the line-of-sight acceleration, whereby $4.0 \cdot 10^{-11} \frac{\mathrm{m}}{\mathrm{s}^2\sqrt{\mathrm{Hz}}} \cdot \mathrm{NSF(f)}$ was defined in equation (5-6).

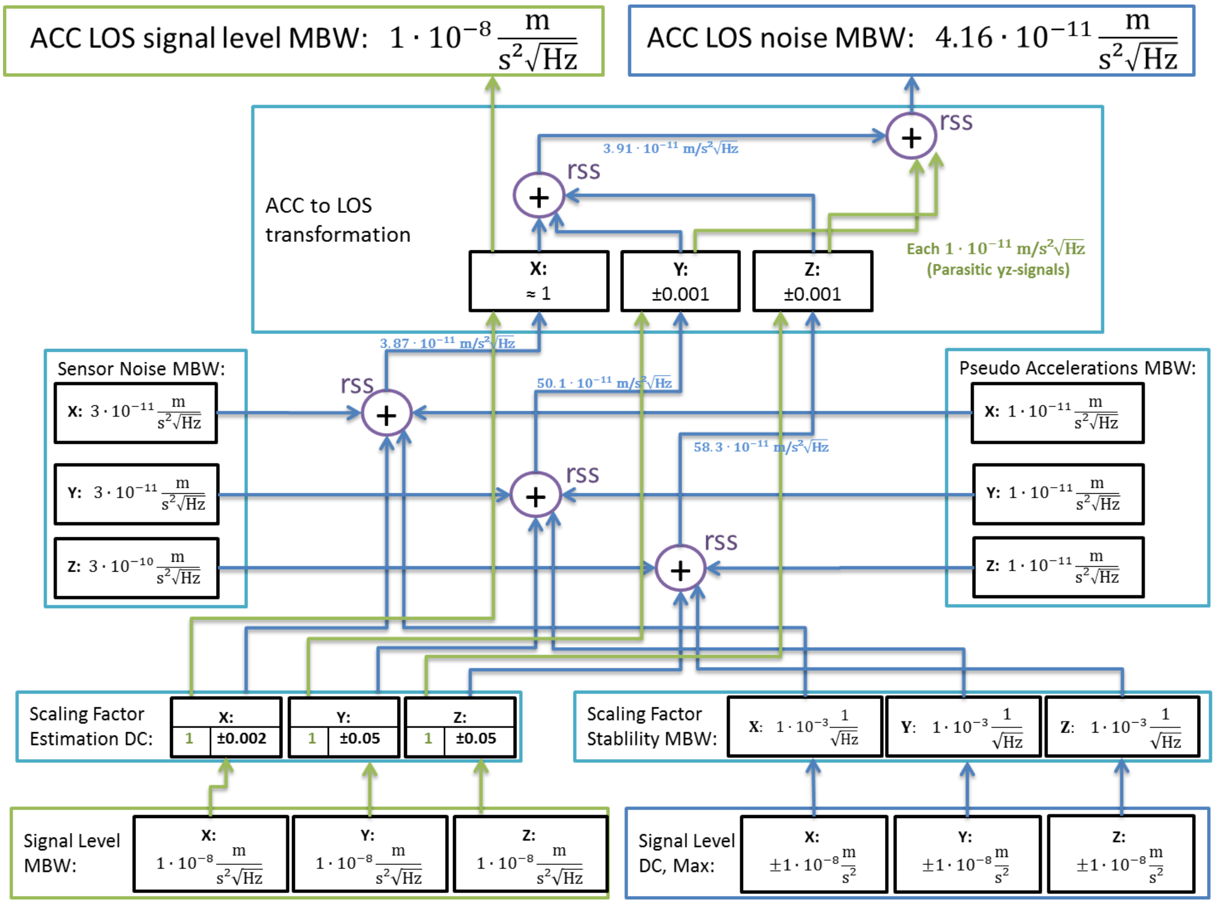

Figure 5-36: Noise composition for the measurement of non-gravitational accelerations along the line-of-sight. The green arrows denote signals (in contrast to noise), which also contribute to the final noise level due to parasitic coupling of yz-signals into the final LOS measurement. Please note that most of the numbers are frequency dependent and that the frequency dependencies (noise-shape functions) have been omitted for the sake of readability. LOS: Line-Of-Sight, ACC: Accelerometer, MBW: Science Measurement Bandwidth (0.18 mHz to 0.1 Hz), DC: low-frequency content (< 0.18 mHz)

5.4.8 Tone Errors

A requirement for the tone error amplitude of the acceleration measurement was given in sec. 5.1.5. The main contribution is assumed to be from the pseudo-acceleration due to gravity gradient coupling. We note that the gravity gradient for e^2.motion inside the satellite has a magnitude of approximately $3.0 \cdot 10^{-6} \frac{1}{\mathrm{s}^2}$ (worst-case) and it is the proportionality factor for offsets between S/C CoM and ACC reference point. If the SC CoM position varies periodically by 10 µm due to differential thermal expansion of the satellite structure and components or propellant flux, the induced tone amplitude is in $30 \cdot 10^{-12} \frac{\mathrm{m}}{\mathrm{s}^2}$.

Additional coupling between periodic temperature variations and internal accelerometer voltages as well as geomagnetic coupling will induce tones, however, an estimation of the magnitude is beyond the scope of this report.

5.4.9 Angular Accelerations

The discussion on the e^2.motion accelerometer so far was only concerned with linear accelerations along the three axes. Modern accelerometer usually also provide the capability to measure angular accelerations [Ref GOCE], which are also required as an input for the gravity field retrieval as for example in the GOCE gradiometry concept. The low-low SST approach does not require angular accelerations in the first place. Angular accelerations can also be derived from star camera data and by a combination of GNSS and LRI DWS data. However, it might be beneficial for the calibration of accelerometer scale factors and biases to measure also the angular acceleration and to compare them to values obtained by other instruments. The necessity of angular acceleration measurements should be assessed at a later stage.

5.4.10 Anti-Aliasing Filter

e^2.motion will use thrusters, which are controlled with a pulse-width-modulation (PWM) scheme. The switching frequency is assumed to be in the order of 1 Hz. The control bandwidth of the drag-free control system is between 0.18 mHz and 30 mHz (see sec. 5.2.1). For the calibration of the accelerometer with the laser interferometer periodic thruster signals shall be generated with frequencies between 0.1 and 0.3 Hz (calibration band).

As a rule of thumb the PWM frequency should be at least a factor 10 higher than the highest control frequency. On the other side the switching frequency cannot be too high, since the thruster lifetime is defined by a maximum number of switching cycles.

The PWM thruster produce a rectangular non-gravitational acceleration, which spectral content consist of a comb of frequencies with integer multiples of the switching frequency. It is important that these PWM thruster peaks at 1 Hz, 2 Hz, 3 Hz, … do not alias into the measurement band

5.5 Additional Instruments

The previous sections concerned the main scientific instruments, the interferometer and the accelerometer, of e^2.motion. In the following subsection the high-performance temperature sensors are addressed, followed by a tabular overview about the overall payload.

5.5.1 High Performance Temperature Sensors

The precise measurement of low-frequency signals (< 1 mHz), e.g. inter-satellite range or non-gravitational acceleration, is in general complicated due to environmental disturbances, in case of e^2.motion due to temperature drifts, geo-magnetic coupling, residual atmosphere, drifts in potential of satellite (charge), etc. Satellite missions with measurement band below 1 mHz require usually advanced thermal stability at the sensitive instruments (e.g. LISA Pathfinder, LISA, GOCE, GRACE Follow-On), to suppress the effect of temperature variations (drifts and tones) and fluctuations (noise) in the measurements.

The variations can usually be subtracted partly in data post-processing, if the coupling coefficients are known. As part of the integrated and comprehensive data analysis approach for NGGM-D (discussed in section 5.2.4), the measurement of temperature variations with high precision and sufficient sampling rate is needed to find and correct for temperature correlations and to validate the temperature stability of the thermal design of the satellite.

The use of high-performance temperature sensors as part of the main payload, contributing to the science data stream equal to ranging and accelerometer data, is advocated for e^2.motion. In particular technology heritage from LISA Pathfinder is emphasized, where temperature sensors with noise below 1 mK/√Hz at 1 mHz have been developed and space qualified. The sensors utilize a Wheatstone bridge with alternating voltages to subtract biases within the electronic. Such temperature diagnostic boards have been used also in GRACE Follow-On LRI testing and in several interferometric laboratory setups (see Figure 5-37).

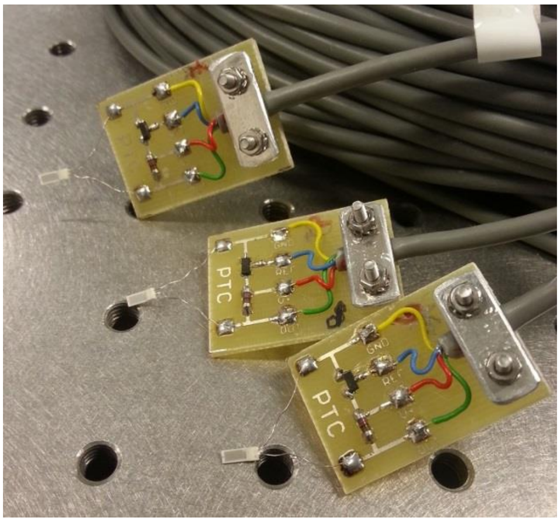

Figure 5-37: Low-noise temperature sensors (with positive temperature coefficients PTC) at laboratories of the AEI Hannover. The read-out of the sensors can be performed with FPGAs, similar to the board shown on Figure 5-31.

5.5.2 Instrument Overview

Figure 5-38 provides a tabular overview of potential payload instruments for e^2.motion together with physical properties. The power subsystem (mainly consisting of solar array, battery, PCDU, harness and corresponding electronic units) requires dedicated power analysis and is not in the scope of the current project phase. Similarly, other subsystems such as on-board data handling, TMTC, thermal control etc. are not discussed here. The corresponding instrumental concepts of these subsystems should be analyzed in further project phases.

The following web links provide some more detailed information about several of these instruments.

Star Tracker:
http://www.sodern.com/sites/en/ref/Star-Trackers-HYDRA_51.html

GPS Receiver:
http://www.space-airbusds.com/en/equipment/mosaicgnss-receiver.html

Magnetometer:
http://www.zarm-technik.de/downloadfiles/ZARMTechnikAG_Magnetomers_web2010.pdf

Magnetorquer:
http://www.zarm-technik.de/downloadfiles/ZARMTechnikAG_MagneticTorquers_web2010.pdf

Coarse Acquisition Sensor:
http://www.dlr.de/Portaldata/49/Resources/dokumente/archiv4/IAA-B4-0706P.pdf

Laser Retro-Reflector:
http://op.gfz-potsdam.de/grace/payload/payload.html#LRR
http://ilrs.gsfc.nasa.gov/docs/GR-GFZ-UM-0001.pdf

AOCS

Unit	Name	Manufacturer	Mass (kg)	Power (W)	Dimensions	Key Performance Parameters	Flight heritage	Radiation /Lifetime
Safe-mode sensor	Advanced CESS	STI	ca. 70 g	-	110 x 60 x 45 mm	Earth-vector error peak value ca. 9.4	many	7
Cold gas thruster	PWM cold gas thruster	AST	45 g per thruster	3.5 W pull, 0.5 W hold	ca. 20 x 30 x 50mm	thrust range: 400 µN - 8 mN, response time <1 ms,	Formosat 5, launch in 2015	12 yr
Star tracker	Hydra	Sodern	1.37 (OH) 1.85 (EU)	11 W (1 EU + 3 OH)	Ø146.5 x 283 mm (OH)	(see datasheet)	Spot-6	10 yr LEO
GPS receiver	Mosaic	Airbus DS	3.9	10	272 x 284 x 92 mm	Accuracy < 10m	Flown since 2006	up to 15 yr/100 krad
Magnetometer	FGM Analogue	ZARM	0.25	<1	82 x 82 x 31 mm	Range = ± 64 µT Accuracy < ± 1 %	Many missions	> 50 krad or > 11 yr
Magnetorquer	MT-140-2	ZARM	5.3	1.9	Ø43 x 680 mm	140 Am²	Many missions	> 7 yr LEO
Coarse acquisition sensor	Acquisition sensor	DTU space	425 g	1.9	DPU: 10 x 10 x 4.5cm*	see link	Many missions	30 + yr

Payload

Unit	Name	Manufacturer	Mass (kg)	Power (W)	Dimensions	Key Performance Parameters	Flight heritage	Radiation /Lifetime
Laser ranging instrument	Off-Axis Racetrack Concept	TBD	ca. 20	ca. 30	300 x 300 x 200 mm	25 nm/sqrt(Hz) at 0.1 Hz	similar to GRACE Follow-On LR	
Accelerometer	Superstar (with modifications)	ONERA	ca. 15	ca. 10	SU : 200 x 200 x 200 cm ICU : 150 x 250 x	4e-11 m/s2/sqrt(Hz) for sensitive axis 4e-10 m/s2/sqrt(Hz)	GRACE	> 11 yr
Laser retro-reflector	Laser retro-reflector	GFZ	0.5	-	ca. 100 x 100 x 48 mm	direct distance measurement: 1 - 2	CHAMP/GRACE/TerraSAR/SWARM	> 11 yr

Figure 5-38: Summary of additional instruments needed for e^2.motion

5.6 Conclusions

The payload concept of e^2.motion was introduced in this chapter. Although the e^2.motion working principle is based on a GRACE-like concept, several distinctive changes were proposed to achieve improved measurement sensitivity:

- use of continuous drag compensation within the measurement band to reduce effects due to accelerometer scale factor variations
- use of a laser interferometer for the ranging measurement with a sensitivity of 25 nm/√Hz (at 0.1 Hz) and for measurements of S/C alignment w.r.t. the line-of-sight
- integrated payload concept where different payload instruments are continuously calibrated, e.g. accelerometer by the interferometer, star camera by the interferometer DWS (Differential Wavefront Sensing). Interferometer, Accelerometer, Star Tracker and GNSS Receiver contribute to the Attitude, Orbit and Line-of-Sight estimation of the spacecraft AOCS.
- High performance temperature sensors (like in LISA Pathfinder) for diagnostics of S/C thermal stability and for correction of measurements in post-processing.

These points are also illustrated in Figure 5-39.

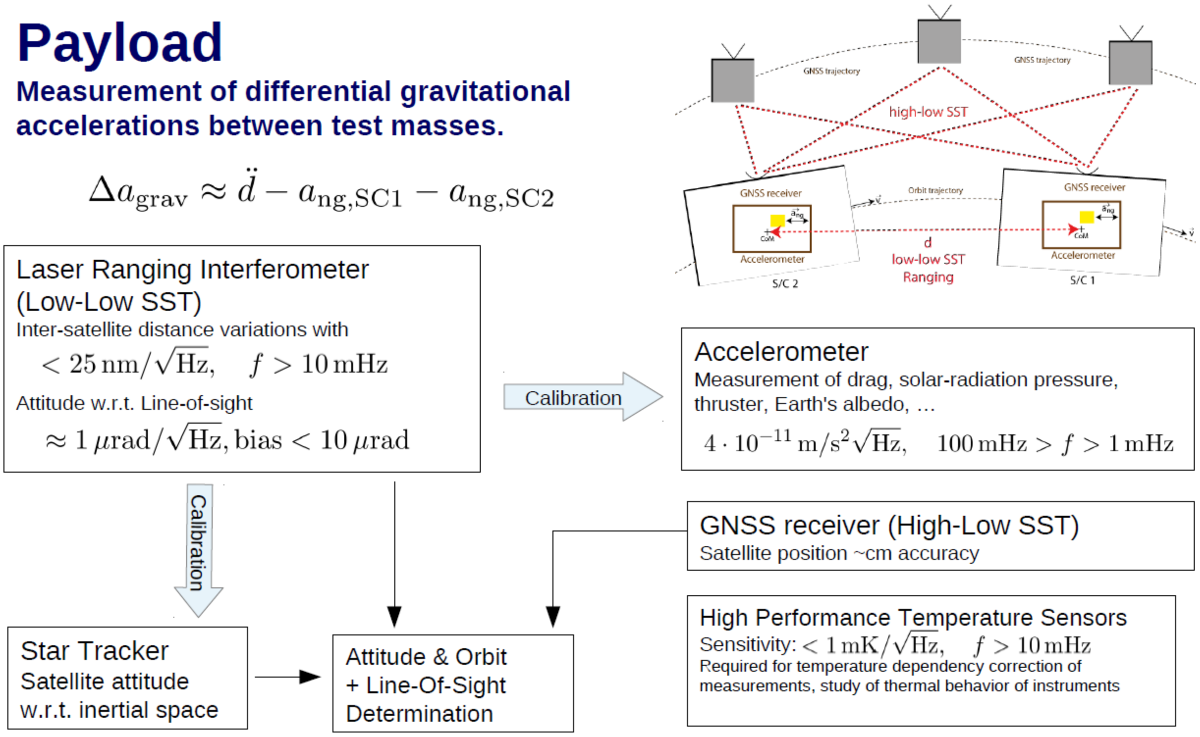

Payload

Measurement of differential gravitational accelerations between test masses.

$$\Delta a_{\mathrm{grav}} \approx \ddot{d} - a_{\mathrm{ng,SC1}} - a_{\mathrm{ng,SC2}}$$

Laser Ranging Interferometer (Low-Low SST)

Inter-satellite distance variations with

$< 25\,\mathrm{nm}/\sqrt{\mathrm{Hz}}, \quad f > 10\,\mathrm{mHz}$

Attitude w.r.t. Line-of-sight

$\approx 1\,\mu\mathrm{rad}/\sqrt{\mathrm{Hz}}, \mathrm{bias} < 10\,\mu\mathrm{rad}$

Accelerometer

Measurement of drag, solar-radiation pressure, thruster, Earth's albedo, ...

$4 \cdot 10^{-11}\,\mathrm{m/s^2}\sqrt{\mathrm{Hz}}, \quad 100\,\mathrm{mHz} > f > 1\,\mathrm{mHz}$

GNSS receiver (High-Low SST)

Satellite position ~cm accuracy

High Performance Temperature Sensors

Sensitivity: $< 1\,\mathrm{mK}/\sqrt{\mathrm{Hz}}, \quad f > 10\,\mathrm{mHz}$

Required for temperature dependency correction of measurements, study of thermal behavior of instruments

Star Tracker

Satellite attitude w.r.t. inertial space

Attitude & Orbit + Line-Of-Sight Determination

Figure 5-39: e^2.motion scientific payload at a glance

The analysis in this chapter concentrated on the interferometer and accelerometer. It is important to note that the sensitivity of gravity field determination is not only determined by the sensitivity of the single instruments, but also by environmental conditions like stability of satellite platform and thermal shielding, which cannot be influenced on instrument level. For example the satellite pointing accuracy is crucial for the interferometer, while variations in the center-of-mass position couple strongly into the accelerometer measurement.

Different drag compensation techniques were assessed w.r.t. accelerometer saturation and sensitivity. Drag compensation requirements as well as AOCS pointing requirements due to the interferometer constraints were derived in section 5.2.

Several missions (GRACE Follow-On, LISA Pathfinder, LISA) will explore and exploit space laser interferometry in the (near) future. E^2.motion continues this path to accomplish the low-low satellite tracking. Different interferometer concepts and optical layouts were introduced and compared and the main noise sources and limitations were addressed. The GRACE Follow-On like off-axis racetrack configuration has been selected as baseline, since it provides a robust setup with low complexity and capability of easy beam steering. A dedicated acquisition sensor has been selected as additional component to reduce complexity in the link acquisition process. Furthermore it was shown that (most) main components are in a mature state and available in Europe due to technology heritage from previous missions. However, the desired mission duration of 11 years implies demanding specifications on reliability, e.g. contamination of components for the interferometer, but also for other instruments.

Section 5.4 was concerned with the e^2.motion accelerometer. Critical parameters like scale factor bias and variations as well as the dependency on center-of-mas variations were addressed. The required sensitivity levels of accelerometer and interferometer for e^2.motion are demanding, but realistic for a future geodesy missions with appropriate improvements in the satellite design concerning e.g. thermal stability and S/C pointing.

6 Generation of Simulated Observations

6.1 Introduction

In the previous sections the mission concept, requirements, configuration and instrument design were defined. The proposed satellite mission consists of two satellite pairs in two different polar and inclined orbits at different altitudes. The final goal is to obtain a geoid accuracy of 1 mm at spatial resolution of about 150-200 km.

In order to assess the feasibility of the proposed mission and to check whether the desired accuracy is achievable, an end-to-end closed-loop simulation is designed. The simulation should mimic the real-world conditions as realistic as possible. To do this in a proper way, the full-scale simulation is done in three steps which are illustrated in Figure 6-1.

In the first step the time-variable gravity signals (and errors) which occur in the simulation time period (32 days) are defined (c.f. Section 6.2). The second step includes the orbit integration based on a set of pseudo-true force models including the static gravity field, the time variable gravity model, an ocean tide model, planetary ephemerids, permanent tide and a simple earth rotation model (c.f. Section 6.3). Finally in the third step, the instrument noise time series for two main satellite sensors (LRI and accelerometer) are generated based on the output of sensor design and instrument concepts (c.f. Section 6.4). The error time series are then added to the error-free observations and will be used in the next major step for the recovery of the Earth’s gravity field.

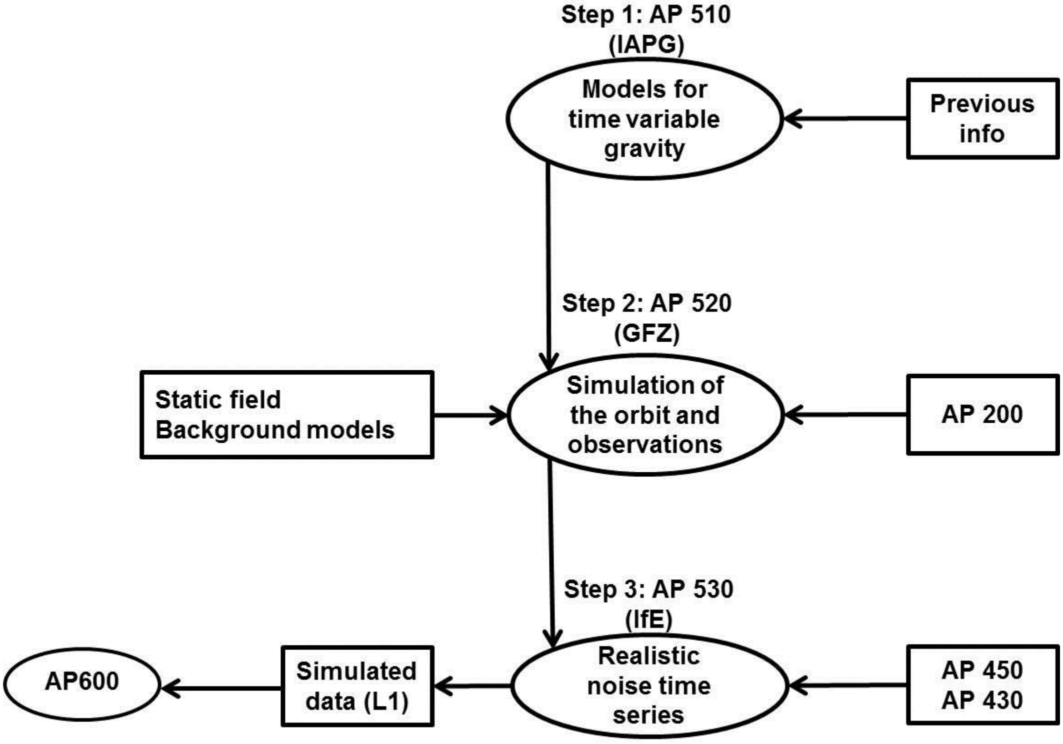

Figure 6-1: Overview of different steps for the simulation of observations and noise time series

6.2 Time Variable Gravity Field – Modelling of Signal and Error

In this section the model environment for the final simulations (see next chapter) is defined. The final simulations are performed in a closed-loop. From a true world scenario (incl. static and time variable gravity) the observations and orbits are derived. In an inversion step starting from a reference world scenario a mean set of spherical harmonic (SH) coefficients is estimated for the observation period. This solution then is compared with the mean state of the true world. Table 6-1

Table 6-1 shows the simulation models representing the true and reference world. As simulation period March 2004 is chosen.

Table 6-1: Simulation models representing the true and reference world (all models given in SH coefficients and used up to l_{max}=150, except for ocean tides)

	True world	Reference world
Static	GOCE DIR 4	GOCO03S
Non tidal time varying gravity	AOHIS	AOHIS + AO-errors
Ocean tides (8 constituents)	EOT08a (l_{max}=50)	GOT4.7 (l_{max}=50)

The non-tidal part of the time varying gravity field is modeled with the geophysical mass transport models described in (Gruber, et al., 2011). It contains the SH coefficients up to degree and order 180 in a six hour resolution for 12 years and the five components Atmosphere (A), Ocean (O), Hydrology (H), Ice (I) and Solid Earth (S). For each epoch the signal is interpolated linearly between two six hour states.

The final simulations aim for estimating the mean HIS signal during the observation period March 2004. Therefore the influence of the AO part is subtracted within the retrieval process. In reality the true AO signal content is not known and therefore it is necessary to define the uncertainties of this part as AO-errors. The starting point of the retrieval then is the true AO state plus the AO-errors.

The AO-errors should represent the uncertainties of these models. There are two options how such errors can be approximated. The first one is the difference between two independent models, how it is done for the ocean tides. The second option is chosen for the AO-errors. It is an empirical approach assessing the errors with a signal depending part and a random part from the full AO-signals. The dominating signal depending part preserves the spatial and temporal variations of the AO-signal. The AO-errors are set up for each epoch in terms of SH coefficients derived from the corresponding signal coefficients. The SH coefficients of the AO-error can be formulated as:

$$\begin{aligned}
&\{C,S\}_{AO-error} = \{C,S\}_{AO-p-signal} + \{C,S\}_{AO-q-random} \\
&\{C,S\}_{AO-p-signal} = p \cdot \{C,S\}_{fullAO}, \quad 0 < p < 1 \\
&\deg RMS\left(\{C,S\}_{AO-q-random}\right) = q \cdot \deg RMS\left(\{C,S\}_{fullAO}\right), \quad 0 < q < p
\end{aligned} \tag{6-1}$$

For current AO-models such as described in (Gruber, et al., 2011) it can be assumed that the uncertainties are in the range of 10% to 15% of the full AO signal content. Therefore for the final AO-errors *p* is chosen to be 10% and *q* is equal to 5%. The random part $\{C,S\}_{AO-q-random}$ is computed based on normally distributed random numbers for all SH coefficients. Then these coefficients are scaled in that way, that the SH degree RMS value of each SH degree is *q* times the SH degree RMS value of the full AO-signal. Figure 6-2 shows the spectral and spatial distribution of the AO-errors in comparison with the mean HIS signal.

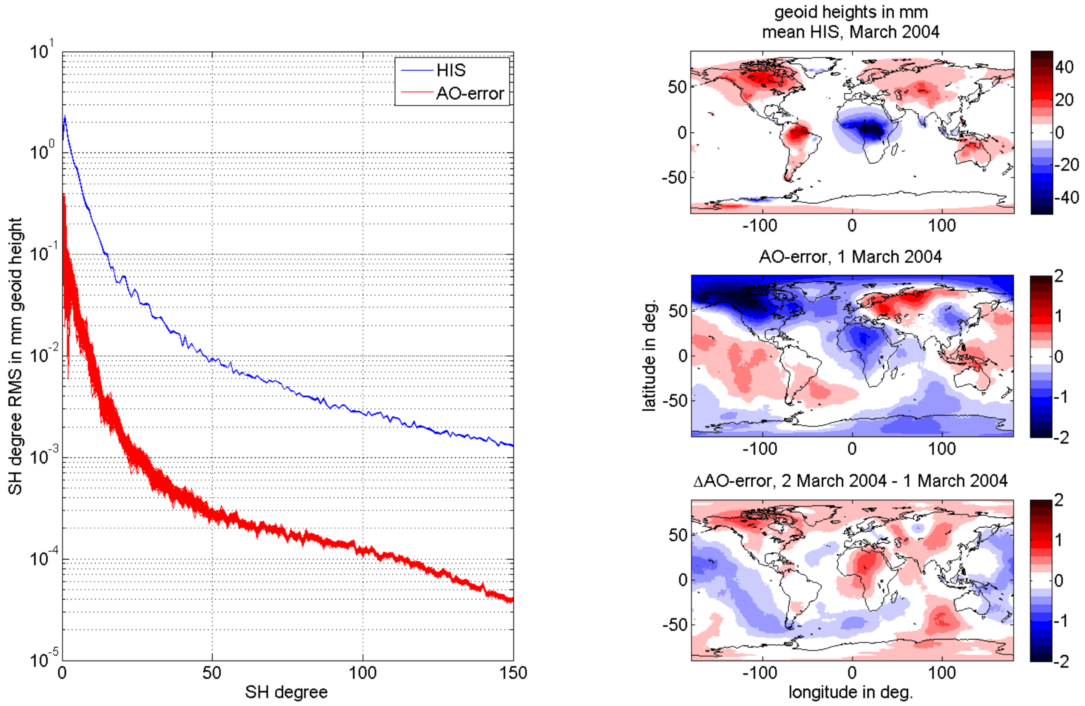

Figure 6-2: Spectral and spatial representation of HIS and AO-errors. Left: SH degree RMS in mm geoid heights of HIS and AO-errors for March 2004 (124 epochs, 6 hour sampling) up to l_{max}=150. Right: global geoid heights in mm of the mean HIS signal for March 2004 (Top, 7.71 mm global RMS) of the AO-errors for 1st of March (Center, 0.45 mm global RMS) and the AO-error change from 1st to 2nd of March (Bottom, 0.29 mm global RMS).

6.3 Simulation of Observations

The simulated data set for the e^2.motion Bender constellation comprises data for 32 days March 1 until April 2 2004 (MJD=53065-53097). All data are provided error-free, the procedure for the error time series is described in section 6.4.

6.3.1 Models Applied

The following models for simulating orbits and observations are applied:

(1) Gravity simulation models of the true world scenario from Table 6-1
(2) Planetary Ephemerides: JPL DE405 only Sun and Moon
(3) No solid Earth tides, except for the permanent tide (added to C20)
(4) Non-gravitational accelerations = null (drag-free)
(5) No relativistic corrections
(6) No pole or ocean-pole tides
(7) Integration step-size 5 sec
(8) Transition inertial → terrestrial frame only via Earth rotation angle (θ) around the z-axis according to IERS 2003 conventions:

$$\theta = 2\pi \cdot \left(0.7790572732640 + 1.00273781191135448 \cdot \mathrm{MJD}\left(\mathrm{UTC}\right) - 51544.5\right)$$

6.3.2 Observations

Orbits

The orbit file names are of the form *_ORB12_* for the first satellite pair and *_ORB34_* for the second satellite pair, where here and in the following the * sign stands for character string identifiers. The files consist for each satellite of an orbit header having the keyword ORBIT. The orbits of a satellite pair are written one after the other in the same file.

The time scale is given in TDT with beginning and time of the arc in Julian date JD2000 (T0) plus the seconds in the day (T1). The keyword REV indicates only the orbit revolution number and appears at a start of a new orbit revolution.

Format first header record:

(“ORBIT: T0 T1 x y z xp yp zp”,” SATELLIT: ”,I7.7)

Format for the time scale and beginning and end of the arc:

(A3,2(F8.1,F12.6))

The satellite position and velocity [m, m/s] in the inertial frame are given by the keyword CIS and the record sequence is: $\mathrm{CIS}, \mathrm{T0}, \mathrm{T1}, x, y, z, \dot{x}, \dot{y}, \dot{z}, \mathrm{flag}$. T0 is given in JD2000 days, T1 seconds in the day (TDT), the last character field is a flag for the orbit (not relevant for this study). In the same way the keyword for the orbit in the terrestrial reference frame is CTS.

Format of the satellite state vector record:

(A3,F8.1,F12.6,3(D22.16:),3D22.16,:A1)

Inter-Satellite Range Measurements (KRA)

The SST range measurement files are of the form: *_KRA12_* for the satellite first pair and *_KRA34_* for the satellite second pair.

Sequence: Measurement type, time in days since arc epoch (MJD = 53065.0), range [m]

FORMAT: ('KRA',3X,D26.19,3x,D26.19)

```
KRA    0.0000000000000000000D+00    0.2216684280565684300D+06
KRA    0.5787037037037036600D-04    0.2216683608241893500D+06
KRA    0.1157407407407407300D-03    0.2216682736186081600D+06
KRA    0.1736111111111110900D-03    0.2216681664392479600D+06
KRA    0.2314814814814814600D-03    0.2216680392883915900D+06
```

Inter-Satellite Range-Rate Measurements (KRR)

The SST range-rate measurement file names are of the form: *_KRR12_* for the satellite first pair and *_KRR34_* for the satellite second pair.

Sequence: Measurement type, time in days since arc epoch (MJD = 53065.0), range-rate [m/s]

FORMAT:('KRR',3X,D26.19,3x,D26.19)

```
KRR    0.0000000000000000000D+00   -0.1144932966223200000D-01
KRR    0.5787037037037036600D-04   -0.1544373091633932700D-01
KRR    0.1157407407407407300D-03   -0.1943852142181512500D-01
KRR    0.1736111111111110900D-03   -0.2343314707654187100D-01
KRR    0.2314814814814814600D-03   -0.2742701926587720600D-01
```

Inter-Satellite Range-Acceleration Measurements (KRX)

The SST range-acceleration measurement file names are of the form: *_KRX12_* for the satellite first pair and *_KRX34_* for the satellite second pair.

Sequence: Measurement type, time in days since arc epoch (MJD = 53065.0), range-acceleration [m/s^2]

FORMAT: ('KRX',3X,D26.19,3x,D26.19)

```
KRX    0.0000000000000000000D+00   -0.3808328657999016098D-03
KRX    0.5787037037037036580D-04   -0.3810380946229485755D-03
KRX    0.1157407407407407316D-03   -0.3811954692530539202D-03
KRX    0.1736111111111110906D-03   -0.3812962161290900376D-03
KRX    0.2314814814814814632D-03   -0.3813334283960245763D-03
```

Satellite Attitude Data

The attitude file names are of the form: *_ATTITUDE12_* for the satellite first pair and *_ATTITUDE34_* for the satellite second pair.

The records starting with a plus sign are header records. The actual data records are given in an example below:

```
tim 1996  2  1 -1 59  8.8160000
att 1111  0.7071067812  0.0000000000  0.0000000000  0.7071067812 1
tim 1996  2  1 -1 59 13.8160000
att 1111  0.7071039760 -0.0019978007  0.0019978007  0.7071039419 1
tim 1996  2  1 -1 59 18.8160000
att 1111  0.7070955266 -0.0039955853  0.0039955853  0.7070954580 1
tim 1996  2  1 -1 59 23.8160000
att 1111  0.7070814331 -0.0059933376  0.0059933376  0.7070813296 1
tim 1996  2  1 -1 59 28.8160000
att 1111  0.7070616956 -0.0079910416  0.0079910416  0.7070615568 1
```

Format for the “tim” record:

(A4,I4,4I3,F11.7)

Format for the “att” record:

(A3,1X,A4,4(1X,F13.10),I2)

The records headed with the code word “tim” are the epoch of the measurement, given in GPS time, civilian notation. The attentive observer may note that it is not on the full second. The reason for this is that the forward simulator, internally, uses the terrestrial dynamical time (TDT) on an epoch grid with full seconds. Both GPS time and TDT are atomic time scales, and the transition from the former to the latter is achieved by adding 51.184 seconds, therefore the digits 816 after the decimal point of the second. The records indicated by the code word “att” give the vehicle attitude with respect to inertial reference frame defined by the background stars. The first item after the “att” code word, namely 1111, and the last, being 1, are flags that that indicate, for real measurements, the data quality, and from what on-board cameras the reference frame is established. For simulated data, they are pure dummy variables. The remaining four entries on each “att” line are attitude quaternions (q1,q2,q3,q4) that establish the attitude of the satellite body in the inertial reference frame, according to the following formulas: If ξSAS and ξCIS are the coordinates of one and the same point in the satellite body system (SAS) and in the inertial reference frame (conventional inertial system, CIS), respectively, then we have:

$$\xi^{CIS} = M\xi^{SAS}$$

$$M = \begin{pmatrix} q_1^2 - q_2^2 - q_3^2 + q_4^2 & 2(q_1q_2 + q_3q_4) & 2(q_1q_3 - q_2q_4) \\ 2(q_1q_2 - q_3q_4) & -q_1^2 + q_2^2 - q_3^2 + q_4^2 & 2(q_2q_3 + q_1q_4) \\ 2(q_1q_3 + q_2q_4) & 2(q_2q_3 - q_1q_4) & -q_1^2 - q_2^2 + q_3^2 + q_4^2 \end{pmatrix} \tag{6-2}$$

The satellite body system depends on the chosen satellite, which is of the GRACE type in all of the scenarios covered in this study. In nominal attitude, the axes of the satellite body are aligned with the RTN system: The first column of M is the unit vector that points from the center of the Earth to the satellite, the third column is the positive normal vector on the plane of the orbit, and the second column is a unit vector that completes a right-hand system, pointing roughly into the direction of the satellite velocity, and in case of a circular orbit exactly into that direction. All of those unit vectors have to be interpreted as vectors in the inertial (CIS) system.

Accelerometer Data

The accelerometer data file names are of the form: *_ACCEL12_* for the satellite first pair and *_ACCEL34_* for the satellite second pair.

The internal format of such a file follows the logic of the above-mentioned satellite attitude file. We have the same tim records for the measurement epoch time, however the att records are replaced with acl lines, giving accelerations in the satellite body-fixed reference frame. The following example may serve as an illustration:

```
tim 1996  2  1 -1 59  8.8160000
acl     -0.0000191829 -0.0119178054 -0.0003992486  1
tim 1996  2  1 -1 59 13.8160000
```

```
acl     -0.0000190543 -0.0118955292 -0.0003985219  1
tim 1996  2  1 -1 59 18.8160000
acl     -0.0000189247 -0.0118730972 -0.0003977758  1
tim 1996  2  1 -1 59 23.8160000
acl     -0.0000187943 -0.0118505183 -0.0003970106  1
```

Format for the “tim” record:

(A4,I4,4I3,F11.7)

Format for the “acl” record:

(A3,5X,3(1X,F13.10),1X,I2)

The three floating point numbers immediately after the “acl” code word give the acceleration of the vehicle, in the satellite body-fixed frame, in the units millimeters per seconds squared.

6.4 Noise Time Series

Within this study, concepts for future gravity field satellite missions are developed. On the basis of several analysis and discussions, the following mission parameters have been fixed:

- Bender configuration @ 420 km
- 2 pairs → 2 low-low SST links
- 1 three-axis accelerometer in each of the 4 satellites
- 5 s sampling for data and noise time series

In order to simulate a ‘real world’, the simulated error-free time series of the main sensors (SST link, accelerometer) are to be complemented by colored noise.

This chapter describes individual noise contributions to each sensor and the way the colored noise is calculated:

- Colored noise is modeled for selected sensors in terms of power spectral densities (PSD), see chapter 6.4.1.
- The colored noise PSDs are transformed into noise time series that can easily be added to simulated error-free data time series (see chapter 6.4.1.3).
- 2nd version of colored noise time series including tone errors are described in chapter 6.4.2.

6.4.1 Sensor Noise Model

<u>Use of colored noise time series</u>

$$X_{real\ world} = X_{error\ free} + X_{noise} \tag{6-3}$$

with:

$X_{error\ free}$ error free time series (refer to chapter 6.3)

X_{noise} noise time series

$X_{real\ world}$ time series including colored noise for simulations

6.4.1.1 Accelerometer

It was suggested that each satellite is equipped with one three-axis accelerometer. ‘Rough’ assignment of the axis directions is as follows:

x-axis:	along track / along line-of-side	highly accurate
y-axis:	cross track	less accurate
z-axis:	radial direction	highly accurate

The following error model is the result of chapter 2.3 and some discussion of the project team. It is considered as a basis for ACC-noise generation.

<u>Noise Model</u>

x- and z-axis (highly accurate):

$$d_{ACC}(f) = 4 \cdot 10^{-11} \sqrt{\left(\frac{0.001\text{Hz}}{f}\right)^4 + 1 + \left(\frac{f}{0.1\text{Hz}}\right)^4} \quad \left[\frac{m}{s^2\sqrt{\text{Hz}}}\right] \tag{6-4}$$

y-axis (less accurate):

$$d_{ACC}(f) = 4 \cdot 10^{-10} \sqrt{\left(\frac{0.001\text{Hz}}{f}\right)^4 + 1 + \left(\frac{f}{0.1\text{Hz}}\right)^4} \quad \left[\frac{m}{s^2\sqrt{\text{Hz}}}\right] \tag{6-5}$$

As shown in Figure 6-3, the error ASD (Amplitude Spectral Density, square root of PSD) is truncated at about $1/5590s/2 = 1.8 \cdot 10^{-4} s/2$ (half orbit frequency) to avoid long term trends in the noise time series. Noise time series are computed via LTPDA-toolbox in MATLAB using ‘noisegen1D’ function.

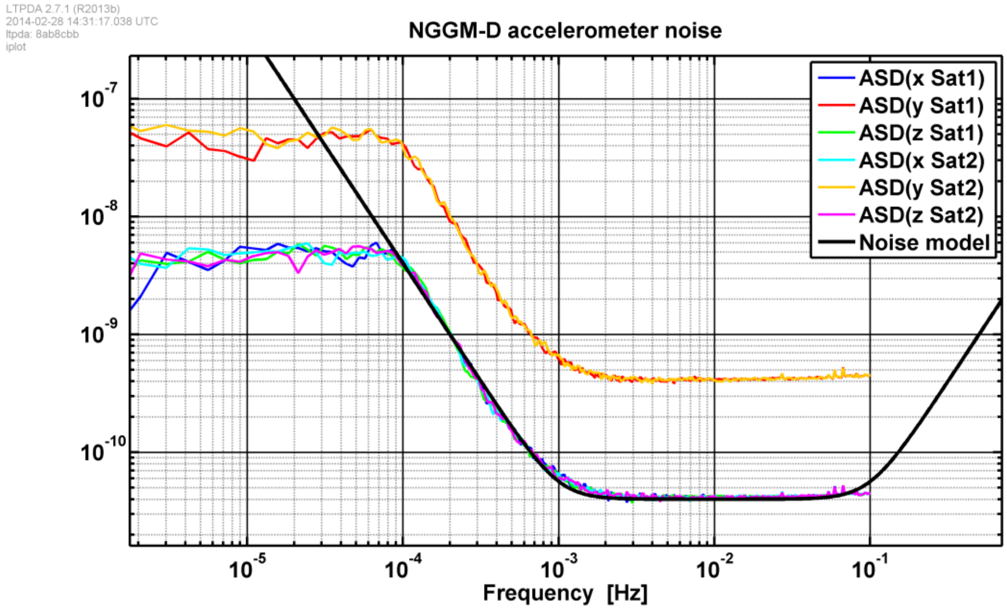

Figure 6-3: ASD (Amplitude Spectral Density) of ACC noise time series of two satellites of a Bender pair and the underlying noise model (black); highly accurate in x- and z-axis, and less accurate in y-axis.

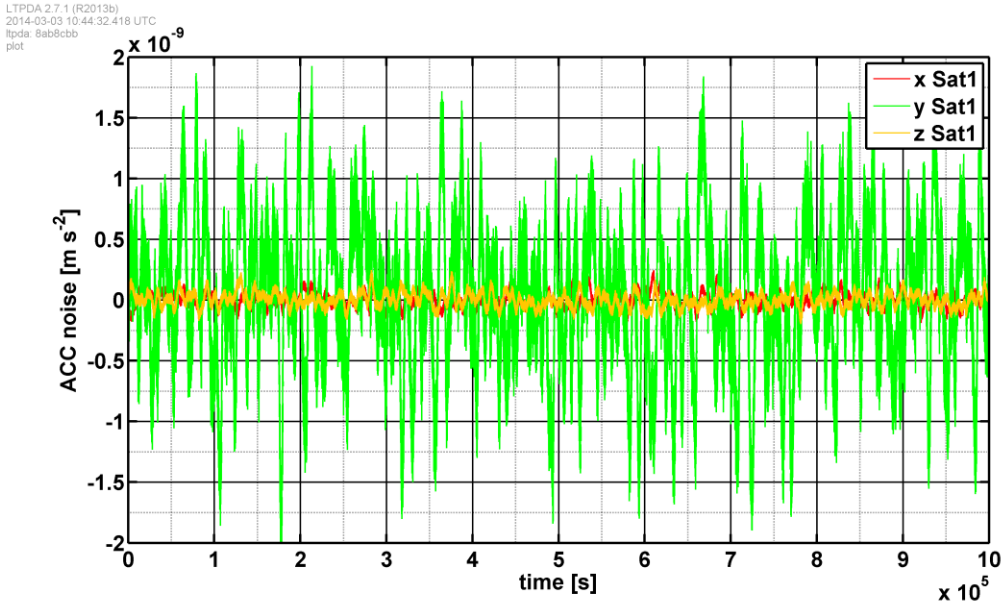

Figure 6-4: Part of accelerometer (ACC) noise time series - highly accurate x- and z-axis, less accurate y-axis

Data Format of ACC Noise Time Series

Identifier, time [s], ACC noise x-axis, ACC noise y-axis, ACC noise z-axis

FORMAT:

“Identifier \t %10.0f \t %+23.16E \t %+23.16E \t %+23.16E\r\n”

Example:

```
ACCnoise   0  +1.3594835167966796E-10  -9.4015415479630668E-10  -6.2650977799674738E-11
ACCnoise   5  +1.5884202401164693E-10  -8.6048173484405473E-10  -4.8844249522247485E-11
ACCnoise  10  +1.3205643731201525E-10  -8.5543399654390286E-10  -4.2929079000361251E-11
ACCnoise  15  +1.4539284510057773E-10  -8.9470427460452778E-10  -3.8205343176208195E-11
ACCnoise  20  +1.4309652570846203E-10  -9.3830082868786049E-10  -3.9884047817023570E-11
ACCnoise  25  +1.4995136232284304E-10  -7.6883702274962825E-10  -5.5332127405311519E-11
```

6.4.1.2 Satellite-to-Satellite Tracking by Laser-Interferometry

The noise model for the laser-interferometer is taken from simulations performed by AEI. It includes:

- Laser Frequency Noise
- Attitude noise of both satellites

Both are modeled via the LTPDA-Toolbox and are based on spectral noise behavior (PSD).

SST data as well as SST noise is provided in terms of

- Ranges (KRA)
- Range rates (KRR)
- Range accelerations (KRX).

Range Noise (KRAnoise)

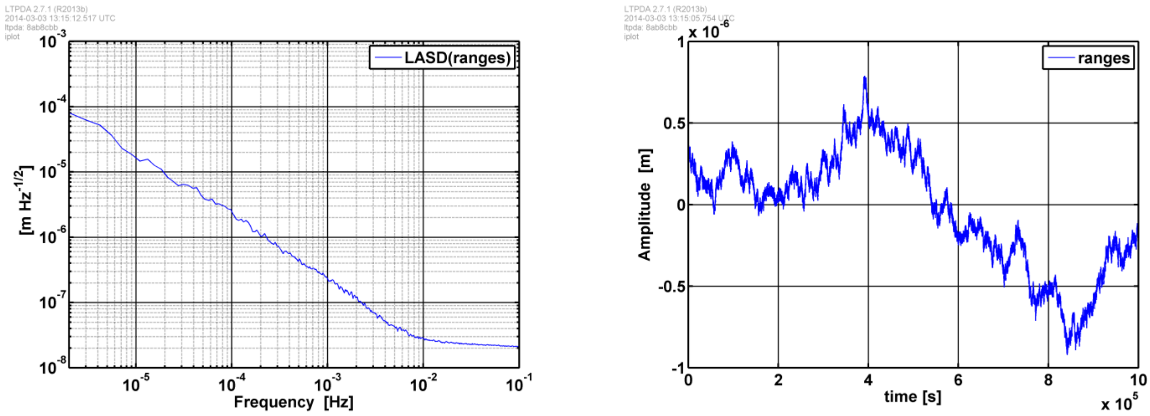

Figure 6-5: ASD of range noise in the frequency domain (left) and in the time domain (right)

Range Rates Noise (KRRnoise)

Range rate noise is derived from range noise using numerical differentiation in the frequency domain. To account for boundary effects, the beginning and the end of the time series are windowed using Hamming window (width: 40 data points i.e. 20 points are 'manipulated' at the beginning and at the end of the time series).

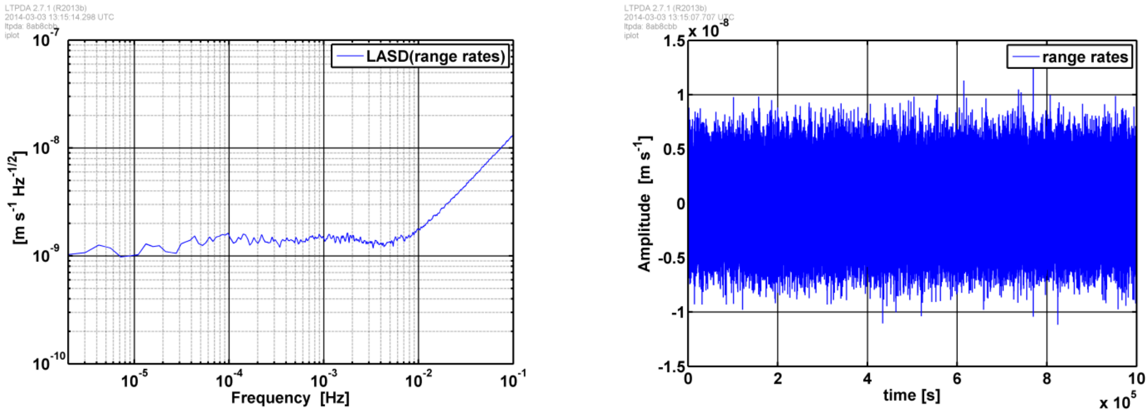

Figure 6-6: ASD of range-rate noise in the frequency domain (left) and in the time domain (right)

Range Acceleration Noise (KRXnoise)

Range acceleration noise is derived from range noise using double numerical differentiation in the frequency domain. To account for boundary effects, the beginning and the end of the time series are windowed using Hamming window (width: 10 data points i.e. 5 points are ‘manipulated’ at the beginning and at the end of the time series).

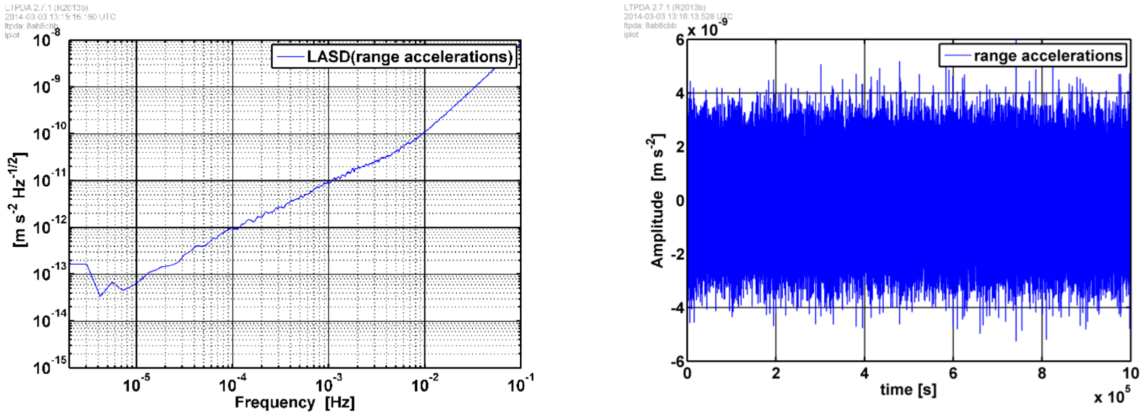

Figure 6-7: ASD of range-acceleration noise in the frequency domain (left) and in the time domain (right)

<u>Data format of SST measurements</u>

Identifier time [s] SST noise

FORMAT:

“Identifier \t %10.0f \t %+23.16E\n”

Example:

```
KRAnoise     0     -3.8347967913410121E-08
KRAnoise     5     -5.4897796713302513E-08
KRAnoise    10     -4.3341118128291659E-08
KRAnoise    15     -4.3489351381086505E-08
KRAnoise    20     -5.5048491260484295E-08
KRAnoise    25     -4.7702062594933945E-08
```

6.4.1.3 Transformation of PSD to Noise Time Series

The computation of colored noise time series on the basis of given power spectral densities (PSDs) is done in Matlab. More precisely the LTPDA-toolbox (Lisa Technology Package Data Analysis) is used.

The Matlab-function ‘noisegen1D’ produces colored noise time series. Main calculation steps are:

- Determination of poles and zeros which are used to characterize the given PSD (pole-zero-model).
- Poles and zeros are used to implement a set of IIR-filters.
- A white-noise time series of the desired time series length is computed.
- The IIR-filters are used to filter the white noise time series. The result is a colored noise time series with equal signal-energy characteristics as the ‘reference’ PSD.

6.4.2 Sensor Noise Model with Tone Errors

The 2nd version of colored noise time series simulated within the e^2.motion mission study contains tone errors. These are harmonic errors caused by periodic environmental variations on the satellite, mainly in temperature. A detailed description of tone errors and their amplitudes is described in the following.

6.4.2.1 Tone Error Requirements

<u>Introduction</u>

The goal of this section is the definition of requirements for so-called tone errors for the e^2.motion. Tone errors e_t are harmonic errors on low-low SST Laser observations caused by periodic environmental variations on the satellite, mainly in temperature. They cannot be described by stochastic means with spectral densities, since the underlying physical process is non-stochastic. A requirement for tone errors must be specified in amplitude (e.g. m) and not in units of a spectral density (e.g. $m/\sqrt{Hz}$). These errors contain discrete frequencies of integer multiples of the orbital frequency f_0.

$$e_t(t) = \sum_{i=1}^{n} a_i \cdot \sin\left(i \cdot 2\pi \cdot f_0 \cdot t + \varphi_i\right) \tag{6-6}$$

In the following paragraphs such tone errors are analysed depending on the latitude, the numerical closed-loop simulation environment is explained, and the results of these simulations in terms of spherical harmonic (SH) coefficients and SH degree RMS for n=3 are shown. As reference values for a_i in terms of inter-satellite ranges we have chosen $a_1 = 20$ µm, $a_2 = 4$ µm and $a_3 = 0.8$ µm. Finally the requirements for the tone error amplitudes are derived from several simulation scenarios at different altitudes. The derived total requirements satisfying a safety factor are the reference values, i.e. $a_1 = 20$ µm, $a_2 = 4$ µm and $a_3 = 0.8$ µm. These total requirements then are formulated to equal parts for the two main contributions, the laser ranging instrument (LRI) and the accelerometer (ACC).

Harmonic Signals in Satellite Observations

Here the tone errors are analysed depending on the latitude in order to get an idea of the spatial mapping. Figure 6-8 shows the situation for 89 and 70 degrees inclination according to a Bender-type double-pair mission. It shows tone errors with normalized amplitudes for 1, 2 and 3 cpr and the sum of these three tone errors (right column). The top row contains sin(*u*)-signals and the bottom row cos(*u*)-signals where *u* is the argument of the latitude.

Figure 6-8 shows the first three tone errors (*i*<4) depending on the latitude. Tone errors contain a mixture of sin(*u*)- and cos(*u*)-terms. Therefore the tone errors show two different latitude-curves during one revolution. For each revolution one of these two curves is reached. This means that the repeat cycle with its spatial sampling defines the distribution of these two values around the globe. From this analysis one can expect the largest SH coefficients of tone errors to be zonals of SH degrees $l \leq 3$. This is analysed in the following sections based on numerical closed-loop simulations.

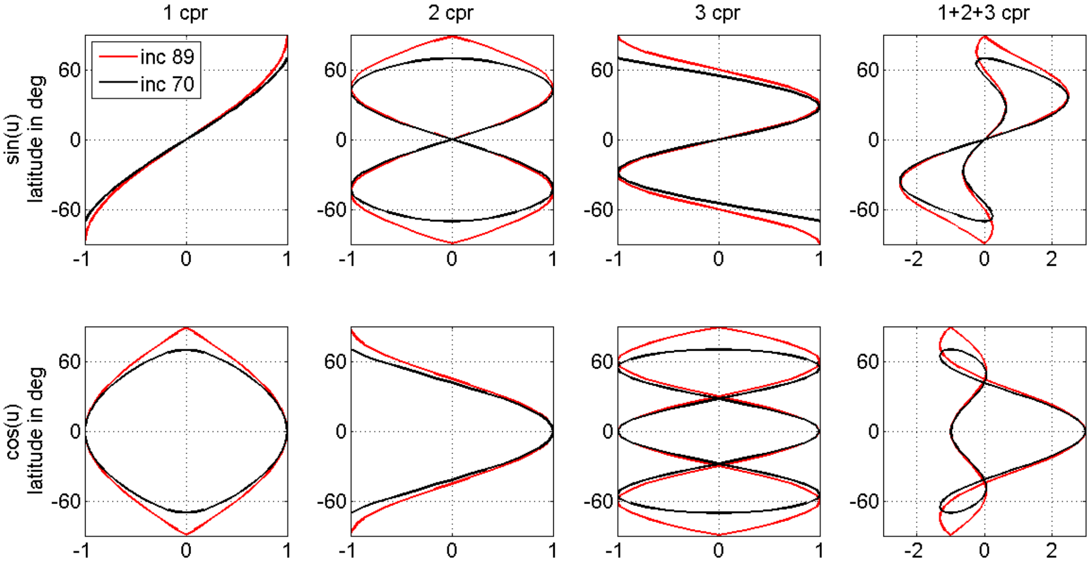

Figure 6-8: Normalized (a_i=1) sin(u)- (top row) and cos(u)-signals (bottom row) for 89 and 70 degrees inclination for 1, 2 and 3 cpr and the sum of these three signals (right column).

Simulation Environment

The closed-loop simulations use acceleration differences along the Line-of-Sight of a low-low Satellite-to-Satellite tracking (SST) mission as observations. More details on the closed-loop simulation software can be found in (Murböck, Pail, Daras, & Gruber, 2014). The scenarios are polar single pair missions with a repeat cycle of 31 days (cf. Table 6-2). The observation noise model is based on the reference noise model for the e^2.motion. The amplitude spectral densities of its different components are shown in Figure 6-9 in terms of range accelerations.

The Laser noise corresponds to a $20\ \mathrm{nm}/\sqrt{\mathrm{Hz}}$ noise limit above 10 mHz. The noise data contains the first three tone errors (i<4) with the reference values $a_1 = 20\ \mu\mathrm{m}$, $a_2 = 4\ \mu\mathrm{m}$ and $a_3 = 0.8\ \mu\mathrm{m}$. In terms of accelerations the amplitudes are $26 \cdot 10^{-12}$, $21 \cdot 10^{-12}$ and $9 \cdot 10^{-12}\ \mathrm{m/s^2}$ (cf. Table 6-2). In Figure 6-9 amplitude spectral densities are shown where these amplitudes are multiplied with the square-root of the duration (31 days). The stochastic model for the observations is modeled with an Autoregressive-Moving-Average (ARMA) Filter (4th order Butterworth band-pass filter). Its filter coefficients are adjusted to the total noise model (black dashed) and its inverse is shown in green. Twelve monthly GRACE-like scenarios on different altitudes are chosen. The orbit parameters together with the basic simulation parameters are shown in Table 6-2.

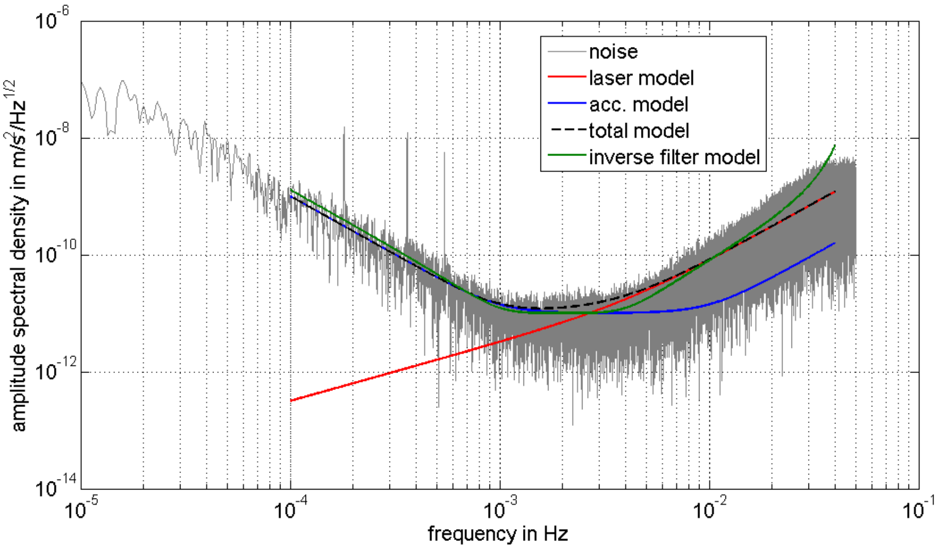

Figure 6-9: Amplitude spectral densities (flat top window) of the different noise model components (red: Laser, blue: accelerometer) in terms of m/s^2/√Hz. The total observation noise (grey) includes the tone errors on 1 cpr (f_0=1.813·10^{-4} Hz), 2 cpr and 3 cpr. The inverse of the adjusted ARMA-filter is shown in green.

Table 6-2: Basic simulation and orbit parameters

Simulation parameters			
• Maximum SH degree	100		
• Observations	Acceleration differences along the Line-of-Sight		
• Stochastic model	4th order Butterworth band-pass filter (cf. Fig. 2)		
• Background model	GOCO02S (Pail et al. 2010), no time variable gravity		
Tone error amplitudes	1 cpr (i=1)	2 cpr (i=2)	3 cpr (i=3)
• Range in µm	20	4	0.8
• Range accelerations in $\mathrm{m/s^2}$	$25.945 \cdot 10^{-12}$	$20.756 \cdot 10^{-12}$	$9.340 \cdot 10^{-12}$
Orbit parameters			
• Repeat cycle in days	31		
• Number of revolutions	475, 476, 477, 478, 479, 480, 481, 482, 483, 484, 485, 486		
• Altitudes in km	448, 439, 429, 420, 410, 401, 391, 382, 373, 363, 354, 345		
• Inter-satellite distance in km	100		
• Inclination in deg.	89		
• Sampling in s	10		

Gravity Retrieval Results

The results of the closed-loop simulations for the scenario with 484 revolutions are shown below. The other scenarios show similar results with slightly different low degree coefficients. This is due to the different repeat cycle and the randomly varied phases of the tone errors. At first we concentrate on the low degree effects which are by far the largest signal contents.

Figure 6-10 shows the $\log_{10}$-scaled absolute values of the SH coefficients of degrees $l \leq 10$. The top left image shows the formal errors according to the ARMA-filter model. The other three images contain the tone errors for 1 cpr (top right), 2 cpr (bottom left) and 3 cpr (bottom right). Due to the stochastic model the largest values are reached for C_{00}.The second largest values at C_{i0} for i cpr are tone error induced.

The SH degree RMS values in terms of geoid heights in mm for all SH degrees can be seen in Figure 6-11. For comparison it contains the mean hydrology, ice and solid Earth signal (black) as possible target signal and the result with observation noise without any tone errors (red). As this error contribution is much larger than the tone errors for SH degrees $l \geq 4$ the requirements for the tone error amplitudes depend purely on the low degrees. The mean tone error (1+2+3 cpr) geoid amplitudes of all 12 scenarios in mm are 1 (max. 2) for l=0, 0.08 (max. 0.2) for l=1, 0.03 (max. 0.04) for l=2 and 0.006 (max. 0.01) for l=3. Neglecting the degree 0 and 1 coefficients these values are accumulated to a mean total geoid error contribution of the tone errors of 0.07 mm (max. 0.1 mm).

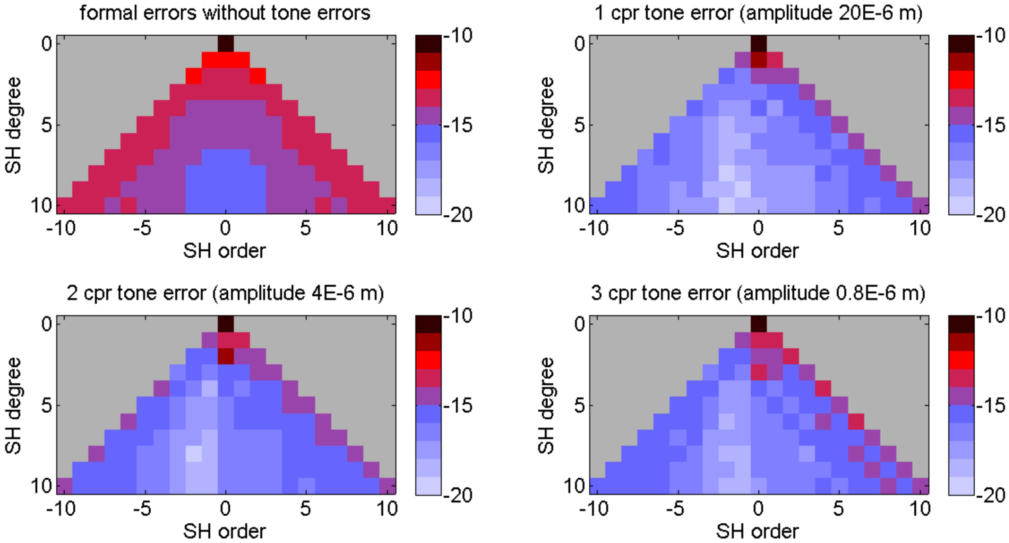

Figure 6-10: $\log_{10}$-scaled absolute values of SH coefficients for the 484 revolution scenario for degrees $l \leq 10$. Top left: formal errors according to the ARMA-filter model. Tone errors: 1 cpr (top right), 2 cpr (bottom left), 3 cpr (bottom right).

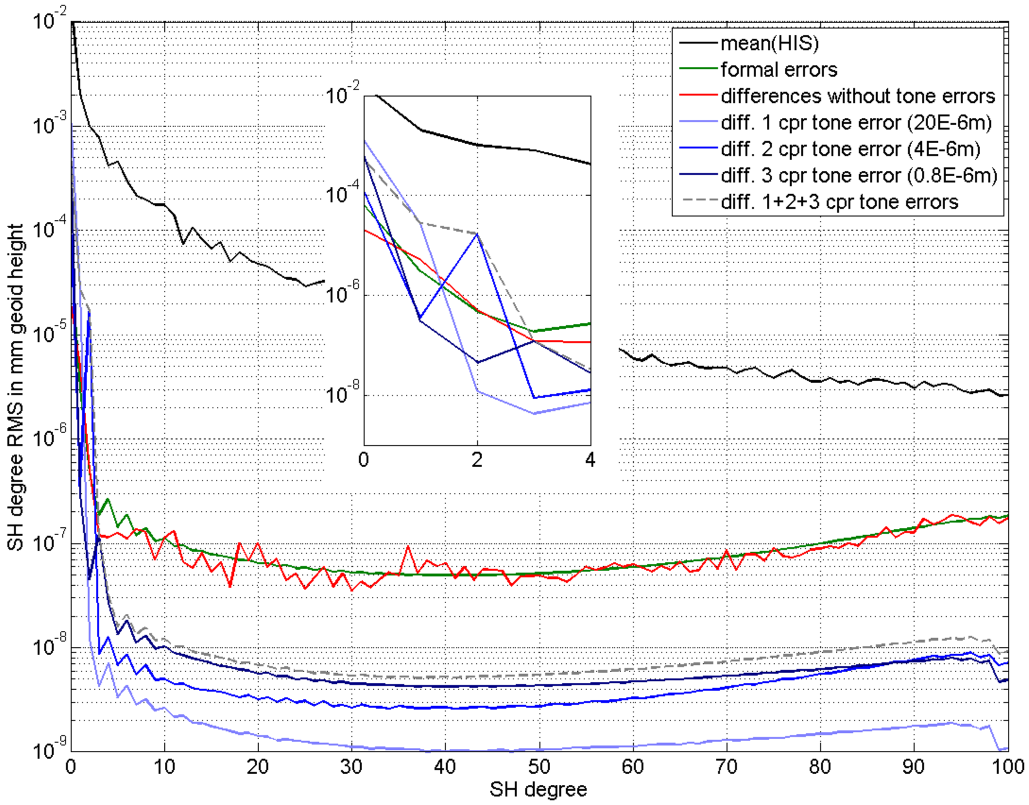

Figure 6-11: SH degree RMS in terms of geoid heights in mm for the tone errors (blue curves), the formal errors (green), the observation noise without tone errors (red) and the mean hydrology, ice and solid Earth signal (black) (incl. a zoom to the first 4 degrees).

Requirements

In real gravity field retrievals from low-low SST observations the SH coefficients of degree 0 and 1 are not estimated. Thus it is not necessary to formulate a strict tone error amplitude requirement for 1 cpr. Therefore only for 2 and 3 cpr tone error amplitude requirements shall be defined in this study.

The geoid goal of the e^2.motion is 1 mm accuracy at 150 km spatial resolution (l_{max}=134). From the simulations of the previous sections it was shown that tone errors with the reference amplitudes affects only the first 3 SH degrees. The maximum total geoid error contribution (l>1) for the tone errors with reference amplitudes for all the scenarios is g_{ref}=0.05 mm. The requirements shall satisfy a safety factor s=2. We define 10% of the total e^2.motion geoid goal as maximum tolerable tone error geoid error contribution g_{req}=0.1 mm. Scaling of the reference amplitude a_{ref} results in the requirement for the tone error amplitude

$$a_{req} = \frac{g_{req}}{g_{ref}} \cdot \frac{a_{ref}}{s} = a_{ref} \tag{6-7}$$

The required amplitudes for the 2 cpr tone error on the range observations within each satellite pair of the e^2.motion is 4 µm (0.8 µm for 3 cpr). As the LRI as well as the ACC contributes to tone errors, this requirement must hold for the total contribution of these two sensors. Therefore 50% of the above requirement holds for LRI and ACC, respectively. The 2 cpr tone error amplitude requirement for the LRI is 2 µm (0.4 µm for 3 cpr). For the ACC in terms of accelerations it is $1.0 \cdot 10^{-11}\ \frac{\mathrm{m}}{\mathrm{s}^2}$ $(0.5 \cdot 10^{-11}\ \frac{\mathrm{m}}{\mathrm{s}^2}$ for 3 cpr).

6.4.2.2 Noise Time Series with Tone Errors

In order to directly specify the influence of tone errors in the gravity field recovery, the colored noise time series version 2 consist of colored noise version 1 (refer to chapter 6.4.1) plus simulated tone errors. As mentioned above tone errors $e_t(t)$ are harmonic errors. They contain discrete frequencies of integer multiples of the orbit frequency f_0 (refer to equation (6-6)).

As a result of total requirements of tone error amplitudes a_i in terms of inter-satellite ranges are derived from several simulation scenarios: a1 = 20 µm, a2 = 4 µm and a3 = 0.8 µm. As the determination of inter-satellite ranges (range-rates respectively) is influenced by SST and ACC measurements, the total requirements are split 50/50 to be induced by SST and ACC instruments. As two accelerometers are involved (one on each satellite), the total requirements are split as follows:

50% SST

50% ACC (25% on satellite 1, 25% on satellite 2)

This results in the following tone error amplitudes a_i:

Table 6-3: Error amplitudes of tone errors for different observables

zero-peak amplitudes	a_1	a_2	a_3	a_4	a_5	a_6
total requirements [m]	$20\cdot10^{-6}$	$4\cdot10^{-6}$	$0{,}8\cdot10^{-6}$	$0{,}16\cdot10^{-6}$	$0{,}032\cdot10^{-6}$	$0{,}0064\cdot10^{-6}$
ACC [m/s²]	$6{,}4\cdot10^{-12}$	$5{,}1\cdot10^{-12}$	$2{,}3\cdot10^{-12}$	$0{,}8\cdot10^{-12}$	$0{,}25\cdot10^{-12}$	$0{,}05\cdot10^{-12}$
SST ranges [m]	$10\cdot10^{-6}$	$2\cdot10^{-6}$	$0{,}4\cdot10^{-6}$	$0{,}08\cdot10^{-6}$	$0{,}016\cdot10^{-6}$	$0{,}0032\cdot10^{-6}$
SST range rates [m/s], computed	$11{,}2\cdot10^{-9}$	$4{,}5\cdot10^{-9}$	$1{,}3\cdot10^{-9}$	$0{,}36\cdot10^{-9}$	$0{,}09\cdot10^{-9}$	$0{,}02\cdot10^{-9}$
SST range accelerations [m/s²], computed	$12{,}6\cdot10^{-12}$	$10{,}1\cdot10^{-12}$	$4{,}6\cdot10^{-12}$	$1{,}6\cdot10^{-12}$	$0{,}51\cdot10^{-12}$	$0{,}15\cdot10^{-12}$

Assumptions included:

- As a result of discussions, we fix to consider tone errors up to 6 times per revolution (a_i with $i = [1,\ldots,6]$).
- Amplitudes decrease by a factor of 5 for each $a_i \rightarrow a_{i+1} \lfloor a_{i+1} = 1/5 \cdot a_i \rfloor$ on the level of ranges.
- The transformation of tone errors in terms of ranges to tone errors in terms of range-rates and range-accelerations is done using first (range-rates) and second (range-accelerations) derivative of equation (6-6). It results in a multiplication with the factor $\left(i \cdot 2\pi \cdot f_0\right)$:

Range-rates:

$$\dot{d}_{SST} = \frac{\partial e_t(t)}{\partial t} = \sum_{i=1}^{n} a_i \cdot \left(i \cdot 2\pi \cdot f_0\right) \cdot \cos\left(i \cdot 2\pi \cdot f_0 \cdot t + \varphi_i\right) \tag{6-8}$$

In the calculation implemented in the form:

$$\dot{d}_{SST} = \frac{\partial e_t(t)}{\partial t} = \sum_{i=1}^{n} \frac{a_0}{5^i} \cdot \left(i \cdot 2\pi \cdot f_0\right) \cdot \sin\left(i \cdot 2\pi \cdot f_0 \cdot t + \varphi_i\right) \tag{6-9}$$

Range-accelerations:

$$\ddot{d}_{SST} = \frac{\partial e_t(t)}{\partial t^2} = \sum_{i=1}^{n} \frac{a_0}{5^i} \cdot \left(i \cdot 2\pi \cdot f_0\right)^2 \cdot \sin\left(i \cdot 2\pi \cdot f_0 \cdot t + \varphi_i\right) \tag{6-10}$$

with: $a_i = \frac{a_0}{5^i};\ a_0 = 5 \cdot \left(10 \cdot 10^{-6}\right)\text{m};\ f_0 \approx 0.00017897$ as derived from orbit data

Example:	ranges	range-rates	range accelerations
	10 µm = $10\cdot10^{-6}$m →	$11{,}2\cdot10^{-9}$m/s →	$12{,}6\cdot10^{-12}$m/s²

The phase φ_i in equation (6-6) is assumed to be fixed and the same for the tone errors of all instruments:

$$\varphi_i = \frac{\pi}{2} + i \cdot 10^{-2} \qquad \text{with } i = [1,\ldots,6] \tag{6-11}$$

Due to the fact that the simulated orbit time series ‘start’ around the equator, the maxima of the tone errors occur around the equator as well.

Tone Errors in ACC Measurements

The simulated tone errors for acceleration measurements are computed via equations (6-6)and (6-11) using the parameters specified in Table 6-3. The tone errors are supposed to be identical for x-, y- and z-axis. Figure 6-12 (left) shows the contributions of 1,…,6 multiples of the orbit frequency f_0 and its sum, which is transformed to the spectral domain (amplitude spectral density, ASD) in Figure 6-12 (right).

ATTENTION: Version 2 of e^2.motion colored noise time series (still) contains the combination of tone errors (e.g. Figure 6-12 (left)) and version 1 coloured noise as illustrated in Figure 6-4. Note that different sections of the long time series are presented.

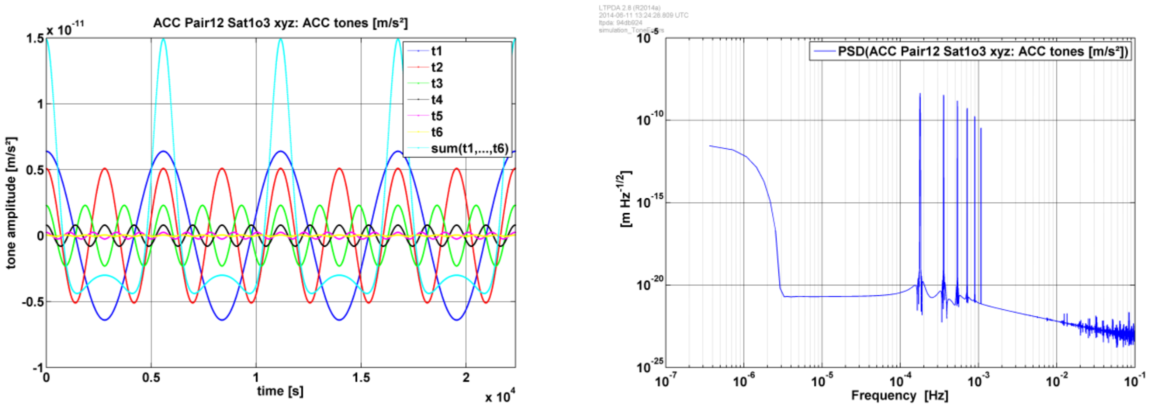

Figure 6-12: Part of ACC tone error time series; identical for x-, y- and z-axis (left); ASD of ACC tone error (sum), computed for an integration time of 1 month (right)

Tone Errors in Terms of Ranges (KRA)

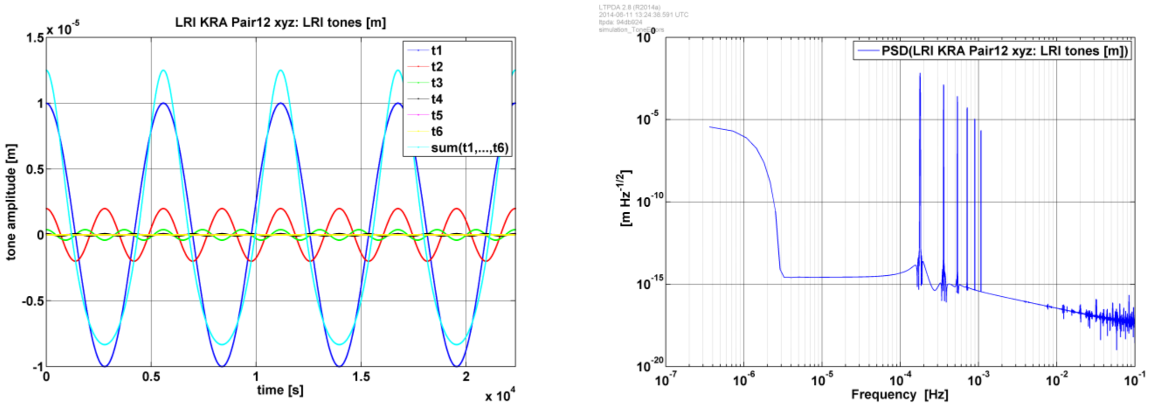

Figure 6-13: Part of SST range tone error time series; identical for x-, y- and z-axis (left); ASD of SST range tone error (sum), computed for an integration time of 1 month (right)

Tone Errors in Terms of Range-Rates (KRR)

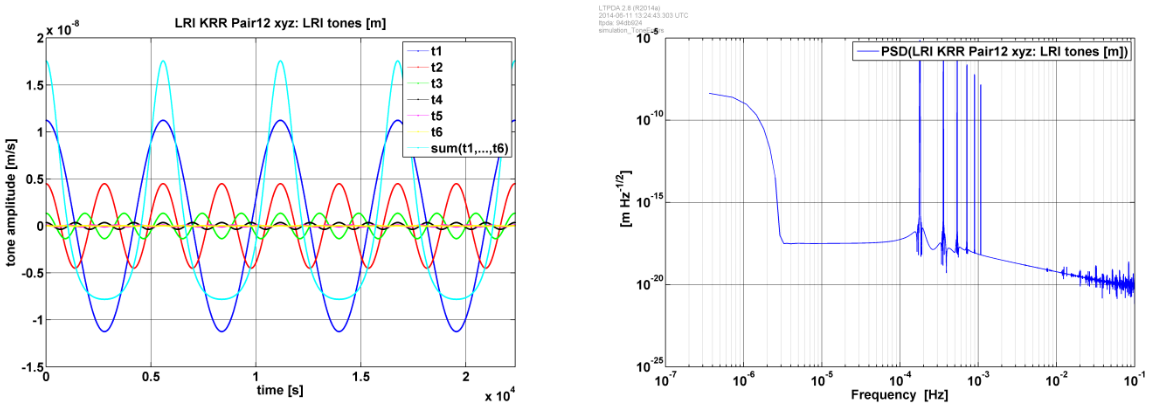

Figure 6-14: Part of SST range-rate tone error time series; identical for x-, y- and z-axis (left); ASD of SST range-rate tone error (sum), computed for an integration time of 1 month (right)

Tone Errors in Terms of Range-Accelerations (KRX)

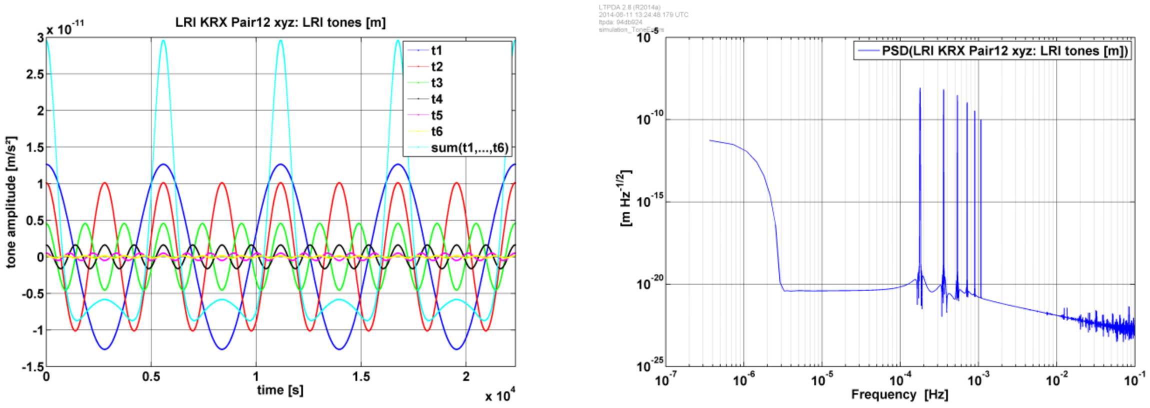

Figure 6-15: Part of SST range-acceleration tone error time series; identical for x-, y- and z-axis (left); ASD of SST range-acceleration tone error (sum), computed for an integration time of 1 month (right)

7 Numerical Simulations

This chapter summarizes the approaches and the results of the numerical simulations. The gravity field recovery for the considered Bender type mission has been simulated using three different approaches described below.

Figure 7-1 gives an overview of the general process used for the simulations. Orbits and observations were generated by GFZ based on the GFZ EPOS (Earth Parameter and Orbit System) software package and observation noises were created as described in chapter 6.

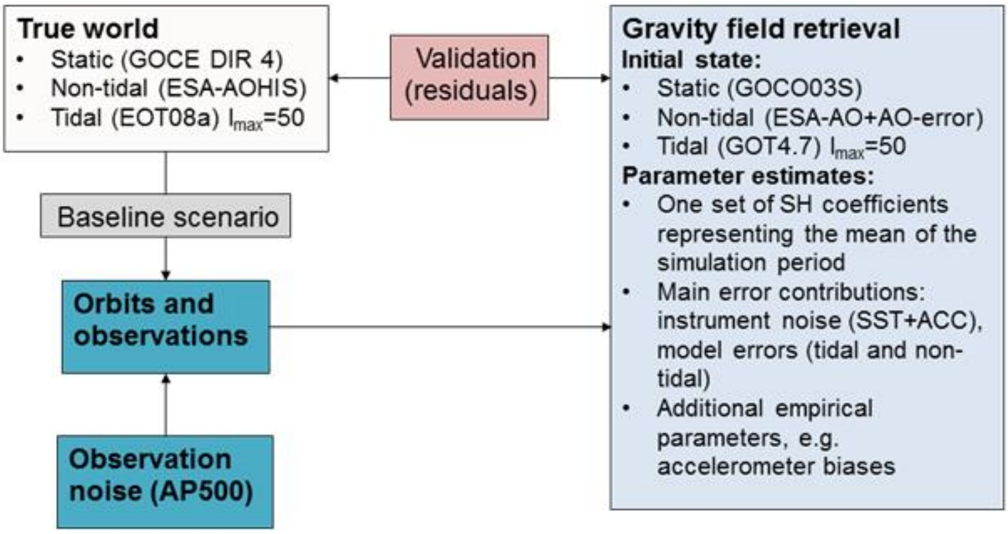

Figure 7-1: General overview of the simulation process

7.1 Simulation Approaches

7.1.1 Acceleration Method

The following description of the acceleration approach is taken from (Murböck, Pail, Daras, & Gruber, 2014). The acceleration approach is used in this study for numerical closed-loop simulations based on full normal equations. One set of SH gravity potential coefficients during the observation period is estimated (no short arcs, no iterations, and no additional parameters). The simulation scheme is shown in Figure 7-2. The main difference to a full-scale simulator is the missing orbit integration part. All observations are set up on independently given positions as linear functionals of the gravity potential *V*. Only low-low SST observations are used, which are implemented as gravitational acceleration differences along the Line-of-Sight (LoS) between the two satellites of one pair (indices 1 and 2, Earth-fixed position vectors $\vec{r}$) in the following way:

$$a_{1-2}^{LoS} = \left(\nabla V(r_1) - \nabla V(r_2)\right) \cdot \frac{r_1 - r_2}{\left|r_1 - r_2\right|} \qquad (7\text{-}1)$$

The input data marked as green boxes in Figure 7-2 are signal, orbit, and the noise related data. The signals can be computed from a static gravity field model in terms of fully normalized SH coefficients, from time varying fully normalized SH coefficients representing non-tidal mass variations of the atmosphere, ocean, hydrology, ice, and the solid Earth (six hour resolution), and from an ocean tide model.

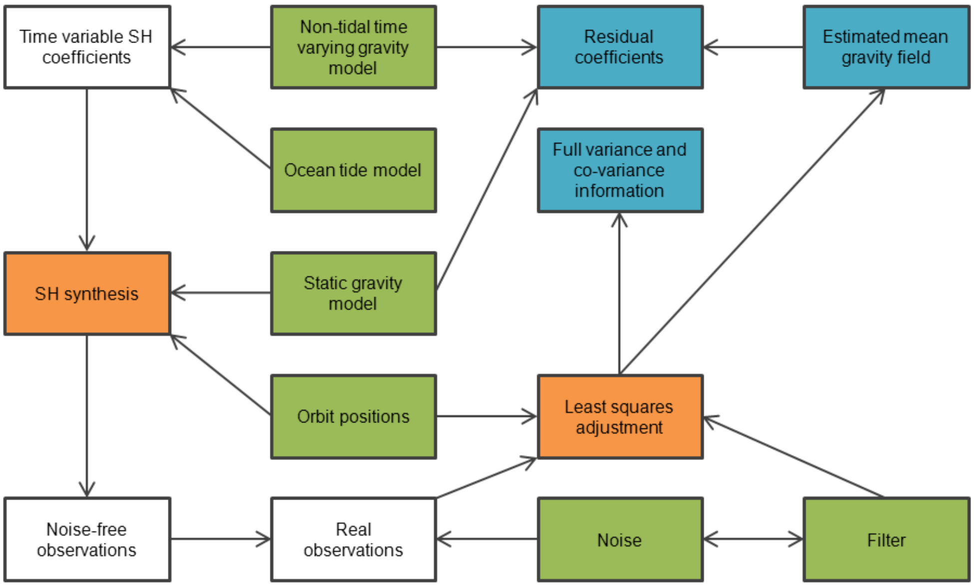

Figure 7-2: Acceleration approach closed-loop simulation scheme with input data (green), processing steps (orange) and output data (blue) (Murböck, Pail, Daras, & Gruber, 2014)

Table 6-2 lists the models and their references used in this study. The non-tidal time varying coefficients are interpolated linearly onto the orbit epochs, and the observations are then computed on the given positions with SH synthesis up to l_{max}. The noise time series is added to these observations. As only linear observation equations are used according to equation (7-1), no linearization is needed, and the design matrix is set up according to the observation equations. The stochastic modeling is done with a de-correlation filter, which represents the inverse of the introduced noise information. This filter is applied to both the observations and the columns of the design matrix (Schuh, 1996), (Klees, Ditmar, & Broersen, 2002). Then the unknown SH coefficients together with their variance and co-variance information are estimated by solving the full normal equation system.

7.1.2 Numerical Integration Method

The *numerical integration* or *numerical perturbation concept* can be characterized by the definitive orbit determination process where differential corrections to the various observed or unknown parameters are determined numerically. It is based on the representation of the geocentric position vector to the satellite as a sum of the topocentric position vector from an observation station to the satellite and the geocentric observation station vector. The topocentric position vector represents the observation model which depends – after linearization - on the various observations (ranges, Doppler, optical etc.) and the approximate values for the (unknown) station coordinates and the respective observation residuals and corrections to the station coordinates. The geocentric position vector to the satellite represents the orbit model which depends on the specific force function which is composed of the Earth-related specific force function (gravitational field, tides, etc.) modeled by unknown model parameters as well as orbit- and satellite-related specific disturbance forces. If Newton-Euler's equation has been selected as equation of motion (orbit model) then a non-linear model, representing the geocentric position vector of the satellite as a function of the force function model can be derived after a two-fold integration. This non-linear model complemented by the observation model and the station coordinates has to be linearized as usual, building a so-called mixed adjustment model. The partial differentials are determined numerically by integrating the variation equations or by approximating the partial differentials by partial differences.

Obviously, this model requires satellite arcs of sufficient lengths because of two reasons. The coverage of the satellite arcs with observations was very poor in the past compared to the situation nowadays, where the GNSS provide a dense coverage of the satellite's arcs with observations. Therefore, to achieve a sufficient redundancy of the adjustment problem it was necessary to use medium or long arcs. In addition, to cover the characteristic periodic and secular disturbances caused by the small corrections to the approximate force function parameters it was necessary - at least useful - to use medium or long satellite arcs as well. This fact becomes even more visible by having a closer look at the *analytical perturbation strategy*. Applying, e.g., the explicit Lagrange's perturbation equations expressed by the classical Keplerian elements and the disturbing potential represented by Kaula's expansions of the disturbing function in terms of the Keplerian elements then we arrive at Kaula's perturbation equations. These perturbation equations represent variations of the Keplerian elements as linear functions of the potential coefficients. They clearly show that secular effects and the various periodicities can be detected only with arcs of sufficient length which are able to cover these typical disturbance patterns of the Keplerian elements. As typical example the dependency of the rotation of the nodal line of the orbit plane and the line of apsides by the zonal spherical harmonics of even degree of a spherical harmonic expansion of the disturbing function has to be mentioned. The situation is similar also in case of the numerical perturbation techniques. The practical experiences underline these numerical characteristics of the perturbation strategies. This classical method of Satellite Geodesy works certainly also in case of a dense coverage of the satellite's arcs with observations as it was first impressively demonstrated in case of CHAMP by using the complex software system EPOS of GFZ Potsdam which is based on this classical procedure. This holds even more in case of the twin-satellite mission GRACE. Already the analysis of the first GRACE gravity field observations proved the feasibility to determine mass variations especially with respect to the continental hydrology in different geographical regions.

GFZ's developed analysis and simulation software EPOS (Earth Parameter and Orbit System) comprises modules for data pre-processing, orbit integration, orbit improvement, orbit predictions, orbit analysis, normal equation handling and solution, and simulation of observations. The EPOS software package was, is and will be used for operational precise orbit determination for various past, present and future satellite missions such as Meteor-3, GFZ-1, ERS-1/2, Lageos-1/2, CHAMP, GRACE-1/2, GRACE-FO, SWARM, TerraSAR-X or TanDEM-X exploiting SLR, RA, PRARE, K-Band-Range, 3D accelerometry, star camera or GPS observation data. Precise orbits are also calculated for GEOSAT, TOPEX, ERS-1/2, GFO, ENVISAT or JASON-1/2 to analyse sea level variations. Additionally, different pre-CHAMP GRIM (GRgs and geodetic Institute in Munich model) and CHAMP, GRACE and GOCE EIGEN (European Improved Gravity field of the Earth by New techniques) gravity field solutions have been computed during the past 2 decades. The latest GRACE solutions are EIGEN-GRACE06S (monthly and weekly gravity field models up to degree and order 90 and 30, respectively, routinely derived since 2002 from GRACE satellite data only within the GRACE Science Data System and within the DFG Special Priority Program “Mass Transports”) as well as the high-resolution gravity field EIGEN-6C up to degree and order 360 derived from combination of the static GRACE satellite-only model EIGEN-6S with terrestrial gravity data. Precursor EIGEN-5S has been chosen by ESA's High Level Processing Facility as the initial gravity field for GOCE data analysis.

EPOS is written in FORTRAN90 and consists of about 70,000 lines of code and 39,000 comment lines with 8 main programs and about 850 functions and subroutines. The load module runs on different UNIX workstations and LINUX clusters, as well as on an IBM. EPOS consists of the following modules:

Table 7-1: Summary of EPOS modules

PPR (Preprocessing) Module		
	PP	preprocessing of tracking and ancillary data (e.g. EOP)
	GP	preprocessing of GPS data
	NP	calculation of normal points (SLR/PRARE/GPS)
	CA	calculation of normal points (RA)
OD (Orbit Determination) Module		
	IN	generation of input control file for OD
	OC	orbit integration, parameter adjustment, simulation
	OA	quality control of orbits
	OU	numerical and graphical presentation of results
	SC	short-arc computations
PRD (Prediction) Module		
	PD	calculation of orbit predictions
PES (Parameter Estimation) Module		
	SG	use of surface gravity data
	CS	manipulation of normal equation systems
	QG	quality check of adjusted kinematic and dynamic parameters

Most important is the core module EPOS-OC with its capacity to integrate orbits, to adjust parameters and to simulate observations such as SLR, altimetry, DORIS, PRARE, GPS, GRACE K-band SST or GOCE gradiometry. A simplified flow chart is shown in the following Figure 7-3.

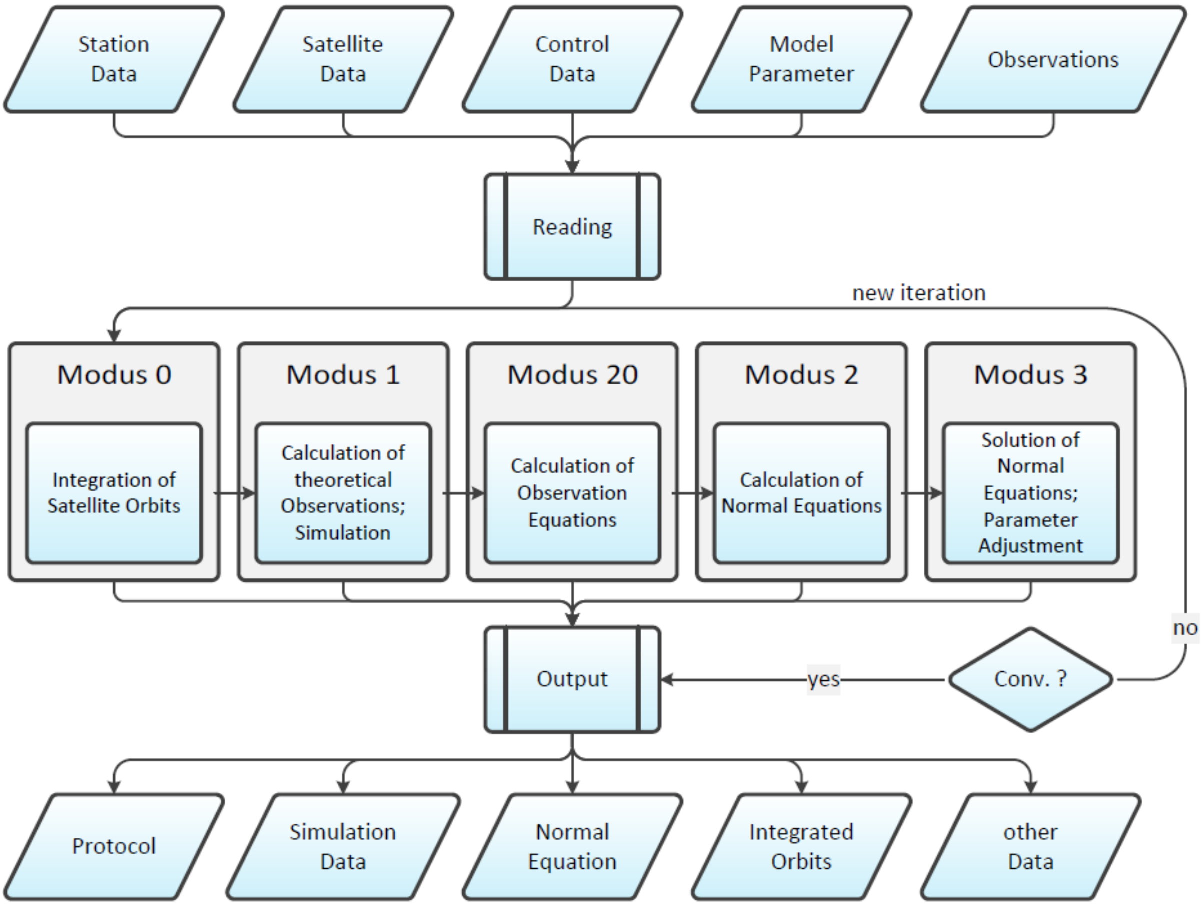

Figure 7-3: Simplified flow chart of EPOS-OC

7.1.3 Integral Equation Method

The integral equation approach (often referred to as “short arc approach”) was proposed by (Schneider, 1968) for orbit determination tasks and later on adopted for the purpose of gravity field recovery. Its implementation in the Bonn software GROOPS is described in detail in (Mayer-Gürr, 2006). The core of the approach is the reformulation of Newton’s equation of motion as solution of a boundary value problem (Fredholm integral equation of the second kind),

$$\mathbf{r}(t) = (1-\tau)\mathbf{r}_A + \tau\mathbf{r}_B - T^2 \int_{\tau'=0}^{1} K(\tau,\tau')\,\mathbf{a}(t;\mathbf{r},\dot{\mathbf{r}},\mathbf{x})\,d\tau' \tag{7-2}$$

which satisfies the boundary values,

$$\mathbf{r}_A := \mathbf{r}(t_A), \quad \mathbf{r}_B := \mathbf{r}(t_B), \quad t_A < t_B \tag{7-3}$$

Herein, $K(\tau,\tau')$ denotes the integral kernel,

$$K(\tau,\tau') = \begin{cases} \tau(1-\tau'), & \tau \le \tau', \\ \tau'(1-\tau), & \tau' \le \tau. \end{cases} \tag{7-4}$$

Eq. (7-2) can easily be used to set up an observation equation for kinematical positions previously derived from GNSS observations. Under the assumption that the kinematical positions are accurate enough to be fixed within the force function, it provides a linear relationship between the observed orbit, the boundary values and the force parameters x, e.g. the potential coefficients x_V. Solving for differential improvements of the boundary values and the gravity field, the observation equation for a single arc then reads:

$$\mathbf{l}_{POD} = \mathbf{B}\,\Delta\mathbf{b} + \mathbf{KG}\,\Delta\mathbf{x}_V, \tag{7-5}$$

where $\mathbf{l}_{POD}$ comprises the series of observed coordinates reduced by computed values and the integrals of the disturbing forces. The vector $\Delta\mathbf{b}$ contains the improvements of the boundary values,

$$\Delta\mathbf{b} = \begin{pmatrix} \mathbf{r}_A - \mathbf{r}_{A,0} \\ \mathbf{r}_B - \mathbf{r}_{B,0} \end{pmatrix} \tag{7-6}$$

and $\mathbf{B}$ the partial derivatives of the orbit w.r.t. the boundary values,

$$\mathbf{B} = \begin{pmatrix} 1-\tau & \tau \end{pmatrix}. \tag{7-7}$$

Analogously, $\mathbf{G}$ is built up of the partial derivatives of the gravitational force w.r.t. the potential coefficients. The Matrix $\mathbf{K}$ is the quadrature operator which can be derived by a discretisation of the Fredholm integral. The reference values for the potential coefficients have to be taken from a reference field, in case of e^2.motion from EGM96. As reference boundary values the observed values of r_A and r_B are used.

A similar expression can be derived for the inter-satellite link. Here, the observed quantity is the range-rate $\dot{\rho}$ defined geometrically as the relative velocity of the satellites projected onto the line of sight,

$$\dot{\rho} = \mathbf{e}_{12} \cdot \dot{\mathbf{r}}_{12} = \frac{x_{12}\dot{x}_{12} + y_{12}\dot{y}_{12} + z_{12}\dot{z}_{12}}{\sqrt{x_{12}^2 + y_{12}^2 + z_{12}^2}} \tag{7-8}$$

The range-rate is a highly nonlinear functional of the satellites' positions and velocities. Therefore, the above expression has to be linearised as follows,

$$\dot{\rho} = \dot{\rho}_0 + \frac{\partial\dot{\rho}}{\partial\mathbf{r}_{12}}\Delta\mathbf{r}_{12} + \frac{\partial\dot{\rho}}{\partial\dot{\mathbf{r}}_{12}}\Delta\dot{\mathbf{r}}_{12}\,. \tag{7-9}$$

The improvements of the relative position, $\Delta\mathbf{r}_{12}$, and the relative velocity, $\Delta\dot{\mathbf{r}}_{12}$, can be expressed using the integral equation approach. However, since the accuracy of the GNSS-derived orbits is far below the accuracy of the measured range-rates, fixing the positions in the force function at the observed positions is not sufficient in the SST equations. Therefore, the orbit model has to be refined based on a further linearization,

$$\mathbf{r} = \mathbf{r}_0 + \frac{\partial\mathbf{r}}{\partial\mathbf{b}}\Delta\mathbf{b} + \frac{\partial\mathbf{r}}{\partial\mathbf{a}}\Delta\mathbf{a}. \tag{7-10}$$

The partial derivatives now include a first-order correction using the gravity gradients taken along the observed positions. As explained in (Mayer-Gürr, 2006), the derivatives then read

$$\bar{\mathbf{B}} := \frac{\partial\mathbf{r}}{\partial\mathbf{b}} = \left(\mathbf{I} - \mathbf{KT}\right)^{-1}\mathbf{B} \tag{7-11}$$

and

$$\mathbf{R} := \frac{\partial\mathbf{r}}{\partial\mathbf{a}} = \left(\mathbf{I} - \mathbf{KT}\right)^{-1}\mathbf{K} \tag{7-12}$$

with $\mathbf{T}$ containing the gravity gradients and $\mathbf{I}$ being the unit matrix. The improvement of the relative position effectuated by the improvements of the boundary values and the field coefficients can be written now by

$$\Delta\mathbf{r}_{12} = \bar{\mathbf{B}}_2\Delta\mathbf{b}_2 + \mathbf{R}_2\mathbf{G}_2\Delta\mathbf{x}_V - \bar{\mathbf{B}}_1\Delta\mathbf{b}_1 - \mathbf{R}_1\mathbf{G}_1\Delta\mathbf{x}_V \tag{7-13}$$

The expression for the relative velocity is similar,

$$\Delta\dot{\mathbf{r}}_{12} = \dot{\bar{\mathbf{B}}}_2\Delta\mathbf{b}_2 + \dot{\mathbf{R}}_2\mathbf{G}_2\Delta\mathbf{x}_V - \dot{\bar{\mathbf{B}}}_1\Delta\mathbf{b}_1 - \dot{\mathbf{R}}_1\mathbf{G}_1\Delta\mathbf{x}_V \tag{7-14}$$

Here, the partial derivatives are given by

$$\dot{\bar{\mathbf{B}}} := \frac{\partial \dot{\mathbf{r}}}{\partial \mathbf{b}} = \dot{\mathbf{B}} + \dot{\mathbf{K}}\mathbf{T}\bar{\mathbf{B}} \tag{7-15}$$

and

$$\dot{\mathbf{R}} := \frac{\partial \dot{\mathbf{r}}}{\partial \mathbf{a}} = \dot{\mathbf{K}} + \dot{\mathbf{K}}\mathbf{T}\mathbf{R} \tag{7-16}$$

The columns of the matrix $\dot{\mathbf{B}}$ are the time derivatives of the columns of $\mathbf{B}$. The sign $\dot{\mathbf{K}}$ denotes an operator effectuating a single quadrature.

After inserting (7-13) and (7-14) in Eq. (7-9), the complete linear model for the range-rates can be set up. For the sake of clarity, the following abbreviations are introduced:

$$\mathbf{l}_{SST} = \left(\dot{\rho} - \dot{\rho}_0\right) \tag{7-17}$$

$$\mathbf{P} = \begin{pmatrix} \dfrac{\partial \dot{\rho}}{\partial \mathbf{r}_{12}} & \dfrac{\partial \dot{\rho}}{\partial \dot{\mathbf{r}}_{12}} \end{pmatrix} \tag{7-18}$$

The observation equation for the range-rates along a single arc then reads:

$$\mathbf{l}_{SST} = \mathbf{P}\begin{pmatrix} \bar{\mathbf{B}}_1 & -\bar{\mathbf{B}}_2 \\ \dot{\bar{\mathbf{B}}}_1 & -\dot{\bar{\mathbf{B}}}_2 \end{pmatrix}\begin{pmatrix} \Delta\mathbf{b}_1 \\ \Delta\mathbf{b}_2 \end{pmatrix} + \mathbf{P}\begin{pmatrix} \mathbf{R}_1 & -\mathbf{R}_2 \\ \dot{\mathbf{R}}_1 & -\dot{\mathbf{R}}_2 \end{pmatrix}\begin{pmatrix} \mathbf{G}_1 \\ \mathbf{G}_2 \end{pmatrix}\Delta\mathbf{x}_V \,. \tag{7-19}$$

The above observation equations are set up for arcs with a default length of 35 minutes and then accumulated to normal equations. In general, the normal equations set up with the SST observations can be solved on their own. However, experience has shown that by adding the orbit observations the gravity field solution becomes more stable especially in the longer wavelengths. The combination of different observation types then entails the choice of appropriate weighting factors. In processing real data, GROOPS solves this problem in an iterative way by estimating a set of variance components. Such a procedure is not applied in the e^2.motion simulations. The observation equations for the range-rates are simply weighted according to the mean of the range-rate noise model (2.48e-9 m/s^2). For the orbit error a fixed value of 2 cm is adopted.

7.2 Results of Numerical Simulations

7.2.1 Results from Acceleration Method

In this section the results from acceleration method (theory in section 7.1.1) are shown. All results in section 6.4.2.1 on tone error requirements are also derived with this method. Here the final results of the basic scenario are shown in the spectral and spatial domain. In the end there is a validation and a comparison with the mission requirements. Emphasis is put on the comparison of the Bender-type double pair and the single polar pair results.

The input data assessment for these simulations is described in section 6. The error free observations in terms of acceleration differences along the LoS are computed from the true world. Then the noise (version 2 including tone errors) is added. Applying an adequate stochastic model as used in section 6.4.2.1 the unknown SH coefficients are estimated together with their variance covariance information. The combination of the polar and the inclined pair is done on normal equation level. Table 7-2 gives an overview on the different simulation scenarios.

Table 7-2: Simulation scenarios with their legend abbreviations used in the following figures (residuals are the differences between the estimated gravity field and the mean true world)

Legend	Description
Formal errors	Formal errors of the least squares adjustment (square-root of the diagonal of the variance covariance matrix of the unknowns)
Static (residuals)	Input: only static (dominating error contribution: instrument noise)
HIS + AO-error (residuals)	Input: static and 6 hour HIS- and AO-error-models (dominating error contr.: temporal aliasing from AO-errors)
Ocean tide diff. (residuals)	Input: differences of two ocean tide models up to d/o 50 (dominating error contr.: temporal aliasing from the residual ocean tides)
Total (error residuals)	Input: whole true world (dominating error contr.: temporal aliasing from the residual ocean tides)

Figure 7-4 shows unit less SH coefficient errors for the two scenarios (single polar pair left, Bender-type double pair right) and three different error cases. As the static case does not contain error contributions from temporal aliasing the formal errors (top) should represent the corresponding residuals (center). The contribution of the inclined pair can clearly be seen in the sectorial SH coefficients. Adding the inclined pair reduces the temporal aliasing errors significantly, which shows the total error cases (bottom).

The different error scenarios are compared with the reference signals in terms of SH degree amplitudes in Figure 7-5. The good accordance of the formal errors and the static residuals for the single (left) and double (right) pair indicates a correct stochastic model. The dominating error contribution is temporal aliasing from the AO-errors and even more from the ocean tide model errors. The largest temporal aliasing effects can be seen for the single polar pair (left) in large resonance effects at SH degrees 77 and 108. These effects are reduced significantly for the basic scenario, the Bender-type double pair. The total error of the single polar pair reaches 1 mm geoid error at SH degree 78 (spatial wavelength 257 km). The basic mission scenario, the Bender-type double pair, reaches 1 mm at SH degree 124 (wavelength 162 km), nearly the optimal mission requirement.

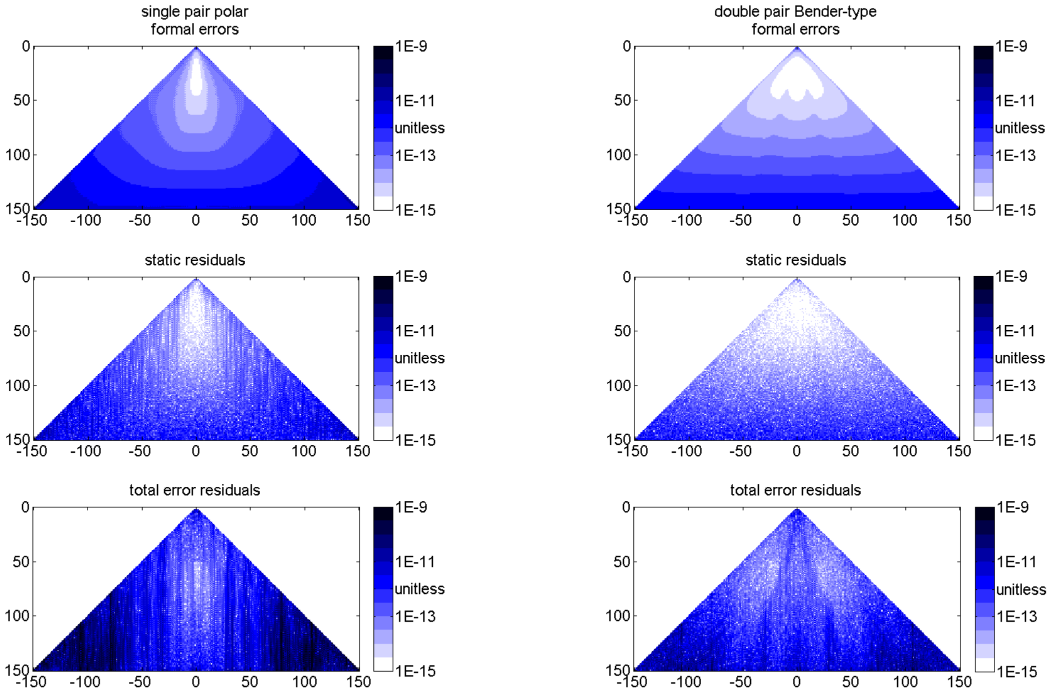

Figure 7-4: Unitless SH coefficient errors for the two scenarios (left: single polar pair, right: Bender-type double pair) and three different error cases (top: formal errors, center: static residuals, bottom: total error residuals) up to SH d/o 150.

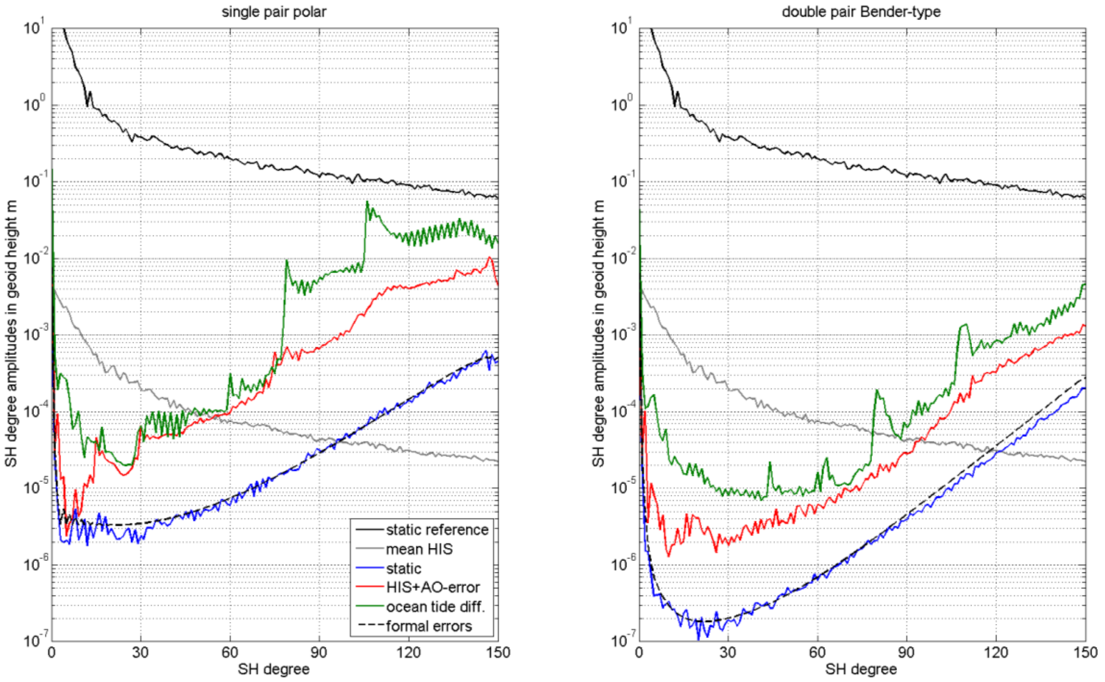

Figure 7-5: SH degree amplitudes in m geoid height for the single polar pair (left) and the Bender-type double pair (right) in comparison with the static reference models (black: static, gray: mean HIS). Different error scenarios (blue: static, red: HIS and AO-errors, green: ocean tide differences) and the formal errors (black dashed) are shown.

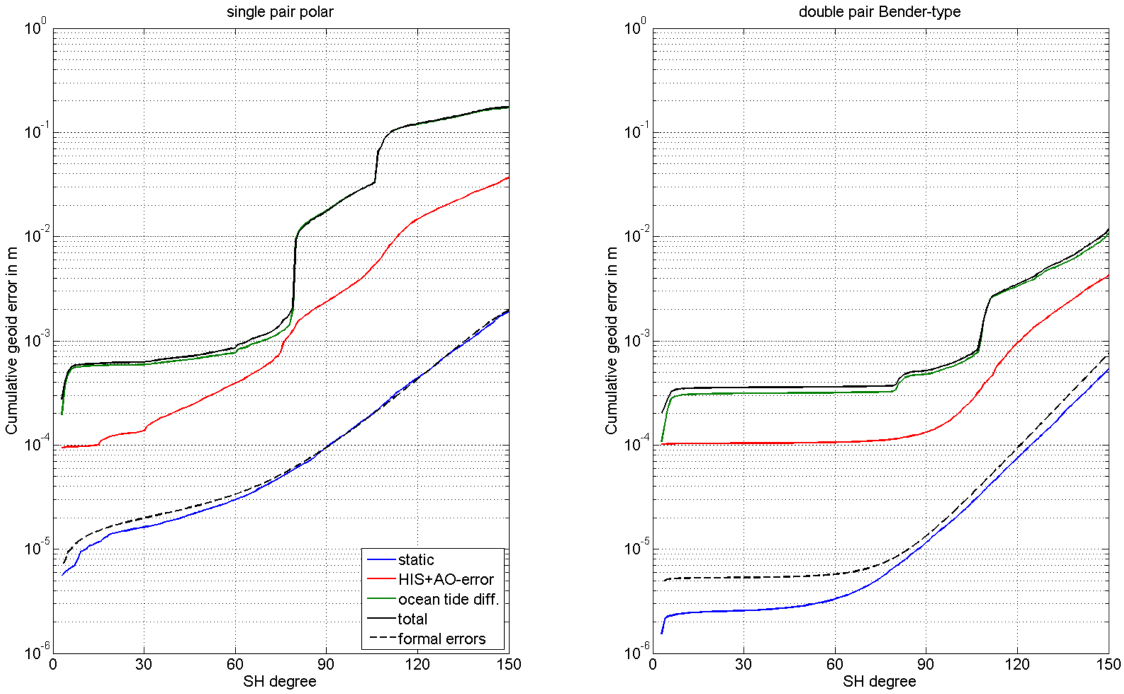

Figure 7-6: Cumulative geoid error per SH degree in m for the single polar pair (left) and the Bender-type double pair (right). Different error scenarios (blue: static, red: HIS and AO-errors, green: ocean tide differences, black: total error) and the formal errors (black dashed) are shown.

Figure 7-6 shows the cumulative geoid errors in m in the same way as Figure 7-5 including the total error case (black). The total error of the single polar pair reaches 1 mm cumulative geoid error at SH degree 65 (spatial wavelength 308 km). The basic mission scenario, the Bender-type double pair, reaches 1 mm at SH degree 108 (wavelength 186 km) fulfilling the minimal mission requirement. The effects of the large resonances can be seen in the stepwise increase at SH degrees 77 and 108.

The optimal mission requirement is formulated for a spatial wavelength of 150 km. This corresponds to SH degree 133. The spatial error distribution for this resolution is shown in Figure 7-7 in terms of geoid heights in mm on a 0.5x0.5 degree grid. The six different plots have different colour bars. Only the static case for the double-pair (top right) shows an uncorrelated geoid error distribution (at least for the latitudes where observations of both pairs are available). All other cases show correlated error structures (mostly north-south stripes). Especially the cases for HIS and AO-errors show localized errors. But it is clearly visible that the Bender-type double pair shows significantly reduced errors (smaller magnitude and higher isotropy) in comparison with the single polar pair.

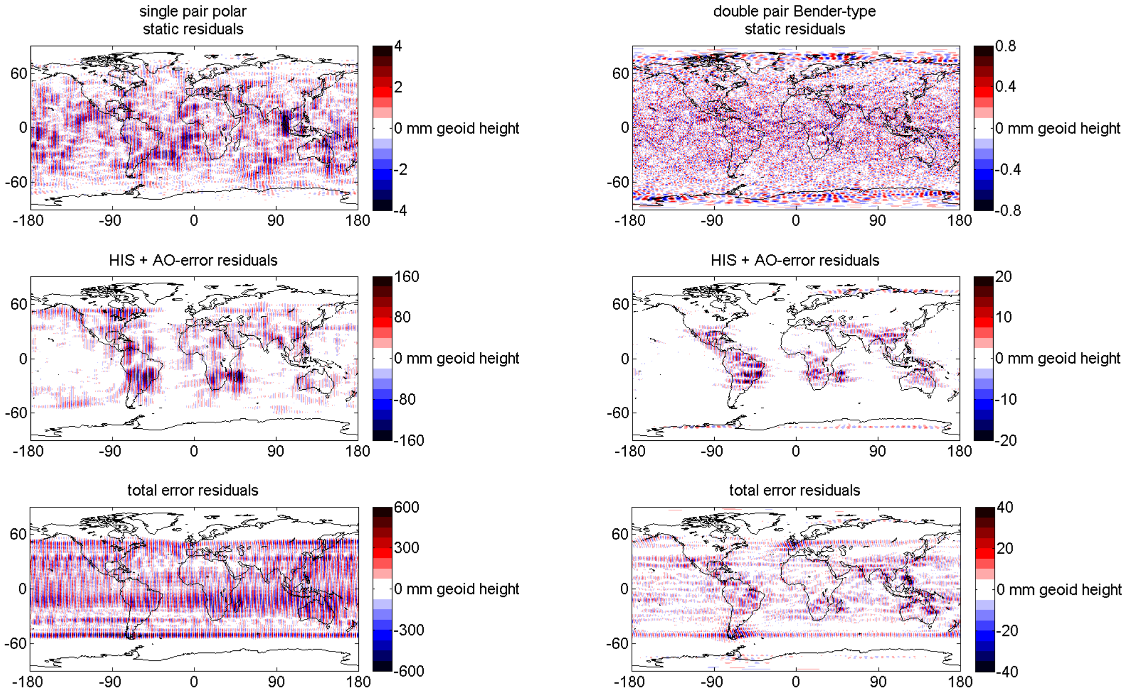

Figure 7-7: Global geoid height errors in mm for the single polar pair (left) and the Bender-type double pair (right) computed up to lmax=133. Different error scenarios (top: static, center: HIS and AO-errors, bottom: total error) are shown (note the different colour bars)

A numerical evaluation of Figure 7-7 in terms of global RMS values is shown in Table 7-3. Eventually the results of the basic mission scenario are compared with the mission requirements (cf.Table 7-4)

). The Bender-type double pair fulfils the 1 mm geoid goal at a spatial wavelength of 186 km (between minimal and optimal requirement). The background model errors (AO-errors and especially the ocean tide model errors) are the largest error contribution. Neglecting those errors the 1 mm goal is reached at wavelengths smaller than 134 km (better than the optimal requirement). Therefore, improved background models lead to increased gravity field resolution. Furthermore, with optimized processing strategies (taking advantage of short period solutions) the impact of temporal aliasing can be further reduced.

Table 7-3: Global RMS (cosine latitude weighted) in mm geoid height (lmax=133)

	Single pair polar	Double pair Bender-type	Single/Double
Static residuals	0.88	0.18	4.9
HIS + AO-error residuals	23	2.1	11
Ocean tide model error residuals	140	5.3	26
Total error residuals	150	5.7	26

Table 7-4: SH degree and wavelength in brackets where the 1 mm geoid goal is reached

	SH degree amplitudes		Cumulative geoid error	
	Single pair polar	Double pair Bender-type	Single pair polar	Double pair Bender-type
Formal errors	> 150 (< 134 km)	> 150 (< 134 km)	136 (147 km)	> 150 (< 134 km)
Static residuals	> 150 (< 134 km)	> 150 (< 134 km)	137 (146 km)	> 150 (< 134 km)
HIS + AO-error residuals	97 (207 km)	145 (138 km)	77 (260 km)	121 (166 km)
Ocean tide model error residuals	78 (257 km)	126 (159 km)	69 (290 km)	108 (186 km)
Total error residuals	78 (257 km)	124 (162 km)	65 (308 km)	108 (186 km)

7.2.2 Results from Numerical Integration Method

In this section the results of the numerical integration approach are presented. To recall this method uses daily arc and GPS and SST observations. The results are given in the spectral domain and in the spatial domain.

Results in the Spectral Domain

The degree amplitudes in geoid heights represent the root sum of the squares (rss) of the error per degree scaled with the radius of the Earth.

To see the progressive error influences on the gravity field recovery in Figure 7-8, each error type was introduced in a given sequence starting from the error free case (green curve), then considering the SST measurement noise (yellow curve), adding the accelerometer noise (orange curve), the time variable gravity field (AOHIS) error (red curve) and finally the ocean tides error to reach the complete error brown curve denoted as all errors.

Based on all errors considered the one mm geoid height error is reached for degree 130 which corresponds to a spatial resolution of about 154 km.

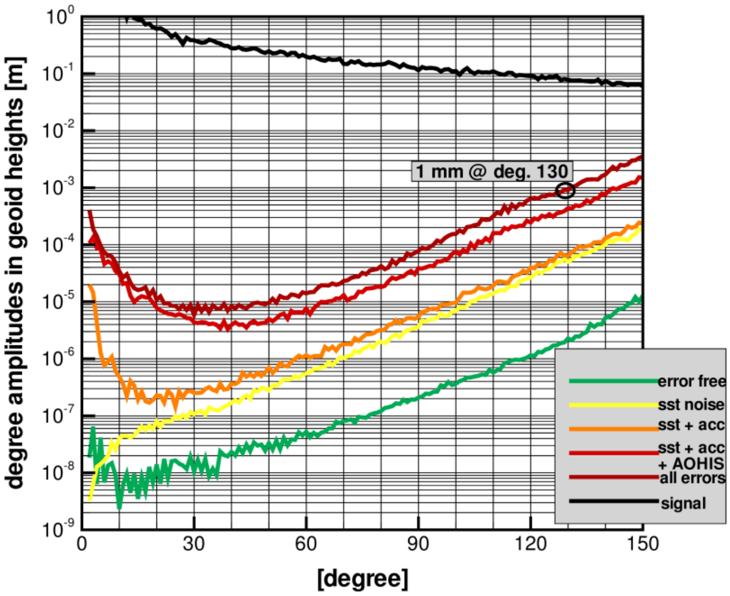

Figure 7-8: Degree amplitudes in geoid heights

The accumulated degree amplitudes error (see Figure 7-9) represents the degree amplitudes error accumulated up to a certain degree n. From the figure it can be seen that the 1 mm cumulative error can be reached for degree 110, which corresponds to a spatial resolution of about 190 km (more exactly 182 km), when considering instrument and background model errors whereas the limiting error case of instrument noise only achieves easily the 1 mm cumulative error at degree 150 corresponding to a spatial resolution of about 134 km.

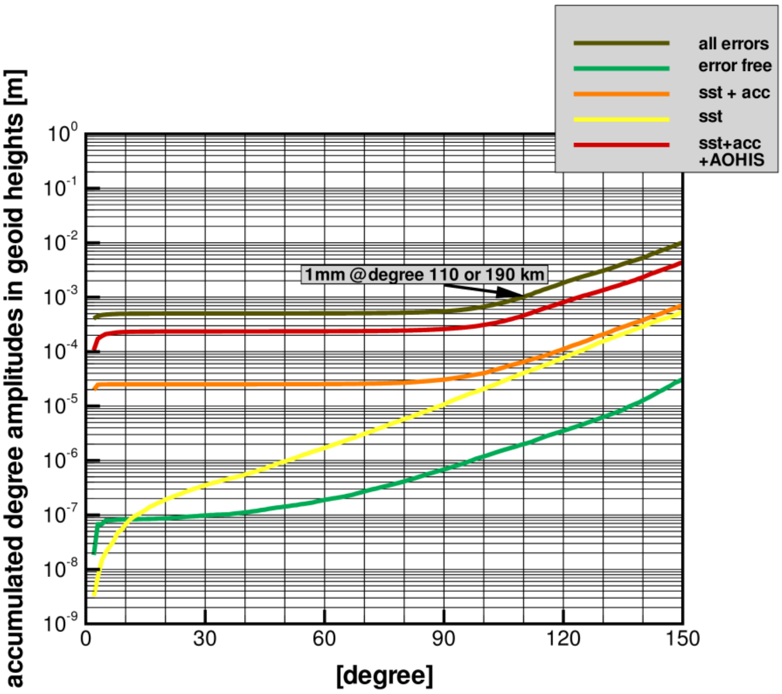

Figure 7-9: Accumulated degree amplitudes in geoid heights

The true (recovered – simulated) errors and the formal errors (solution sigmas) are plotted for the individual spherical coefficients.in the case of instrument noise only (refer to Figure 7-10) and in the case of instrument noise plus background model errors (Figure 7-11).

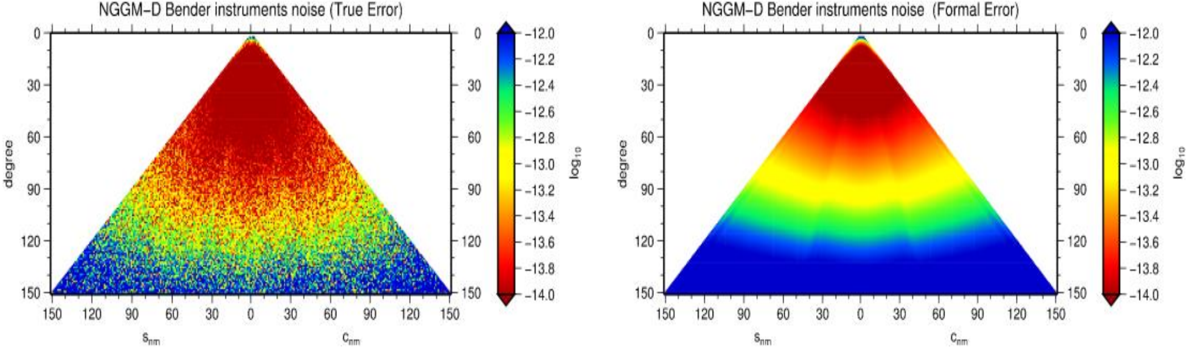
NGGM-D Bender instruments noise (True Error)

NGGM-D Bender instruments noise (Formal Error)

Figure 7-10: True (left) and formal errors (right) for instrument only noise

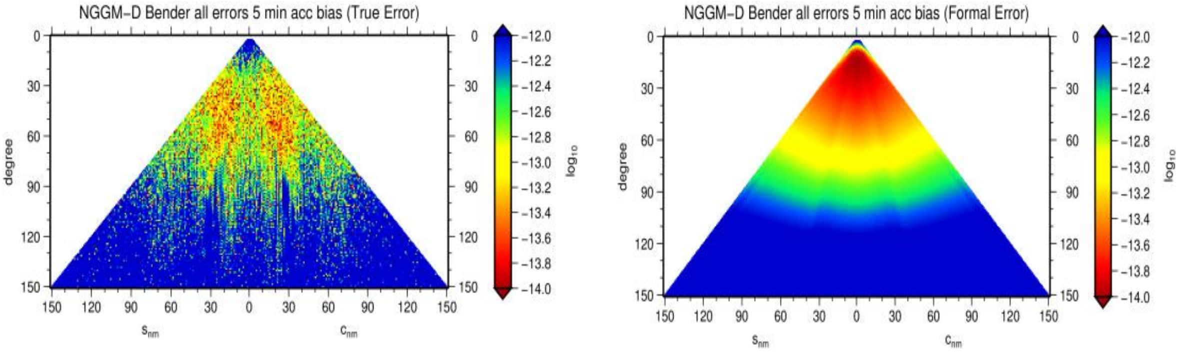
NGGM-D Bender all errors 5 min acc bias (True Error)

NGGM-D Bender all errors 5 min acc bias (Formal Error)

Figure 7-11: True (left) and formal errors (right) for instrument noise plus background model errors

Results in the Spatial Domain

The error representation in the spatial domain in term of geoid height differences shows the differences between the recovered and true world gravity fields. The left picture in Figure 7-12 shows the differences in the case of instrument noise only (rms = 0.7 mm) and the right picture in the case of instrument noise and background model errors (rms = 0.9cm). Global rms given are cosine latitude weighted rms.

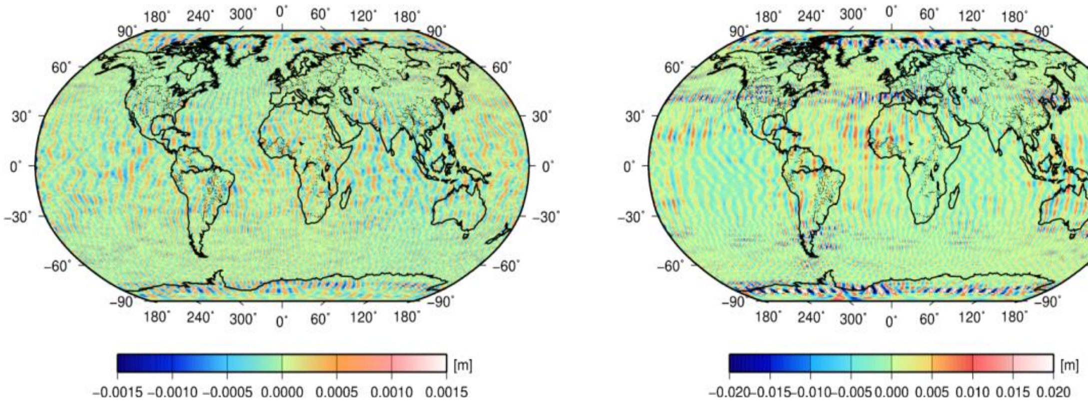

Figure 7-12: Geoid recovery errors in the spatial domain: Left: instrument only noise, Right: instrument noise plus background model errors

7.2.3 Results from Integral Equation Method

In this section the results of the integral equation approaches are presented. To recall the integral equation approach is based on 35 minutes short arc with the orbit and the SST measurement as observations.

Results in the Spectral Domain

Here again (Figure 7-13 and Figure 7-14) similar to what has been done in the numerical integration approach error sources were added sequentially in the same order to follow the influence of the various error types on the degree amplitudes in geoid heights from the error free case (green curve) up to the instrument noise plus background model errors case (brown curve).

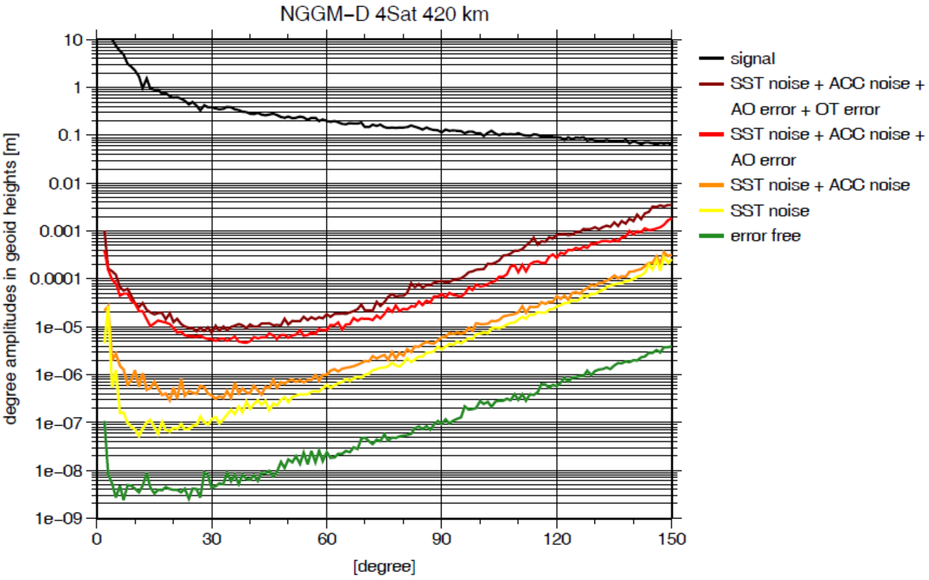

Figure 7-13: Degree amplitudes in geoid heights

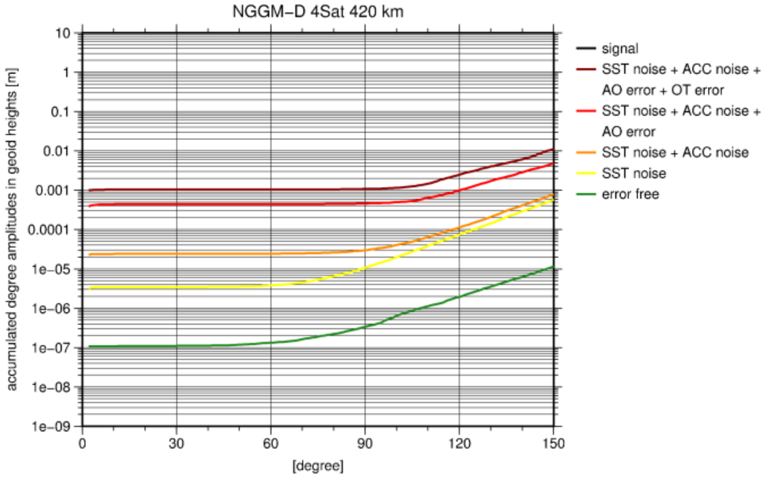

Figure 7-14: Accumulated degree amplitudes in geoid heights

In Figure 7-15 and Figure 7-16 the errors for the individual spherical harmonic coefficients are plotted as true errors (left pictures) and formal errors (right pictures) for the instrument only case (Figure 7-15) and for the all errors case (Figure 7-16).

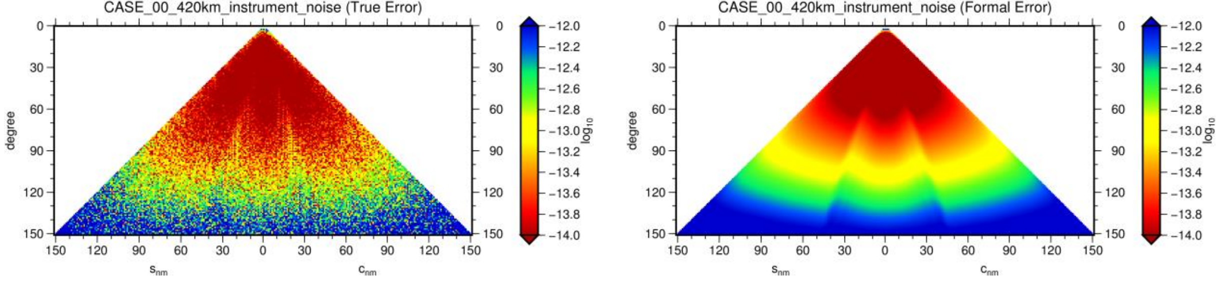

Figure 7-15: True (left) and formal errors (right) for instrument only noise

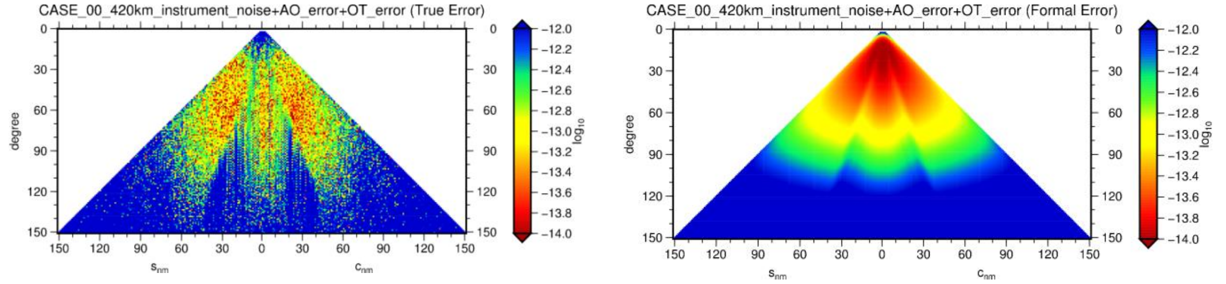

Figure 7-16: True (left) and formal errors (right) for instrument noise plus background model errors

Results in the Spatial Domain

In the spatial domain the instrument noise only solution yields a global weighted rms of 1 mm (Figure 7-17 left) and the instrument noise plus background model errors solution yields an rms of 1.2 cm (right picture Figure 7-17).

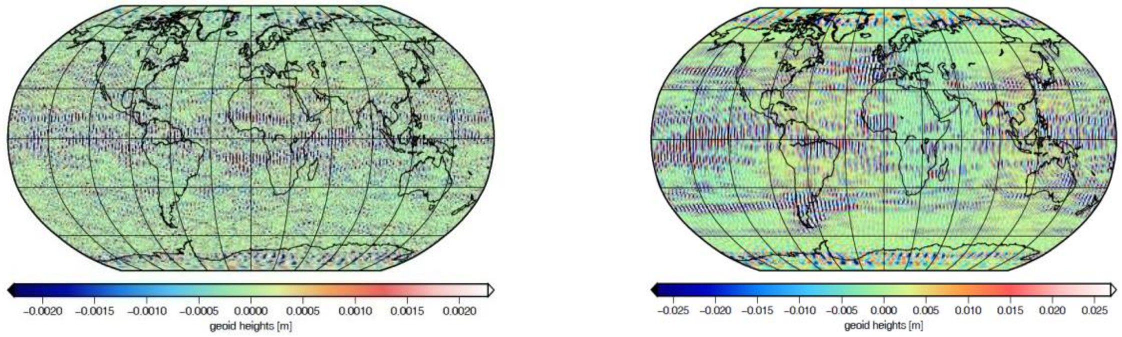

Figure 7-17: Geoid recovery errors in the spatial domain: Left: instrument only noise, Right: instrument noise plus background model errors

Influence of the Tone Errors in the Instrument Colored Noise

An investigation on the influence of noise with tone errors has been carried out using time series of instrument colored noise, where tone errors have been included. It shows an effect on lower spherical harmonics as well as for higher tesseral and sectorial terms. In the spatial domain the effect can be seen as a belt (+/- 15 degrees) around the equator.

The following plot in the spatial domain shows the influence of the tone errors in the case of instrument noise only. The weighted rms of the difference in gravity field recovery using instrument noise with and without tone errors being 0.37 mm.

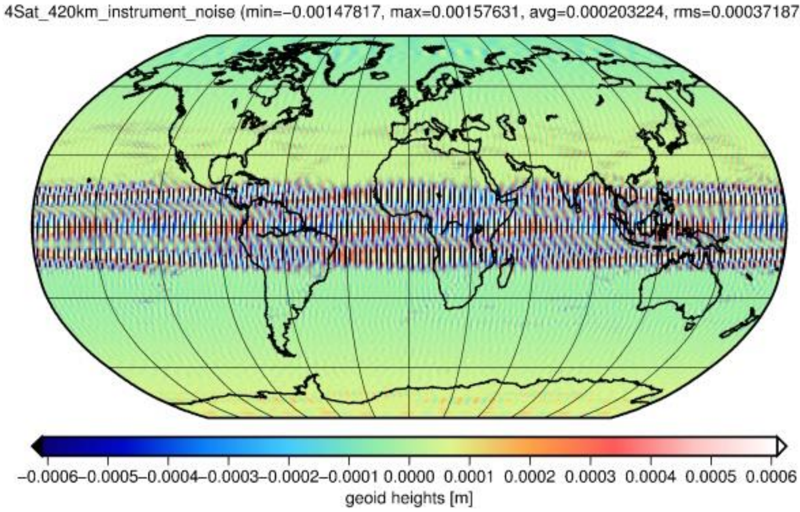

Figure 7-18: Influence of tone errors in spatial domain

The following plots (Figure 7-19) show the degree amplitudes in geoid heights and the accumulated degree amplitudes in geoid heights when tone errors are considered for the instrument colored noise time series.

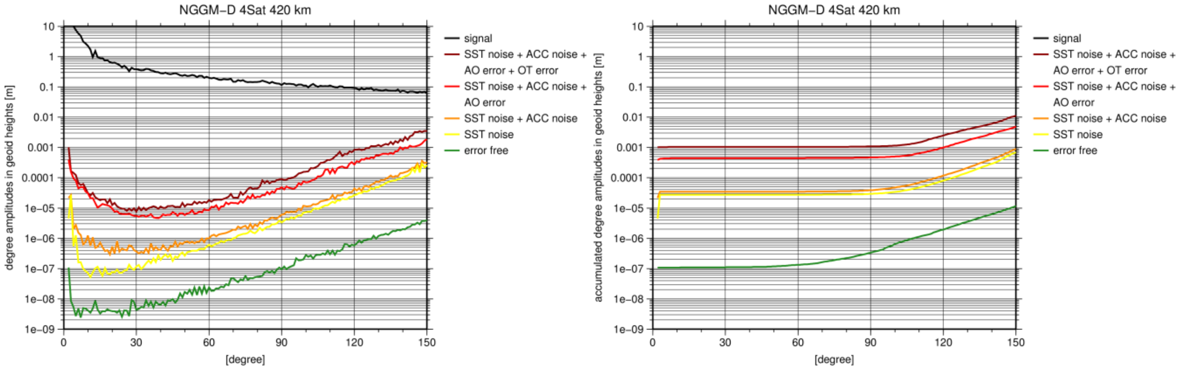

Figure 7-19: Influence of tone errors in spectral domain

Comparison between Double Pair versus Single Pair

In the following paragraph a comparison between a single satellite pair and a double satellite pair is presented.

In the spatial domain

In case of a double pair satellite mission (Bender type) the left picture indicates an error of 1.0 mm RMS when instrument noise only are considered, the right picture shows an error of 1.2 cm RMS when instrument noise and background model errors are introduced.

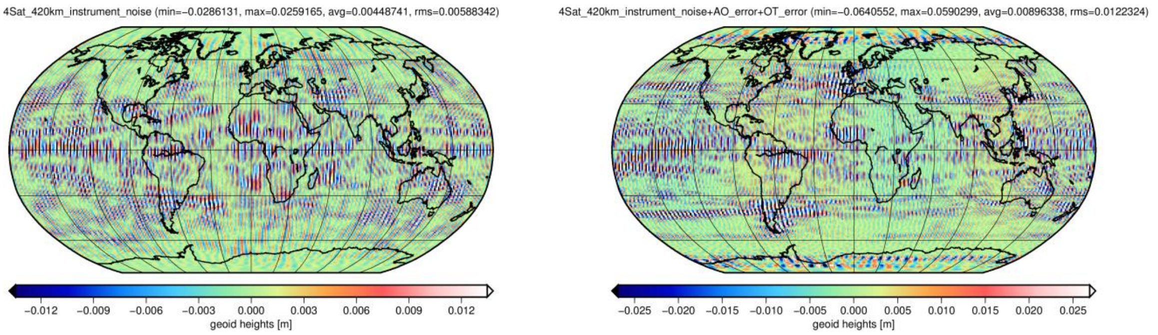

Figure 7-20: Double pair mission results for instrument only noise (left) and instrument only plus background model errors (right)

For a single pair mission the left picture (Figure 7-21) indicates an error of 5.9 mm RMS when instrument noise only are considered, the right picture (Figure 7-21) shows an error of 14.8 cm RMS when instrument noise and background model errors are introduced. When looking to Figure 7-21 in comparison to Figure 7-20 we can see an increase in the stripes is for a single pair satellite compared to a double pair satellite.

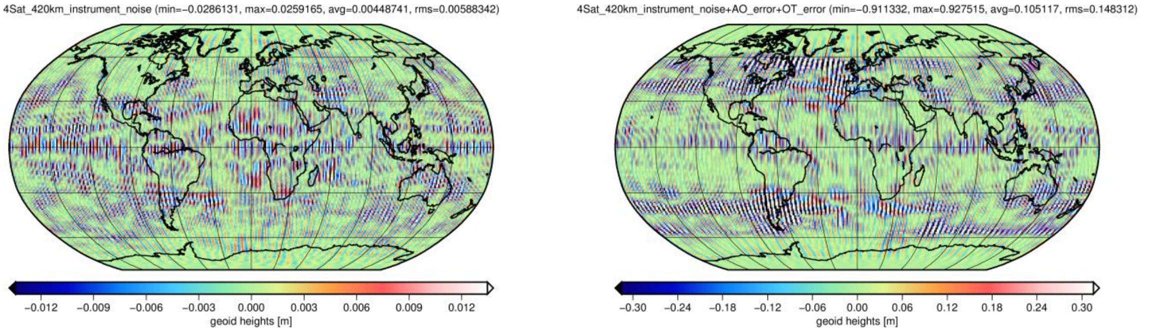

Figure 7-21: Single pair mission results for instrument only noise (left) and instrument only plus background model errors (right)

In the spectral domain

In the case of instrument noise only (Figure 7-22) the 1 mm geoid is achieved easily at degree 150 (134 km) for the double satellite pair whereas it is already reached the limit at degree 140 (143 km) for the single satellite pair.

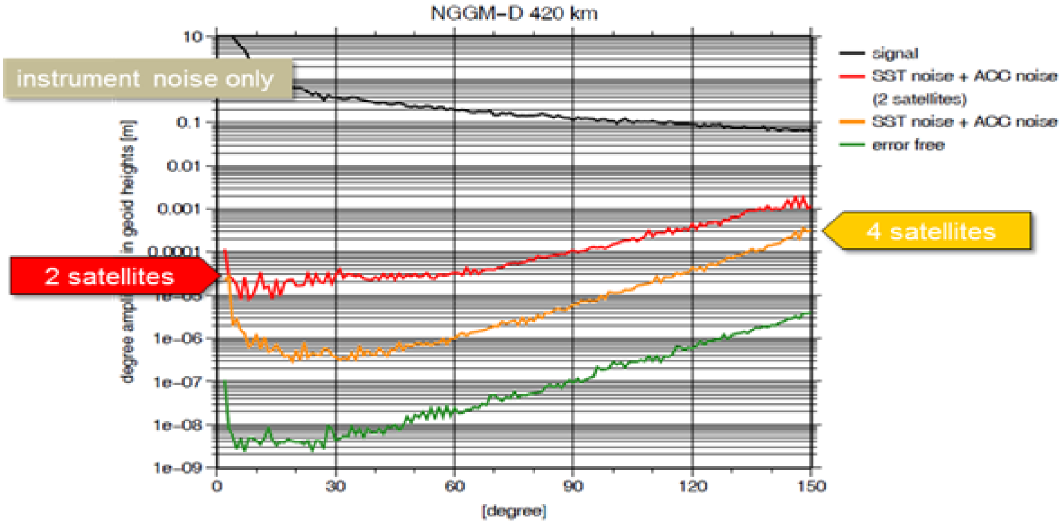

Figure 7-22: Degree amplitudes comparison single pair versus double pair in the noise only case

In the case of instrument noise only plus background model errors (Figure 7-23) the 1 mm geoid is achieved at degree 130 (154 km) for the double satellite pair whereas it is already reached at degree 65 (308 km) for the single satellite pair.

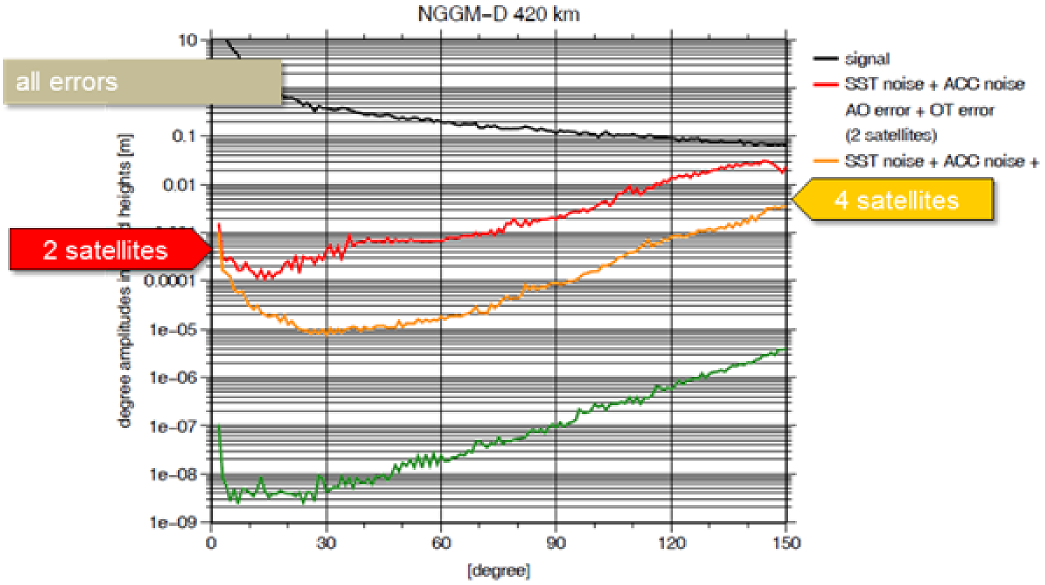

Figure 7-23: Degree amplitudes comparison single pair versus double pair in the instrument noise plus background model errors

Finally from the following plots (Figure 7-24 and Figure 7-25) showing the individual coefficient errors a large improvement for the determination of the tesseral and sectorial spherical harmonics is visible when using two satellite pairs (Figure 7-24) instead of a single pair (Figure 7-25).

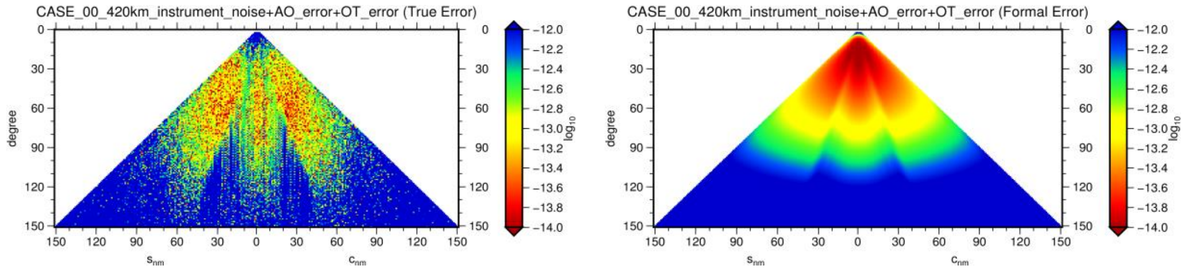

Figure 7-24: True and formal errors for a double pair mission

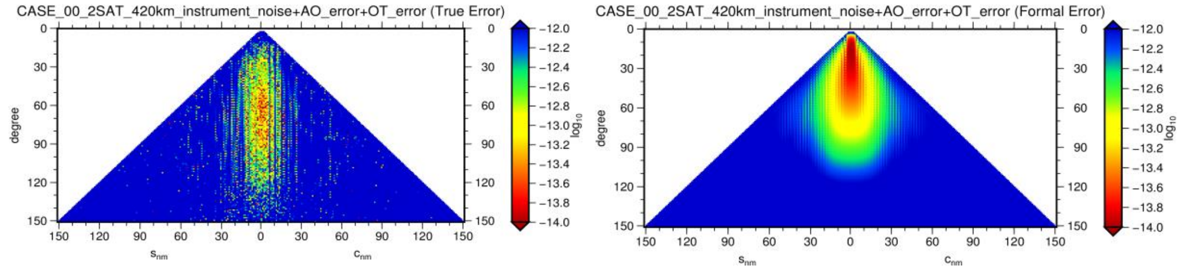

Figure 7-25: True and formal errors for a single pair mission

7.2.4 Intercomparison of Simulation Results

The three different approaches from GFZ (numerical integration), IGG (integral equation) and IAPG (acceleration) use different types of observation and solve-for parameters besides the gravity field. Table 7-5 below lists all observations and solve-for parameters in the gravity field recovery process. Moreover the degree of freedom (redundancy) of each individual solution is indicated.

Table 7-5: Summary of simulation parameters for the 3 approaches

		GFZ	IGG	IAPG
observations	**GNSS**	**5112558**		
	POD		**6635520**	
	SST	**1105920**	**1105920**	**1105920**
	Total	**6218478**	**7741440**	**1105920**
Parammeters	Initial values	768		
	Boundary values		31608	
	Accelero. biases	111360	31608	
	SST biases	3200		
	GNSS ambiguities	1664		
	Gravity field	22801	22797	22801
	Total	139793	86013	22801
	Redundancy	6078685	7655427	1083119

Figure 7-26 depicts the degree amplitudes in geoid heights (m) for the three solutions. The agreement between the solutions is very good especially when all errors (instrument noise plus background model errors) are considered. The IAPG solution departs a little bit from the other two solutions around some resonance terms.

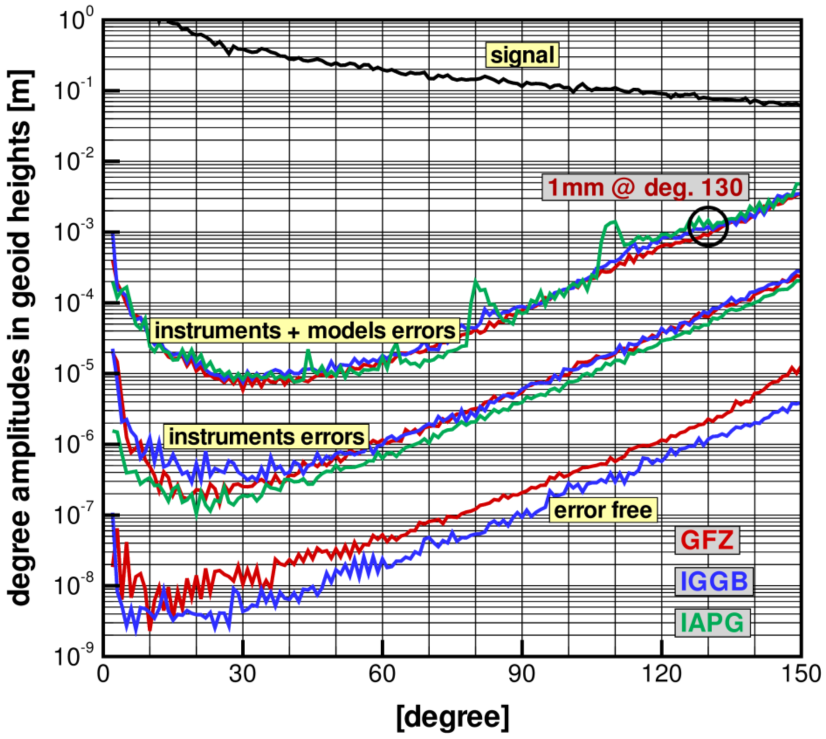

Figure 7-26: Comparison of simulation results from the 3 approaches in terms of degree amplitudes

In Figure 7-27 below the accumulated degree amplitudes in geoid heights (m) are shown for the GFZ and IGG solution in the case of error-free, instrument error and instrument errors plus background model errors. The 1 mm cumulative geoid error when all errors are considered is achieved for degree 110 (182 km spatial resolution) with the GFZ solution and about degree 100 (200 km spatial resolution) with the IGG solution.

In the case of instrument noise only being the limitating case, that is the minimum error which could be achieved in the gravity field recovery process, both solutions GFZ and IGG reach easily the optimum goal of 1 mm at degree 150 (133 km spatial resolution).

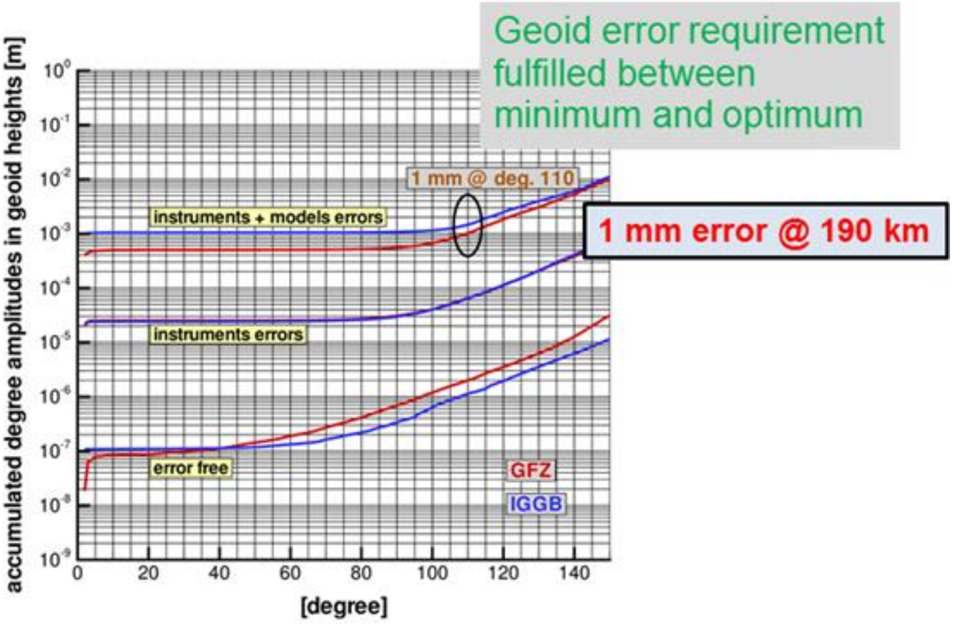

Figure 7-27: Comparison of simulation results from the 3 approaches in terms of accumulated degree amplitudes

In the following figures the individual spherical harmonic coefficient errors are plotted for the true errors left and the formal errors right for the GFZ solution (Figure 7-28) and for the IGG solution (Figure 7-29).

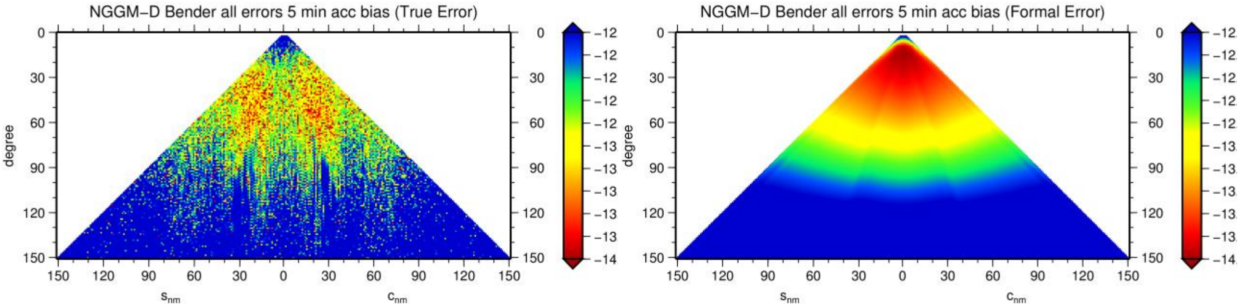

Figure 7-28: True and formal errors per coefficient for the GFZ simulation results

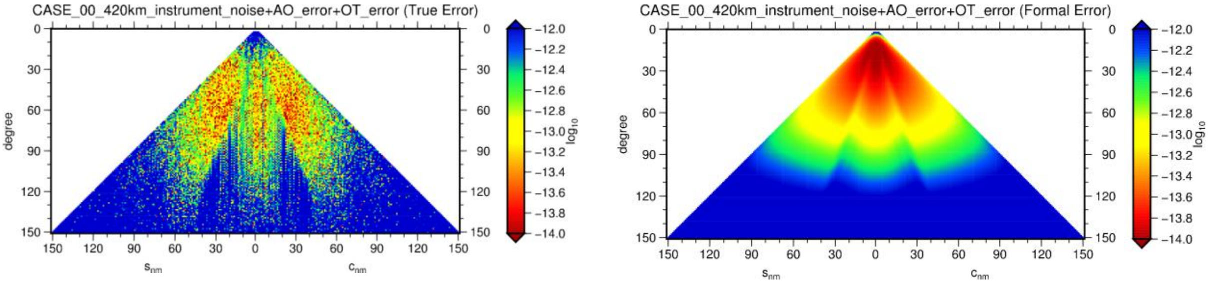

Figure 7-29: True and formal errors per coefficient for the IGG simulation results

7.2.5 Conclusions from Simulation Results

In spite of the independent techniques using a different amount of observation and solving for a different amount of parameters the agreement between the three solutions is quite good.

Based on the taken error assumptions the minimum requirement of one mm cumulative geoid error for a 200 km spatial resolution is achieved

Concerning the optimum requirement of one mm cumulative geoid error for a 150 km spatial resolution it is not quite reached but it should be kept in mind that the assumption for the model errors could be too pessimistic. The conducted simulations yield a one mm cumulative geoid error for a spatial resolution of ca 182km but in the limitating case of instrument noise only (minimum achievable error) the three solutions of GFZ , IGG and IAPG are satisfying this goal.

The effect of tone errors in the instrument noise time series can be seen for the lower spherical harmonic coefficients and some high sectorial and tesseral harmonic coefficients.

The Bender type (two satellite pairs) outperforms in the spatial domain the one satellite pair by a factor 6 in the case of instrument noise only and by a factor of about 12 in the case of instrument noise plus background model errors. The 1 mm cumulative geoid error is achieved for ca. degree 65 (308 km) for the single satellite pair and for ca. degree 110 (182 km) for the double satellite pair

8 e^2.motion Mission Concept

In this chapter the main findings are summarized and concluded in the e^2.motion mission concept. The structure follows the work plan starting with the definition of the science requirements and initial instrument requirements. The second part addresses the orbit configuration. Then there are the two main technical chapters, the design of the attitude and orbit control system and the design of the overall instrument concept for e^2.motion. In the end there are the full-scale simulation parts. After simulating all required observations, sensor errors and background model errors the results of independent full-scale gravity retrievals are compared with the mission requirements from the beginning in order to quantify if the mission requirements can be fulfilled.

8.1 Science and Mission Requirements

There has been conducted a number of previous studies defining sets of science requirements for a next generation gravity mission (NGGM). For e^2.motion mainly three of the most recent studies were analysed and compared to identify a consolidated set of science requirements. These three studies are two ESA studies, one led by Thales Alenia Italy (NGGM) and the other led by Astrium (now Airbus Defence & Space) (NG2), and the e.motion mission proposal for Earth Explorer 8. For different subsystems of the Earth these three studies define requirements for important signals to be measured.

After analysing all relevant subsystems each study came up with generalized requirements in terms of monthly geoid errors. A monthly geoid height error of 1 mm is required for spatial resolutions of 100 km (NGGM), 150 km (NG2) and 200 km (e.motion). 200 km can be seen as the minimum requirement to outperform GRACE (1mm at approx. 400 km). Therefore this is chosen for e^2.motion as the minimal geoid height science requirement. The optimal science requirement is chosen as 1 mm at 150 km spatial resolution.

A second science requirement is that a long time series of mass variation observations is available from the e^2.motion mission concept. Therefore, the mission duration must be at least one decade and the technical components need to be designed such that their lifetime copes with this requirement.

In the next step, based on an initial mission scenario top level requirements for the core instruments are derived. This initial mission scenario is a Bender-type low-low SST double pair mission with instrument accuracies of 10 nm for the distance measurements and 10^{-11} m/s^2 for the accelerometer observations. These requirements roughly represent the instrument performances which are needed in order to meet the chosen science requirements. Obviously they depend on the orbit configuration (specifically the orbit height) and need to be further refined. Based on the previous NGGM studies an orbit height range between 300 and 500 km and a satellite distance of 100 to 200 km is envisaged. The initial mission parameters are summarized in Table 8-1.

Table 8-1: Parameters of the initial mission scenario (double low-low SST pair)

Inclination	Polar pair and 75 deg. inclined pair
Altitude	From 300 to 500 km
Inter-satellite distance	100 - 200 km
Ranging instrument accuracy	10 nm
Accelerometer accuracy	10^{-11} m/s^2

In order to derive the top level instrument requirements a few initial simulations are performed. Figure 8-1 shows the cumulative geoid errors in mm for the initial mission scenario for five altitudes from 300 to 500 km and spherical harmonic (SH) degrees from 0 to 150. It is obvious that the requirements on instrument performance are less stringent the lower the mission altitude is (due to higher sensitivity of the satellite to the Earth gravity field). The scaling factor between the cumulative geoid errors in Figure 8-1 and the optimal science requirements give the instrument requirements with respect to the initial instrument accuracies (cf. Table 8-1). Considering some technical aspects the maximum mission altitude is set to 450 km and the top level instrument requirements are 40 nm for the ranging instrument accuracy and $4 \cdot 10^{-11}$ m/s^2 for the accelerometer accuracy.

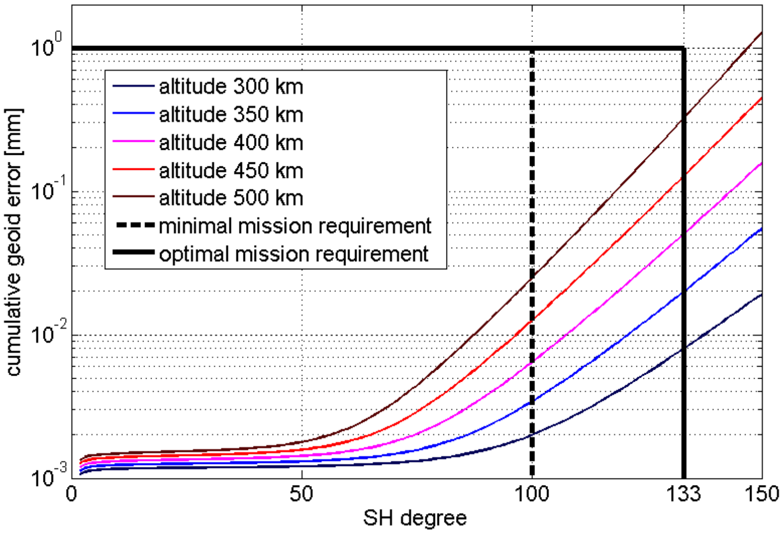

Figure 8-1: Cumulative geoid errors in mm from semi-analytical simulations for monthly solutions of the initial mission scenario (cf. Table 8-1) in comparison with the minimal and optimal science requirements.

Above, the geoid height accuracy requirements are formulated for a temporal resolution of one month. In order to enable the observation of higher temporal mass variations as one month (which would reduce the de-aliasing errors), for e^2.motion the science requirement related to the minimum temporal resolution has been specified to one week or shorter. This needs to be addressed in the orbit configuration by identifying orbits with shorter repeat cycles, meaning that after a few days the orbit reaches a global homogeneous coverage.

Summarizing the paragraphs above the following science and mission requirements have been identified for e^2.motion. Specifically the requirements on orbit height and repeat cycles are further refined in the follow-on section about choosing an optimal orbit configuration (section 8.2).

Table 8-2: e^2.motion science and mission requirements

Monthly geoid error	1 mm at 200 km (minimum) 1 mm at 150 km (optimum)
Temporal resolution of the global gravity field	Weekly or shorter
Mission duration	One decade
Orbital height	350 to 450 km
Ground track coverage	Number of satellites revolutions in the full repeat cycle of satellite mission at least equal to the maximum spherical harmonic degree to be detected
Key instrument accuracies	Ranging instrument: 40 to 200 nm/Hz$^{1/2}$ (f > 10 mHz) Accelerometer: $4\cdot10^{-11}$ to $2\cdot10^{-10}$ m/s^2/Hz$^{1/2}$ ($1 < f < 10$ mHz)

8.2 Orbit Configuration

The e^2.motion mission concept foresees a double-pair mission with different inclinations for each pair (polar and inclined). Previous NGGM studies investigated a single pair polar mission in a pendulum configuration (pendulum means that the LoS between the satellites is changing direction during each revolution). Within this study a trade-off analysis between the two mission configurations has been performed in order to identify the benefits and drawbacks of both. Table 8-3 shows the main outcome of the comparison between these two concepts.

Table 8-3: Advantages and disadvantages of a polar single-pair pendulum mission concept compared to a double-pair Bender-type mission

	Advantages	Disadvantages
Pendulum (single polar pair)	Only two satellites, and therefore only one launch is needed. This fact can make the mission less expensive if the cost for technology development remains inferior to an additional launch and two extra satellites.	Accurate pointing of the laser is more difficult to achieve From full-scale simulations it has been shown that the pendulum mission becomes competitive with Bender only for large yaw angles leading to large SST range-rate and therefore a more challenging technology. There is a need to fly higher than Bender due to increased atmospheric drag (satellite needs to be turned by yaw axis).
Bender-type (polar and inclined pair)	Reduced demand on the technology (SST range-rate < 1m/s) Can fly at a lower altitude due to the comparatively reduced atmospheric drag (no rotation in yaw necessary). Better performance for the lower spherical harmonics below degree 50, more isotropy in the errors leading to better science return.	Four satellites and probably two launches are needed (due to the very different inclinations of the orbital planes), meaning an increase in cost.

From the trade-off analysis the double-pair Bender-type concept has been favored instead of the single pair polar pendulum orbit. For this concept optimized basic orbit parameters are identified from various preliminary simulations. For example, from quick-look semi-analytical simulations in connection with the analysis of technical feasibility an optimal inter-satellite distance of 100 km has been identified. The optimal orbit inclination of the inclined pair in a similar way was investigated. Figure 8-2 shows the geoid height errors per latitude for a Bender-type mission with varying inclination of the inclined pair (from 55 to 80 degrees) as a result of the quick-look simulator. Taking into account, that important signals to be observed are in high latitudes (ice mass variations in Greenland and Antarctica) 70 degrees inclination was identified as an good compromise regarding coverage and geoid error.

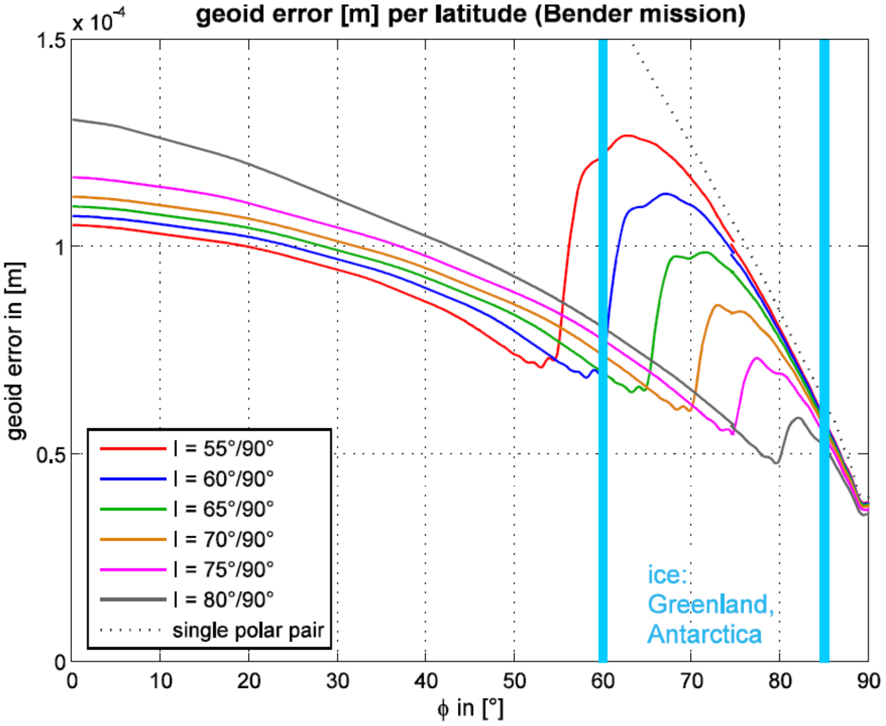

Figure 8-2: Geoid height errors in m depending on the latitude for a Bender-type mission (inter-satellite distance 100 km, max. SH degree and order 130, monthly period, instrument accuracies as in Table 8-1 for varying inclination of the inclined pair from 55 to 80 degrees.

Furthermore maximum resonance effects due to temporal aliasing (under-sampled high-frequency mass variations) shall be avoided by selecting specific altitude bands. Again the semi-analytical simulator was applied in order to identify these bands. A detailed description of this method is provided in (Murböck, Pail, Daras, & Gruber, 2014). From Figure 8-3 an optimal altitude band of around 420 km has been identified if one takes also technical conditions like propellant demand and complexity of the AOCS into account. The final baseline scenario, which is used for the full-scale simulations in the end is summarized in Tab. 4.

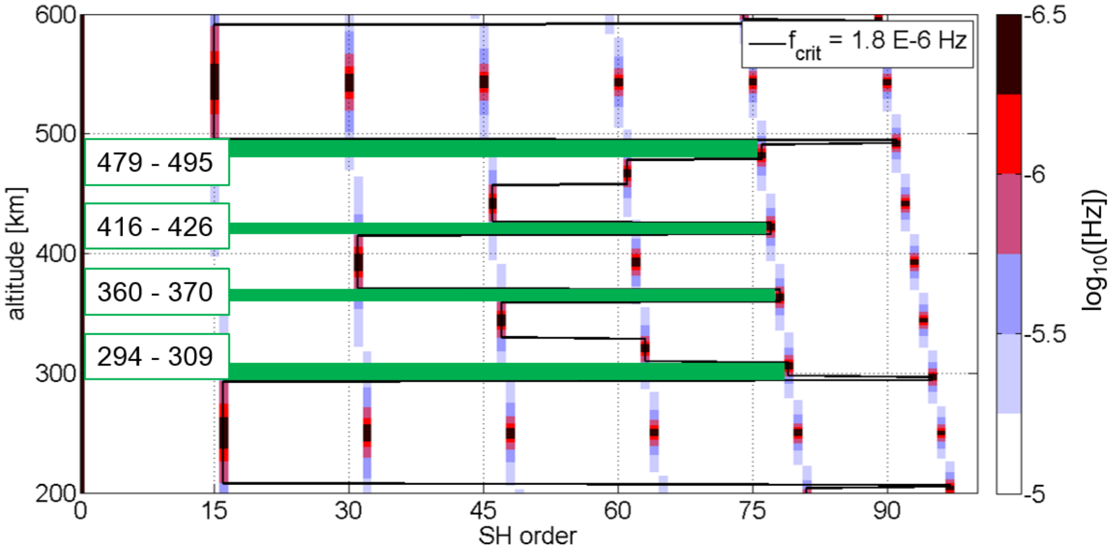

Figure 8-3: Absolute minimum frequencies for polar orbits between 200 and 600 km altitude in $\log_{10}(|f\ [Hz]|)$ together with four optimal bands (green) according to a critical frequency of $1.8 \cdot 10^{-6}$ Hz.

Table 8-4: Orbit parameters chosen for the baseline scenario

Double low-low SST pair	
Inclinations	Near polar (89.5 deg.) and inclined (70 deg.)
Altitude	420 km
Inter-satellite distance	100 km
Repeat cycle	31 days with 478 (polar pair) and 474 revolutions (inclined pair) respectively

8.3 Attitude and Orbit Control System

The attitude and orbit control system (AOCS) must fulfill drag-compensation and laser pointing requirements. The selected instrumental concept consists of the following sensors.

- Star camera (for inertial attitude determination)
- GPS sensor (for positioning and as a secondary pointing option)
- Magnetometer (supporting the magneto torquers)
- Coarse Earth and Sun Sensor (for safe mode attitude control)
- Payload ACC (regarded as a sensor for drag control)
- Payload DWS (differential wavefront sensing for fine pointing control)
- Dedicated laser acquisition sensor on optical bench
- Dedicated acquisition laser source on optical bench

As actuators pulse width modulated cold gas thrusters and magnetic torquers are chosen, which are adequate for formation control and pointing at the chosen orbit altitude. Pointing simulations show that with that concept the laser pointing requirements (2 mrad for roll and 0.1 mrad for pitch and yaw) can be fulfilled. As pointing strategy spacecraft pointing is selected instead of using steering mirrors.

Figure 8-4 shows that the drag compensation requirements can be fulfilled as well with 1 Hz thruster pulses. The accelerations without drag compensation are decreased below the requirement spectrum within the measurement bandwidth (MBW). Furthermore it is analysed that with the foreseen propulsion system at the chosen orbital height a mission lifetime of more than 10 years is feasible. Figure 8-5 finally identifies that with the chosen AOCS concept the pointing requirements to be achieved in order to keep the laser link locked are reachable.

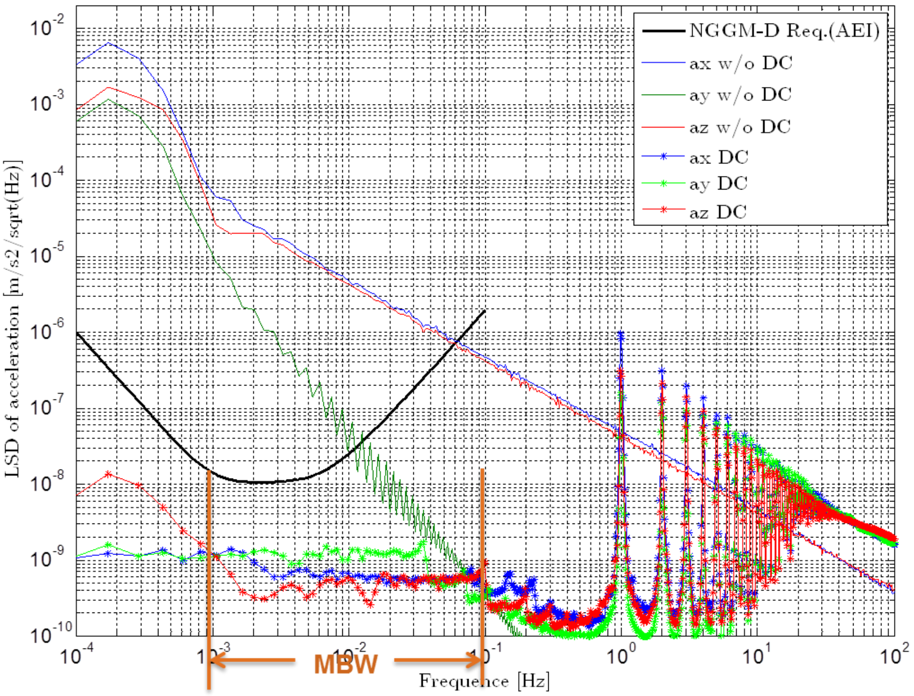

Figure 8-4: Accelerations with and without drag compensation using the selected AOCS concept in comparison with the e^2.motion requirement for the residual drag (black).

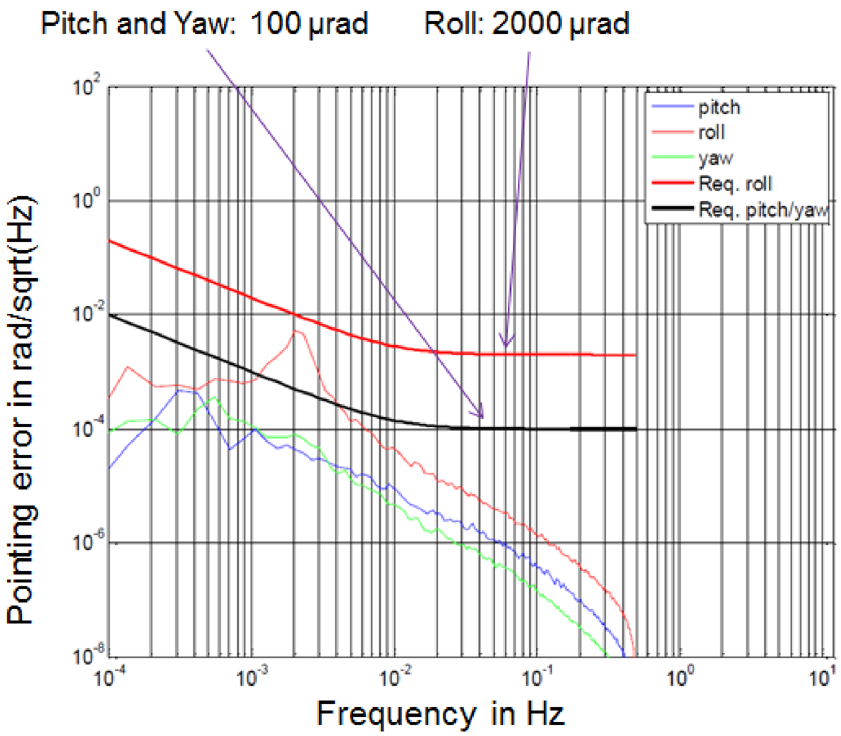

Figure 8-5: Pointing requirements versus achievable pointing accuracies for all three axes

8.4 Instrument Concept

In close connection with the design of the AOCS concept the instrument concept of e^2.motion is designed. The payload consists of the following main instruments.

- Laser ranging interferometer (LRI)
- Accelerometer (ACC)
- GNSS receiver

- Star tracker
- High performance temperature sensors

Figure 8-6 point out the instrument concept and how the individual instruments are linked to each other. The main instruments required to achieve the science requirements are the laser interferometer and the accelerometer. GNSS receiver, star trackers as well as temperature sensors are essential for attitude and orbit control and for calibration purposes.

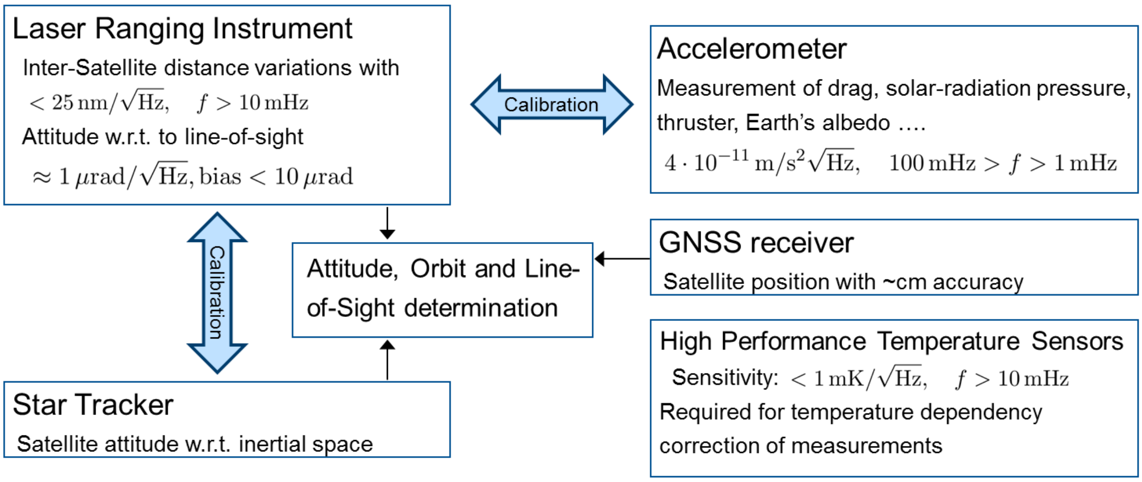

Figure 8-6: Instrument (payload) concept

The laser interferometer and the accelerometer as core instruments observe differential accelerations between each satellite pair originating from gravitational and non-gravitational forces. This measurement concept is similar to the existing GRACE and GRACE-FO missions except that the instruments are more sensitive, i.e. they deliver observations with higher accuracies. Technology for both instruments already is in place and partly has been flown on satellites. In order to avoid saturation of the highly sensitive accelerometer a drag compensation at least in flight direction is required. Different drag compensation concepts are available. These are (1) average drag compensation, (2) average and measurement bandwidth compensation with feedback from the accelerometer to the AOCS and (3) full drag free such that the proof mass is kept in free-fall. For e^2.motion options (1) or (2) are foreseen in order to keep the complexity of the drag-free system at a reasonable level.

Together with the star trackers, the laser interferometer and the accelerometer form an integrated payload concept. They deliver independent information, which can be used for in-orbit calibration and validation of the individual instruments. In addition the GNSS receiver provides independent information for attitude determination and timing issues. Finally, high performance temperature sensors are required in order to apply temperature dependent corrections to the measurements. So-called tone errors in the measurements, which are harmonic errors at multiples of the orbit frequencies and which are caused by periodic environmental variations (mainly temperature) can play a dominant role in the overall error budget.

Figure 8-7 shows the frequency dependent amplitude spectral densities for the requirements of the two core instruments, their combination as well as for the drag compensation requirements and the upper limit of the drag signal. As it can be identified the long wavelength errors are dominated by the accelerometer performance, while the high frequencies are driven by the laser interferometer performance. This means it is essential, that both core instruments in terms of their spectral performance do not "disturb" each other, or in other words, none of both instruments should be the limiting factor over the designed measurement bandwidth (which is determined from the target spatial resolution). The drag compensation requirement has to be regarded versus the non-gravitational forces in the spectral domain. From Figure 8-7 it becomes obvious that drag compensation is required in the measurement bandwidth in order to avoid saturation of the accelerometer. At the upper limit of the measurement bandwidth the drag signal is below the requirement, which implies that there is no need for drag compensation in this frequency range.

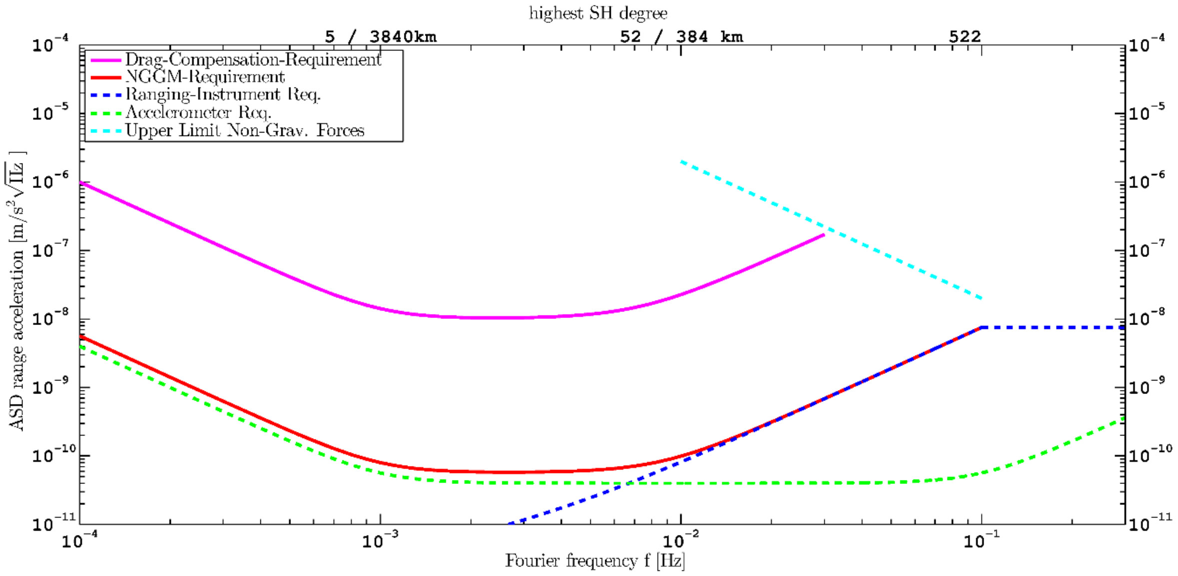

Figure 8-7: Laser interferometer and accelerometer requirements versus drag compensation requirement and non-gravitational forces signal in terms of amplitude spectral densities for range accelerations.

8.5 Observation Simulations

In order to enable a full numerical simulation simulated observation and their errors have been generated. For this a true world, which represents the signal to be recomputed and a reference world, which represents the knowledge prior to e^2.motion has been defined. Table 8-5 specifies the models applied.

In a first step observations for a selected simulation time period (1.3.2004 to 2.4.2004 = 32 days) and for each measurement epoch orbits, inter-satellite ranges, range-rates and range-accelerations, satellite attitude and non-gravitational accelerations were computed from the true world and a number of standard models. This task was performed for each satellite pair separately.

Table 8-5: Simulation models representing the true and reference world (all models given in spherical harmonic coefficients and used up to degree 150, except for ocean tides)

	True world	Reference world
Static	GOCE DIR 4	GOCO03S
Non tidal time varying gravity	AOHIS	AOHIS + AO-errors
Ocean tides (8 constituents)	EOT08a (l_{max}=50)	GOT4.7 (l_{max}=50)

For the reference world in addition an error for the non-tidal time variable gravity field has been estimated, which shall account for errors of the de-aliasing process applied during gravity field recovery. Here only errors for the atmosphere and oceans (AO) are taken into consideration as de-aliasing only is required for time variable gravity field signals with temporal frequencies shorter than the recovery period of 32 days. One can assume that the other signals involved as hydrology, ice masses and solid Earth (HIS) do not vary significantly within a month and therefore are observed with the monthly gravity field solution. For this study an empirical approach for the AO error modelling was applied, which includes a 10% signal dependent part and a 5% random part, assuming that the uncertainty is at the order of 15% of the full AO signal. Figure 8-8 shows the AO errors versus the HIS signal.

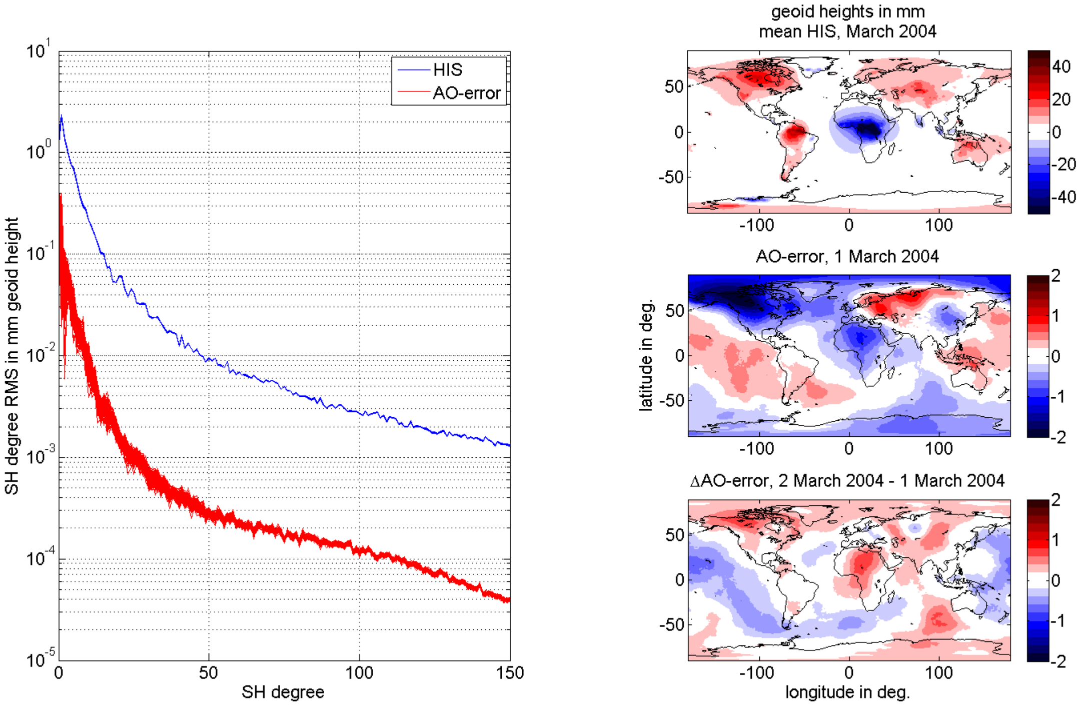

Figure 8-8: Spectral and spatial representation of HIS and AO-errors. Left: SH degree RMS in mm geoid heights of HIS and AO-errors for March 2004 (124 epochs, 6 hour sampling) up to l_{max}=150. Right: global geoid heights in mm of the mean HIS signal for March 2004 (Top, 7.71 mm global RMS) of the AO-errors for 1st of March (Center, 0.45 mm global RMS) and the AO-error change from 1st to 2nd of March (Bottom, 0.29 mm global RMS).

To take into account instrumental errors coloured noise PSD’s for the accelerometer and the laser interferometer were taken into consideration. Here we made use of the spectral error curves as shown in Figure 8-7 (refer to accelerometer and ranging instrument requirements). These coloured noise PSD’s were transformed into noise time series and added to the error free measurements. By this one gets realistic noisy measurement data sets, which corresponds to the specifications of the instruments. As a second version tone errors for both instruments were taken into consideration and additionally added to the noisy instrument data sets in order to identify the impact of the tone errors on the retrieved gravity field. The impact was analysed in a separate simulation activity and it was identified that only the very low degree coefficients (up to degree 3) are influenced by these harmonic tone errors.

In summary as preparatory step for the full numerical simulations two versions of noisy instrument time series were created, in addition for the retrieval errors for the atmosphere and ocean geophysical models were added to the reference world in order to simulate the impact of the de-aliasing error.

8.6 Numerical Simulations

Finally, numerical simulations applying different approaches have been performed in order to retrieve the true world monthly gravity field making use of simulated observations and the reference models (including errors for the atmosphere and ocean models). Figure 8-9 shows the processing flow of the numerical simulations. In order to derive quality estimates about how good the gravity field retrieval could be performed one simply compares the resulting field with the true world model. Differences for a number of scenarios have been computed to isolate the effects of instrumental and model errors.

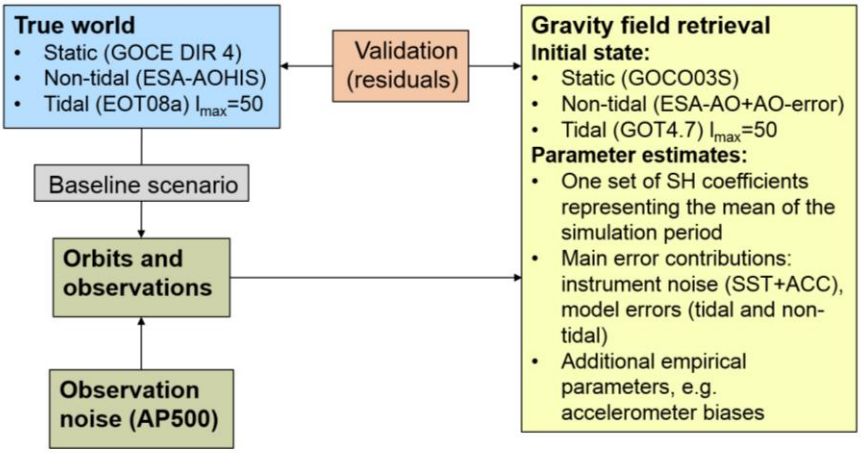

Figure 8-9: Flow chart for numerical simulation procedure

Figure 8-10 shows the results for different numerical simulation approaches applying different error scenarios. As a first result one can observe that the different approaches provide mostly consistent results, which gave us confidence that all approaches are correctly implemented. As a second result we can derive that model errors dominate the overall monthly gravity field retrieval error when compared to the results one can determine with instrumental errors only. This is a strong hint that there is a need to either make use of improved geophysical models (tidal and non-tidal) or to improve observability of high frequency mass variations by the satellite configuration in order to reduce the impact of model errors. One can compare these results with the science requirements as they have been defined in Table 2-14. Taking all error sources into account one can identify that the 1 mm geoid height performance roughly is reached at degree 130, which corresponds to about 154 km spatial resolution. This is slightly above the optimum science requirements.

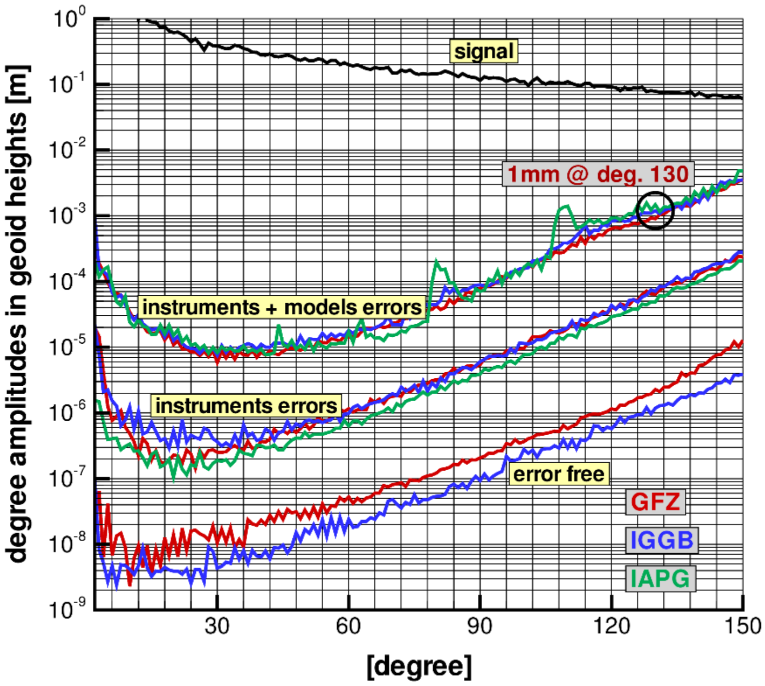

Figure 8-10: Degree amplitude differences in terms of geoid heights between the true world and the retrieved gravity field for 1 month applying different numerical simulation approaches (IAPG: acceleration approach, GFZ: numerical integration method, IGGB: integral equation approach) and different error scenarios (error free, instrument errors only, instrument and model errors).

In order to get a complete picture about the mission performance one needs to look to the cumulative geoid height errors. Figure 8-11 shows the results for one of the numerical simulation approaches (integral equation). Of special interest are the cumulative geoid errors for the minimum and optimum science requirements, which are 1 mm for 200 km spatial resolution (corresponding to degree 100) and 1 mm for 150 km spatial resolution (corresponding to degree 133), respectively. As already identified above one can conclude from the results that model errors play a dominant role for the error level, while the pure instrument performances by far are good enough to reach the science goals. From Figure 8-11 we can read that the minimum mission goals can be easily reached while the optimum monthly science requirements cannot be met with the current knowledge of the external models. Taking all model errors (atmosphere/ocean and tides) into account the 1 mm geoid height error can be achieved up to degree 110 corresponding to 182 km spatial resolution.

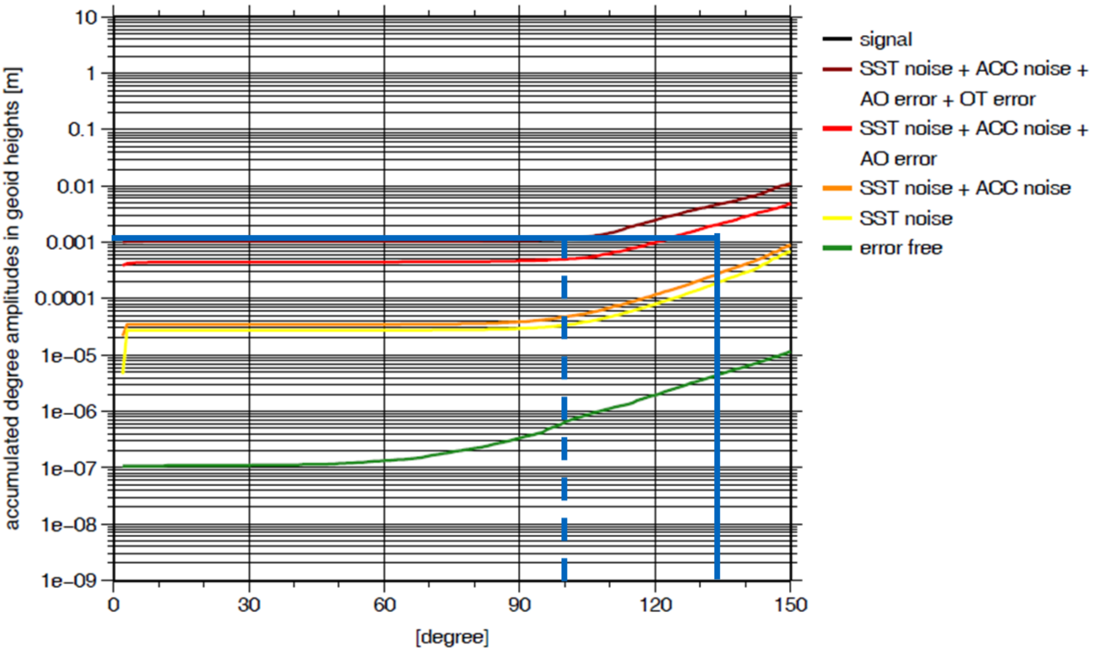

Figure 8-11: Cumulative geoid height errors from numerical simulations (integral equation approach) for different error scenarios (error free; satellite-to-satellite tracking (SST) instrument noise; SST plus accelerometer (ACC) noise; total instrument plus atmosphere/ocean (AO) model error; Instrument plus AO plus ocean tide (OT) model errors); blue lines mark the science requirements as identified in chapter 2 (dashed line refers to minimum, solid line to optimum).

In order to identify the spatial structure of the resulting geoid height errors in Figure 8-12 the corresponding maps for the numerical integration (GFZ) and the integral equation (IGGB) approaches are shown for the instrument noise and the instrument plus model error cases. The results show the cumulative geoid errors up to degree 150 corresponding to a spatial resolution of 133 km (lower than the optimal science requirement). Results show slightly more optimistic results for the numerical integration approach. An important feature in Figure 8-12 is that both approaches show a somehow well balanced geographical structure of the geoid errors without the well-known longitudinal stripes of a single pair GRACE like mission (refer also to Figure 8-13). In both simulations one can identify some latitude dependent structures, which need to be investigated in more detail. This is supported by the results shown in Figure 8-13 where results for a single pair polar mission and a double pair polar/inclined mission scenario are compared applying the same instrumental and model errors. While for the single pair mission longitudinal stripes can be clearly identified, the double pair mission exhibits a factor of 25 smaller global rms of geoid height residuals without such stripes. By reducing the colour bar range again one can identify some latitude dependent structures.

As a result of these numerical simulations one can conclude that a double pair mission significantly will improve the geoid performance, but that model errors still play a prominent role in the error budget. Under the assumption that the model errors as they have been defined in this study are realistic (may be they are even pessimistic), there is a need either to improve the background models to some extend or alternatively to improve observability of the higher frequent mass variable signal. This is ensured by the mission requirement to obtain global orbit coverage with weekly or shorter periods with a reduced spatial resolution. This was not subject of this work and is currently investigated in a separate study.

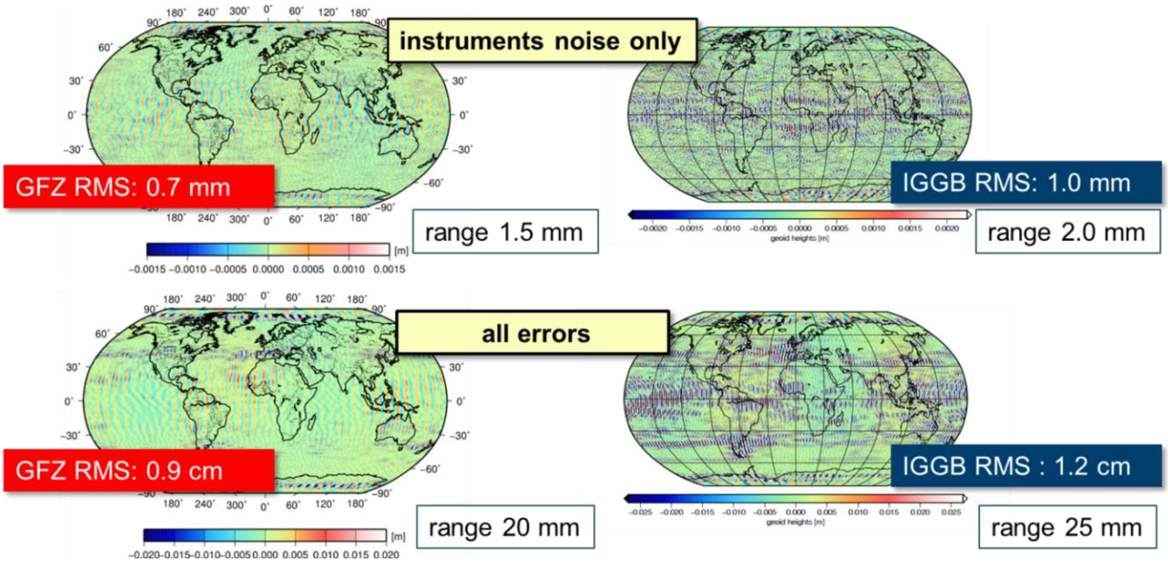

Figure 8-12: Geographical maps of geoid height residuals from the integral equation (IGGB) and numerical integration (GFZ) approaches up to degree and order 150 (cumulative).

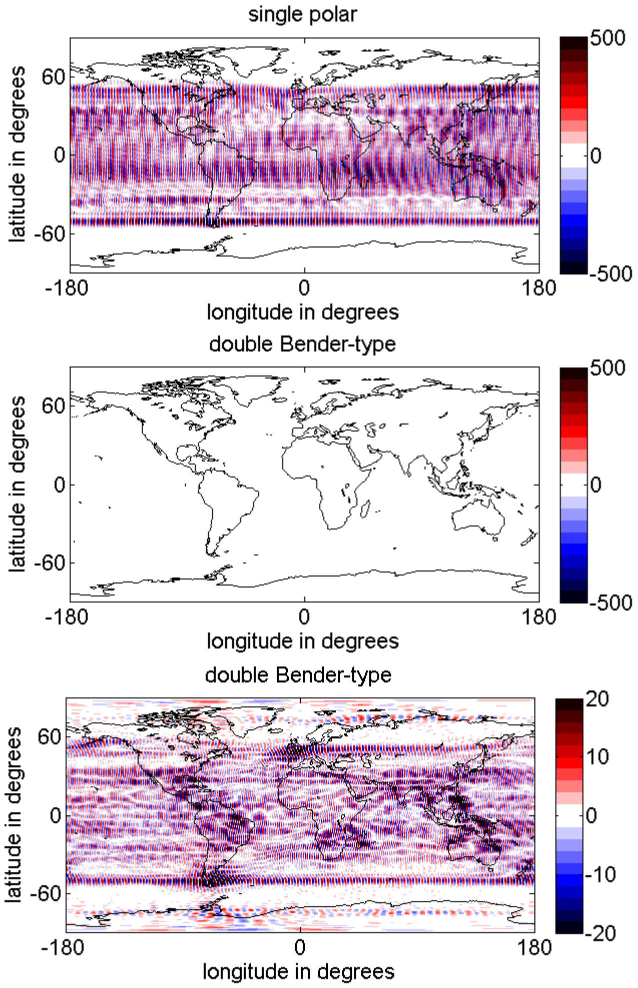

Figure 8-13: Single-pair polar versus double pair (polar/inclined) geoid height residuals up to degree 133 (corresponding to 150 km spatial resolution) from the acceleration approach. Top: single polar-pair with geoid height rms of 146.2 mm; Middle: double pair (Bender configuration) with geoid height rms of 5.7 mm; Bottom: same as middle but different colour bar.

8.7 Summary

The following table provide a summary of the mission concept and the results obtained from simulations as it has been described in detail in the previous chapters.

Science and Mission Requirements
1mm monthly geoid error @ 150 km spatial resolution (minimum @200 km)
Decadal mission duration
Weekly and shorter temporal resolution
Monthly repeat cycle with good ground-track coverage for shorter periods
Orbital height between 350 and 450 km
Key instrument accuracies: Distance: 40-200 nm/Hz$^{1/2}$ (f > 10 mHz) Accelerometer: 4x10^{-11} and 2x10^{-10} m/s²/Hz$^{1/2}$ (1 < f < 10 mHz)
Orbit Configuration
Double pair low-low SST mission (polar and inclined pair)
Near polar (89.5 deg.) and inclined (70 deg.)
Both altitudes around 420 km
100 km inter-satellite distance
Repeat cycle: 31 days with 478 (polar pair) and 474 (inclined pair) revolutions respectively
AOCS Concept
AOCS concept fulfils laser pointing requirements
AOCS fulfills drag compensation requirements: Residual drag < 1E^{-8} m/s²
PWM cold gas thrusters
Magnetic torquers
Instrument Concept
First mission with inter-satellite interferometer as main instrument: Laser noise < 25 nm
Accelerometer: ACC noise <4x10^{-11} m/s^2
GNSS Receiver
Star Tracker
High performance temperature sensors
Observation Simulation
Tone error requirements identified
Realistic orbits and error free observation
Realistic noise time series
Definition of background models (true and reference world)
Definition of background model errors
Numerical Simulations
Consistent independent solutions
Main error contribution: atmosphere/ocean and tide model errors (current state)
1 mm cumulative geoid error @ 182 km (without ocean tides 160 km)
Total errors: double Bender-type better than single polar by a factor of 25

9 References

9.1 Previous Study Reports

[1] Scientific Objectives for Future Geopotential Missions, Technical Note, R. Rummel, J. Flury, R. Haagmans, Ch. Hughes, P. LeGrand, J. Riegger, E. Schrama, N. Sneeuw, B. Vermeersen, P. Woodworth; Draft Version 6, 29. October 2001.

[2] Enabling Observation Techniques for Future Solid Earth Missions, Final Report ESA Contract 16668/02/NL/MM, Document: SolidEarth-TN-ASG-009 Issue 2, EADS Astrium GmbH, 15. July 2004.

[3] Laser Doppler Interferometry Mission for Determination of the Earth's Gravity Field, Executive Summary ESA Contract 18456/04/NL/CP, Document: SD-RP-AI-0447, Alcatel Alenia Space, 19. December 2005.

[4] The Future of Satellite Gravimetry, Report from the Workshop on The Future of Satellite Gravimetry, 12-13. April 2007 Noordwijk, The Netherlands, R. Koop, R. Rummel (Eds.), Technische Universität München, 27. February 2008.

[5] Laser Interferometry High Precision Tracking for LEO, Summary Report, Document: SD-RP-AI-0584, Thales Alenia Space, 10. September 2008.

[6] Monitoring and Modelling individual Sources of Mass Distribution and Transport in the Earth system by means of Satellites, Final Report ESA Contract 20403, T. van Dam, P. Visser, M. Losch, N. Sneeuw, M. Bierkens, M. King, J. Bamber, T. Gruber, M. Smit, November 2008.

[7] System Support to laser Interferometry Tracking Technology Development for Gravity Field Monitoring, Summary Report, Document: SD-RP-AI-0589, Thales Alenia Space, 11. December 2008.

[8] Objectifs scientifiques pour une future mission de gravimétrie spatiale – Projet Microméga, I. Panet, G. Ramillien, A. Lombard, March 2009.

[9] e.motion Earth System Mass Transport Mission, Proposal for Earth Explorer Opportunity Mission EE-8, e.motion Proposal Team, May 2010.

[10] Assessment of a Next Generation Mission for Monitoring the Variations of Earth's Gravity, Final Report, Document SD-RP-AI-0668, Thales Alenia Space, 22. December 2010.

[11] Assessment of a Next Generation Mission for Monitoring the Variations of Earth's Gravity, Final Report, Document NG2-ASG-FR, Astrium GmbH, 10. October 2011.

[12] NGO ASSESSMENT STUDY REPORT (YELLOW BOOK), January 2012, ESA/SRE(2011)19

[13] Laser Interferometer Space Antenna: A Cornerstone Mission for the Observation of Gravitational Waves System and Technology Study Report, July 2000, ESA-SCI (2000)11

9.2 Scientific Papers

Bender, P., Wiese, D., & Nerem, R. (2008). A possible dual-GRACE mission with 90 degree and 63 degree inclination orbits. *Third Int. Symposium on Formation Flying*. Noordwijk, Netherlands.

Ellmer, M. (2011). *Optimization of the orbit parameters of future gravity missions using genetic algorithms.* Master Thesis, Universität Stuttgart, Geodetic Institute.

Elsaka, B. (2010). *Simulated satellite formation flights for detecting temporal variations of the earth's gravity field.* Bonn: Universität Bonn.

Elsaka, B., Raimondo, J., Brieden, P., Reubelt, T., Kusche, J., Flechtner, F., . . . Müller, J. (2014). Comparing seven candidate mission configurations for temporal gravity retrieval through full-scale numerical simulation. *Journal of Geodesy, 88*, pp. 31-43.

Flechtner, F., Dahle, C., Neumayer, K., König, R., & Förste, C. (2010). The release 04 CHAMP and GRACE EIGEN gravity field models. In F. Flechtner, T. Gruber, A. Güntner, M. Mandea, M. Rothacher, T. Schöne, & J. Wickert, *System Earth via geodetic-geophysical space techniques* (pp. 41-58). Heidelberg, Dordrecht, London, New York: Springer.

Gruber, T., Bamber, J., Bierkens, M., Dobslaw, H., Murböck, M., Thomas, M., . . . Visser, P. (2011). Simulation of the time-variable gravity field by means of coupled geophysical models. *Earth System Science Data, 3*(1), S. 19-35.

Iran-Pour, S. (2013). *Sampling the Earth's time-variable gravity field from satellite orbit - Design of future gravity satellite missions.* Ph Thesis, Universität Stuttgart.

Iran-Pour, S., Reubelt, T., & Sneeuw, N. (2013). Quality assessment of sub-Nyquist revovery from future gravity satellite missions. *Advances in Space Research, 52*(5), pp. 916-929.

Klees, R., Ditmar, P., & Broersen, P. (2002). How to handle coloured observation noise in large least-squares problems. *Journal of Geodesy, 76*, S. 629-640.

Kusche, J., Schmidt, R., Petrovic, S., & Rietbroek, R. (2009). Decorrelated GRACE time-variable gravity solutions by GFZ, and their validation using a hydrological model. *Journal of Geodesy, 83*(10), pp. 903-913.

Lyard, F., Lefevre, F., Lettelier, T., & Francis, O. (2006). Modelling the global ocean tides: a modern insight from FES2004. *Ocean Dynamics, 56*, pp. 394-415.

Mayer-Gürr, T. (2006). *Gravitationsfeldbestimmung aus der Analyse kurzer Bahnbögen am Beispiel der Satellitenmissionen CHAMP und GRACE.* Schriftenreihe des Instituts für Geodäsie udn Geoinformation der Universität Bonn, Bonn.

Mayer-Gürr, T., Eicker, A., Kurtenbach, E., & Ilk, K. (2010). ITG-GRACE: Global static and temporal gravity field models from GRACE data. In F. Flechtner, T. Gruber, A. Güntner, M. Mandea, M. Rothacher, T. Schöne, & J. Wickert, *System Earth via geodetic-geophysical space techniques* (pp. 159-168). Heidelberg, Dordrecht, London, New York: Springer.

Murböck, M., Pail, R., Daras, I., & Gruber, T. (2014). Optimal orbits for temporal gravity recovery regarding temporal aliasing. *Journal of Geodesy, 88*(2), pp. 113-126.

Panet, I., Flury, J., Biancale, R., Gruber, T., Johannessen, J., van den Broeke, M., . . . Thomas, M. (2013). Earth System Mass Transport Mission (e.motion): A Concept for Future Earth Gravity Field Measurements from Space. *Surveys in Geophysics, 34(2)*, pp. 141-163.

Reubelt, T., Sneeuw, N., & Sharifi, M. (2010). Future mission design options for spatio-temporal geopotential recovery. In S. Mertikas (Ed.), *Gravity, Geoid and Earth Observation. International Association of Geodesy Symposia Vol. 135.* Chania, Greece: Springer.

Reubelt, T., Sneeuw, N., Iran-Pour, S., Hirth, S., Fichter, W., Müller, J., . . . Pelivan, L. (2014). Future gravity field satellite missions. In F. Flechtner, N. Sneeuw, & W. Schuh, *Observation of te system earth from space - CHAMP, GRACE, GOCE and future missions* (Vol. GEOTECHNOLOGIEN Science Report No. 20). Springer.

Savcenko, R., & Bosch, W. (2008). *EOT08a - empirical ocean tide model from multi-mission satellite altimetry.* München: DGFI.

Schneider, M. (1968). *A general method of orbit determination.* Library Translation 1279, Royal Aircraft Establishment, Ministry of Technology, Farnborough, England.

Schuh, W. (1996). *Tailored numerical solution strategies for the global determination of the Earth's gravity field.* Graz: Mitteilungen der Geodätischen Institute der Technischen Universität Graz.

Sharifi, M., Sneeuw, N., & Keller, W. (2007). Gravity recovery capabilities of four generic satellite formations. In A. Kilicoglu, & R. Forsberg (Ed.), *Gravity Field of the Earth. Special Issue 18*, pp. 211-216. Istanbul: General Command of Mapping.

Sheard, B., Heinzel, G., Danzmann, K., Shaddock, D., Klipstein, W., & Folkner, W. (2012). Intersatellite laser ranging instrument for the GRACE follow-on mission. *Journal of Geodesy*, pp. 1083-1095.

Smutny, B., Lange, R., Kämpfner, H., Dallmann, D., Mühlnikel, G., Reinhardt, M., . . . Czichy, R. (2008). In-orbit verification of optical inter-satellite communication links based on homodyne BPSK. *Proc. SPIE 6877, Free-Space Laser Communication Technologies XX, 687702.* San Jose, CA.

Sneeuw, N. (2000). *A semi-analytical approach to gravity field analysis from satellite observations.* München: Deutsche Geodätische Kommission bei der Bayerischen Akademie der Wissenschaften.

Swenson, S., & Wahr, J. (2002). Methods for inferring regional surface-mass anomalies from Gravity Recovery and Climate experiment (GRACE) measurements of time-variable gravity. *Journal of Geophysical Research, 107*(B9), pp. ETG 3-1 - ETG-3-13.

Visser, P., Sneeuw, N., Reubelt, T., Losch, M., & van Dam, T. (2010). Space-borne gravimetric satellite constellations and ocean tides aliasing effects. *Geophysical Journal International, 181*, pp. 789-805.

Weigelt, M., Sneeuw, N., Schrama, E., & Visser, P. (2012). An improved sampling rule for mapping geopotential functions of a planet from a near polar orbit. *Journal of Geodesy.*

Wiese, D., Folkner, W., & Nerem, R. (2009). Alternative mission architectures for a gravity recovery satellite mission. *Journal of Geodesy, 83*, pp. 569-581.

Wiese, D., Nerem, R., & Lemoine, F. (2011). Design considerations for a dedicated gravity recovery satellite mission consisting of two pairs of satellites. *Journal of Geodesy*, pp. 81-98.

Wiese, D., Visser, P., & Nerem, R. (2011). Estimating low resolution gravity fields at short time intervals to reduce temporal aliasing errors. *Advances in Space Research, 48*(6), S. 1094-1107.

Zenner, L. (2013). *Atmospheric and oceanic mass variations and their role for gravity field determination.* München: Deutsche Geodätische Kommission.

Annexes

List of Acronyms

ACC	Accelerometer
AEI	Max-Planck-Institut für Gravitationsphysik – Albert Einstein Institut, Teilinstitut Hannover
AOCS	Attitude and Orbit Control System
ASD	Amplitude Spectral Density
ASG	Airbus Defence & Space, Immenstaad
AST	Advanced Space Technologies GmbH
CESS	Coarse Earth and Sun Sensor
CoM	Center of Mass
CoS	Center of Satellite
DWS	Differential Wavefront Sensing
e^2.motion	Earth System Mass Transport Mission – Version 2
EWH	Equivalent Water Heights
GFO	GRACE-Follo-On
GFZ	Helmholtz-Zentrum Potsdam Deutsches GeoForschungsZentrum (GFZ)
GIA	Glacial Isostatic Adjustment
GIS	Geodätisches Institut, Universität Stuttgart
GRACE	Gravity Recovery and Climate Experiment
GRACE-FO	GRACE-Follow-On
IAPG	Institut für Astronomische und Physikalische Geodäsie, Technische Universität München
IfE	Institut für Erdmessung, Leibnitz Universität Hannover
IGG	Institut für Geodäsie und Geoinformation, Universität Bonn
KoS	Coordinate System
ll-SST	low-low Satellite-to-Satellite-Tracking
LoS	Line of Sight
LSD	Linear Spectral Density
LTAN	Local Time of Ascending Node
LTPDA	Lisa Technology Package Data Analysis
LVLH	Local Vertical Local Horizontal
MoI	Moment of Inertia
µRIT	micro Radio-frequency Ion Thruster
NGGM	Next Generation Gravity Field Mission
NSF	Noise Shape Function
OBA	Optical Bench Assembly
PSD	Power Spectral Density
PWM	Pule Width Modulation
QLT	Quick-Look Tool
RMS	Root Mean Square
SC	Spacecraft
SST	Satellite-to-Satellite Tracking
STI	Space Tech GmbH
TAS	Thales Alenia Space
TMA	Triple Mirror Assembly
TransMIT	Gesellschaft für Technologietransfer mbH, Gießen